CHARM JETS

PRODUCTION AND FRAGMENTATION OF D^0-TAGGED CHARGED-PARTICLE JETS IN SMALL COLLISION SYSTEMS

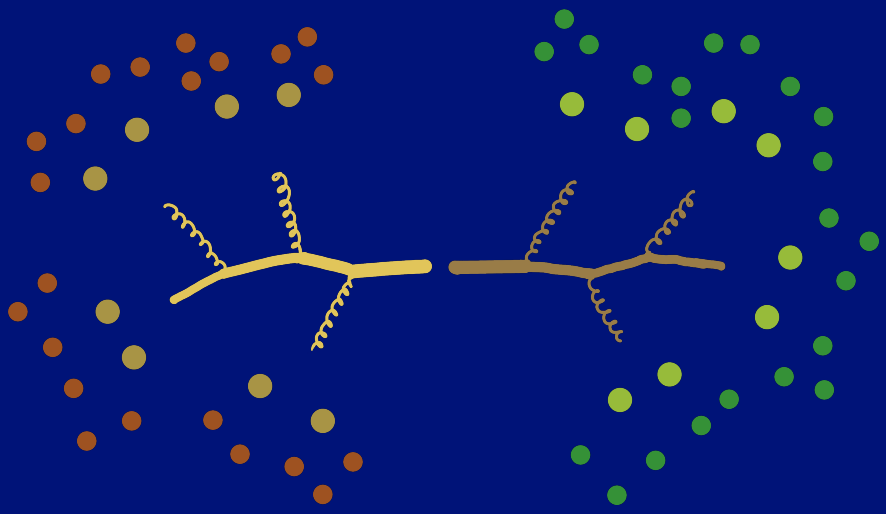

AURO PRASAD MOHANTY

CHARM JETS

PRODUCTION AND FRAGMENTATION OF D^0-TAGGED CHARGED-PARTICLE JETS IN SMALL COLLISION SYSTEMS

AURO PRASAD MOHANTY

DOI: https://doi.org/10.33540/2018

A catalogue record is available from the Utrecht University Library.

Cover design by Auro Prasad Mohanty. *The Charm Tree*: Visualizing the parton showers resulting from a charm quark and an anticharm quark in the form of a tree, its branches, and its roots.

Printed on recycled paper.

CHARM JETS

PRODUCTION AND FRAGMENTATION OF D^0-TAGGED CHARGED-PARTICLE JETS IN SMALL COLLISION SYSTEMS

CHARM JETS

PRODUCTIE EN FRAGMENTATIE VAN D^0-GEMERKTE JETS VAN GELADEN DEELTJES IN KLEINE BOTSINGSSYSTEMEN

(met een samenvatting in het Nederlands)

ଚାର୍ମ୍ ଜେଟ୍

କ୍ଷୁଦ୍ର ସଂଘର୍ଷ ପ୍ରଣାଳୀରେ ଡି୦-ଜଡ଼ିତ ଆବେଶିତ-କଣିକା ଜେଟ୍ ର ଉତ୍ପାଦନ ଏବଂ ଖଣ୍ଡବିଖଣ୍ଡନ

(ଓଡିଆରେ ଏକ ସାରାଂଶ ସହିତ)

PROEFSCHRIFT

ter verkrijging van de graad van doctor aan de
Universiteit Utrecht
op gezag van de rector magnificus, prof.dr. H.R.B.M. Kummeling,
ingevolge het besluit van het college voor promoties
in het openbaar te verdedigen op

dinsdag 7 november 2023 des middags te 12:15 uur

door

AURO PRASAD MOHANTY

geboren op 18 Augustus 1992 te Bhubaneswar, India

PROMOTOR:	Prof. dr. T. Peitzmann
CO-PROMOTORS:	Dr. A. Mischke †
	Dr. A. Grelli
ASSESSMENT COMMITTEE:	Prof. dr. C.F.F. van den Broeck
	Prof. dr. E.L.M.P. Laenen
	Prof. dr. P.J. Mulders
	Prof. dr. R.J.M. Snellings
	Dr. B.A. Trzeciak

This research was partially funded by the Netherlands Organization for Scientific Research/Nederlandse Organisatie voor Wetenschappelijk Onderzoek (NWO).

CONTENTS

1 CURIOSITY 1
- 1.1 Curiosity about the hottest thing in the universe 1
- 1.2 Jets 2
- 1.3 Heavy-flavour jets 2
- 1.4 Charm jets 2
- 1.5 Thesis organization 3

2 INTRODUCTION TO STRONG INTERACTIONS 5
- 2.1 QCD Lagrangian 5
- 2.2 Connecting theories with experiments 7
  - 2.2.1 Scattering 8
- 2.3 Solving QCD: the perturbative approach 9
- 2.4 Asymptotic freedom and confinement 10
- 2.5 Solving QCD: the non-perturbative approach 12
- 2.6 Parton shower and hadronization 14
  - 2.6.1 PYTHIA and the String model 15
- 2.7 Conclusion 17

3 HEAVY-FLAVOUR JETS 19
- 3.1 Physics goal 19
- 3.2 Quark–gluon plasma 19
- 3.3 Perturbative QCD 20
- 3.4 Cold-nuclear matter effects 22
- 3.5 Heavy flavours or heavy-flavour jets 23

4 EXPERIMENTAL FRAMEWORK 25
- 4.1 The ALICE detector 26
  - 4.1.1 Time Projection Chamber 27
  - 4.1.2 Inner Tracking System 28
  - 4.1.3 Time-Of-Flight detector 29
- 4.2 Reconstruction of tracks and vertices 29
- 4.3 The ALICE offline framework 30

5 ANALYSIS STRATEGY FOR CHARM JETS 31
- 5.1 D^0-meson reconstruction 31
  - 5.1.1 Distance of closest approach 32
  - 5.1.2 Decay angle 33
  - 5.1.3 Impact parameters of D^0 daughters, and their product 33
  - 5.1.4 Pointing angle 34
  - 5.1.5 Normalized decay length (lifetime) 35
  - 5.1.6 Invariant mass 35
- 5.2 Jet reconstruction 36
  - 5.2.1 Finding jets 36
  - 5.2.2 Jet finding algorithms: k_T and anti-k_T 37
  - 5.2.3 Correcting for the underlying event 39
  - 5.2.4 Random cones for background fluctuations 41

5.2.5 Unfolding algorithms 41
5.2.6 Bayesian Unfolding 43
5.2.7 Singular Value Decomposition 44
5.2.8 Choosing regularization in unfolding 45
5.3 Charm-jet candidates 46
6 CHARM-JET PRODUCTION IN VACUUM 47
6.1 Physics goals 47
6.2 Raw yields differential in $p_{\mathrm{T,ch\,jet}}$ 47
6.3 Corrections 49
6.3.1 Reconstruction efficiency 49
6.3.2 B-meson decay contribution 50
6.3.3 Unfolding the jet spectra 51
6.4 Systematic uncertainties 53
6.4.1 Topological selection 54
6.4.2 Raw-yield extraction: multi-trial 54
6.4.3 Raw-yield extraction: signal and sideband ranges, and D^0 reflections 57
6.4.4 B-feed-down subtraction 57
6.4.5 Unfolding: Stability in Bayesian approach 59
6.4.6 Unfolding: Stability against SVD unfolding 61
6.4.7 Unfolding: Closure test 61
6.4.8 Tracking efficiency 63
6.4.9 Correlated uncertainties 63
6.5 Physics results 64
6.5.1 Cross sections differential in $p_{\mathrm{T,ch\,jet}}$ 64
6.5.2 Collision-energy cross-section ratios 67
6.5.3 D^0-jet fraction of inclusive charged jets 68
6.5.4 Cross-section ratios for different R 69
6.6 Summary 70
7 COLD NUCLEAR-MATTER EFFECTS ON CHARM-JET PRODUCTION 73
7.1 Physics goals 73
7.2 Nuclear modification factor R_{pPb} 73
7.3 Underlying-event subtracted $p_{\mathrm{T,ch\,jet}}$-differential raw yields 74
7.4 Corrections 75
7.4.1 Underlying event and background fluctuations 75
7.4.2 Reconstruction efficiency 76
7.4.3 B-meson decay contribution 77
7.4.4 Unfolding 78
7.5 Systematic uncertainties 80
7.5.1 Topological selection 80
7.5.2 Raw-yield extraction: multi-trial 82
7.5.3 Raw-yield extraction: signal and sideband ranges 83
7.5.4 Raw-yield extraction: reflections 84
7.5.5 B-feed-down subtraction 85
7.5.6 Unfolding: Stability in Bayesian approach 85

7.5.7 Unfolding: Stability against change in ranges and SVD unfolding 86
7.5.8 Background-fluctuation matrix 87
7.5.9 Tracking efficiency 88
7.5.10 Correlated systematic uncertainties for R_{pPb} 89
7.6 Physics results 92
7.7 Summary 94
8 FRAGMENTATION OF CHARM JETS IN VACUUM 97
8.1 Physics target 97
8.2 Raw yields differential in $z_{\parallel}^{\mathrm{ch}}$ 97
8.3 Corrections 98
8.3.1 Reconstruction efficiency 98
8.3.2 B-meson decay contribution 100
8.3.3 Unfolding the two dimensional spectra 101
8.3.4 Response matrix and reconstruction-efficiency correction 102
8.3.5 Correction of spectra by kinematic efficiency 103
8.4 Systematic uncertainties 106
8.4.1 Topological selection 106
8.4.2 Raw-yield extraction: multi-trial 107
8.4.3 Raw-yield extraction: signal and sideband ranges 108
8.4.4 Raw-yield extraction: D^0 reflections 109
8.4.5 B-feed-down subtraction 109
8.4.6 Bayesian unfolding and a closure test 111
8.4.7 Tracking efficiency 112
8.5 Physics results 113
8.6 Summary 115
9 SUMMARY 125
10 OUTLOOK 127

BIBLIOGRAPHY 129
SAMENVATTING 137
ସାରାଂଶ 139
ACKNOWLEDGEMENTS 141
COURSE OF LIFE 145

1 CURIOSITY

1.1 CURIOSITY ABOUT THE HOTTEST THING IN THE UNIVERSE

Our fundamental understanding of Nature has come a long way to this day in the twenty-first century. Major developments occurred last century with Einstein's theory of relativity describing gravitation in the first half, followed by the advent of particle physics in the second. In the gravitation theory, matter defines spacetime, and the structure of space-time determines how matter moves through it. With particle physics, we started exploring the fundamental structure of matter.

All ordinary matter in this universe is made up of atoms. Every atom consists of a nucleus surrounded by a cloud of electrons. The nucleus is made up of protons and neutrons except for hydrogen that has only one proton. Protons and neutrons are a family of composite particles called hadrons which are made of quarks bound together by gluons. As yet, quarks and gluons, collectively referred to as partons, have never been observed in isolation and are always found confined in hadronic nuclear matter. This observation is usually known as confinement.

The theory of the strong nuclear force, quantum chromodynamics (QCD), predicts that the partons in nuclear matter can deconfine when sufficiently high energy densities are reached [1]. Free flowing quarks and gluons present in a deconfined state due to conditions of extreme temperatures and pressures constitute a state of matter called the quark-gluon plasma (QGP). The QGP is thought to have been the state our universe was in within the first few microseconds after the Big Bang [2]. Recent evidence [3] suggests that the quark-gluon plasma could be present in today's universe as a constituent in the core of neutron stars.

This deconfined phase of quarks and gluons has also been observed in ultrarelativistic heavy-ion collisions [4–6] where heavy nuclei are accelerated at speeds close to that of light itself before colliding with each other. The energy involved in such collisions creates an environment of extremely high temperature and pressure, causing the matter to transition into a quark-gluon plasma state.

This particular state of matter drives the curiosity of many researchers who collaborated and conducted many experiments that led to the creation of the QGP in laboratories. One such collaboration was formed in 1993 to establish and run A Large Ion Collider Experiment (ALICE) by using the Large Hadron Collider (LHC) in order to study the QGP. LHC is today the largest and highest-energy particle collider in the world. It was built and is operated by the European Organization for Nuclear Research (CERN). CERN is based in Geneva on the France-Switzerland border and hosts nine experiments including ALICE.

1.2 JETS

In ultrarelativistic collisions of two protons, two heavy ions, or even a proton and a heavy ion, quarks and gluons interact with each other and are sometimes scattered to large angles in so-called *hard scatterings*. Through the process of *hadronization*, these scattered quarks and gluons combine and reorganize themselves to form hadrons.

These newly formed hadrons tend to travel close to each other in a narrow tight cone called a jet. Jets are studied as a means to understand the original partons. Jets are also important to heavy-ion physics because when one of the two back-to-back jets goes through QGP, it can lose a significant amount of its energy, and can therefore get *quenched* [7, 8]. Measuring jets also provides a lens to look into the properties of the astonishingly hot and dense soup of QGP.

1.3 HEAVY-FLAVOUR JETS

Quarks are available in six flavours: up (u), down (d), strange (s), charm (c), beauty (b), and top (t), arranged in the order of growing mass. Up and down are the lightest of all quarks making them generally stable and abundantly available in the universe. Heavy quarks are mostly produced in high-energy collisions like in particle colliders on earth and cosmic rays from beyond earth (so stars and galaxies). So, once they are produced in high-energy collisions, they either decay into lighter quarks which ultimately hadronize, or they do not and end up in heavy-flavour hadrons[1]. Aside from primary interactions, light quarks (u, d, and s) can also be produced in secondary interactions, e. g. in a thermal system. This makes it challenging to determine the precise origin of light quarks. Do they come from high-energy collisions or from decays of heavy quarks that were created in said collisions? Consequently, light quarks are not ideal probes of QGP but heavy quarks (c and b) are. Heavy-flavour jets, which consist of hadrons containing heavy quarks, can provide valuable insights into the behaviour of heavy quarks, from their creation at the collision point to their detection as hadrons. By studying these jets, researchers can gain a deeper understanding of perturbative quantum chromodynamics (pQCD) as well as investigate the properties of the QGP by observing energy loss if heavy quarks interact with it.

1.4 CHARM JETS

This thesis contains results from studies on charm jets produced in proton–proton and proton–lead collisions. The charm jets studied by ALICE are firstly made up of charged particles which are quite easy to detect as compared to neutral particles. Secondly, the presence of a charm quark in each of the jets is determined by the presence of a D^0 ($c\bar{u}$ pair) or a $\overline{D^0}$ ($\bar{c}u$ pair) in it. D mesons are special because they are the lightest of all hadrons that contain a charm quark (c) or a charm antiquark

1 Top quark is the heaviest quark and does not hadronize [9]. Due to its high mass, the top quark decays very quickly, with a lifetime on the order of 10^{-25} seconds. This timescale is so short that the top quark does not have enough time to undergo the process of hadronization.

($\bar{c}$). Therefore, they are the most abundantly produced heavy-flavour hadrons. A D^0 ($\overline{D^0}$) meson decays into oppositely charged kaons - $s\bar{u}$ ($\bar{s}u$) - and pions - $u\bar{d}$ ($\bar{u}d$) - which are actually detected, and the parent meson is simply reconstructed back from the kaon-pion pair.

Particles and antiparticles have some common properties (e. g. mass, spin), and other properties that are equal in magnitude but opposite in sign (e. g. electric charge, baryon number, flavour). They are connected via symmetry (e. g. charge conjugation), and their production probability is similar. So, a D^0 meson when mentioned in this thesis, unless otherwise specified, refers to both the particle and its antiparticle.

1.5 THESIS ORGANIZATION

In the next chapter, quantum chromodynamics is briefly introduced and several phenomenological models for charm production at LHC energies are discussed. The experimental setup and analysis-software framework are discussed in Ch. 4. Chapter 5 discusses the common strategy on which the analyses of D^0 jets are built. Chapter 6 presents the measurements of momentum spectra of D^0 jets produced in proton–proton collisions. Similar measurements were also done for D^0 jets produced in proton–lead collisions. This is presented in Ch. 7. The momentum fraction of jets carried by their constituent D^0 mesons is measured for proton–proton collisions and is presented in Ch. 8. Chapter 9 summarizes the thesis, followed by an outlook in Ch. 10.

2 INTRODUCTION TO STRONG INTERACTIONS

Of the four fundamental forces in nature, the strongest one occurs at the subatomic level and is quite unimaginatively called the strong nuclear force. It is experienced by quarks and gluons, the elementary particles that are a fundamental constituent of matter. The latter act as mediators of the strong force. The theory of quantum chromodynamics (QCD) describes the strong nuclear interaction experienced by quarks and gluons.

2.1 QCD LAGRANGIAN

QCD Lagrangian controls the dynamics of quarks and gluons. Spin is an essential part of elementary particles as described in quantum mechanics. Particles that need to be rotated by two full rotations of 2π radians each to be brought back to the same *quantum state* are considered to be spin-$\frac{1}{2}$ particles. The quantum state of a system simply gives the probability of every possible outcome when a measurement is done on the system. So, quarks are spin-$\frac{1}{2}$ particles and are therefore described by the Dirac equation, a relativistic wave equation derived by Paul Dirac.

Working in natural units[1], the Lagrangian for a freely moving spin-$\frac{1}{2}$ particle ψ of mass m is given by two terms, one for its momentum and a second for its rest mass energy.

$$\mathcal{L} = \overline{\psi}(i\partial\!\!\!/ - m)\psi \tag{2.1}$$

The wave function ψ is a *Dirac spinor*, a four-component column vector in the *spinor field*. One intuition is that two components represent spin-up and spin-down states of the particle and the other two represent the spin-up and spin-down states of the corresponding antiparticle. The *Dirac adjoint* $\overline{\psi}$ is $\psi^\dagger\gamma^0$, and $\psi^\dagger = (\psi^*)^T$ is the complex-conjugated and transposed version of ψ. The matrix γ^0 is the time component of the gamma matrices γ^μ with the space components being $\gamma^{1,2,3}$. Gamma matrices bridge spacetime fields with the spinor fields, thus making the Lagrangian a *Lorentz invariant* quantity. The term $i\partial\!\!\!/$ is $i\gamma^\mu\partial_\mu$ and $i\partial_\mu$ is the quantum mechanical operator corresponding to the four-momentum p_μ. The four-gradient ∂_μ is $\frac{\partial}{\partial x^\mu}$, partial derivatives in the four spacetime coordinates.

Quarks and gluons possess a special degree of freedom, a quantum number called the *colour charge* that each quark or gluon carries. Even if it is unrelated to

1 Natural units are a system of measurement where the units of measurement are defined exclusively in terms of four fundamental physical constants, i. e. the speed of light in vacuum (c), reduced Planck's constant ($\hbar$), the Gravitational constant (G), and the Boltzmann constant (k_B) are set to equal 1. This choice simplifies mathematical expressions and eliminates the need for explicit unit conversions. These units are *natural* because their definition relies on fundamental properties of nature, particularly the properties of free space, rather than being based on a specific prototype object or arbitrary choices.

the everyday meanings of colour, an analogy was drawn and the three colours in QCD were termed red (r), green (g) and blue (b). Just as QED has a single charge, the electric charge (e), which can have different values (e.g. $+e$ for protons, $-e$ for electrons, 0 for neutrons, $+\frac{2}{3}e$ for up, charm and top quarks, $-\frac{1}{3}e$ for down, strange and beauty quarks), likewise, QCD has three distinct charges, r, g and b. The values for red charge can be red (r) and antired $(\overline{r})$ and similarly, g and $\overline{g}$ for green charge, and b and $\overline{b}$ for blue charge.

So, the Lagrangian for a free quark is given by Eq. 2.1 where the quark field ψ is a three-component colour-vector

$$\psi = \begin{pmatrix} \psi_r \\ \psi_g \\ \psi_b \end{pmatrix} \tag{2.2}$$

and each of the colour components ψ_r, ψ_g, ψ_b is a four-component Dirac spinor. The QCD Lagrangian needs a contribution term for quarks, $\mathcal{L}_q$, one for gluons, $\mathcal{L}_g$, and also one for quark-gluon interactions, $\mathcal{L}_{qg}$.

$SU(3)$ Lie group has $3^2 - 1 = 8$ *generators* from which all possible elements of the group can be generated from. In QCD, this corresponds to 8 *Gell-Mann* matrices λ_a and therefore eight gluon potentials A^a_μ where a goes from 1 to 8, while μ goes from 0 to 3 representing the spacetime coordinates. Combined, they give a four-potential $A_\mu = \frac{1}{2}\lambda_a A^a_\mu$. The Lagrangian for the gluon fields is given by

$$\mathcal{L}_g = -\frac{1}{2} tr(F^{\mu\nu} F_{\mu\nu}) \tag{2.3}$$

where the trace (tr) of a matrix represents the sum of its diagonal elements, and $F_{\mu\nu}$ is a *tensor*, a mathematical object from algebra with the simplest examples being *scalars* and *vectors*. $F_{\mu\nu}$ is given by

$$F_{\mu\nu} = \frac{1}{ig_s}(D_\mu D_\nu - D_\nu D_\mu) \tag{2.4}$$

where g_s is the coupling constant for strong interactions and D_μ is the *covariant derivative*. The covariant derivative is a consequence of gauge theories and is composed of the four-gradient ∂_μ and the four-potential describing the gauge fields (gluon fields in QCD). It is given by

$$D_\mu = \partial_\mu - ig_s A_\mu \tag{2.5}$$

The four-potential term above leads to the Lagrangian for quark-gluon interactions

$$\mathcal{L}_{qg} = \overline{\psi}\Big(g_s \gamma^\mu A_\mu\Big)\psi. \tag{2.6}$$

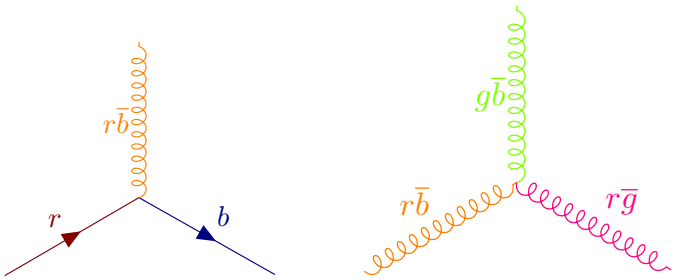

(a) Red quark r changes to a blue quark b emitting a gluon $r\bar{b}$.

(b) Gluons interacting at a vertex i. e. a three-gluon vertex.

Figure 2.1: Some fundamental QCD interactions.

It can be merged into the free-quark Lagrangian by replacing the four-gradient with the covariant derivative,

$$\begin{aligned} \mathcal{L}_{q,qg} &= \overline{\psi}(i\not{D} - m)\psi \qquad (2.7)\\ &= \overline{\psi}(i\not{\partial} - m)\psi + \overline{\psi}\left(g_s\not{A}\right)\psi \\ &= \mathcal{L}_q + \mathcal{L}_{qg} \end{aligned}$$

The final Lagrangian for QCD is thus

$$\begin{aligned} \mathcal{L}_{QCD} &= \mathcal{L}_q + \mathcal{L}_{qg} + \mathcal{L}_g \qquad (2.8)\\ &= \overline{\psi}(i\not{D} - m)\psi - \frac{1}{2}tr(F^{\mu\nu}F_{\mu\nu}) \qquad (2.9) \end{aligned}$$

This QCD Lagrangian represents a very basic interaction between quarks and gluons. A possible fundamental process depicting this interaction can be a quark field ψ in the colour state r changes to a quark field in the colour state b by emitting a gluon in the colour state $r\bar{b}$ (see Fig. 2.1a). The interaction point between the quark (solid line) and the gluon (curly line), represented here as a vertex shared between the incoming quark, the outgoing quark and the emitted gluon, is described by the interaction term $\mathcal{L}_{qg}$ in $\mathcal{L}_{QCD}$ containing the coupling constant g_s. The separate quark and gluon fields in the diagram are of course described by the other terms in $\mathcal{L}_{QCD}$. If the emitted gluon had been absorbed by another incoming quark, say in colour state b, the quark would have changed its colour state finally to r. And the extra interaction vertex would have led the interaction term to be of second order in the coupling constant g_s. The figure on the right (Fig. 2.1b) shows another basic QCD interaction involving only gluons.

2.2 CONNECTING THEORIES WITH EXPERIMENTS

Probing the relativistic dynamics and interactions of elementary particles boils down to two sources [10]: (a) scattering events, in which one particle collides with

another and (some of) the final particles are measured, and (b) decays, in which a particle disintegrates spontaneously to a number of other particles, that can in turn be measured. With quantum field theory, one can calculate probabilities for these interactions so that the resulting theoretical calculations can be compared with the experimental data. The procedure always starts with evaluating the *amplitude* of the concerned process before computing the *decay rates* (Γ) or scattering *cross sections* (σ) as required. Most particle physicists, these days, conduct particle-collider experiments to study scattering events and compare the scattering cross sections calculated theoretically with the ones determined experimentally for the processes they are interested in. Let us look briefly into scattering processes, their amplitudes and cross sections.

2.2.1 *Scattering*

When particles collide with each other, they undergo interactions and scattering processes. As a result of scattering, the particles experience changes in their direction of motion and, in some cases, even alterations in the magnitude of their momentum.

Scattering interactions can be elastic or inelastic. In an elastic scattering, the colliding particles change their direction of motion, but the total kinetic energy of the particles is conserved. The particles retain their original identities. Whereas, in an inelastic scattering, the total kinetic energy of the system is not conserved. The energy can be lost in the form of heat or radiation, or even by producing new particles. The colliding particles may or may not survive an inelastic scattering. For example, an electron colliding into a proton can scatter in an elastic process (e. g. $e^- + p^+ \rightarrow e^- + p^+$) or in inelastic processes by emitting an extra photon ($e^- + p^+ \rightarrow e^- + p^+ + \gamma$) or an extra pion ($e^- + p^+ \rightarrow e^- + p^+ + \pi^0$).

The probability of a scattering event occurring is described using a quantity called the cross section σ [11]. When a particle hits a target and gets scattered, cross section helps us quantify the effect of the scattering centre on the particle. In other words, it gives a measure of the effective area presented by a target particle that the other particle can interact with. It represents the likelihood that a given interaction will occur. The larger the cross section, the more likely the projectile particle is to collide with the target particle. The cross section is a characteristic of the colliding particles, allowing us to compare different experiments that involve varying beam sizes and intensities.

In a particle collider, particles are accelerated in bunches in opposite directions using powerful electromagnetic fields before being brought into collision at relativistic energies at a specific point in the collider. Luminosity gives a measure of how densely particles are packed into a given bunch and the rate at which the particles collide in a particle collider. It is defined as the number of particle collisions per unit time per unit area. A higher luminosity means more particles collide, and greater becomes the chance of having the desired interaction. Luminosity is thus a property of the collider experiment itself, and increasing luminosity is often a key goal for particle collider experiments.

Say, we have particles of type A with number density ρ_A as a target at rest. We are aiming a bunch of particles of type B with number density ρ_B at the target. If l_A and l_B are the lengths of the particle bunches, the number of scattering events in unit time (dN/dt) we expect should be proportional to ρ_A, ρ_B, l_A, l_B, and the cross-sectional area C common to the two bunches. The luminosity in this example becomes $L = \rho_A l_A \rho_B l_B C$. The cross section σ is then given by

$$\sigma = \frac{1}{L}\frac{dN}{dt} \tag{2.10}$$

Cross sections are important when designing an experiment because they tell us if certain particles can indeed be produced and in how much amount for a given flux or intensity of the colliding beam particles. The fundamental interactions of quarks and gluons are described by the QCD Lagrangian, and these interactions are why particles scatter. The QCD Lagrangian provides a mathematical framework for calculating the scattering cross section of these processes.

Solving QCD is a complex problem that requires different approaches depending on the energy scales involved. The scattering cross section can be calculated in QCD using perturbative and non-perturbative methods by using the QCD Lagrangian to model the interactions between quarks and gluons.

2.3 SOLVING QCD: THE PERTURBATIVE APPROACH

Perturbative methods can be used to solve QCD for scattering events occurring at high energies. They involve expanding the QCD Lagrangian in a series of terms, known as a perturbation series, and calculating scattering amplitudes for processes involving quarks and gluons using Feynman diagrams. These diagrams represent the different ways that quarks and gluons can interact with each other. However, the calculations become more complex as we go to higher orders, making the perturbative approach increasingly challenging. The scattering cross-section is obtained by summing over all possible Feynman diagrams that contribute to the scattering process, albeit to a certain degree of accuracy. This sum is typically truncated at a certain order in the expansion of the coupling constant. The degree of accuracy depends on order of the expansion used in the calculation.

Consider the process where two gluons interact to give a pair of charm and anti-charm quarks $gg \to c\bar{c}$. This is well represented in a *Feynman diagram* (see Fig. 2.2a). Taking the flow of time horizontally from left to right, we see two gluons (curly lines) interacting at a *vertex* and emitting a gluon which splits at another vertex into two quarks (solid lines). The arrow heads on each quark line represent the true time direction of a particle, where an antiparticle is represented by a particle going backwards in time. This is because, mathematically, an antiquark moving forward in time behaves the same way as its quark moving backward in time and vice-versa. This is one LO process that leads to the formation of a $c\bar{c}$ pair. More LO processes producing a $c\bar{c}$ pair from two interacting partons are shown in the same figure to the right (see Fig. 2.2). One can observe that each of these LO processes has two vertices of couplings or interaction points. So, their contribution to the calculation of scattering amplitude (called $\mathcal{M}$ in relativistic processes) are terms of second order in the coupling constant $\alpha_s = g_s^2/(4\pi)$ $(O(\alpha^2))$.

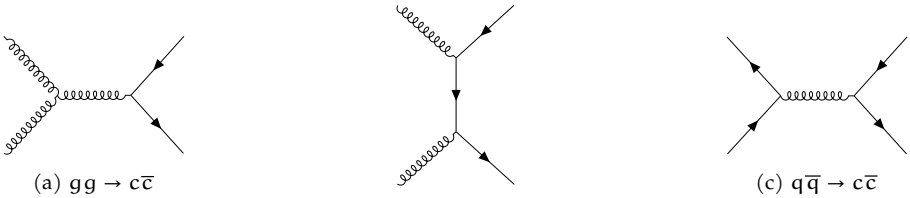

(a) $gg \to c\bar{c}$ (b) $gg \to c\bar{c}$ (c) $q\bar{q} \to c\bar{c}$

Figure 2.2: Some LO Feynman diagrams for the production of $c\bar{c}$ pair from two interacting partons.

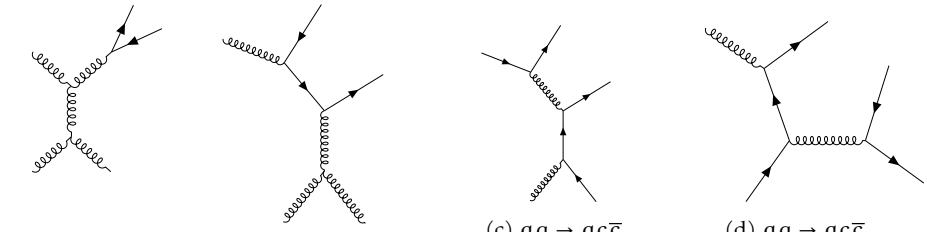

(a) $gg \to gc\bar{c}$ (b) $gg \to gc\bar{c}$ (c) $qg \to qc\bar{c}$ (d) $qg \to qc\bar{c}$

Figure 2.3: Some NLO Feynman diagrams for the production of $c\bar{c}$ pair from two interacting partons.

The NLO processes in Fig. 2.3 have three couplings, one more than LO processes, and are less likely than LO processes because the coupling constant is $\alpha_s \ll 1$ here and this reduces the probability of NLO processes as compared to LO processes. So, the total cross section for producing a $c\bar{c}$ pair up to a Next-to-Leading-Order accuracy is a sum of the cross sections of all the LO and NLO processes with their probabilities taken into consideration.

2.4 ASYMPTOTIC FREEDOM AND CONFINEMENT

The perturbative expansion is based on the coupling constant. It measures the strength of the interaction between quarks and gluons. The coupling constant for QCD is, however, not really a constant. At high energies, the coupling constant is small, and the perturbative expansion is valid because the interactions between quarks and gluons can be treated as small perturbations on top of a free-field theory. Take the process $q\bar{q} \to c\bar{c}$ shown in Fig. 2.2(c). Quark-antiquark bubbles can form in the propagating gluon leading to a *screening* of colour charges.

Fig. 2.4 shows two simple examples of the so-called *quark-loop diagrams* where quark-antiquark bubbles are formed. The first diagram on the left shows the propagating gluon splitting momentarily into a quark-antiquark pair while the next diagram shows the gluon splitting twice into such pairs. The quark-antiquark pairs appearing when the propagating gluon splits have a specific colour

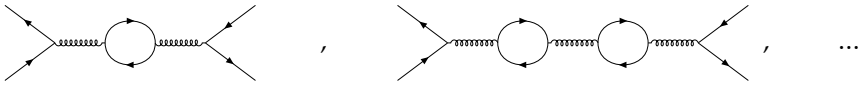

Figure 2.4: Some quark-loop diagrams

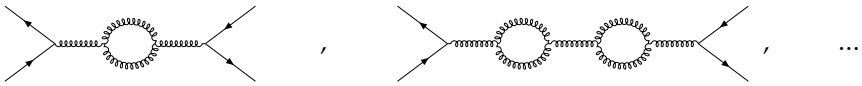

Figure 2.5: Some gluon-loop diagrams

configuration that reduces the effective colour charge of the interacting partons. From this mechanism, the reduction in the effective coupling strength is higher for partons interacting at larger distances. The large-distance behaviour is related to small-momentum transfer processes. That the distance and momentum are inversely related can be inferred from the de Broglie relation $p = h/\lambda$ between the wavelength λ and the momentum p of a matter wave with h being the Planck constant.

So, this reduction in the effective colour charge or the effective coupling strength is known as the *screening effect*. It is similar to the effect experienced in QED by electric charges. However, the force carrying particles in QED, or the photons, do not possess any QED charge (electric). Photons are invisible to other photons. Otherwise, they would have an *anti-screening effect* as experienced in QCD. This is because in QCD, the force carrying particles, or the gluons, are coloured and gluons interact with other gluons. Such a process in which a background field of interaction (QED or QCD) produces short-lived virtual particle–antiparticle pairs (leptons or quarks or gluons) is called vacuum polarization as the virtual pairs end up changing the effective charge and current of the original field.

Some loop diagrams showing the propagating gluon splitting into gluon pairs are shown in Fig. 2.5. These splittings lead to an increase in the coupling strength at large distances. It turns out that anti-screening effect is always stronger than the screening effect in QCD at all energies. Therefore, the overall coupling strength will decrease as the colour charges interact very close to each other. So, when probed at high energies, the quarks in hadrons behave more or less as free particles. This phenomenon is referred to as *asymptotic freedom* in QCD. Smaller coupling implies that perturbative QCD (pQCD) is valid for hard processes, i. e. in the region of high momentum transfers.

As the colour charges get farther from each other, the coupling strength increases and the phenomenon of *confinement of colours* takes precedence. This is why quarks are always found confined within hadrons in nature.

The coupling constant is therefore called the *running coupling constant* because it is running as a function of momentum transfers (see Fig. 2.6).

Let the four-momentum transferred across two vertices between the interacting partons be q^μ. Using $Q^2 = -q^2 = -q^\mu q_\mu$ relation for momentum transfer and

expressing the coupling constant g_s as $g_s = \sqrt{4\pi\alpha_s}$, the one-loop running coupling constant $\alpha_s(Q^2)$ is given by

$$\frac{1}{\alpha_s(Q^2)} = \frac{1}{\alpha_s(\mu^2)} + \beta_0 \ln(Q^2/\mu^2) \tag{2.11}$$

where $\beta_0 = \frac{11n-2f}{12\pi}$. Here n is the number of colours and f is the number of flavours ($n = 3$ for colours r, b, g and $f = 6$ for quark flavours up, down, charm, strange, top and beauty in the Standard Model). The first term $11n/12\pi$ is due to antiscreening while the second term $-2f/12\pi$ is due to screening. In Standard Model, β_0 turns out to be positive which means that α_s decreases with increasing Q^2.

The energy scale μ^2 in Eq. 2.11 is a reference scale based on which an input value for α_s is specified. It is called the *renormalization scale* since it is used to make sense of divergent integrals appearing in the calculation of scattering amplitude from loop diagrams [10]. It is done using the *renormalization group equation* which reflects the changes in a physical system as viewed from different energy scales and is given for the strong coupling constant (g_s or α_s) by the so-called β function

$$\beta(g_s) = \frac{\partial g_s}{\partial \ln(Q)} \equiv \frac{\partial \alpha_s}{\partial \ln(Q^2)} = \beta(\alpha_s) \tag{2.12}$$

It can be seen that $\beta(g_s)/\beta(\alpha_s) = 4\pi$ from the relation $g_s = \sqrt{4\pi\alpha_s}$. The perturbative expansion of the β function in QCD [12] is

$$\beta(\alpha_s) = -(\beta_0\alpha_s^2 + \beta_1\alpha_s^3 + O(\alpha_s^4)) \tag{2.13}$$

The accuracy in calculating the running coupling constant can be increased further from Eq. 2.11 by including more higher-order processes in the calculation. Then apart from β_0, other higher order coefficients like β_1 will also appear in Eq. 2.11.

The running coupling constant in Eq. 2.11 can be further simplified by defining a QCD scale parameter $\mu = \Lambda$ such that the coupling $\alpha_s(\Lambda^2)$ is infinitely large. The equation then becomes

$$\alpha_s(Q^2) = \frac{1}{\beta_0 \ln(Q^2/\Lambda^2)} \tag{2.14}$$

The parameter Λ has been found experimentally to be around $200 - 300$ MeV and has not been defined unambiguously yet [13, 14]. But the coupling has been quite accurately determined at $Q^2 = m_Z^2$ to be $\alpha_s(m_Z^2) = 0.1179 \pm 0.0010$ with m_Z being the mass of Z boson [15].

2.5 SOLVING QCD: THE NON-PERTURBATIVE APPROACH

The non-perturbative approach is used to solve QCD in cases where perturbation theory is not applicable. Perturbation theory breaks down for interactions that occur at large distances, resulting in a large coupling constant that renders perturbative calculations unusable. Numerical calculations from non-perturbative QCD explain

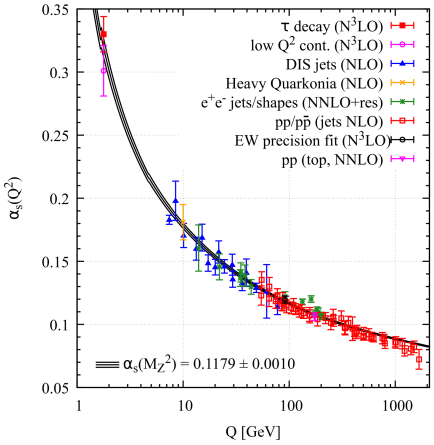

Figure 2.6: Running coupling in QCD

phenomena such as colour confinement and the phase transition between hadronic matter and quark–gluon plasma (QGP), which occur at large distances. Lattice QCD calculations are one example of a non-perturbative approach to studying QCD.

That the spacetime can be discretized into a grid or lattice of individual points forms the foundation behind the gauge theory of lattice QCD. The assumption here is that the QCD interactions take place on a discrete lattice of four dimensional spacetime. The field values of quarks at various points in spacetime are assigned accordingly to each lattice point. QCD interactions by gluon fields are defined on the links connecting the neighbouring lattice points. The interaction links are of eight kinds representing the eight gluon fields. The symmetry is still $SU(3)$ but because of three quark flavours, two light quarks (up and down) and a heavier quark (strange) implying a $2+1$ flavour calculation. The reason behind considering the three lightest quarks is that the heaviest quark, top, does not hadronize [16], and including charm and beauty quarks poses a challenge due to their significant mass resulting in large discretization errors. These are errors arising due to the finite lattice spacing and are directly proportional to the product of the lattice spacing and the quark mass. In order to use the same formalism of lattice QCD for charm and beauty quarks as the up, down and strange quarks, the lattice spacing has to be very fine. This brings a huge strain on the already computationally intensive nature of lattice QCD calculations. There are other options in considering charm and beauty quarks like the Heavy Quark Effective Theory or the Non-Relativistic QCD. Nevertheless, the lightest three quarks provide reasonably correct calculations of macroscopic QCD phenomena.

Unlike pQCD, lattice QCD calculations are not analytic, but rather numerical. In principle, the continuum QCD can be recovered if the lattice points are infinitesimally close to each other in an infinitely large lattice.

2.6 PARTON SHOWER AND HADRONIZATION

In a high-energy collision, two partons from the colliding hadrons can interact strongly in a hard scattering process and can result in new partons. In the perturbative regime, each energetic parton can split or branch into two partons thus sharing its energy between them. Each of the partons produced can split into more partons leading to a *parton shower* (see Fig. 2.7). Once the partons reach a

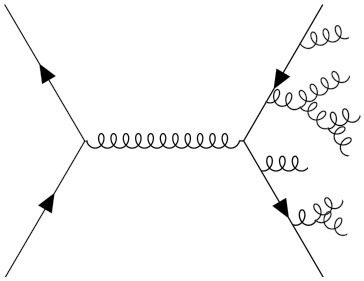

Figure 2.7: A possible parton shower in a QCD process $q\overline{q} \rightarrow q\overline{q}$

small enough energy scale, the strong coupling becomes sufficiently high for the partons to enter a low momentum-transfer, long-distance region where non-perturbative effects kick in. The most important of these effects is *hadronization* which confines partons into observable compound particles called hadrons. The process by which such a high-energy parton breaks apart and produces a shower of hadrons is known as *fragmentation*.

A perturbative treatment of QCD as well as a non-perturbative model of QCD can be effectively combined within a Monte Carlo method, a program that provides a complete model involving the interaction and production of hadrons for processes of our interest. This is known as a QCD-event generator.

The mechanism of hadronization can be classified into the following three kinds.

- *Independent fragmentation*. This mechanism assumes that partons fragment independently to form hadrons. The fragmentation process requires the creation of a $q\overline{q}$ pair out of vacuum. The fragmenting parent quark then combines with the antiquark from the $q\overline{q}$ pair to form a meson, together carrying an energy fraction z. The leftover quark with energy $1 - z$ fragments further until a cut-off energy is reached. The distribution assumed for z, often denoted as $D(z)$, is known as the *fragmentation function*. Gluon fragmentation in this mechanism involves the splitting of a gluon into a quark-antiquark pair, either assigning all the momentum to one or the other quark with equal probability or using the Altarelli-Parisi splitting function[2]. The independent fragmentation scheme has been successful in describing the features of two-jet and three-jet final states in electron-positron annihilation, but it has some limitations, such as violations of momentum conservation and difficulties in merging collinear jets.

2 The AP splitting functions quantify the probability of a parton splitting into two other partons with different momentum fractions [17].

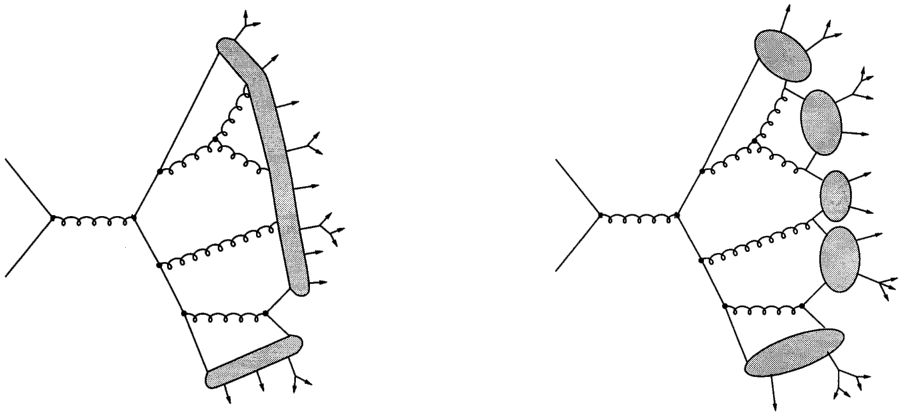

(a) String hadronization

(b) Cluster hadronization

Figure 2.8: Two classes of hadronization models, string and cluster, in a possible QCD process.

- *String model*. In this model, the quark and antiquark produced in a collision move away from each other, losing energy to the colour field. This energy forms a string-like structure with a constant energy per unit length. Eventually, the string breaks into smaller pieces resembling hadrons by spontaneously generating $q\bar{q}$ pairs (see Fig. 2.8a). In simple quark-antiquark systems, the string model is similar to independent fragmentation but provides a more consistent and covariant framework. When gluons are present, they create kinks in the string, resulting in a different angular distribution of hadrons in three-jet final states compared to independent fragmentation.

- *Cluster model*. After parton branching, colour-singlet clusters of partons form and decay into observed hadrons. Gluons can split into quark-antiquark pairs, and neighbouring quarks and antiquarks combine into singlets.

Two modern programs widely used in particle physics to generate events in high-energy collisions between particles are PYTHIA [18] and Herwig [19] which fundamentally use the string model and the cluster model respectively for describing hadronization. The experimental results presented in this thesis have been compared to various LO and NLO PYTHIA models, which rely on the string model for hadronization.

2.6.1 *PYTHIA and the String model*

In the string model, the QCD potential between a quark and an antiquark is expected to grow linearly with increasing distance between them. String models try to determine which partons form confining potentials of string pieces between

them. Monte Carlo event generators trace the flow of colour[3] on an event-by-event basis [15, 20] by using the so-called leading-colour (LC) approximation [21]. The LC approximation neglects subleading colour contributions, focusing on the dominant colour flow between the interacting particles. This leads to partonic final states where every quark is colour-connected to one other unique parton in the event. The colour connections established in the primary scattering process are extended to the beam remnants, which are the leftover particles that did not directly participate in the main interaction. By assigning colour flow to the beam remnants, the colour relationships established in the primary scattering process are tied together, maintaining consistency and continuity of colour interactions throughout the event. As a result, the event generator maintains the expected qualitative behaviour of leading-colour QCD and ensures that the colour dynamics are accurately simulated. This is an ambiguous procedure and currently, two models are implemented in PYTHIA. The original model reconstructs the colour flow such that a Leading Order Parton Shower would produce the beam remnants [22]. The qualitative behaviour expected from leading-colour QCD is captured in this model.

A more recent model uses the full QCD colour configuration. Initially, the partons involved in multiple parton interactions (MPI) are considered to have no specific colour relationships with each other. The beam particles (initial protons) are considered to be in a colourless state, called a colour singlet. This means that the colour configuration of the beam remnants (leftover particles) must be the opposite or complementary to the colour configuration of the outgoing partons. Both the leading-colour approximation and the full QCD colour configuration model have limitations and cannot fully describe all aspects of colour flow in an event. Therefore, the colour connections need to be further modified. This process is called colour reconnection. It involves readjusting the colour relationships between particles in order to better match the observed data and provide a more realistic description of colour flow within the event.

During colour reconnection, the model minimizes the potential string energy and incorporates the QCD colour rules. It determines the probability of allowing a reconnection to adjust the colour relationships between particles. This approach allows for the influence of colour correlations beyond the leading colour and enables a more comprehensive description of the formation of confining potentials in multiparton systems during hadronization.

QCD processes are categorized into two distinct groups: soft processes and hard processes. Elastic, diffractive and minimum-bias (inelastic and nondiffractive) events are included in soft processes. The normal $2 \to 2$ processes including charm and beauty production are categorized under hard processes. In PYTHIA, the hard processes form a subset of the soft processes via the multiparton interactions [23].

The POWHEG BOX [24] was used to generate partonic events at NLO. In this model, the partonic events are loaded into PYTHIA which takes care of the

3 The "flow of colour" refers to the exchange of colour charges between the partons as they interact, resulting in a dynamic evolution of the colour configurations during the interaction. This exchange of colour charges is responsible for the creation and annihilation of colour-carrying particles and the generation of colour correlations among the participating particles.

remaining partonic events and hadronization. The NLO pQCD calculations from POWHEG are matched with the parton shower from PYTHIA using the original hadronization scheme.

2.7 CONCLUSION

In this chapter, we introduced the theoretical basis of quantum chromodynamics which describes the strongest interactions of nature occurring at high energies. We also looked at the basics of how experiments can help us validate the theoretical concepts in high-energy physics, the key being the *cross section* of particle collisions. It is the fundamental concept connecting theories and experiments with which we can probe specific physics processes of our interest.

Chapters 6 and 7 present the cross-section measurements of charm jets in pp and p–Pb collisions respectively. In Ch. 8 presented are studies on fragmentation of charm jets in pp collisions. The question arises now is why we are studying charm jets. Let us gain some insights about this in the following chapter (Ch. 3).

3 HEAVY-FLAVOUR JETS

3.1 PHYSICS GOAL

The physics goal has always been about gaining a deeper understanding of the strong interactions we briefly looked into in the previous chapter. In this chapter, we look into three aspects of that goal and how charm jets can help us achieve that.

3.2 QUARK–GLUON PLASMA

In Ch. 1, we have discussed briefly the QGP and why the ALICE collaboration is very interested in unravelling the properties of this hot and dense state of matter. However, detecting the QGP directly poses significant challenges. As outlined in the preceding chapter, strong interactions are exceptionally powerful at low energies, resulting in the confinement of quarks and gluons (partons) within protons and neutrons (nucleons). Therefore, to enable interactions among these partons, it is necessary to collide massive lead ions at ultrarelativistic speeds. Such collisions create a finite amount of the QGP, which rapidly cools down due to its short lifetime of approximately 10 fm. This short duration makes it very difficult for a direct measurement of the QGP using our detectors. Therefore, physicists resort to exploring indirect methods to study this elusive state of matter.

One ideal probe to study the QGP, a collection of deconfined coloured particles (partons), is a parton that can be traced back from its hadronized form it is found in to its production in an ultrarelativistic collision. The parton must therefore be exclusively produced in hard scatterings, and not during in-medium interactions. This is so that the parton is formed very early in the initial stages of the collision, when the energy density is still high and the medium has not undergone significant expansion and cooling, and therefore has not fully developed yet. By having the parton formed early, it has a chance to interact with the QGP as it evolves over time. These interactions lead to energy loss and modifications of the parton's properties. That would allow us to investigate how the partonic probe evolves over time in the medium [25].

The two lightest quarks, up and down, are part of everyday matter, so it is difficult to determine if they were freshly produced in collisions or if they were present in the colliding nucleons. However, strange, charm, beauty, and top quarks must be freshly produced in relativistic nuclear collisions. The mass of a strange-antistrange pair ($2 * 95$ MeV) is on a similar energy scale as the phase transition of hadronic matter into quark matter (QGP). Johann Rafelski and Rolf Hagedorn [26] proposed that the enhancement of strange quarks could be an observable signature of QGP, but it is important to note that *strangeness enhancement* can also occur in a thermalized hadronic system. Therefore, strangeness enhancement alone does not conclusively prove the formation of QGP. However, the magnitude and energy independence of

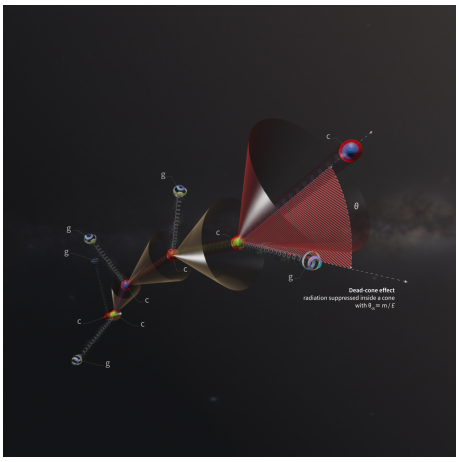

Figure 3.1: A charm quark (c) in a parton shower loses energy by emitting radiation in the form of gluons (g). The shower displays a "dead cone" of suppressed radiation around the quark for angles smaller than the ratio of the quark's mass (m) and energy (E), which decreases at each stage of the shower. The changing colour of the quark illustrates its changing "colour charge" [31].

strangeness enhancement observed in experiments like CERN WA97 [27], CERN NA57 [28], and RHIC STAR [29] provide evidence that the QGP has been created once a minimal energy threshold is reached.

While strangeness enhancement is not a definitive QGP signature, it has provided valuable evidence for the creation of this hot and dense state of matter. However, to study the properties of QGP in detail, we need probes that can interact with it and have been produced just before the hot liquid formed. Strange quarks do not meet these criteria and the very heavy top quarks ($\sim$ 173 GeV [9]) are neither produced enough nor do they hadronize. That leaves us with charm ($\sim$ 1.3 GeV [9]) and beauty quarks ($\sim$ 4.5 GeV [9]) as our ideal probes. These heavy quarks are not as abundantly available as light quarks, making them slow-moving, coloured probes that can explore the QGP medium and the QCD interactions inside it. Additionally, due to the dead-cone effect, heavy quarks lose a smaller amount of energy through the radiation of gluons which are suppressed at an angle m/E around the direction of the quark's momentum (m and E are the quark's mass and energy respectively). The effect gradually becomes more prominent as the energy of the quark reduces. This phenomenon has been directly observed by the ALICE collaboration [30] for charm quarks using jets containing a D^0 meson in pp collisions (See Fig. 3.1).

This brings us to the next part in our physics goal, testing perturbative QCD.

3.3 PERTURBATIVE QCD

We discussed in the previous chapter as to how the perturbative approach to solving QCD was valid only when the strong coupling was much smaller than unity. We could see the strong coupling running as a function of momentum transfer in

Fig. 2.6. The energy threshold for the production of different quarks is governed by the mass (m) of the quarks being produced. So, for producing a quark-antiquark pair, the momentum transfer should at least be $Q^2 \sim (2m)^2$. Given the mass of the heavy quarks, they can therefore be produced only in hard scatterings. Since their production cross section can be calculated down to p_{T} lower than 150 MeV in the pQCD framework [32], measuring the production of heavy flavours is an important tool in testing perturbative QCD (pQCD).

Chapter 6 presents the production cross section of charm jets in pp collisions, with the goal of testing pQCD in mind. This thesis studies open-heavy-flavour hadrons, i. e. particles consisting of a heavy flavour (charm or beauty) and other lighter quarks. They are a cleaner probe because the alternatives, i. e. hidden-heavy-flavour hadrons (particles containing a heavy flavour quark and its antiquark such that the net heavy-flavour content in the hadron is zero), tend to be affected by the formation of the QGP due to various competing mechanisms [33].

A fragmentation function $D_{q\to h_q}(z)$ describes the probability of a quark q with momentum p_q hadronizing into a hadron h_q that carries a fraction z of the parton momentum $p_h = z\,p_q$. This is useful in calculating $d\sigma_{h_i h_j \to h_q}$, the production cross section of a hadron h_q produced from the collisions of two hadrons h_i and h_j. This calculation is important because, loosely speaking, an experimentalist has access only to these hadrons, the ones being collided h_i and h_j, and the one being detected h_q, but not the partons themselves. But in reality, the strong interactions taking place in hard scatterings are between the two partons i from h_i and j from h_j. Let the partonic hard process producing the quark of our interest, a heavy quark Q, be $i + j \to Q + X$ and the corresponding partonic cross section be $d\tilde{\sigma}_{ij\to Q+X}$. Based on the factorization theorem [34], the cross section of heavy quarks Q is given by

$$d\sigma_Q(s, p_{\mathrm{T}}, y, m_Q) = \sum_{i,j} \int_0^1 dx_i \int_0^1 dx_j\, f_i(x_i, \mu_{\mathrm{F}}^2)\, f_j(x_j, \mu_{\mathrm{F}}^2) \otimes d\tilde{\sigma}_{ij\to Q+X}(x_i, x_j, s, p_{\mathrm{T}}, y, m_Q, \mu_{\mathrm{F}}^2, \mu_{\mathrm{R}}^2). \tag{3.1}$$

Here, f_k (where $k = i, j$) describes the probability of finding a parton of flavour k in the colliding proton (i. e. the hadron h_k) and carrying a fraction x_k of the proton's momentum. The probabilities f_k are called parton distribution functions (PDFs) and are functions of x_k and μ_{F}^2. The variable μ_{F} is known as the *factorization scale* which, like the *renormalization scale* μ_R, is an arbitrary scale that a user defines to perform calculations like the one described above. The reader can refer to Eq. 2.11 from the previous chapter where the *renormalization scale* is mentioned (referred to as μ instead of μ_{R} as in the current chapter). These scales can be arbitrarily chosen because ideally, they should cancel. However, in practice, they do not, and we obtain a scale dependence as a systematic uncertainty in the numerical simulations. Assuming that the scattering processes are independent of the parton fragmentation, and with the fragmentation function $D_{Q\to h_Q}(z)$, the cross section of the heavy-flavour hadron h_Q is given by

$$d\sigma_{h_i h_j \to h_Q + X} \simeq d\sigma_Q \otimes D_{Q\to h_Q}(z). \tag{3.2}$$

The fragmentation function has been studied for charm jets, and the results are presented in Ch. 8. The momentum of a charm quark ($Q = c$) is calculated by identifying it with a jet containing a charm hadron (h_c) whose momentum is calculated and presented as a fraction of the jet momentum, represented by the observable

$$z_{\parallel} = \frac{\vec{p}_{\text{jet}} \cdot \vec{p}_{\text{D}}}{\vec{p}_{\text{jet}} \cdot \vec{p}_{\text{jet}}} \tag{3.3}$$

A jet cannot exactly be a parton but its kinematic properties are the best representation as yet of the kinematics of the concerned parton. We briefly touched on this in Ch. 1, and shall discuss more later.

While one can make reference measurements as well as heavy-ion measurements by studying pp and Pb–Pb collisions respectively, it is equally important to disentangle any possible cold-nuclear matter (CNM) effects.

3.4 COLD-NUCLEAR MATTER EFFECTS

CNM effects refer to the differences observed between pp and p–Pb collisions. The effects are said to be cold to distinguish them from the hot-nuclear matter effects observed due to the presence of a hot medium produced in Pb–Pb collisions. CNM effects are expected to be induced by the presence of heavy nuclei in the initial state of ultrarelativistic collisions.

One dominant CNM effect for heavy flavours at the LHC energies is the modification of the effective luminosity of partons[1]. Partons can have large densities in the nuclei of heavy ions thus modifying the PDFs. This is because a highly energetic nucleus is more than just a superposition of its constituent nucleons devoid of any interaction. This difference can be characterized by the nuclear ratio, R_f, given by

$$R_f = \frac{f^A}{A \cdot f^p}, \tag{3.4}$$

where f^p (or $f^p(x, \mu_{\text{F}}^2)$) is the PDF of a free proton while f^A (or $f^A(x, \mu_{\text{F}}^2)$) is the PDF of a proton bound in a nucleus of A nucleons. The term f^A is commonly referred to as the nuclear PDF (nPDF). Modifications to the nuclear ratio, R_f, can be attributed to various phenomena such as *shadowing* [36] ($R_f < 1$ at $x \lesssim 10^{-2}$), *anti-shadowing* [37] ($R_f > 1$ at $10^{-2} \lesssim x \lesssim 10^{-1}$), and others. Heavy-flavour production in the midrapidity region at LHC energies is sensitive to x values of approximately 10^{-4} for charm and 10^{-3} for beauty [38]. Therefore, it is expected that heavy-flavour production in p–Pb collisions will be influenced primarily by the modification of nuclear PDFs in the shadowing region.

Another CNM effect that can influence heavy-flavour production is the possibility of partons colliding elastically multiple times against the target nucleus

1 In collider physics, luminosity is a more important measure than the number of particle collisions. It is a measure of how tightly packed the particles are in the beams that cross. The probability of collisions increases with a tighter packing, i. e. with a higher luminosity [35].

after a hard scattering thus acquiring additional momentum after each elastic scattering. This can lead to a shift in the transverse momentum spectra, known as k_{T}-broadening, or the Cronin effect [39]. Also, the parton can lose energy by radiative or collisional energy-loss mechanisms when traversing through cold-nuclear matter. Qualitatively, this behaviour is similar to the final-state energy loss in the hot medium, albeit with a smaller magnitude [40].

The differences in pp and p–Pb collisions at $\sqrt{s_{\mathrm{NN}}} = 5.02$ TeV are characterized in the nuclear modification factor measured for charm jets and presented in Ch. 7. Nuclear modification in Pb–Pb or p–Pb collisions are determined by comparing their respective yields with the yields in pp collisions. For p–Pb collisions, the nuclear modification factor is given by

$$R_{\mathrm{pPb}} = \frac{d\sigma_{\mathrm{pPb}}/dt}{A \cdot d\sigma_{\mathrm{pp}}/dt} \tag{3.5}$$

where $d\sigma_{\mathrm{pPb}}/dt$ and $d\sigma_{\mathrm{pp}}/dt$ are differential cross sections in p–Pb and pp collisions respectively, and A is the number of nucleons in the heavy ion (i. e. Pb ion).

3.5 HEAVY FLAVOURS OR HEAVY-FLAVOUR JETS

The D^0 meson ($c\overline{u}$) is the lightest and most abundantly produced heavy-flavour hadron. Many single-particle measurements have been done where the p_{T}-differential production-cross-section of D mesons produced directly from charm quarks has been measured in pp, $\mathrm{p\overline{p}}$, p–Pb, and Pb–Pb collisions at various centre-of-mass energies [41–52]. Compared to the measurements of charm hadrons however, measurements of jets containing charm hadrons should help in making more differential characterization of the production and fragmentation of heavy quarks. This is because charm jets can provide a more accurate picture of the kinematics of the parent charm quarks. Since fragmentation is a non-perturbative phenomenon and known with large uncertainties [53], its intricacies can be avoided through measurements of charm jets instead of measuring just the charm hadrons.

Some heavy-flavour-jet measurements have also been done. The STAR experiment at RHIC measured parallel momentum fraction $z_{\parallel}$ of jets carried by $\mathrm{D}^{*\pm}$ mesons at $\sqrt{s} = 200$ GeV [54] and compared data with Monte Carlo predictions using the leading-order pair creation processes $\mathrm{gg} \to \mathrm{c\overline{c}}$ and $\mathrm{q\overline{q}} \to \mathrm{c\overline{c}}$ only. They inferred that higher order processes like gluon splitting and flavour excitation also have a small but significant contribution to the charm content in jets at RHIC energies. The ATLAS experiment at LHC measured also measured jets containing $\mathrm{D}^{*\pm}$ mesons. They found that the $z_{\parallel}$ distribution differed significantly from PYTHIA 6, HERWIG 6, and POWHEG predictions in their low p_{T} interval $25 < p_{\mathrm{T}} < 30$ GeV/c. A recent global QCD analysis of fragmentation functions based on the ZM-VFNS [56] scheme provided a much better agreement to the ATLAS measurement highlighting the importance of such data analyses in constraining momentum fraction dependence of the gluon fragmentation function, which is largely unconstrained. The ALICE experiment measured $z_{\parallel}$ of jets containing D^0 mesons in pp collisions at $\sqrt{s} = 7$ TeV (see Fig. 3.2 [57]). Only charged particles were clustered with D^0 mesons to get

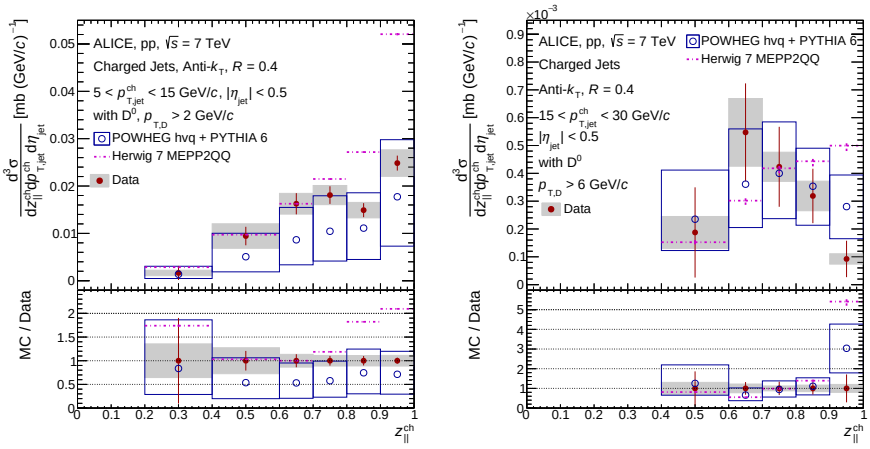

Figure 3.2: Fragmentation function of D^0 jets in pp collisions at $\sqrt{s} = 7$ TeV in $5 < p_{T,\mathrm{ch\,jet}} < 15$ GeV/c (left) and $15 < p_{T,\mathrm{ch\,jet}} < 30$ GeV/c (right) [57].

those jets. The fragmentation function ($z_{\parallel}$-differential cross section) was measured in two intervals of jet transverse momentum ($p_{T,\mathrm{ch\,jet}}$) between 5 and 30 GeV/c. Approximately 390 million events were analysed. Results presented in this thesis for pp collisions (Ch. 6 and 8) at $\sqrt{s} = 5.02$ TeV are with $\sim$ 900 million events analysed. A larger data sample allowed for a more differential measurement of the fragmentation function of charm jets in four $p_{T,\mathrm{ch\,jet}}$ intervals between 5 and 50 GeV/c (see Ch. 8).

The collision energy of $\sqrt{s_{\mathrm{NN}}} = 5.02$ TeV is also the same energy at which p–Pb collision data were recorded by the ALICE experiment in 2016. This meant that a measurement of the nuclear modification factor R_{pA} of charm jets could complement a measurement done by the CMS experiment in p–Pb collisions at $\sqrt{s_{\mathrm{NN}}} = 5.02$ TeV [58]. They measured R_{pA} from 55 to 400 GeV/c and found the jets to be consistent with an absence of final-state energy loss for charm quarks in p–Pb collisions. The measurement presented in this thesis in Ch. 7 is done for charm jets from 5 to 50 GeV/c, a very low momentum region that ALICE is well-placed to make a unique contribution to.

4 EXPERIMENTAL FRAMEWORK

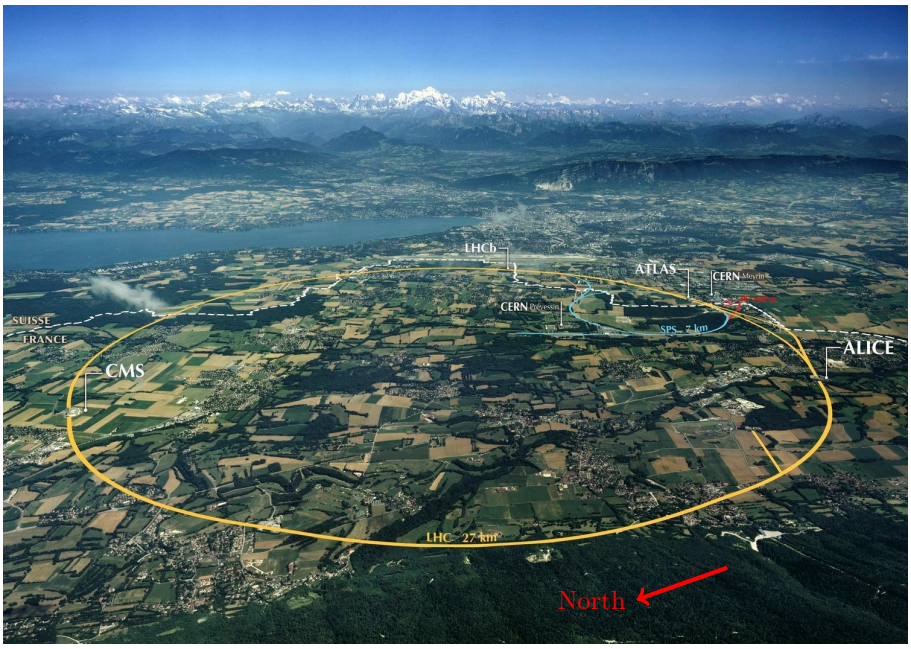

Figure 4.1: Where is CERN [59]?

Conseil Européen pour la Recherche Nucléaire (CERN), French for 'European Council for Nuclear Research', was a provisional council established in 1952 for building a particle-physics laboratory. The council was later dissolved in favour of establishing the European Organization for Nuclear Research in 1954. The organization however continues to use the acronym CERN. The laboratory operated by CERN in Geneva is the largest physics laboratory and runs the highest-energy particle collider in the world. Figure 4.1 shows where the accelerator, known as the Large Hadron Collider (LHC), is located. It is in a $\sim$ 27-kilometre circular tunnel sandwiched between the Jura mountains on the west and Lake Geneva on the east with the Geneva International Airport to its south-east. The Swiss Alps can be seen in the background, to the far east and far south-east of the LHC. The LHC lies at an average depth of 100 metres (50 to 175 metres [60]). It is designed to collide protons with a centre-of-mass energy of $\sqrt{s} = 14$ TeV as well as lead ions with an energy of $\sqrt{s_{\mathrm{NN}}} = 5.6$ TeV per nucleon-nucleon pair. The ions are accelerated in two parallel superconducting circular rings and are allowed to collide at four different points by having the beam pipes cross in the tunnel. There are four major experiments at

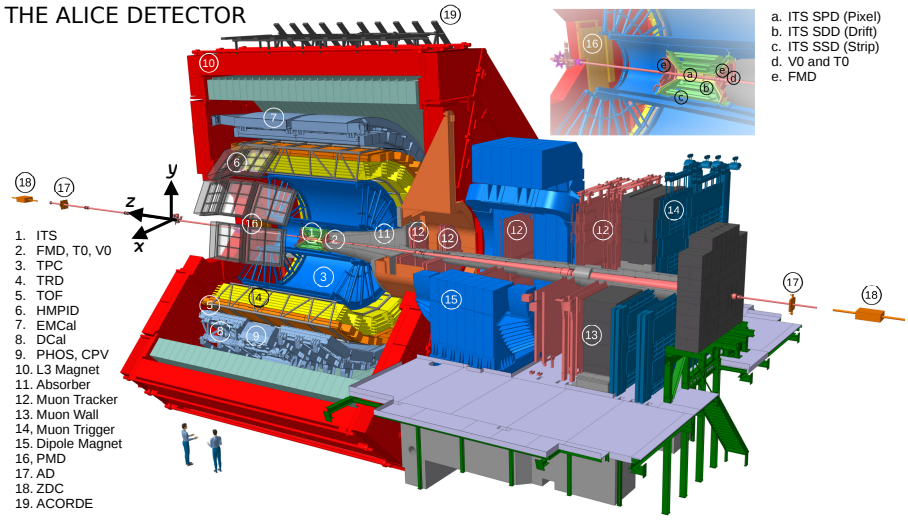

Figure 4.2: A schematic view of the ALICE detector during LHC Run 2 [65].

these interaction points, namely, ATLAS (A Toroidal LHC Apparatus) [61], CMS (Compact Muon Solenoid) [62], ALICE (A Large Ion Collider Experiment) [63] and LHCb (Large Hadron Collider beauty) [64]. These experiments have their own physics programs and are operated by thousands of collaborating scientists from $\approx$ 200 institutions each from all over the world.

The first run of particle collisions at the LHC, known as Run 1, went on from November 2009 up until February 2013. Proton–proton (pp) collisions in Run 1 were recorded at $\sqrt{s} = 0.9, 2.76, 7$ and 8 TeV . Lead–lead (Pb–Pb) and proton–lead (p–Pb) collisions were also recorded in Run 1 at $\sqrt{s_{\mathrm{NN}}} = 2.76$ and 5.02 TeV respectively. The second run of LHC, dubbed Run 2, ran from April 2015 till December 2018 and collected data for pp collisions at $\sqrt{s} = 5.02$ and 13 TeV, for p–Pb collisions at $\sqrt{s_{\mathrm{NN}}} = 5.02$ and 8.16 TeV, for Pb–Pb collisions at $\sqrt{s_{\mathrm{NN}}} = 5.02$ TeV and for Xe–Xe collisions at $\sqrt{s_{\mathrm{NN}}} = 5.44$ TeV . The results presented in this thesis are based on Run-2 data collected by ALICE for pp and p–Pb collisions, both at $\sqrt{s_{\mathrm{NN}}} = 5.02$ TeV . Let us briefly look into the ALICE detector.

4.1 THE ALICE DETECTOR

The ALICE detector (shown in Fig. 4.2) is designed for recording ultrarelativistic heavy-ion collisions to study the physics of the quark-gluon plasma [63]. It therefore can track particles of very low momenta (down to about 100 MeV for pions) in environments of high particle multiplicities [66]. The ability to identify particles is also another important feature of the ALICE detector and has proved crucial in achieving many of the collaboration's targets in physics research.

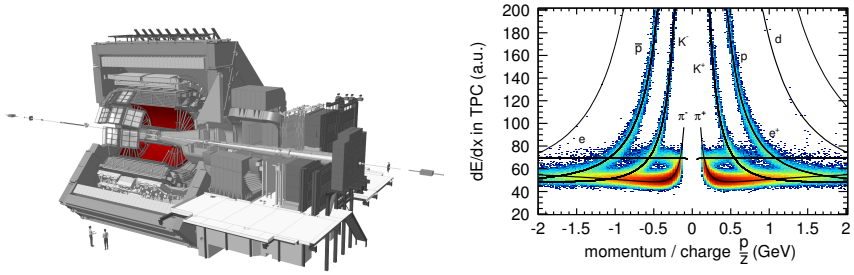

Figure 4.3: ALICE detector with its Time Projection Chamber [70] (left) and the specific energy loss dE/dx vs. momentum/charge in pp collisions at $\sqrt{s} = 900$ GeV [71] (right).

The convention used by ALICE is a right-handed coordinate system with the x-axis towards the centre of the LHC ring, y-axis pointing up, and z-axis along the beam axis. The kinematics of a particle can be described by its four-vector $p_\mu = (E, p_x, p_y, p_z)$. Transverse momentum $p_\mathrm{T} = \sqrt{p_x^2 + p_y^2}$ is one commonly used variable because of azimuthal symmetry of particle production around the beam axis (z). Paired with p_T is the longitudinal momentum which is simply p_z, such that the three-momentum squared is $p^2 = p_x^2 + p_y^2 + p_z^2 = p_\mathrm{T}^2 + p_z^2$ Similarly, a commonly used spatial coordinate describing the angle of a particle relative to the beam axis is pseudorapidity $\eta = -\ln\left[\tan\left(\frac{\theta}{2}\right)\right]$, where θ is the angle between the particle three-momentum and the z-axis. In the limit of massless particles where particles are travelling at the speed of light, pseudorapidity becomes equivalent to rapidity $y = \frac{1}{2}\ln\frac{E+p_z}{E-p_z}$, a quantity whose differences are Lorentz invariant under boosts along the longitudinal axis (z-axis). Rapidity, and therefore pseudorapidity, is convenient because particle production at colliders is approximately independent of rapidity.

Three sub-detectors relevant to analyses presented in this thesis are the Time Projection Chamber (TPC) [67], the Inner Tracking System (ITS) [68], and the Time-Of-Flight detector (TOF) [69]. They are present inside the central barrel of ALICE operated in a 0.5 T solenoidal magnetic field parallel to its axis.

4.1.1 *Time Projection Chamber*

The TPC (see Fig. 4.3, left panel) is the main detector in the ALICE experimental system used for tracking and identifying charged particles. It is a hollow cylinder with an active volume of about 90 m^3. Its inner radius is about 85 cm, and outer radius about 250 cm with an overall length of about 500 cm along the beam direction. It has full coverage of azimuthal angle ($\phi = 2\pi$) around the beam axis, and a pseudorapidity range of $|\eta| < 0.9$. A conducting electrode, charged to 100 kV, is present at the centre of the cylinder providing a precise axial electric field of 400 V/cm together with a voltage dividing network at the surface of the inner and

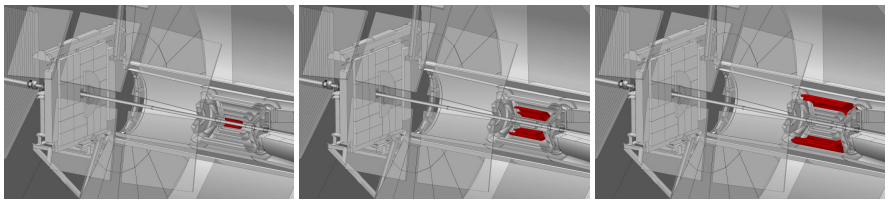

Figure 4.4: ALICE detector with three separate parts of its Inner Tracking System highlighted: (left) Silicon Pixel Detector, (centre) Silicon Drift Detector, and (right) Silicon Strip Detector.

outer cylinder. The chamber is filled with a $Ne - CO_2 - N_2$ gas mixture which can get ionized by the traversing charged particles. As the charged particles ionize the gas, electrons are freed to drift towards the outer ends of the cylinder under the influence of the uniform axial electric field, thus providing precise tracking information. The drift time combined with the hit location on the end-plates helps in reconstructing a three-dimensional trajectory of the charged track. The TPC also helps in identifying charged particles by using their specific energy loss (dE/dx) information. This is possible because different hadrons have different dE/dx based on their mass and total electric charge (see Fig. 4.3, right panel).

4.1.2 *Inner Tracking System*

The ITS is a six-layer silicon detector located at the centre of ALICE and closest to the collision point, wrapped around the beam axis. The six layers are at a radial distance of $3.9 - 43\ cm$ from the beam axis covering a pseudorapidity range $|\eta| < 0.9$. The ITS helps in measuring the trajectories of charged particles. A charged particle registers hits in multiple layers of the ITS while traversing it. Combining such hits provides the track information of the charged particle. The two innermost layers are Silicon Pixel Detectors (SPD), the two intermediate layers are Silicon Drift Detectors (SDD) and the outermost two layers are Silicon Strip Detectors (SSD), as shown in Fig. 4.4. The ITS was designed to assist the TPC in improving the position, angle, and momentum resolution for the reconstructed tracks. It can also identify the secondary vertices of the decaying strange, charm and beauty hadrons as well as reconstruct the interaction vertex with a resolution better than $100\mu m$. It provides better momentum resolution of high momentum particles traversing the TPC. The ITS, with its standalone tracking, helps recover low momentum particles ($p < 0.1 - 0.2$ MeV$/c$) missed by the TPC due to the curvature induced by the magnetic field. The TPC has a region that does not participate in the measurement of particle tracks. This inactive area consists of regions where the readout electronics and field cage electrodes are located. Very high momentum particles moving in this inactive area of the TPC are also caught by the ITS.

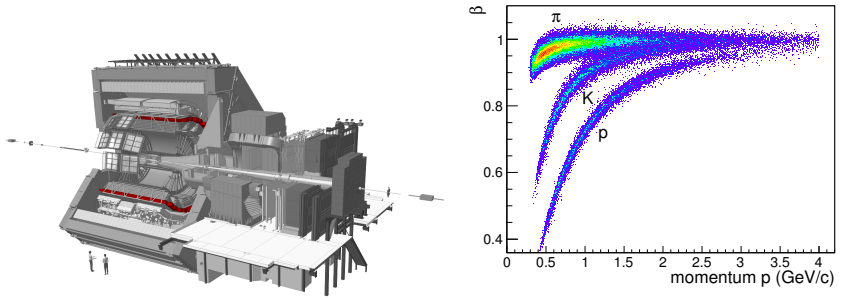

Figure 4.5: ALICE detector with its Time-Of-Flight detector [70] (left) and β vs. momentum in pp collisions at $\sqrt{s} = 900$ GeV [71] (right).

4.1.3 *Time-Of-Flight detector*

The Time-Of-Flight (TOF) detector (see Fig. 4.5, left) is a collection of 1593 glass Multi-gap Resistive Plate Chambers (MRPCs). It is positioned at $370 - 399$ *cm* from the beam axis, and covers a pseudorapidity range of $|\eta| < 0.9$ along with the full azimuthal angle. The TOF thus covers a total active area of 141 m^2. The main purpose it serves is the identification of particles in the intermediate momentum range, $0.5 < p_T < 4$ GeV/c, overlapping with the particle identification provided by the TPC and extending the p_T reach. The particle identification (PID) capability of the TOF is based on velocity (β) distribution of particles measured in it as a function of the particle momentum measured by the TPC (see Fig. 4.5, right). This is based on the time-of-flight information of charged particles from the interaction point to the TOF. Therefore, it depends on the efficiency of TPC tracks matched to TOF hits. This matching efficiency falls rapidly to zero for tracks with $p_T < 0.7$ GeV/c, owing to their energy loss.

4.2 RECONSTRUCTION OF TRACKS AND VERTICES

CLUSTERIZATION Firstly, raw detector data are converted into various *clusters*, which are characterized by information like position, time, amplitude etc. This step of clusterization is done individually for each detector. Track segments (or *tracklets*) are reconstructed by pairing clusters from the two SPD layers. An interaction vertex is the space point where tracks appear to originate from. A preliminary interaction vertex is determined from these SPD clusters by minimizing the distance between their tracklets.

TRACK AND VERTEX RECONSTRUCTION Tracks are reconstructed in three stages with an inward-outward-inward scheme. The first inward stage starts from the periphery of the TPC with some TPC cluster. A track candidate is identified by joining the peripheral TPC cluster, the next inner cluster and the preliminary interaction vertex. This serves as a seed for building or reconstructing the full track.

The track candidate is updated with the nearest inward TPC cluster found by using the Kalman Filter algorithm [72] iteratively. Track candidates are extended in this manner until the inner side of the TPC is reached. This is continued into the ITS by matching the TPC tracks to clusters in the outermost SSD layer. The outermost SSD clusters serve as seeds for a similar extension of the track up to the interaction vertex, as closely as possible. The outward stage then begins at the vertex, and the extrapolation continues to the outermost side of the TPC, which can further be propagated outwards into other detectors of the ALICE set-up like the TOF. A final inward step is performed by refitting the tracks back to a point as close to the primary vertex on the beam axis as possible. Obtaining the point of closest approach to the primary vertex can help distinguish between tracks that are more closely associated with the primary vertex, indicating a stronger correlation to the interaction of interest, and tracks that are farther away, potentially originating from secondary processes or unrelated interactions.

4.3 THE ALICE OFFLINE FRAMEWORK

The goal for the offline framework here is to have a software that is capable of storing, reconstructing and analysing billions of bits of data generated by the ALICE detector every second [73]. It is called AliRoot [74] and is based on ROOT [75]. ROOT is an open-source object-oriented data analysis and visualization framework designed to analyse petabytes of data scientifically. It is written in C++, comes with an interpreter for C++ and integrates well with PYTHON.

Real and simulated data are stored in the ROOT format as Event Summary Data (ESD) files containing all the physical information that can be used as a starting point in physics analyses. The computing speed of the analyses can be increased further by reducing the file size to be analysed. This is done by keeping only the information required for physics analyses in the so-called Analysis Object Data (AOD) files. All computationally heavy tasks are performed on the LHC computing grid, a large-scale distributed data processing infrastructure connecting several computing centres worldwide.

5 ANALYSIS STRATEGY FOR CHARM JETS

Charm jets treated in this thesis are identified by the presence of a D^0 meson among their constituents. However, the mean lifetime of D^0 mesons is too short for them to be detected directly, and therefore, the topology of the decay can be exploited for a proper reconstruction by means of topological selections and subsequent invariant mass analysis. The D^0 meson is reconstructed in its hadronic decay channel:

$$D^0 \rightarrow K^-\pi^+ (\text{and the charge conjugate } \overline{D^0} \rightarrow K^+\pi^-). \tag{5.1}$$

Such a channel presents a few advantages. It is 2-pronged, with the daughters being electrically charged and has a relatively high branching ratio BR = $3.950 \pm 0.031\%$ [76]. Since particles and their antiparticles are almost equally produced at the CERN LHC due to the high-energy scale at which the hadron collider operates, a D^0 meson and its antiparticle are treated equivalently in this thesis unless stated otherwise. Apart from the electrically neutral D^0 meson, which is actually reconstructed from its charged daughters, all the other constituents in the analysed jets are electrically charged particles. In this manuscript, charm jets will sometimes be referred in a more technical jargon as D^0-tagged charged-particle jets, D^0-tagged jets, or just D^0 jets.

In this chapter, we discuss the basic strategy for reconstructing charm jets, i. e. how D^0 mesons are reconstructed, how jets are found and consequently, how *D^0 jets* are identified. The idea, based on an event by event approach, is simply to identify D^0 mesons, and verify if they are a constituent while reconstructing jets. The key parameters and technical terms defined in this chapter will be used as general knowledge in the following three analysis chapters.

5.1 D^0-MESON RECONSTRUCTION

To reconstruct a D^0 meson, possible candidates ($K^{\mp}\,\pi^{\pm}$ pairs) are first identified. A D^0 candidate is only a combination of two tracks with the correct charge combination. Charged tracks are selected as possible daughters if they have $p_T > 300$ MeV/c, $|\eta| < 0.8$, and satisfy certain requirements in the TPC. These requirements include having at least 70 rows in the TPC traversed or crossed by the charged particles, with at least 80% of these crossed rows having an associated cluster. Additionally, the tracks should have at least two hits in the ITS, with a minimum of one hit in the first two layers. Tracks with $p_T < 3$ GeV/c are additionally required to have a hit in the first layer of the ITS. The D^0 candidates, which are simply formed due to such combinations or pairings of oppositely charged tracks but are not real D^0 mesons, contribute towards the so-called *combinatorial background*. The first step towards reducing such background is by using the topological properties of the decay and the kinematic properties of the daughter particles. The decay topology is illustrated in Fig. 5.1. The trajectories of

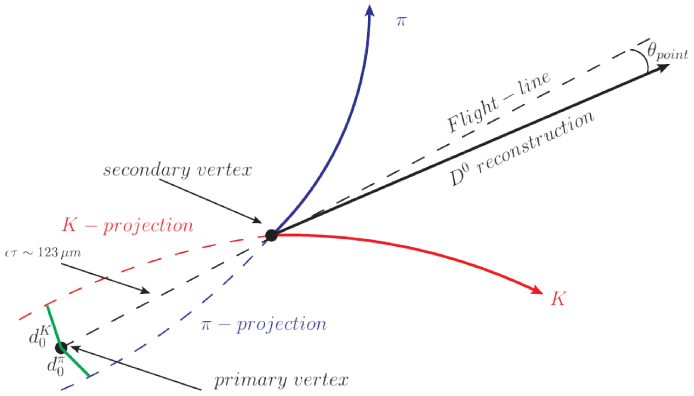

Figure 5.1: D^0-meson decay topology

the daughters in each pair can be projected back in order to identify the decay vertex (secondary vertex), and certain parameters helpful in reducing combinatorial background can then be defined as represented in the schematic view. These parameters are called *topological-selection variables* as they exploit the D^0-decay topology and pose a set of selection criteria for a D^0 candidate to be discarded or further processed. These topological selections are applied in several D^0-candidate momentum bins in the region $2 < p_T < 36$ GeV/c. After the candidates have passed the topological selections, their daughters are identified, and the correct pairs undergo the final reconstruction step that is the invariant mass analysis. We will discuss five such important topological-selection variables in the following sub-sections.

5.1.1 *Distance of closest approach*

The distance of closest approach (DCA) between the daughter tracks of a D^0 meson, (K and π), is the shortest distance between them. When a D^0 meson decays at the secondary vertex, its oppositely charged daughters are expected to originate from the same point and travel in a plane. However, due to detector limitations, the daughter tracks of a real D^0 meson would not seem to intersect perfectly at the secondary vertex, resulting in a non-zero DCA value between them. A background D^0 candidate may have a higher DCA value between its daughter tracks which are actually coming from separate decays and are uncorrelated. To reduce the combinatorial background, DCA values are limited to less than about 0.03 *cm*, significantly improving signal detection.

5.1.2 *Decay angle*

Another interesting topological-selection variable defined is the angle formed between the momentum of a daughter particle (K or π) from the decay in the rest frame of the mother particle (D^0) and the momentum of the mother particle in the lab frame. If we have two momentum axes, one parallel and one perpendicular to the momentum of D^0 in lab frame, the corresponding momenta of a daughter particle could be $p_{\parallel}$ and $p_{\perp}$ in lab frame, and $p'_{\parallel}$ and $p'_{\perp}$ in D^0 rest frame.

If the D^0 is moving at velocity v (and $\beta = v/c$, $\gamma = \frac{1}{\sqrt{1-\beta^2}}$) in the lab frame, and so the lab frame is moving at velocity $-v$ relative to the D^0-rest frame, the Lorentz transformation for the daughter particle's energy and momenta dictates that

$$\begin{pmatrix} E \\ p_{\parallel} \\ p_{\perp} \end{pmatrix} = \begin{pmatrix} \gamma & \gamma\beta & 0 \\ \gamma\beta & \gamma & 0 \\ 0 & 0 & 1 \end{pmatrix} \begin{pmatrix} E' \\ p'_{\parallel} \\ p'_{\perp} \end{pmatrix} \tag{5.2}$$

The daughter particle chosen is K. Its parallel momenta are related by $p_{par} = \gamma\beta E' + \gamma p'_{\parallel}$. As per our definition, ${p'_{\parallel}}^2 + {p'_{\perp}}^2 = {p'}^2$ and $p'_{\parallel} = p' \cos\theta^*$. So, our selection parameter was defined in our analysis software [77] as

$$\cos\theta^* = \frac{\frac{p_{\parallel}}{\gamma} - \beta E'}{p'}. \tag{5.3}$$

Since there is no special direction for the daughter particles to fly away in the D^0-rest frame, it is expected that the yield of kaons measured should be independent of $\cos\theta^*$. However, for combinatorial background, which are simply random combinations of K and π, the relation Eq. 5.3 does not hold, and some dependence of yield on $\cos\theta^*$ should be expected. It was found in MC simulations that the background overwhelmed the signal yield as we moved towards $\cos\theta^* = \pm 1$, while it got significantly lowered as we moved towards $\cos\theta^* = 0$ (see Fig. 5.2 right panel). A selection cut was therefore decided to be made at around $|\cos\theta^*| \leq 0.8$ especially for low-momentum D^0 candidates ($p_{T,D^0} < 8$ GeV/c). For high-momentum candidates, this selection was gradually loosened and therefore increased to 1 as momentum increased ($|\cos\theta^*| \leq 0.9$ for $8 \leq p_{T,D^0} < 12$ GeV/c and $|\cos\theta^*| \leq 1$ for $p_{T,D^0} \geq 12$ GeV/c).

5.1.3 *Impact parameters of D^0 daughters, and their product*

The closest distance between the backward extrapolation of a daughter track in the magnetic field and the primary interaction vertex is defined as the impact parameter (d_0) of the daughter track. Since the impact parameters of the daughter tracks of the background candidates are expected to randomly lie on either side of the primary vertex, their product becomes symmetric. However, for the signal candidates, one daughter is more massive than the other, thus making the product asymmetric (see Fig. 5.3 left panel) and a stronger selection parameter for D^0 candidates than the

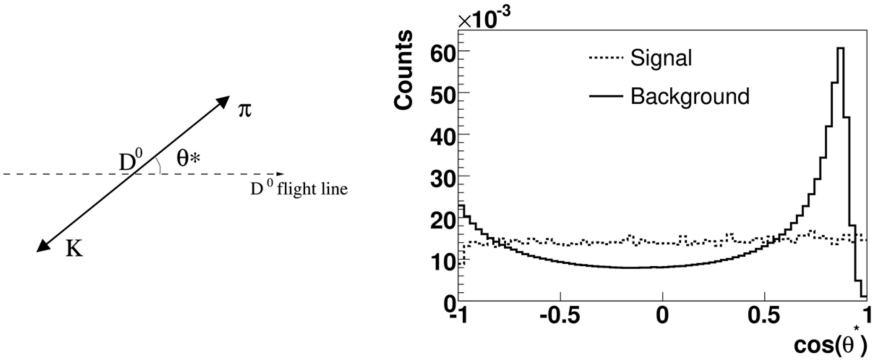

Figure 5.2: Left panel: definition of θ^*, the decay angle; right panel: distribution of $\cos(\theta^*)$ for background (solid line) and signal (dashed line) D^0 candidates [78].

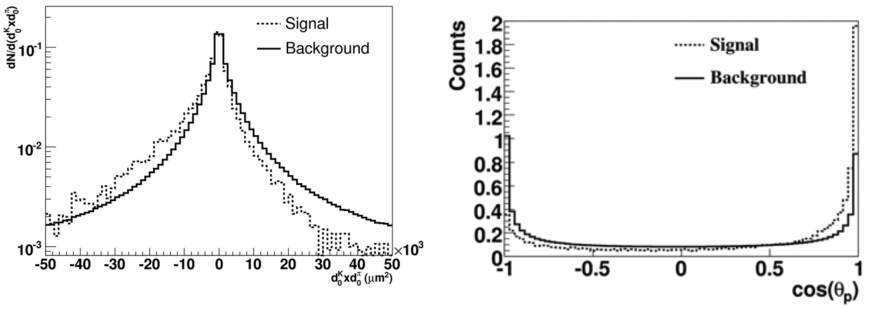

Figure 5.3: Left panel: product of impact parameters of background (solid line) and signal (dashed line) D^0 candidates with $p_{T,D^0} < 10$ GeV/c; right panel: cosine of the pointing angle for signal (dashed line) and background combinations (solid line) [78].

individual impact parameters. So, d_0^K and d_0^π were both generously restricted to less than 0.1 cm, whereas their product $d_0^K \times d_0^\pi$ was strongly restricted to $\leq -0.0003\ cm^2$ for low-p_T ($2-4$ GeV/c) D^0 candidates. This restriction was gradually loosened by increasing the upper limit to about $0.0001\ cm^2$ for high-p_T ($12-36$ GeV/c) D^0 candidates.

5.1.4 *Pointing angle*

In principle, the momentum sum of the daughters K and π should lie along the flight line of D^0 joining the primary and secondary vertices. However, detectors have limited resolution. So, it is natural to define an angle, called pointing angle θ_{point}, between these two vectors: D^0 momentum and D^0-flight line (See Fig. 5.3 right

Table 5.1: D^0 cuts for pp collisions at $\sqrt{s} = 5.02$ TeV. Default set.

p_{T,D^0} (GeV/c)	0.5 – 1	1 – 2	2 – 3	3 – 4	4 – 5	5 – 6	6 – 7	7 – 8	8 – 10	10 – 12	12 – 16	16 – 24	24 – 36
DCA (cm) ≤	0.03	0.03	0.03	0.03	0.03	0.03	0.03	0.03	0.03	0.03	0.03	0.03	0.03
$\lvert\cos(\theta^*)\rvert \leq$	0.8	0.8	0.8	0.8	0.8	0.8	0.8	0.8	0.9	0.9	1	1	1
$p_{T,K}$ (GeV/c)≥	0.5	0.5	0.7	0.7	0.7	0.7	0.7	0.7	0.7	0.7	0.7	0.7	0.7
$p_{T,\pi}$ (GeV/c)≥	0.5	0.5	0.7	0.7	0.7	0.7	0.7	0.7	0.7	0.7	0.7	0.7	0.7
$d_0^K \leq$ (cm)	0.1	0.1	0.1	0.1	0.1	0.1	0.1	0.1	0.1	0.1	0.1	0.1	0.1
$d_0^\pi \leq$ (cm)	0.1	0.1	0.1	0.1	0.1	0.1	0.1	0.1	0.1	0.1	0.1	0.1	0.1
$d_0^K \cdot d_0^\pi$ (10^{-4}cm^2) ≤	−5	−3.5	−3	−3	−1.5	−1	−0.8	−0.8	−0.5	−0.5	1	1	1
$\cos(\theta_{point})$ ≥	0.95	0.95	0.95	0.95	0.95	0.95	0.95	0.95	0.95	0.95	0.95	0.90	0.90
$L_{xy}/\sigma_{L_{xy}}(cm)$ ≥	5	5	5	5	5	4	4	4	3	3	3	3	3

panel). The signal-D^0 candidates should be expected to peak close to $\cos\theta_{point} \sim 1$ as their momentum should point back to the primary vertex. Thus, the restriction imposed was $\cos\theta_{point} \geq 0.95$, and this was sometimes loosened for high-p_T D^0 candidates down to about 0.85.

5.1.5 *Normalized decay length (lifetime)*

The decay length of a D^0 meson is defined as the distance between the primary and the secondary vertices, the path travelled by the D^0 before it decays into its daughter particles. But, the uncertainty on the decay length for D^0 mesons is dependent on their momentum. Slow-D^0 mesons have a smaller uncertainty than fast-D^0 mesons. Additionally, the best vertex resolution is obtained in the xy-plane, transverse to the beam axis (z). So, the projection of the decay length on the xy-plane normalized by the experimental uncertainty ($L_{xy}/\sigma_{L_{xy}}$) became another useful topological-selection parameter. A stronger cut of $L_{xy}/\sigma_{L_{xy}} > 5\ cm$ was applied to low-p_T D^0 mesons which had lower $\sigma_{L_{xy}}$. As the uncertainty increased for high-p_T D^0 mesons, the selection cuts applied were $L_{xy}/\sigma_{L_{xy}} > 4\ cm$ for $5 < p_{T,D^0} < 8$ GeV/c and $L_{xy}/\sigma_{L_{xy}} > 3\ cm$ for $p_{T,D^0} > 8$ GeV/c.

A summary of the default set of topological-selection variables, along with the selection on transverse momenta of daughter particles, is shown in the following table.

5.1.6 *Invariant mass*

The invariant mass of any particle or system of particles is one of its fundamental features. For a D^0 candidate ($K^\mp\ \pi^\pm$ pair), the invariant mass is:

$$M_{K\pi} = \sqrt{(E_K + E_\pi)^2 - (\vec{p}_K + \vec{p}_\pi)^2}. \tag{5.4}$$

The 3-momentum vector $\vec{p}$ of any particle is measured with our detector (see previous chapter on the ALICE detector). Once a D^0 candidate passes through the topological-selection criteria, the D^0-candidate daughter particle is subjected to particle identification (PID) based on a selection of n standard deviations ($n\sigma$, with $n = 3$) on the specific energy loss in TPC and the time-of-flight in TOF. If it is

identified conclusively as a K or a π, its corresponding invariant mass is assigned to it. Its energy then can be calculated using $E^2 = \vec{p}^2 + m^2$.

The D^0 meson is neutral, so if particle identification of its daughter particles is inconclusive, we cannot unequivocally assign an invariant mass to either of them. Instead, we consider two mass hypotheses for the pair of oppositely charged $(-+)$ tracks that may have originated from a D^0 meson: $K^-\ \pi^+$ and $\pi^-\ K^+$. The invariant masses of a K and a π are 493.677 ± 0.016 and 139.57039 ± 0.00018 MeV/c respectively. If the D^0 candidate is a real D^0 meson, one mass hypothesis will give a correct mass for the D^0 candidate with a relatively narrow distribution. The other mass hypothesis leads to a different mass for the D^0 candidate, resulting in a much broader distribution. We call this hypothesis a D^0 reflection, and the value of the mass the *reflected* mass. So in the modelling of a distribution of D^0 candidates, we need to consider three components: the signal, the combinatorial background, and the D^0 reflections.

To reduce the amount of computing time spent on processing background candidates, we limited the analysis to D^0 candidates with an invariant mass ($M_{K\pi}$) within the range

$$|\Delta M_{D^0}| = |M_{K\pi} - M_{D^0,PDG}| < 400 \text{ MeV}/c. \tag{5.5}$$

The value of $M_{D^0,PDG}$ in the above equation is 1864.83 ± 0.05 MeV/c [76]. In the next chapter (Ch. 6), we will explore the invariant-mass distributions in more detail to identify true D^0 mesons.

5.2 JET RECONSTRUCTION

Experimentally, jet production is analysed with a set of algorithms[1] to assess

- the raw jet signal,
- the jet background due to underlying event (to subtract from raw signal), and then
- the true jet spectra by correcting for detector effects through unfolding.

The charged particles used for jet reconstruction are required to have $p_T > 150$ MeV/c and $|\eta| < 0.9$.

5.2.1 *Finding jets*

When an energetic parton hadronizes, a group of particles collimated in a narrow angular cone is emitted. This is a jet. Particle detectors can only observe jets but not partons, but jets can be seen as representing the partons from which they originate. So a parton's existence and therefore, its kinematic properties can be inferred by studying jets. Reconstructing jets from detected particles needs to be performed by combining those particles in a step-by-step procedure following a

1 Algorithms used for jet reconstruction are encoded in the `FastJet` package [79] while the unfolding algorithms used are from `RooUnfold`[80] package.

suitable algorithm [81]. Also required is a recombination scheme [79] that helps assign a momentum to the reconstructed jet. This is most commonly done by summing up the 4-momenta of all particles in a jet to get the jet's final 4-momentum. So, an algorithm associated with a recombination scheme forms a *jet definition*.

One basic principle to keep in mind while developing jet definitions is that the algorithms used are collinear- and infrared-safe. This means that a set of hard energetic jets should not be changed when the event is modified by a collinear splitting or addition of an extra soft emission (see Fig. 5.4 and 5.5). Otherwise, it would be difficult to compare experimental-jet results with theoretical-jet observables. A jet observable should remain unchanged even if there is a collinear splitting:

$$O(X; p_1, p_2, \dots, p_n \| p_{n+1}) = O(X; p_1, p_2, \dots, p_n + p_{n+1}) \tag{5.6}$$

or emission of an infinitely soft particle:

$$O(X; p_1, p_2, \dots, p_n, p_{n+1} \to 0) = O(X; p_1, p_2, \dots, p_n). \tag{5.7}$$

Illustrated in Fig. 5.4 is a jet (on left) and how a particle in it could split into two (jet on right). When that happens, a collinear-unsafe algorithm could give a different set of jets that it counted. In this case, the number of jets increases, and that should not happen. Similarly in Fig. 5.5, initially two jets are counted on the left. But a mere addition of a soft gluon makes an infrared-unsafe algorithm redefine the set of jets and gives us a single jet. This kind of fluctuation should be avoided by adapting infrared- and collinear-safe algorithms. In both the figures, such algorithms would maintain the set of jets unmodified, safe from these QCD effects.

Currently, two highly efficient algorithms are used that include infrared and collinear safety up to all orders in perturbative QCD.

5.2.2 *Jet finding algorithms: k_T and anti-k_T*

To cluster particles into jets, the k_T algorithm uses successive steps. At each step, entities are compared in pairs. In the beginning, all entities considered in this thesis are charged particles (tracks). At later stages, either of the entities can be a pseudojet, i. e. a cluster of particles which have already been combined in the previous steps. For each pair of entities i and j, the k_T algorithm calculates a distance parameter d_{ij} based on their angular separation $\Delta R_{ij}^2 = (\eta_i - \eta_j)^2 + (\phi_i - \phi_j)^2$ in the pseudorapidity-azimuth $(\eta - \phi)$ cylindrical plane. This angular separation is then normalized by the jet-cone radius R in $\eta - \phi$, and weighted with the minimum of their squared transverse momentum, $\min(p_{Ti}^2, p_{Tj}^2)$. The distance parameter is then given by

$$d_{ij} = \min(p_{Ti}^2, p_{Tj}^2) \frac{\Delta R_{ij}^2}{R^2}. \tag{5.8}$$

An additional reference parameter d_i is introduced, which is just the transverse momentum squared of a given entity i. It is

$$d_i = p_{Ti}^2. \tag{5.9}$$

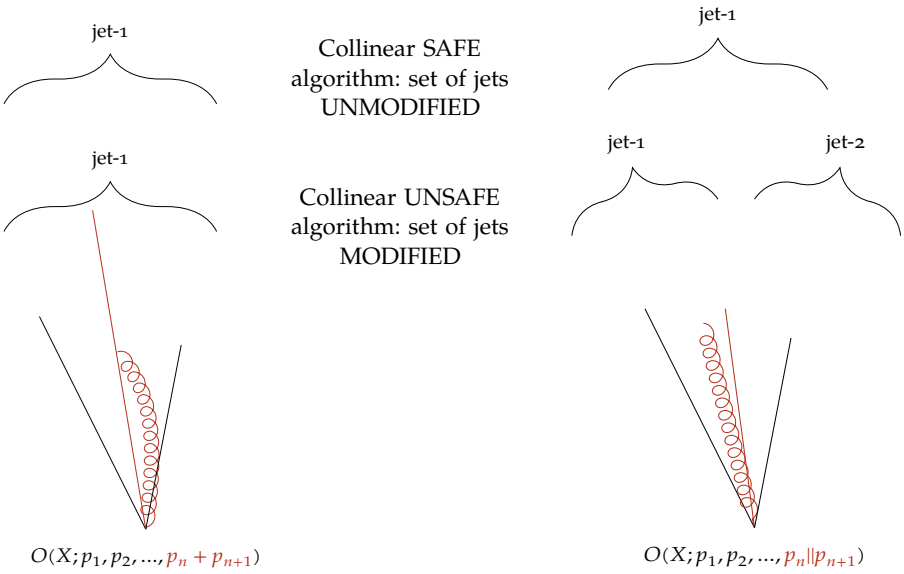

Figure 5.4: Collinear safety: a set of jets ($O(X)$) are modified due to a collinear splitting if the algorithm is collinear unsafe. Collinear splitting is represented by the jet constituent on the left with momentum $p_n + p_{n+1}$ splitting into two parallel constituents with momenta p_n and p_{n+1} on the right.

Next, the minimum of all the distances calculated and the reference parameter is found. If the minimum is a d_{ij}, i. e. from a pair of entities, these two entities are merged into a new entity k using the pt-recombination scheme [79] with its new transverse momentum, pseudorapidity, and azimuth given respectively by

- $p_{Tk} = p_{Ti} + p_{Tj}$,
- $\eta_k = \frac{p_{Ti}\eta_i + p_{Tj}\eta_j}{p_{Tk}}$, and
- $\phi_k = \frac{p_{Ti}\phi_i + p_{Tj}\phi_j}{p_{Tk}}$.

If the minimum is a d_i instead, i. e. the reference parameter, the entity is declared a final-state jet, and removed from the set of entities to undergo clustering again in the next steps. These clustering steps are repeated until no entity remains to be grouped into a jet.

This k_T algorithm groups softer entities within a required angular separation first. It is suitable for finding a soft-jet background in an event, especially in heavy-ion collisions. However, to find hard clusterings[2], a similar algorithm (anti-k_T) is used, where the distance parameter between two entities i and j is modified as

$$d_{ij} = min(p_{Ti}^{-2}, p_{Tj}^{-2}) \frac{\Delta R_{ij}^2}{R^2}. \tag{5.10}$$

2 Hard clusterings refer to the formation of high-momentum jets of particles that result from the fragmentation of a high-energy parton in a collision.

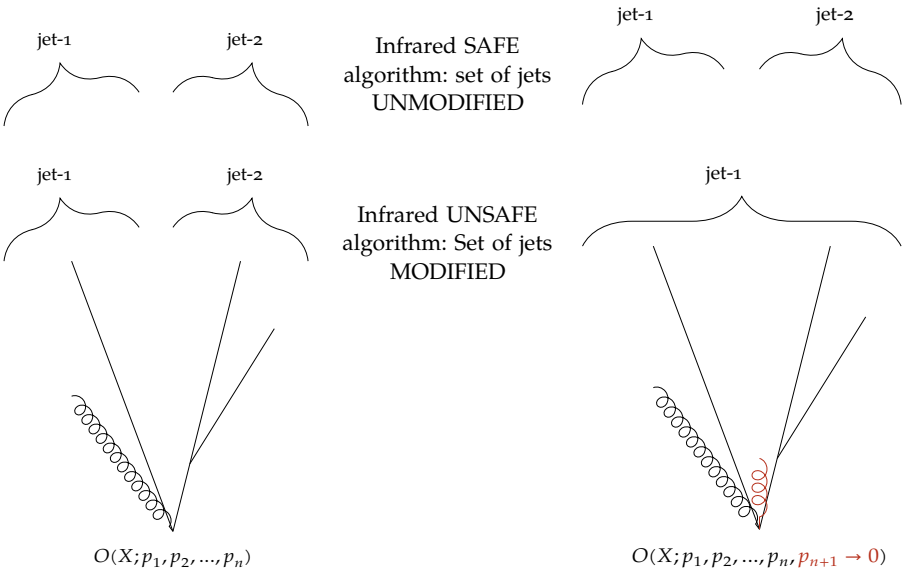

Figure 5.5: Infrared safety: a set of jets ($O(X)$) are modified due to addition of a soft (*infrared*) emission if the algorithm is infrared unsafe. An infrared (soft) emission added is shown on the right with momentum $p_{n+1} \to 0$.

and the reference parameter for entity i is changed to

$$d_i = p_{Ti}^{-2}. \tag{5.11}$$

The reciprocal of transverse momentum squared is considered in this algorithm which ensures that a jet grows by clustering the hardest entities first. The anti-k_{T} algorithm is most favoured for finding the *signal* jets in events at the hadron colliders. Many other algorithms exist, also for other purposes, but in this thesis, these two algorithms are used.

5.2.3 *Correcting for the underlying event*

In collisions involving heavy ions, like p–Pb and Pb–Pb collisions, a significant event background is formed, called the underlying event. It does not originate from the primary hard-scattering processes but mostly consists of remnants of scattering interactions like beam-beam remnants, initial- and final-state radiation, and multiparton interactions. In AA collisions at mid-rapidity, the dominant contribution to the underlying event comes mostly from soft binary nucleon-nucleon collisions. In each event, the jets would carry this extra 4-momentum from the underlying event that needs to be subtracted.

Removal of the underlying event's momentum contribution from signal (anti-k_T) jets is based on the idea that in any event, the underlying event tends to have mostly a uniform density of soft particles. The density ρ is defined to be the median of the transverse momentum densities of all k_T-clustered jets in the event [82, 83].

Transverse momentum density of the i^{th} k_T jet is $p_{T,i}/A_i$ where A_i is the jet's area. So,

$$\rho = \text{median}\left\{\frac{p_{T,i}}{A_i}\right\}. \tag{5.12}$$

The concept of a jet's area was specifically developed to address the issue of measuring a jet's susceptibility to additional contribution from the underlying event and any other soft background. A naive expectation for the area of a jet with radius R would be πR^2, which is consistent with the results obtained through the *passive area* method [79]. However, the *active area* of a k_T jet provides a more realistic picture for the jet background. Calculating the area of a jet uses the concept of *ghost* particles. *Ghosts* are called so because they are artificially created massless particles with an infinitesimally small transverse momentum. Their softness and the infrared safety of the jet algorithms ensure that the presence of ghosts does not impact the group of actual particles that ultimately form a specific jet.

JET-PASSIVE AREA The concept of passive areas involves adding a single ghost particle at a time to an event and observing which jet it ends up in. This process is repeated multiple times such that the passive area of a jet is proportional to the probability of it containing the ghost particle. The passive area provides a measure of how sensitive a jet is to point-like background noise.

JET-ACTIVE AREA The concept of active areas involves adding a uniform background of ghosts to an event, and clustering them together with the actual particles. The number of ghosts contained within a jet is proportional to its area. Active areas provide a measure of a jet's sensitivity to diffuse background noise.

A reconstructed jet's area is found by using the *active area* method. In each event, after a set of particles have been clustered into a set of jets by an infrared- and collinear-safe jet algorithm, a dense coverage of *ghost particles* are distributed randomly on the pseudorapidity-azimuth $(\eta - \phi)$ plane. This new set of particles, comprised of real and ghost particles, are again reclustered together into jets. The number of ghosts (N_g) contained in a jet divided by the number of ghosts per unit area (ν_g) would give the scalar active area of said jet:

$$A = \frac{N_g}{\nu_g} \tag{5.13}$$

The number of ghosts per unit area ν_g determines how precise the determination of the jet area is. A higher ν_g means greater precision in area determination. This also means increased computation time and memory consumption because of the increase in number of ghosts to be clustered. In this analysis, a ghost area $(a_g = 1/\nu_g)$ of 0.005 units was used.

The area is *active* because ghost particles actively participate in the jet reconstruction process. This is different from the *passive area* method, where a single ghost is scanned over the pseudorapidity-azimuth plane, and the area of a jet is defined by the region over which the ghost is clustered within that jet.

With a median density ρ (Eq. 5.12) for an event, scalar area A_j (Eq. 5.13) of an anti-k_T signal jet j in the event, and transverse momentum $p_{T,j}$ of the jet, the corrected transverse momentum of the jet is given by

$$p_{T,j}^{\text{corr}} = p_{T,j} - \rho A_j. \tag{5.14}$$

Events in p–Pb collisions are sparser than Pb–Pb collision events. To deal with such sparse systems, the background density is modified to

$$\rho = \text{median}\left\{\frac{p_{T,i}}{A_i}\right\}.C, \text{with } C = \frac{\text{Covered area}}{\text{Total area}} = \frac{\sum_j A_j}{A_{acc}}. \tag{5.15}$$

The factor C is calculated as the ratio of the *area covered* by the k_T jets that contain at least one real track over the *total area* of all k_T jets including pure ghost jets. The total area of all k_T clusters is basically the charged particle acceptance. Taking the median of all densities for the density of the underlying event (UE) instead of the average ensures that the contribution from hard scatterings to the UE density estimation is reduced. Additionally, the two hardest-leading k_T clusters (jets with the highest p_T) are excluded from the estimation of the median density ρ of the UE and of *background fluctuations* in the event.

The underlying event does not actually have a uniform density, it rather fluctuates over the pseudorapidity-azimuth plane. Each i^{th} k_T jet cluster's momentum density $p_{T,i}/A_i$ fluctuates about the momentum density ρ of the UE (Eq. 5.15). Since it is impossible to exactly estimate the fluctuating background, a statistical approach is taken. A method of *random cones* is used to estimate the background fluctuations.

5.2.4 *Random cones for background fluctuations*

This method consists of selecting a *cone* of a given jet radius at a *random* position η, ϕ in the pseudorapidity-azimuth plane and within the jet-detector acceptance in every reconstructed event [84]. The transverse momenta of all the tracks in the event lying within the cone are summed to get the transverse momentum of the cone $p_{T,\text{cone}}$. The total transverse momentum of the cone is recalculated based on the underlying event's momentum density ρ (Eq. 5.15). Their difference gives the background fluctuation in the said event:

$$\delta_{p_\text{T}} = p_{T,\text{cone}} - \rho\pi R^2. \tag{5.16}$$

The distribution of background fluctuations in p–Pb and Pb–Pb collision events is then included in the *detector-response matrix* used in the unfolding procedure described next.

5.2.5 *Unfolding algorithms*

Jet spectra determined from experiments still carry detector effects due to momentum smearing caused by finite detector resolution. Due to this smearing, the observable of a jet is modified such that it migrates from a given bin in the true

distribution to a different one in the measured distribution. The *unsmearing* of our measured observable can be done in two ways. One approach would involve assuming a mathematical function that represents the true distribution and estimating its free parameters. The second approach of inferring the *unsmeared* distribution is non-parametric and more prevalent in High Energy Physics [85] for reasons briefly discussed in the following.

A detector's response to the passage of elementary particles through it can be encoded in a function called the detector-response function. It is difficult and complex to analytically determine this function because of the intricate and complicated nature of the interactions between the particles and the detector material. Factors such as the geometry and composition of the detector, as well as the type and energy of the particles passing through it, can all contribute to the complexity of the detector response function. Therefore, it is often more practical to use Monte Carlo methods to simulate the passage of particles through the detector and extract the necessary information from the simulated data. We can use event generators like PYTHIA [86] to generate high-energy events and transport the particles formed through a particle-transport software like GEANT 3 [87]. Mathematically, the process of smearing the distribution of a true observable, x, into a smeared function of a measured variable y via a detector-response function, $F(x, y)$ can be seen as

$$s(y) = \int F(x, y)t(x)dx, \tag{5.17}$$

where $s(y)$ is the smeared function and $t(x)$ is the true distribution.

The straightforward approach in comparing high-energy-physics results would be to *smear* or *fold* the theory distributions with the response of the detector used and compare the resulting smeared distribution $s(y)$ with the experimentally measured distribution. However, physicists tend to conduct multiple experiments using different detectors. So modifying a theory curve every time to a new experimental result is quite tedious. Moreover, we may not have theory predictions on multiple occasions in spite of having a measurement. This necessitates the extraction of a true distribution from the experimentally measured distribution, making it more practical to do so. This procedure is called *unfolding* the measured distribution.

In experiments, the measured distribution is rather discrete. The above statement Eq. 5.17 can thus be rewritten as

$$s_y = F_{x,y}t_x. \tag{5.18}$$

In this matrix equation, s_y and t_x are vectors representing the measured and true distributions respectively, while $F_{x,y}$ represents the response function, or rather the response matrix. So by inverting the response matrix, the unfolding procedure now translates into an *inverse problem*:

$$t_x = F^{-1}_{x,y}s_y. \tag{5.19}$$

The matrix inversion method by numerical linear algebra would be ideal if we had negligible bin migrations, resulting in a response matrix F with a dominating diagonal. Since in practice, we have sizeable bin migrations, this leads to significant negative entries off the diagonal and quite large entries along the diagonal of the inverse matrix F^{-1}. So simply multiplying $F^{-1}_{x,y}$ with the experimentally measured distribution s_y as in Eq. 5.19 would result in a non-physical and wildly fluctuating solution [85]. This is a clear example of an *ill-posed* inverse problem [88, 89]. A numerical approach involving regularization is thus essential where prior assumptions are typically used to solve such ill-posed problems. We used two unfolding algorithms from the RooUnfold package [80] for this purpose in analyses reported in this thesis. One algorithm uses a Bayesian approach [90–92] and the other uses the method of Singular Value Decomposition [93].

5.2.6 *Bayesian Unfolding*

If we have several *causes* C_i having an *effect* E, the conditional probability can help define the *smearing* function as the probability $P(E|C_i)$. With Bayes' theorem, the probability of the observed effect having occurred due to the i^{th} cause is proportional to the probability of C_i causing the effect and the probability of the cause itself, and is given by

$$P(C_i|E) = \frac{P(E|C_i)P(C_i)}{P(E)}. \tag{5.20}$$

If the causes are independent of each other, $P(E) = \sum_i P(E|C_i)P(C_i)$. When multiple effects E_j are possible because of a cause C_i, then

$$P(C_i|E_j) = \frac{P(E_j|C_i)P(C_i)}{\sum_l P(E_j|C_l)P(C_l)}. \tag{5.21}$$

If we observe $n(E_j)$ events with effect E_j, the number of events assigned to every cause C_i would take into account all events $n(E_j)$ and is given by $n_{obs}(C_i) = \sum_j n(E_j)P(C_i|E_j)$. Thus, the true number of events would be

$$n_{true}(C_i) \quad = \quad \frac{n_{obs}(C_i)}{\sum_k P(E_k|C_i)} = \frac{\sum_j n(E_j)P(C_i|E_j)}{\sum_k P(E_k|C_i)}. \tag{5.22}$$

where $P(E_k|C_i)$ denotes the probability of getting an effect E_k having occurred due to a known cause C_i. Its sum over all effects k is the efficiency of detecting the cause C_i from all possible effects. From 5.22 and 5.21, the *unsmearing* function that *unsmears* or unfolds $n(E_j)$ to $n_{true}(C_i)$ should be given by U_{ij}, such that

$$n_{true}(C_i) \quad = \quad \sum_j U_{ij} n(E_j), \tag{5.23}$$

and

$$\begin{aligned} U_{ij} \quad &= \quad \frac{1}{\sum_k P(E_k|C_i)} \frac{P(E_j|C_i)P(C_i)}{\sum_l P(E_j|C_l)P(C_l)} \\ &= \quad \frac{1}{\sum_k P(E_k|C_i)} \frac{P(E_j|C_i)n_{prior}(C_i)}{\sum_l P(E_j|C_l)n_{prior}(C_l)} \end{aligned} \tag{5.24}$$

where $P(C_i)$ can easily be scaled in numerator as well as denominator to give the prior function $n_{prior}(C_i)$. With every iteration, this prior $n_{prior}(C_i)$ can be replaced by $n_{true}(C_i)$ from the previous iteration. The regularized solution or the true distribution can be determined after a certain and appropriate number of iterations before wild fluctuations are introduced to the solution. *A priori* information is generally derived from a Monte Carlo model or the measured distribution or variations in between. A flat distribution is also common in being used as a priori function, even if it can be quite far from the truth. However, the choice of prior does not strongly influence the solution in most problems.

In practice, we can determine the detector response matrix that represents the *smearing* function $P(E_j|C_i)$ from Monte Carlo simulations. Using unfolding algorithms, the *unsmearing* matrix or function U_{ij} is internally determined during the unfolding procedure.

5.2.7 *Singular Value Decomposition*

The approach to unfolding using this method is linear as opposed to the non-linear iterative procedure used in Bayesian unfolding. The core idea here is that given an $m \times t$ detector response or *smearing* matrix F, one can decompose it as a matrix product of an $m \times m$ orthogonal matrix M, an $m \times t$ diagonal matrix S with non-negative diagonal elements and a $t \times t$ orthogonal matrix T, i. e.

$$F = MST^T. \tag{5.25}$$

When acted upon a distribution n_t, T^T rotates the vector n_t, S scales it, and M rotates it again. The off diagonal elements σ_{ij} of S are zero, while its diagonal elements are non-negative.

$$\sigma_{ij} = 0 \text{ for } i \neq j, \text{ and } \sigma_{ii} \geq 0. \tag{5.26}$$

The non-negative diagonal quantities σ_{ii} are called *singular values* of the smearing matrix F, while the columns of M and N are known as the left and right *singular vectors*. So, if F smears a true distribution n_t to give n_m, the inversion calculations follow as:

$$\begin{aligned} Fn_t &= n_m, && (5.27)\\ MST^T n_t &= n_m, \\ ST^T n_t &= M^T n_m, \\ Sz &= d, \text{ where } z = T^T n_t \text{ and } d = M^T n_m. && (5.28)\\ z &= S^{-1} d, \\ n_t &= Tz = TS^{-1}d = TS^{-1}M^T n_m. \\ \text{And now, } F^{-1} &= TS^{-1}M^T && (5.29) \end{aligned}$$

This method of matrix inversion would be sustainable if the singular values σ_{ii} of S weren't too small. If they are, S^{-1} would contain values like $1/\sigma_{ii}$ leading to large fluctuations, and the problem is now ill-determined and needs regularization. The folding relation 5.27 can otherwise be expressed as a minimization problem:

$$(Fn_t - n_m)^T (Fn_t - n_m) = min.$$

And with regularization added, the problem becomes

$$(Fn_t - n_m)^T(Fn_t - n_m) + \tau \cdot (Cn_t)^T Cn_t \quad = \quad min, \tag{5.30}$$

where τ is the regularization parameter that determines the relative weight of the *a priori* condition defined by matrix C. With this, the new decomposition problem corresponding to Eq. 5.25 is

$$FC^{-1} = MST^T. \tag{5.31}$$

With non-zero regularization τ, the regularized i^{th} values d_i of vector d are

$$d_i^{(\tau)} = d_i \frac{s_i^2}{s_i^2 + \tau}, \tag{5.32}$$

where s_i are singular values of matrix FC^{-1}.

The vector d is related to the measured distribution as defined in Eq. 5.28. Post regularization, i. e. beyond the regularized i^{th} values d_i, values of the d vector are expected to be large, but then they exponentially fall off and attain a plateau at unity. After attaining unity at some i, the solutions of matrix inversion are dominated by statistical fluctuations. So, the regularization parameter τ is determined by finding an effective rank k, where the d_i values approach unity and $k = i$. The value of τ is then set to s_k^2 and used in finding the final solution.

The detailed description of the linear algebra with all technicalities is given in Ref. [93]. Bayesian unfolding is the default method used in all analyses in the thesis because it can be applied to multidimensional problems, and can handle non-square response matrices very well. This method is cross-checked against SVD unfolding wherever applicable. Both methods are well implemented in the *RooUnfold* package.

5.2.8 *Choosing regularization in unfolding*

The correlation developed between bin X of the unfolded distribution and bin Y of the measured distribution can be seen using Pearson correlation coefficients

$$\rho_{X,Y} = \frac{cov(X,Y)}{\sigma_X \sigma_Y}, \tag{5.33}$$

where σ_X and σ_Y are standard deviations of bins X and Y, while $cov(X,Y)$ is the corresponding covariance between those bins. Pearson's coefficients, being normalized covariances, lie between -1 and 1 corresponding to maximum anti-correlation and maximum correlation between two bins of concern. Auto-correlation is mostly expected where diagonal elements are ≈ 1 along with some mild correlation between neighbouring bins. In Bayesian unfolding, too few iterations would correspond to very strong regularization, while too many iterations would give very weak regularization. Similarly, in SVD unfolding, the higher is the regularization parameter, the weaker is the regularization and the more fluctuating is the unfolded result. Such extreme cases of regularization

would translate to extreme structures in Pearson correlation coefficients. So the suitable regularization parameter is the one with the minimum anti-correlation and the least extreme structures in Pearson correlation coefficients. For SVD unfolding, as mentioned in the previous section, the d-vector is generally used in finding the regularization parameter.

An additional method of finding the appropriate regularization parameter in any unfolding procedure is finding the parameter with which the unfolded result when folded back with the detector response, matches best with the yet-to-be-unfolded distribution.

5.3 CHARM-JET CANDIDATES

Now, we want to find jets that contain D^0 mesons. So, prior to reconstructing jets from the charged particles in each event, the daughter tracks were replaced by the 4-momentum of their reconstructed mother-D^0 candidate. Then, jets were reconstructed using the anti-k_T algorithm as illustrated in the previous section. This procedure was repeated for each D^0 candidate in the event. Following this, we had reconstructed charged-particle jets, with each jet containing only one D^0 candidate. Each D^0-jet candidate therefore had an associated jet transverse momentum ($p_{T,\text{ch jet}}$), transverse momentum (p_{T,D^0}) of the D^0 candidate, and the invariant mass (m_{inv}) of the same D^0 candidate. Armed with this information, the signal and background were separated statistically. Following this, the analysis chain generally accounts for reconstruction efficiency of D^0 jets, removal of contributions from B-hadron decays and unfolding of jets. These steps specific to the physics goal are explained in their respective Chapters 6, 7 and 8.

6 CHARM-JET PRODUCTION IN VACUUM

6.1 PHYSICS GOALS

In this chapter, the charm-jet production in vacuum (proton–proton collisions) is investigated. Such a measurement, besides being a valuable quantum-chromodynamics (QCD) test tool, will allow building the necessary *vacuum* reference in order to make a qualitative and quantitative assessment of heavy-flavour (charm) interaction with the cold and hot nuclear matter formed respectively in p–Pb and Pb–Pb collisions. Using the pp data ALICE collected in 2017 at $\sqrt{s} = 5.02$ TeV, we will investigate the production-cross section of charged-particle jets as a function of jet-transverse momentum. Each jet is required to contain a D^0 meson, thus becoming a so-called *D^0-tagged jet*.

We present such a measurement of these D^0-tagged jets in an extremely low momentum range, $5 < p_{T,\text{ch jet}} < 50$ GeV/c, that is inaccessible to the other LHC experiments. The studies include the investigation of charm jets with different jet-cone radii, $R = 0.2, 0.3, 0.4$, and 0.6 in the pseudorapidity-azimuth $(\eta - \phi)$ plane. By comparing the properties of charm jets produced with different jet-cone radii, we can study how energy is distributed in different angular cones. Smaller jet-cone radii (i. e. $R = 0.2$ and 0.3) indicate more collimated jets, while radii (i. e. $R = 0.4$ and 0.6) indicate less collimated jets. A comparison is also performed with a similar measurement done for pp collisions at $\sqrt{s} = 13$ TeV for $R = 0.2$, 0.4, and 0.6 [94, 95] and with theoretical models.

6.2 RAW YIELDS DIFFERENTIAL IN $p_{T,\text{ch jet}}$

D^0-jet candidates were reconstructed as per the analysis strategy outlined in Ch. 5. A D^0-jet candidate is an anti-k_T clustered jet consisting of charged particles and a D^0-meson candidate. To identify the jets with a signal-D^0 meson, an invariant-mass analysis of the D^0 candidates was performed. The invariant-mass distribution of D^0 candidates in each interval of p_{T,D^0} within $2 < p_{T,D^0} < 36$ GeV/c (see Fig. 6.1) was described by a combination of three functions: a Gaussian for the signal, an exponential for the combinatorial background, and a double Gaussian for the reflected D^0-candidates (see Sec. 5.1.6). The combined function describing an invariant-mass ($M_{K\pi}$) distribution of D^0 candidates is given by

$$f(M_{K\pi}) = f_{\text{signal}}(M_{K\pi}) + f_{\text{comb bkg}}(M_{K\pi}) + f_{\text{reflection}}(M_{K\pi}) \tag{6.1}$$

$$= Ce^{-\left(\frac{M_{K\pi}-\mu_{\text{fit}}}{2\sigma_{\text{fit}}}\right)^2} + ae^{bM_{K\pi}} + f_{\text{reflection}}(M_{K\pi}) \tag{6.2}$$

where $f_{\text{reflection}}(M_{K\pi})$ is the double-Gaussian fit to MC templates for D^0 reflections as described in Sec. 5.1.6. We defined the signal range as $|M_{K\pi} - \mu_{\text{fit}}| < 2\sigma_{\text{fit}}$, where

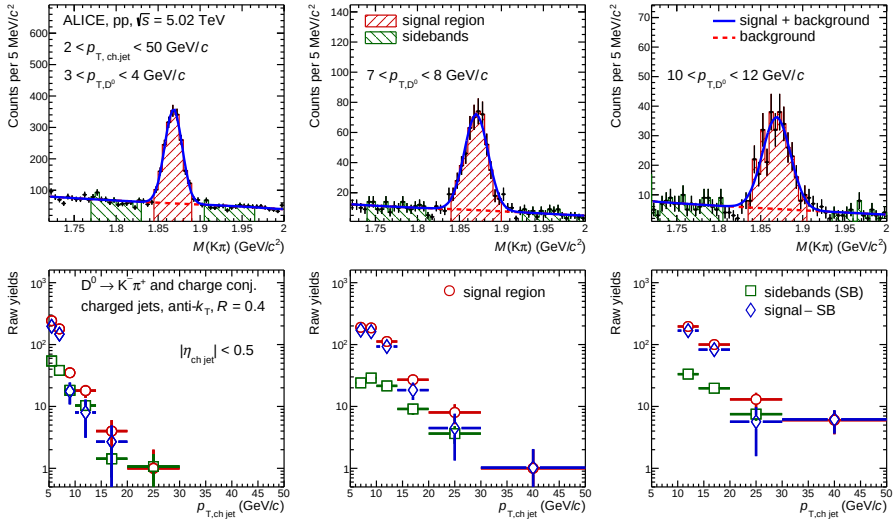

Figure 6.1: Top panel: invariant-mass distribution of D^0-jet candidates with $5 < p_{T,ch\,jet} < 50$ GeV/c for $R = 0.4$ in pp collisions at $\sqrt{s} = 5.02$ TeV and the required D^0-meson transverse momenta in intervals $3 < p_{T,D^0} < 4$ GeV/c (left), $7 < p_{T,D^0} < 8$ GeV/c (centre), $10 < p_{T,D^0} < 12$ GeV/c (right). The total fit function is represented by the blue solid line while the red solid line represents the total-background-fit function. The red and green shaded areas correspond to the peak and sideband regions respectively. Bottom panel: distributions of the D^0-meson tagged jet candidates in the peak region are shown in red circles, while in the sideband region are shown in green squares. The blue diamonds represent the subtracted distributions corresponding to the raw signals.

μ_{fit} and σ_{fit} are the mean and width of the Gaussian-fit component, respectively. The background regions (sidebands) were chosen within: $4\sigma_{fit} < |M_{K\pi} - \mu_{fit}| < 9\sigma_{fit}$. Figure 6.1 shows raw $M_{K\pi}$ distributions for $3 < p_{T,D^0} < 4$ GeV/c, $7 < p_{T,D^0} < 8$ GeV/c and $10 < p_{T,D^0} < 12$ GeV/c for the full jet-p_T range for $R = 0.4$. The signal and sideband regions are represented by the shaded red and green areas, respectively. The sidebands contain both combinatorial and reflection background, devoid of any real signal-D^0 mesons, whereas the signal region contains a mixture of real D^0-mesons, combinatorial background as well as reflection-background candidates.

The $p_{T,ch\,jet}$ distributions for the signal (red circles) and sideband (green squares) $M_{K\pi}$ regions were extracted in each p_{T,D^0} as presented in the bottom panel of Fig. 6.1. The sideband-$p_{T,ch\,jet}$ distributions were scaled to match the background yield under the signal-Gaussian peak and subtracted from the signal-region $p_{T,ch\,jet}$ distributions.

6.3 CORRECTIONS

The ultimate goal is to have a p_{T} spectrum of charged-particle jets, each of which contains a D^0 meson. So, after the invariant-mass analysis described above, which was done to identify signal-D^0 mesons, we could simply sum up the raw yields of D^0 jets from each $p_{\mathrm{T,D^0}}$ interval and get their $p_{\mathrm{T,ch\,jet}}$ spectrum. However, we need to make some corrections as well. There are three-fold corrections done to the raw spectra described in the previous section. They are for, firstly, the efficiency of D^0-jet reconstruction within the detector acceptance region, secondly, the subtraction of jets containing a D^0 meson coming from a B-meson decay, and thirdly, the impact of momentum smearing introduced by detector effects.

6.3.1 *Reconstruction efficiency*

In order to estimate how many D^0 jets our detectors could efficiently reconstruct, we used Monte Carlo PYTHIA 6 event generator and GEANT 3 simulations to calculate a reconstruction efficiency coupled with the detector acceptance. This efficiency coupled with the detector acceptance is defined as a ratio of the matched[1] detector-level D^0-jets that passed all the data-analysis selection-requirements to all the generator-level D^0-jets within the detector's acceptance region of $|\eta_{jet}| < 0.9 - R$. It should be noted that this efficiency depends on the topological cuts applied on D^0 mesons, which is why there is a minimal dependence of the reconstruction efficiency of D^0 jets on $p_{\mathrm{T,ch\,jet}}$. So, the reconstruction efficiencies were extracted as a function of $p_{\mathrm{T,D^0}}$ and can be seen for D^0 jets reconstructed with $R = 0.4$ in Fig. 6.2 (left panel).

The smaller reconstruction efficiency observed in the low-$p_{\mathrm{T,D^0}}$ region can be attributed to the stricter topological-selection criteria applied on low-$p_{\mathrm{T,D^0}}$ D^0-candidates. This was done to avoid the more abundant combinatorial background in the said kinematic region. The raw $p_{\mathrm{T,ch\,jet}}$-yield in every $p_{\mathrm{T,D^0}}$ interval was corrected by the corresponding reconstruction-efficiency value of prompt-D^0 jets ($\epsilon_{c\to \mathrm{D^0}}$). The efficiency-corrected $p_{\mathrm{T,ch\,jet}}$ distributions were then summed over all the $p_{\mathrm{T,D^0}}$ intervals to get the efficiency-corrected $p_{\mathrm{T,ch\,jet}}$-dependent yield as

$$N(p^{\mathrm{det}}_{\mathrm{T,ch\,jet}}) = \sum_{p_{\mathrm{T,D^0}}} \frac{N^{raw}(p_{\mathrm{T,D^0}}, p^{\mathrm{det}}_{\mathrm{T,ch\,jet}})}{\epsilon^{c\to \mathrm{D^0}}(p_{\mathrm{T,D^0}})} \tag{6.3}$$

The jet-momentum range covered in the efficiencies matches the one obtained in data, i. e. $5 < p_{\mathrm{T,ch\,jet}} < 50$ GeV/c. However, lower bins $2 < p_{\mathrm{T,ch\,jet}} < 5$ GeV/c were kept for the unfolding procedure. Due to the negligible $p_{\mathrm{T,ch\,jet}}$-dependence of the efficiency, it is safe to say that this choice also had a negligible effect.

1 Entries for D^0 jets are said to be matched if their information is available at both the generator and detector levels, and within the selection requirements.

6.3.2 *B-meson decay contribution*

Direct fragmentation of charm quarks is the major contributor to the production of D^0 mesons. These are called prompt D^0-mesons, our main target of investigation. However, the next significant contribution comes from beauty-quark fragmentation into B mesons which subsequently decay to D^0 mesons. This contribution is referred to as non-prompt D^0-mesons, or *B feed-down*, and we need to subtract it.

For each p_{T,D^0} bin, the D^0-jet spectra are related by:

$$N^{raw} = \epsilon^{c\to D^0} N^{c\to D^0} + \epsilon^{b\to D^0} N^{b\to D^0} \tag{6.4}$$

$$\Longrightarrow \sum_{p_{T,D^0}} \left(\frac{N^{raw}}{\epsilon^{c\to D^0}} = N^{c\to D^0} + \frac{\epsilon^{b\to D^0}}{\epsilon^{c\to D^0}} N^{b\to D^0} \right). \tag{6.5}$$

The detector-level non-prompt D^0-jet contribution, $N^{b\to D^0}(p_{T,D^0}, p^{det}_{T,ch\,jet})$, was estimated from the particle-level POWHEG + PYTHIA 6 simulations, $N^{POWHEG}(p_{T,D^0}, p^{part}_{T,ch\,jet})$, by a series of calculations. These particle-level simulations needed to be smeared with detector effects using a detector-response matrix, $RM^{b\to D^0}(p^{part}_{T,ch\,jet}, p^{det}_{T,ch\,jet})$, calculated from PYTHIA 6 + GEANT 3 simulations. This smearing procedure, or *folding*, can be shown as

$$N^{b\to D^0}(p_{T,D^0}, p^{det}_{T,ch\,jet}) = RM^{b\to D^0}(p_{T,D^0}, p^{part}_{T,ch\,jet}, p^{det}_{T,ch\,jet}) \cdot N^{POWHEG}(p_{T,D^0}, p^{part}_{T,ch\,jet}), \tag{6.6}$$

where $N^{b\to D^0}(p_{T,D^0}, p^{det}_{T,ch\,jet})$ and $N^{POWHEG}(p_{T,D^0}, p^{part}_{T,ch\,jet})$ are two vectors, and $RM^{b\to D^0}(p_{T,D^0}, p^{part}_{T,ch\,jet}, p^{det}_{T,ch\,jet})$ is a linear operator.

The resulting $N^{b\to D^0}(p_{T,D^0}, p^{det}_{T,ch\,jet})$ should then be scaled by the non-prompt reconstruction efficiency $\epsilon^{b\to D^0}$ to get the *raw non-prompt* D^0-jet spectra. Finally, the D^0-jet distributions after correcting for the prompt efficiency would contain properly corrected prompt D^0-jets as well as $\frac{\epsilon^{b\to D^0}}{\epsilon^{c\to D^0}}$-scaled non-prompt D^0-jets.

Eq. 6.5 should then translate into

$$\sum_{p_{T,D^0}} \left\{ \frac{N^{raw}}{\epsilon^{c\to D^0}} = N^{c\to D^0} + \frac{\epsilon^{b\to D^0}}{\epsilon^{c\to D^0}} \cdot \left(RM^{b\to D^0} \cdot N^{POWHEG} \right) \right\} \tag{6.7}$$

Realizing that the folding procedure shown in Eq. 6.7 is simply a matrix multiplication, the terms there can be interchanged as

$$\sum_{p_{T,D^0}} \left\{ \frac{N^{raw}}{\epsilon^{c\to D^0}} = N^{c\to D^0} + RM^{b\to D^0} \cdot \left(\frac{\epsilon^{b\to D^0}}{\epsilon^{c\to D^0}} \cdot N^{POWHEG} \right) \right\} \tag{6.8}$$

This step was essential because the response matrix $RM^{b\to D^0}$ was created in two dimensions, $p^{part}_{T,ch\,jet}$ and $p^{det}_{T,ch\,jet}$, and not p_{T,D^0} so as to make it statistically less

taxing. As a result, the scaling of the smeared spectra ($RM^{\mathrm{b}\to\mathrm{D}^0} \cdot N^{\mathrm{POWHEG}}$) by $\frac{\epsilon^{\mathrm{b}\to\mathrm{D}^0}}{\epsilon^{\mathrm{c}\to\mathrm{D}^0}}$ in Eq. 6.7 was not possible as $\frac{\epsilon^{\mathrm{b}\to\mathrm{D}^0}}{\epsilon^{\mathrm{c}\to\mathrm{D}^0}}$ was only $p_{\mathrm{T,D}^0}$-dependent. This hurdle was overcome by preparing the N^{POWHEG} simulations as a function of $p^{\mathrm{part}}_{\mathrm{T,ch\,jet}}$ in different bins of $p_{\mathrm{T,D}^0}$, then scaling them by $\frac{\epsilon^{\mathrm{b}\to\mathrm{D}^0}}{\epsilon^{\mathrm{c}\to\mathrm{D}^0}}$ before summing over all $p_{\mathrm{T,D}^0}$ bins.

$$\begin{aligned}\sum_{p_{\mathrm{T,D}^0}} \left(\frac{N^{raw}(p_{\mathrm{T,D}^0}, p^{\mathrm{det}}_{\mathrm{T,ch\,jet}})}{\epsilon^{\mathrm{c}\to\mathrm{D}^0}(p_{\mathrm{T,D}^0})} \right) &= \sum_{p_{\mathrm{T,D}^0}} N^{\mathrm{c}\to\mathrm{D}^0}(p_{\mathrm{T,D}^0}, p^{\mathrm{det}}_{\mathrm{T,ch\,jet}}) \\ &+ RM^{\mathrm{b}\to\mathrm{D}^0}(p^{\mathrm{part}}_{\mathrm{T,ch\,jet}}, p^{\mathrm{det}}_{\mathrm{T,ch\,jet}}) \cdot \\ &\sum_{p_{\mathrm{T,D}^0}} \left(\frac{\epsilon^{\mathrm{b}\to\mathrm{D}^0}}{\epsilon^{\mathrm{c}\to\mathrm{D}^0}}(p_{\mathrm{T,D}^0}) \cdot N^{\mathrm{POWHEG}}(p_{\mathrm{T,D}^0}, p^{\mathrm{part}}_{\mathrm{T,ch\,jet}}) \right)\end{aligned} \tag{6.9}$$

The left part of the equation above is from Eq. 6.3. With $N^{\mathrm{c}\to\mathrm{D}^0}(p^{\mathrm{det}}_{\mathrm{T,ch\,jet}}) = \sum_{p_{\mathrm{T,D}^0}} N^{\mathrm{c}\to\mathrm{D}^0}(p_{\mathrm{T,D}^0}, p^{\mathrm{det}}_{\mathrm{T,ch\,jet}})$, the reconstruction-efficiency corrected and B-feed-down subtracted D^0-jet spectra are given by

$$\begin{aligned}N^{\mathrm{c}\to\mathrm{D}^0}(p^{\mathrm{det}}_{\mathrm{T,ch\,jet}}) &= N(p^{\mathrm{det}}_{\mathrm{T,ch\,jet}}) \\ &- RM^{\mathrm{b}\to\mathrm{D}^0}(p^{\mathrm{part}}_{\mathrm{T,ch\,jet}}, p^{\mathrm{det}}_{\mathrm{T,ch\,jet}}) \cdot \\ &\sum_{p_{\mathrm{T,D}^0}} \left(\frac{\epsilon^{\mathrm{b}\to\mathrm{D}^0}}{\epsilon^{\mathrm{c}\to\mathrm{D}^0}}(p_{\mathrm{T,D}^0}) \cdot N^{\mathrm{POWHEG}}(p_{\mathrm{T,D}^0}, p^{\mathrm{part}}_{\mathrm{T,ch\,jet}}) \right)\end{aligned} \tag{6.10}$$

$$\text{i. e. } N^{\mathrm{c}\to\mathrm{D}^0}(p^{\mathrm{det}}_{\mathrm{T,ch\,jet}}) = N(p^{\mathrm{det}}_{\mathrm{T,ch\,jet}}) - N^{\mathrm{b}\to\mathrm{D}^0}(p^{\mathrm{det}}_{\mathrm{T,ch\,jet}}) \tag{6.11}$$

The B-feed-down fraction $\frac{N^{\mathrm{b}\to\mathrm{D}^0}(p^{\mathrm{det}}_{\mathrm{T,ch\,jet}})}{N(p^{\mathrm{det}}_{\mathrm{T,ch\,jet}})}$ is shown in Fig. 6.2 (right panel) for D^0 jets with jet radius $R = 0.4$.

6.3.3 *Unfolding the jet spectra*

The third and final step of correction in obtaining the true $p_{\mathrm{T,ch\,jet}}$-differential D^0-jet spectrum involves correcting for track momentum smearing due to the finite detector resolution. This is opposite to the procedure of *folding* the true spectrum $N^{\mathrm{POWHEG}}(p_{\mathrm{T,D}^0}, p^{\mathrm{part}}_{\mathrm{T,ch\,jet}})$ with a detector response $RM^{b\to\mathrm{D}^0}(p^{\mathrm{part}}_{\mathrm{T,ch\,jet}}, p^{\mathrm{det}}_{\mathrm{T,ch\,jet}})$ to get the detector-level smeared distribution $N^{b\to\mathrm{D}^0}(p^{\mathrm{det}}_{\mathrm{T,ch\,jet}})$ for non-prompt D^0-jets as shown in Eq. 6.6. We require the particle-level *unsmeared* or *true* $p_{\mathrm{T,ch\,jet}}$-distribution $N^{c\to\mathrm{D}^0}(p^{\mathrm{part}}_{\mathrm{T,ch\,jet}})$ found by *unfolding* the detector-level distribution $N^{c\to\mathrm{D}^0}(p^{\mathrm{det}}_{\mathrm{T,ch\,jet}})$ with the detector-response matrix $RM^{c\to\mathrm{D}^0}(p^{\mathrm{part}}_{\mathrm{T,ch\,jet}}, p^{\mathrm{det}}_{\mathrm{T,ch\,jet}})$ for prompt D^0-jets.

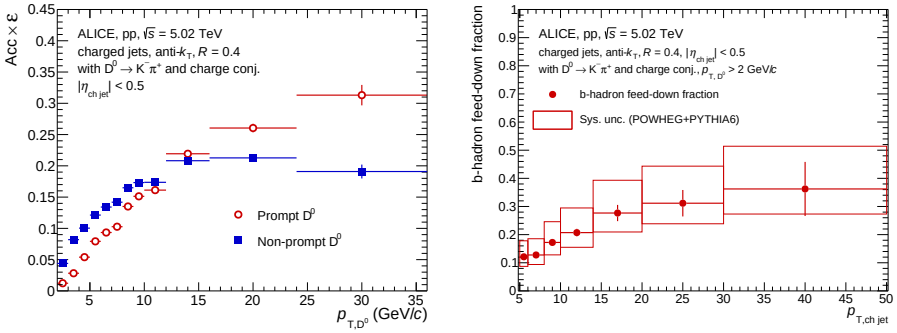

Figure 6.2: Left panel: product of acceptance and efficiency for prompt (red) and non-prompt (blue) D^0-meson jet reconstruction as a function of $p_{\mathrm{T,D}^0}$ with $R = 0.4$, and $5 < p_{\mathrm{T,ch\,jet}} < 50$ GeV/c. Right panel: B-feed-down fraction of D^0-meson jets from b-hadrons for $R = 0.4$ shown as a function of $p_{\mathrm{T,ch\,jet}}$ in $5 < p_{\mathrm{T,ch\,jet}} < 50$ GeV/c. Systematic uncertainties shown as boxes are explained in Sec. 6.4.

Here, $N^{\mathrm{c}\to\mathrm{D}^0}(p^{\mathrm{det}}_{\mathrm{T,ch\,jet}})$, and $N^{\mathrm{c}\to\mathrm{D}^0}(p^{\mathrm{part}}_{\mathrm{T,ch\,jet}})$ would be two vectors and $RM^{\mathrm{c}\to\mathrm{D}^0}(p^{\mathrm{part}}_{\mathrm{T,ch\,jet}}, p^{\mathrm{det}}_{\mathrm{T,ch\,jet}})$ would represent a linear operator.

$$N^{\mathrm{c}\to\mathrm{D}^0}(p^{\mathrm{det}}_{\mathrm{T,ch\,jet}}) = RM^{\mathrm{c}\to\mathrm{D}^0}(p^{\mathrm{part}}_{\mathrm{T,ch\,jet}}, p^{\mathrm{det}}_{\mathrm{T,ch\,jet}}) \cdot N^{\mathrm{c}\to\mathrm{D}^0}(p^{\mathrm{part}}_{\mathrm{T,ch\,jet}}). \quad (6.12)$$

The *unfolding* procedure is then

$$N^{\mathrm{c}\to\mathrm{D}^0}(p^{\mathrm{part}}_{\mathrm{T,ch\,jet}}) = \left(RM^{\mathrm{c}\to\mathrm{D}^0}(p^{\mathrm{part}}_{\mathrm{T,ch\,jet}}, p^{\mathrm{det}}_{\mathrm{T,ch\,jet}})\right)^{-1} \cdot N^{\mathrm{c}\to\mathrm{D}^0}(p^{\mathrm{det}}_{\mathrm{T,ch\,jet}}). \quad (6.13)$$

As introduced earlier in Sec. 5.2, such a direct solution of matrix inversion is impractical. To tackle this problem, sophisticated methods are employed to determine the particle-level *unfolded/unsmeared/true* distribution, $N^{\mathrm{c}\to\mathrm{D}^0}(p^{\mathrm{part}}_{\mathrm{T,ch\,jet}})$.

We used the Bayesian approach [91] to prepare an *unsmearing* matrix within the algorithm from a *smearing* detector-response matrix for unfolding D^0-jet distributions which have already been corrected for reconstruction efficiency and subtracted for B-feed-down contribution. As discussed in Sec. 5.2.8, Pearson correlation coefficients can be used to determine optimal regularization parameters in unfolding. Five iterations seemed good enough. The unfolded spectrum was then folded back using the same detector-response matrix; good convergence was seen between the folded spectrum and the measured spectrum. Unfolding was performed in the range: $2 < p_{\mathrm{T,ch\,jet}} < 50$ GeV/c, but the result was finally reported in $5 < p_{\mathrm{T,ch\,jet}} < 50$ GeV/c. The jet information in $2 < p_{\mathrm{T,ch\,jet}} < 5$ GeV/c was kept to correct for bin migration and avoid any biasing if the said information were removed. The unfolding procedure was performed twice, once including the jet information > 50 GeV/c and once excluding. But said jet information was found to be too negligible to impact the unfolding results and was therefore ultimately not used in the final procedure.

In Fig. 6.3, the left panel shows our *smearing* detector-response matrix for prompt D^0-jets with $R = 0.4$ used in the unfolding procedure for said jets. One can observe significant bin migration between the required observable $p_{\mathrm{T,ch\,jet}}^{\mathrm{part}}$ and the measured observable $p_{\mathrm{T,ch\,jet}}^{\mathrm{det}}$ in the response matrix. Bin migration can occur when the measured values of the observable fall in a different bin in the reconstructed spectrum compared to the true bin in the generated (particle-level) spectrum. To study the resolution of the $p_{\mathrm{T,ch\,jet}}$ measurement, the probability density distributions of the residuals

$$\Delta_{p_{\mathrm{T}}} = \frac{p_{\mathrm{T,ch\,jet}}^{\mathrm{det}} - p_{\mathrm{T,ch\,jet}}^{\mathrm{part}}}{p_{\mathrm{T,ch\,jet}}^{\mathrm{part}}} \tag{6.14}$$

were examined. The resolution on $p_{\mathrm{T,ch\,jet}}$ can be obtained as the width of the distribution of residuals $\Delta_{p_{\mathrm{T}}}$. They are shown on the right panel in different intervals of the true observable $p_{\mathrm{T,ch\,jet}}^{\mathrm{part}}$. This resolution measures how much a detector-level jet observable, $p_{\mathrm{T,ch\,jet}}^{\mathrm{det}}$, would deviate from its true particle-level jet observable $p_{\mathrm{T,ch\,jet}}^{\mathrm{part}}$ in a given interval of $p_{\mathrm{T,ch\,jet}}^{\mathrm{part}}$. As seen on the right panel in Fig. 6.3, the resolution shows a strong peak at zero, with a general shift towards the left. This shows that the detector effects are small, but tend to provide a lower measurement of the $p_{\mathrm{T,ch\,jet}}$ than determined at the particle level.

The bins involved in the migration between the measured and unfolded spectra, which are affected by bin migration and corrected by the unfolding procedure, are commonly referred to as *feed-in and feed-out bins*. In unfolding, "feed-in" and "feed-out" refer to the inputs and outputs of the unfolding algorithm. The feed-in bin is the bin in the measured spectrum that is used as input to the unfolding algorithm. This bin contains the observed data, such as the number of D^0 jets in a particular range of jet-transverse momentum. The feed-out bin, on the other hand, is the bin in the unfolded spectrum that corresponds to the feed-in bin. The unfolded spectrum is an estimate of the true distribution of the observed data, corrected for detector effects. The feed-out bin therefore represents the best estimate of the true distribution in the same range of jet-transverse momentum.

6.4 SYSTEMATIC UNCERTAINTIES

Systematic uncertainties were studied from several sources. They can be separated into the following groups:

1. Topological selection,
2. Raw-yield extraction,
3. B-feed-down subtraction,
4. Unfolding,
5. Track-reconstruction efficiency, and
6. Normalization.

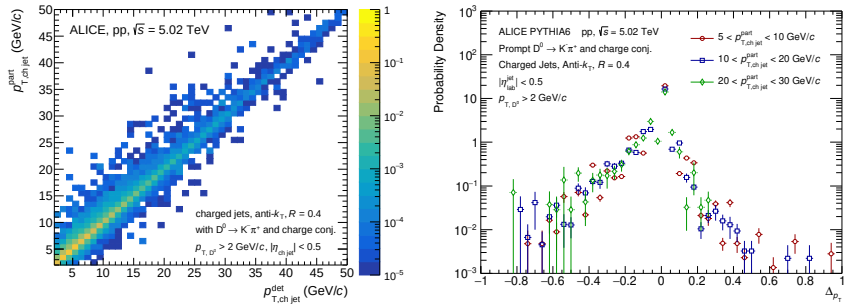

Figure 6.3: Left: detector-response matrix used for unfolding $p_{\mathrm{T,ch\,jet}}$ distribution with $R = 0.4$ in pp collisions at $\sqrt{s} = 5.02$ TeV with both detector and particle levels in $2 < p_{\mathrm{T,ch\,jet}} < 50$ GeV/c. Right: probability density distributions of the residuals $\Delta_{p_{\mathrm{T}}}$ of $p_{\mathrm{T,ch\,jet}}$ in $5 < p^{\mathrm{part}}_{\mathrm{T,ch\,jet}} < 10$ GeV/c, $10 < p^{\mathrm{part}}_{\mathrm{T,ch\,jet}} < 20$ GeV/c and $20 < p^{\mathrm{part}}_{\mathrm{T,ch\,jet}} < 30$ GeV/c.

6.4.1 *Topological selection*

Monte Carlo simulations were used for correcting the results at different stages of data analysis. Some residual discrepancies between data and MC distributions are expected in the D^0-meson topological-selection variables that can influence the D^0-jet reconstruction efficiency. In order to assign a systematic uncertainty from this source, the D^0-meson topological-selection requirements, in particular the product of impact parameters of daughter particles K and π, the cosine of the pointing angle, and the normalized decay length were varied by $\pm 5\%$ and $\pm 10\%$ with an aim to create four extra sets of selection cuts: cut-1 $(+5\%)$, cut-2 $(+10\%)$, cut-3 (-5%) and cut-4 (-10%). The whole analysis procedure was repeated for each variation up to the subtraction of the *b*-jet contribution. This is because the first two steps of correction (for reconstruction efficiency and *b*-jet contribution) involve topological-selection criteria directly, while the third and final step of unfolding deals mainly with detector response and momentum-tracking resolution. The whole procedure resulted in the reconstruction efficiency varying between 10% and 25%, depending on the D^0-meson p_{T}. The final uncertainty was then estimated by taking the root-mean-square deviations of the results obtained with these different D^0-meson selection criteria. The uncertainty increases with the $p_{\mathrm{T,ch\,jet}}$ and is between 1% and 10% in most cases.

6.4.2 *Raw-yield extraction: multi-trial*

An invariant-mass fit to the D^0-jet candidates was used to determine signal and background D^0-meson distributions and thereby get the raw yield, as described in Sec. 6.2. The stability of this raw-yield extraction procedure was assessed by

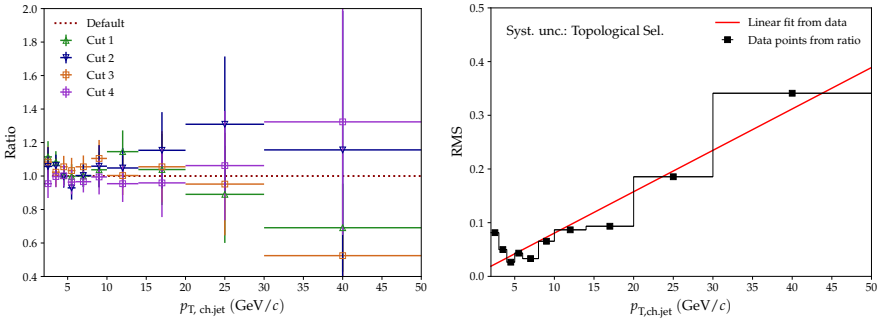

Figure 6.4: Systematic uncertainties due to topological selection cut variation. Left panel: Ratios of B-feed-down subtracted D^0-jet yields from different sets of topological cut selection compared to the default set of cuts used with jets of $R = 0.4$ in pp collisions at $\sqrt{s} = 5.02$ TeV. Right panel: Root-mean-square values of deviations from unity from the left panel. A linear trend is assumed and uncertainties are taken from a linear fit to the values.

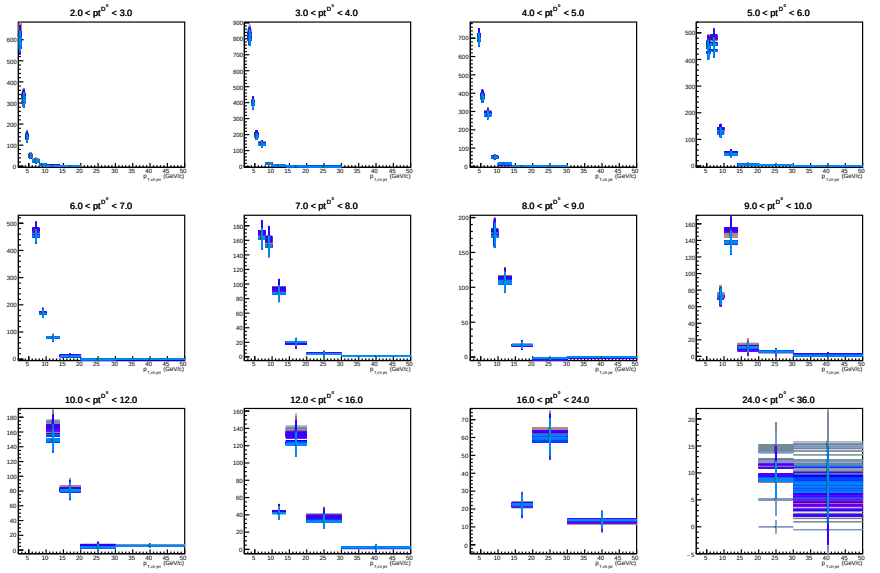

Figure 6.5: Multi-trial raw yield extraction of D^0-jet yields with jets of $R = 0.4$ in pp collisions at $\sqrt{s} = 5.02$ TeV. Yields are shown in every p_{T,D^0} bin in 2–36 GeV/c.

considering possible variations to the invariant-mass fitting conditions. The conditions that were varied are

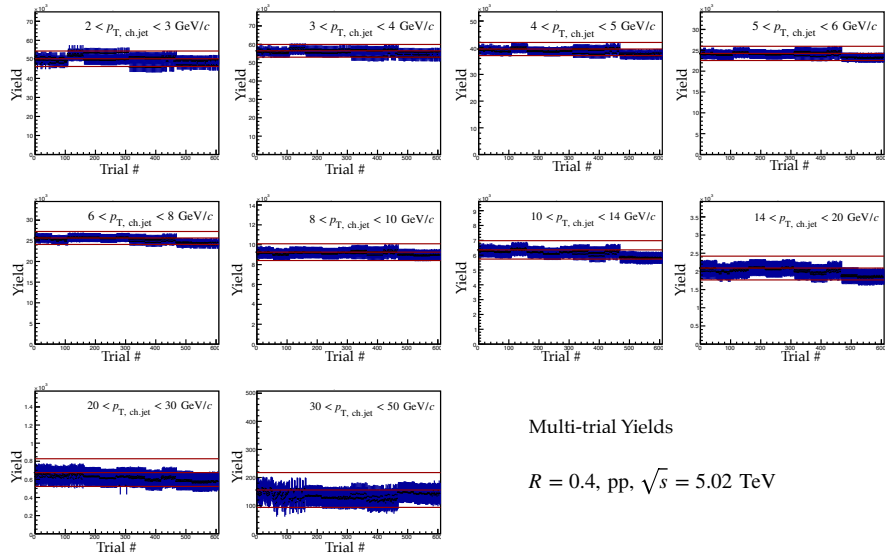

Figure 6.6: Multi-trial raw yield extraction. Yields as a function of trial number in all bins of $p_{\mathrm{T,ch\,jet}}$ between 2–50 GeV/c for jets with $R = 0.4$ in pp collisions at $\sqrt{s} = 5.02$ TeV.

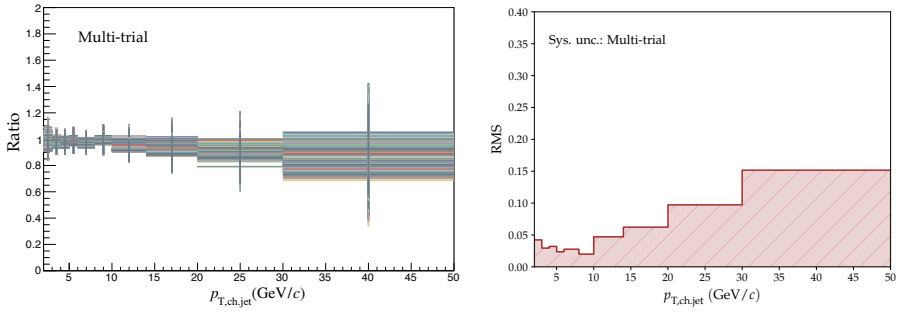

Figure 6.7: Systematic uncertainties due to multi-trial extraction of $p_{\mathrm{T,ch\,jet}}$ yields. Left: Ratios of efficiency-corrected yields from different trials to the yield from the default configuration, for jets with $R = 0.4$ in pp collisions at $\sqrt{s} = 5.02$ TeV. Right: Root-mean-square values of deviations from unity (from the left panel) are taken as systematic uncertainty values.

- the width (σ_{fit}) of the Gaussian signal which was either kept free or fixed to the MC values, or fixed to 10% above or lower than MC values (σ = free, σ_{MC}, $1.1\sigma_{MC}$, $0.9\sigma_{MC}$: 4 variations),
- the assumed shape of the background function (default exponential was replaced by linear and polynomial: 3 variations),

- the mean (μ_{fit}) of the Gaussian signal was either free or fixed to the MC values from Particle Data Group (2 variations),
- the lower limit of the fit ranges (default was 1.71 GeV/c^2, two more variations were 1.72 and 1.70 GeV/c^2: 3 variations),
- the upper limit of the fit ranges (default was 2.10 GeV/c^2, two more variations were 2.09 and 2.11 GeV/c^2: 3 variations), and
- the mass bin width (default was 5 MeV/c^2, two more variations were 10 and 2.5 MeV/c^2: 3 variations).

So with all the above conditions considered, a maximum total of $4\times3\times2\times3\times3\times3 = 648$ *multiple* trials of fitting the invariant-mass distributions were done. Not every trial would give a proper fit while some of them even did not give any meaningful results and were therefore ignored. What we see in Fig. 6.5 are the sideband-background-subtracted spectra in different bins of $p_{\text{T,D}^0}$, like on the bottom panel of Fig. 6.1. All the bins of $p_{\text{T,D}^0}$ in $2 < p_{\text{T,D}^0} < 36$ GeV/c are shown. Efficiency-corrected yields from each trial are shown against the trial number in Fig. 6.6, in different bins of $p_{\text{T,ch jet}}$ in $2-50$ GeV/c. Since the variations were done in a *for loop* as listed above, σ changed with every $3\times2\times3\times3\times3 = 162$ trials; background changed with every $2\times3\times3\times3 = 54$ trials; D^0-mass condition changed with every $3\times3\times3 = 27$ trials; the lower limit of invariant-mass fitting condition changed with every $3\times3 = 9$ trials; the upper limit changed with every 3 trials; and finally, mass bin width changed with every trial. The ratio of every trial to the default configuration is plotted on the left panel of Fig. 6.7. The root-mean-square values of the relative yield-differences obtained from these trials compared to the default yield were taken as another part of the systematic uncertainties from the raw-yield extraction. They are shown on the right panel of Fig. 6.7.

6.4.3 *Raw-yield extraction: signal and sideband ranges, and D^0 reflections*

Another source of systematic uncertainties for raw-yield extraction procedure was explored by varying the defined signal and sideband ranges in units of the signal width, and then relative systematic uncertainties were calculated. These uncertainties yielded about 1% and 2%, respectively. A third systematic uncertainty for the raw-yield extraction was assigned by varying the relative contribution of reflections by $\pm50\%$ and the maximum deviation in the raw yield was taken as the systematic uncertainty. The total uncertainty on the raw-yield extraction was estimated to reach a maximum of 20% for the $p_{\text{T,ch jet}}$-differential cross section.

6.4.4 *B-feed-down subtraction*

The systematic uncertainty from the subtraction of the B-meson decay contribution was determined by varying parameters of the non-prompt D^0-jet POWHEG + PYTHIA 6 simulations. They were varied individually in the following ways: (i) the beauty-quark mass was changed to 4.5 GeV/c^2 and

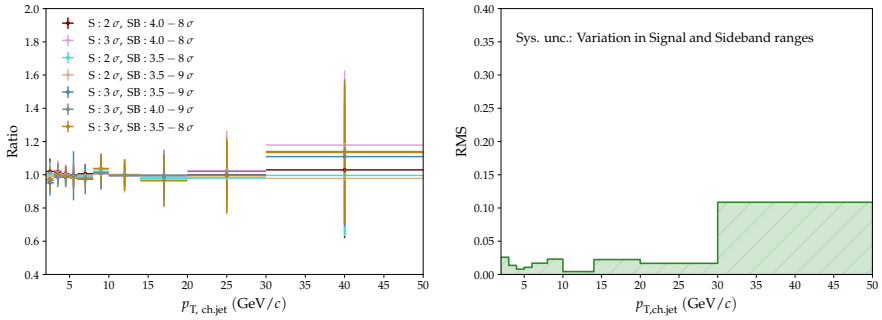

Figure 6.8: Systematic uncertainties due to the variation in ranges of signal and sideband regions during the extraction of $p_{\mathrm{T,ch\,jet}}$ yields. Left: Ratios of efficiency-corrected yields from different variations to the yield from the default configuration, for jets with $R = 0.4$ in pp collisions at $\sqrt{s} = 5.02$ TeV. Right: Root-mean-square values of deviations from unity (from the left panel) are taken as systematic uncertainty values.

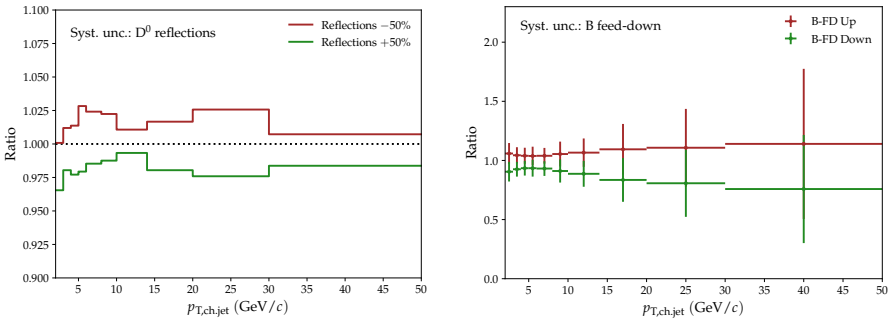

Figure 6.9: Left panel: Ratio of raw $p_{\mathrm{T,ch\,jet}}$-yields with 50% higher and lower reflections compared to the default $p_{\mathrm{T,ch\,jet}}$ raw-yield for D^0 jets with $R = 0.4$. Right panel: B-feed-down subtracted $p_{\mathrm{T,ch\,jet}}$ spectra for said jets with upward and downward variations shown in red and green (see text for more details).

5 GeV/c^2 from the default 4.75 GeV/c^2 (ii) the μ_R and μ_F were either halved or doubled from their nominal value which was the transverse mass of the beauty quark. The largest upward and downward variations were taken as the systematic uncertainties. The uncertainty on the feed-down was estimated for the $p_{\mathrm{T,ch\,jet}}$-differential cross section to be 4–40%.

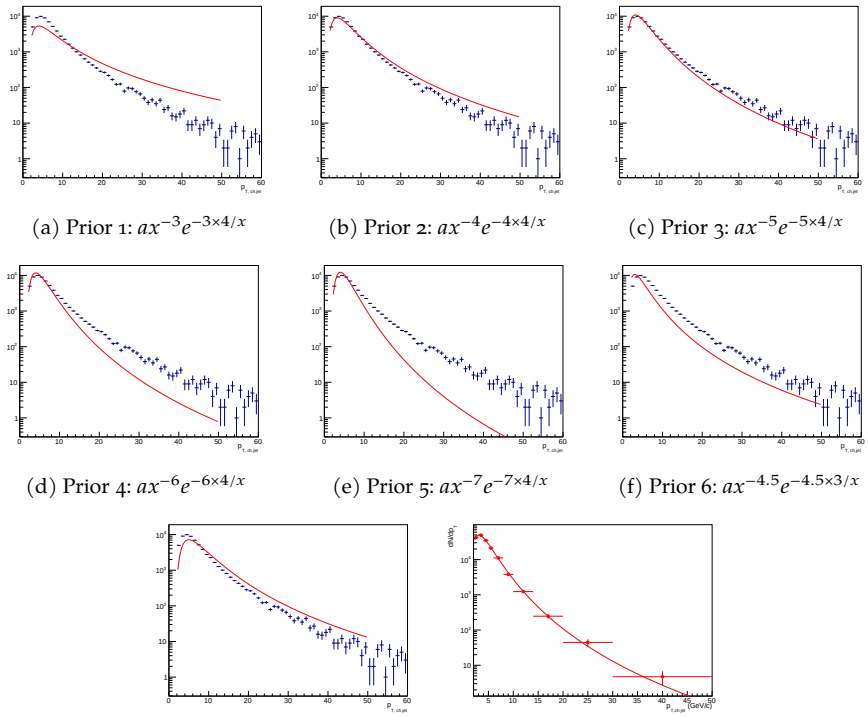

(a) Prior 1: $ax^{-3}e^{-3\times4/x}$ (b) Prior 2: $ax^{-4}e^{-4\times4/x}$ (c) Prior 3: $ax^{-5}e^{-5\times4/x}$

(d) Prior 4: $ax^{-6}e^{-6\times4/x}$ (e) Prior 5: $ax^{-7}e^{-7\times4/x}$ (f) Prior 6: $ax^{-4.5}e^{-4.5\times3/x}$

(g) Prior 7: $ax^{-4.5}e^{-4.5\times5/x}$ (h) Prior 8: Fit to the measured spectrum.

Figure 6.10: Different priors used to evaluate stability in the unfolding procedure are shown for D^0 jets in pp collisions at $\sqrt{s} = 5.02$ TeV for $R = 0.4$.

6.4.5 *Unfolding: Stability in Bayesian approach*

Several checks were done to understand the stability of the unfolding procedure from Sec. 6.3.3.

- *Priors*: For the default unfolding procedure with the Bayesian approach, the true Monte Carlo distribution was provided as a prior. For assessing the stability with regards to providing priors, a set of other priors were instead provided to the unfolding procedure. The different priors considered were of the form $ax^{-b}e^{-bc/x}$ where 'x' was $p_{\mathrm{T,ch\,jet}}$, parameter 'a' was a scaling factor and was kept free, 'b' was the power-law and 'c' was the position of the local maximum of the distribution. The exponential factor $e^{-bc/x}$ was helpful in avoiding infinities at zero and thus providing a more realistic spectrum. The variations used are:
  1. prior-1: $b = 3, c = 4$
  2. prior-2: $b = 4, c = 4$
  3. prior-3: $b = 5, c = 4$

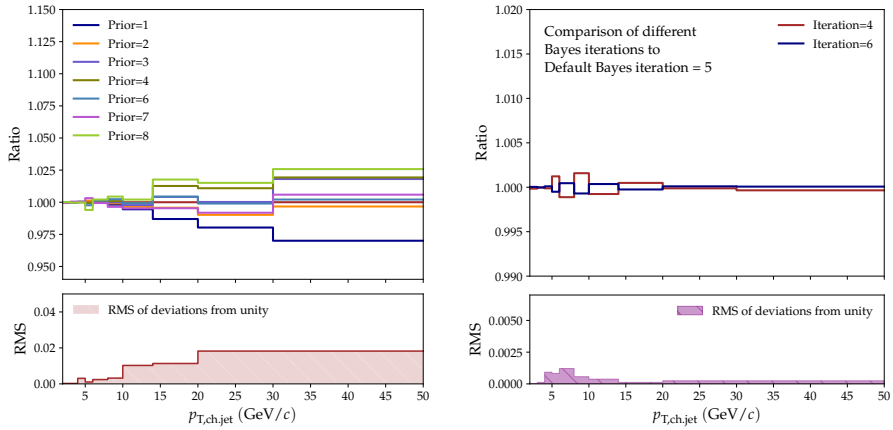

Figure 6.11: Stability checks for Bayesian unfolding for D^0 jets with $R = 0.4$. Top left: Bayesian unfolded $p_{T,ch\,jet}$ yields with different set of priors compared to the yield with MC prior. Bottom left: Root-mean-square values of the ratios above. Top right: Bayesian unfolded distributions with iteration = 4 (red) and = 6 (blue) taken as a ratio to the default one with iteration = 5. Bottom right: RMS values of the deviations from unity of the ratios above.

4. prior-4: $b = 6, c = 4$
5. prior-5: $b = 7, c = 4$
6. prior-6: $b = 4.5, c = 3$
7. prior-7: $b = 4.5, c = 5$
8. prior-8: fit to the measured spectrum.

Prior-5 was later discarded for being too extreme and away from the true spectrum to be considered. Normalized versions of these priors were then used in the unfolding procedure. These priors are shown in Fig. 6.10. The uncertainties are shown in Fig. 6.11 (left panel) where a maximum of $\sim 2\%$ can be seen.

- *Regularization*: Another way to check the stability in Bayesian unfolding is to check the regularization used. The iteration parameter that regularized the Bayesian unfolding procedure was changed by plus and minus one from the default value. Their ratios were taken to the default parameter and the root-mean-square (RMS) values were taken as uncertainty from this source. This can be seen in Fig. 6.11 (right panel). The ratios are in red for iteration = 4 and blue for iteration = 6. The RMS values are shown above the lower limit (by shifting by an amount of lower limit on y-axis.) The relative uncertainties are practically zero and therefore negligible.

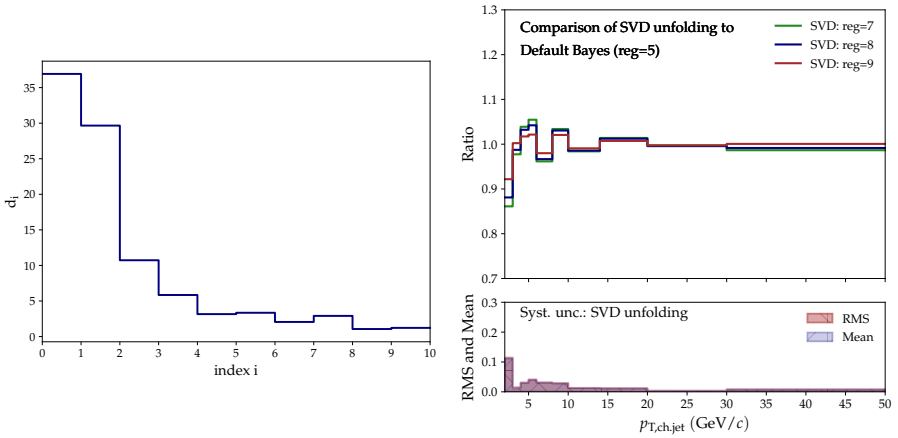

Figure 6.12: Left: The d-vector is shown with its d_i values on vertical y-axis plotted against the indices i on horizontal x-axis. The d-vector flattens out at about $i = 8$ as the effective rank provided for regularization in SVD unfolding of D^0 jets with $R = 0.4$ (see text for more details). Right: Stability checks against SVD unfolding for D^0 jets with $R = 0.4$. Along with default effective rank for regularization $= 8$, plus and minus one from 8, i. e., 9 and 7 were also considered and their ratios to the default regularization were taken. RMS and mean values of the ratios are shown. Both are similar. To find the bias SVD procedure has against Bayesian approach, mean values were taken as final uncertainties even if they were similar to RMS values.

6.4.6 *Unfolding: Stability against SVD unfolding*

To further validate the stability of the Bayesian approach, a comparison was made with an alternative method that uses the Singular Value Decomposition technique to inverse a detector-response matrix (See Sec. 5.2.7). The resulting d-vector, defined in in Eq. 5.28, is plotted in Fig. 6.12 (left) as a distribution of d_i values on the y-axis against their corresponding index i on the x-axis. The vector d decreases rapidly, and at an effective rank of $i = 8$, it reaches unity and flattens out. This effective rank was used to determine the regularization parameter τ and applied to the SVD unfolding procedure, as previously explained in Sec. 5.2.7. The results obtained using the SVD approach with regularization parameter $= 7$, 8, and 9 were compared with the result obtained using the default Bayesian approach. The comparison is shown in Fig. 6.12 (right) with ratios (of the SVD results to the Bayesian result) shown in the top panel and the RMS and mean values shown in the bottom panel, which stay under 4% for $p_{\mathrm{T,ch\,jet}} > 5$ GeV/c.

6.4.7 *Unfolding: Closure test*

The previous sub-sections described various tests performed on the unfolding procedure, which demonstrated its stability. The systematic uncertainty on the

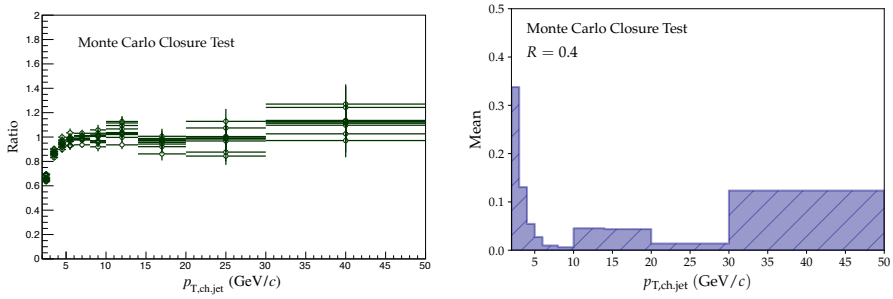

Figure 6.13: MC closure test for Bayesian unfolding of D^0 jets with $R = 0.4$. Left panel: ratio of unfolded distribution to true MC distribution for 10 trials. Each trial comprised of 20% MC sample randomly selected, while the rest 80% was used for building detector response matrix. Right panel: arithmetic mean of all the 10 trial-*experiments* conducted for $R = 0.4$ shown on left to depict the bias in them as a function of $p_{T,ch\,jet}$ reported in $5 < p_{T,ch\,jet} < 50$ GeV/c.

unfolding procedure was then determined through a Monte Carlo closure test. This test involves Monte Carlo simulations and is intended to verify if the unfolding procedure applied to the D^0-jet measurements at the detector level can accurately reproduce the original distribution. To conduct the Monte Carlo Closure test on the unfolding procedure, the Monte Carlo sample was randomly split into an 80 : 20 fraction. The larger 80% portion was utilized to construct the response matrix, while the remaining 20% was employed as a test sample, ensuring that the response matrix contained sufficient statistics to enable the successful implementation of the unfolding procedure. The division of Monte Carlo sample into a detector response portion and a test sample is done to keep them separate and prevent any potential correlation. The efficiency correction was applied to the test sample, following the method used in the data analysis. The same unfolding procedure used in the data analysis was then applied, and the resulting distributions were compared to the generator-level true Monte-Carlo distributions. To simulate multiple independent experiments, the random division was conducted ten times. Figure 6.13 (left panel) illustrates the various trials as a ratio to the true Monte Carlo distribution for each trial. The deviation from unity observed between $2 < p_{T,ch\,jet} < 5$ GeV/c is significant and can be attributed to the fact that these are border bins, and therefore such deviations are to be expected. This is one main reason why the final spectrum is reported starting from 5 GeV/c. The corresponding *bias* was estimated from the trial experiments by using the mean value from these trials. This is shown in Fig. 6.13 (right panel). This mean value was taken as the final uncertainty of the unfolding procedure, resulting in a maximum of 10–15% relative systematic uncertainty estimated from the Monte Carlo closure test on the unfolding procedure.

6.4.8 *Tracking efficiency*

The measurement is affected by uncertainties on the efficiency of track reconstruction as well. This was because the tracking of charged particles by the TPC and ITS was not 100% efficient. The related systematic uncertainties are determined in the following two ways.

- Jet-energy scale: The energy scale of jets was affected due to the tracking efficiency of the detectors. It was found in past studies at $\sqrt{s} = 5.02$ TeV for charged-particle jets to be about 4% [96]. Therefore, we assumed the same uncertainty in this analysis. To assess the systematic uncertainty from this source, a new detector-response matrix was prepared where 4% of all reconstructed charged tracks in the detector simulations were randomly rejected. With this reduced efficiency of 96% of its normal value, the unfolding procedure was performed on B-feed-down-subtracted spectrum, and the outcome was compared to the original result obtained using 100% of the tracks. This ratio is shown in Fig. 6.14, and the deviation from unity should provide the relative uncertainty from this source. It has a linearly increasing trend maximizing at $\sim$ 10% for the highest-p_{T} jets. Therefore, a linear fit to the ratio was used to determine the final values of the relative systematic uncertainty.
- D^0-meson reconstruction efficiency: The tracking efficiency of the detectors introduces an uncertainty on the D^0-meson reconstruction efficiency. This was evaluated for the D^0-meson spectra to be between 3% and 5% for $\sqrt{s} = 5.02$ TeV studies [97]. The reconstruction efficiency of D^0 mesons does not depend on $p_{\mathrm{T,ch\,jet}}$, but only on $p_{\mathrm{T,D^0}}$. Therefore, a $p_{\mathrm{T,ch\,jet}}$-independent conservative systematic uncertainty of 5% was assigned.

Finally, the normalization of the $p_{\mathrm{T,ch\,jet}}$-differential cross section was affected by a 0.8% uncertainty on the D^0-meson branching ratio and by the uncertainty on the luminosity determination which was 2.1% for $\sqrt{s} = 5.02$ TeV. The relative systematic uncertainties for D^0-meson tagged jets on their $p_{\mathrm{T,ch\,jet}}$-differential cross sections for $R = 0.4$ in $\sqrt{s} = 5.02$ TeV are summarized in Tab. 6.1.

6.4.9 *Correlated uncertainties*

The total systematic uncertainties for the D^0-meson tagged $p_{\mathrm{T,ch\,jet}}$-differential cross sections were obtained by summing in quadrature the uncertainties estimated from each of the aforementioned sources. In the case of cross-section ratios for different jet radii, as shown in Fig. 6.18, the systematic uncertainties are assumed to be fully correlated from the following sources: tracking efficiency of the D^0 mesons and the global uncertainties. It is assumed that they cancel in the ratios. The systematic uncertainties resulting from the D^0-meson topological-cut selection exhibit partial correlation. Therefore, the uncertainties for two jet radii R were averaged. This approach results in a smaller uncertainty than the conventional growth by quadratic summation, which assumes that the

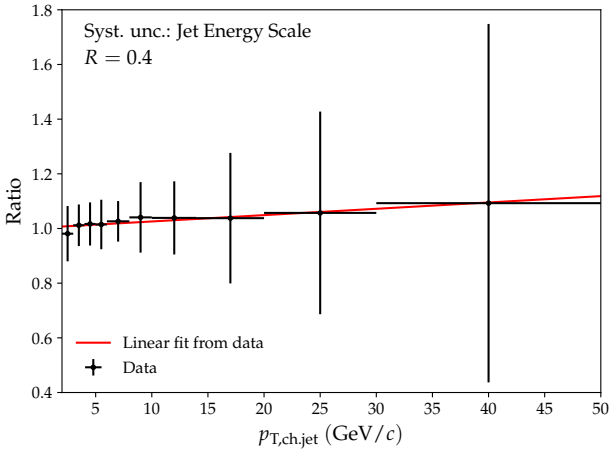

Figure 6.14: Systematic uncertainty from jet energy scale effects on unfolding: unfolded results from a modified response having a random selection of 96% of simulated tracks are compared to the results from using default response having all 100% tracks for D^0 jets with $R = 0.4$, $2 < p_{\mathrm{T,ch\,jet}} < 50$ GeV/c and reported from > 5 GeV/c.

uncertainties are uncorrelated. The influence of the tracking efficiency on the jet-energy scale is also expected to exhibit partial correlation. We used a *simultaneous variations* method to determine the uncertainty. This involved varying the detector-response matrices for two R values simultaneously and calculating the relative uncertainty on the cross-section ratio by comparing the final ratio obtained with modified and nominal response matrices. Systematic uncertainties on the ratios of cross sections for the two colliding energies $\sqrt{s} = 13$ TeV [94, 95] and $\sqrt{s} = 5.02$ TeV [95] shown in Fig. 6.16 were obtained by adding them in quadrature, except for the branching-ratio uncertainty which is treated as fully correlated. No other correlation was considered given that the data taking periods were different.

6.5 PHYSICS RESULTS

6.5.1 *Cross sections differential in $p_{T,ch\,jet}$*

The $p_{\mathrm{T,ch\,jet}}$-differential cross section of D^0-meson tagged charged jets is defined as

$$\frac{\mathrm{d}^2\sigma}{\mathrm{d}p_{\mathrm{T,ch\,jet}}\mathrm{d}\eta_{\mathrm{jet}}}(p_{\mathrm{T,ch\,jet}}) = \frac{1}{\mathcal{L}_{\mathrm{int}}}\frac{1}{\mathrm{BR}}\frac{N(p_{\mathrm{T,ch\,jet}})}{\Delta\eta_{\mathrm{jet}}\Delta p_{\mathrm{T,ch\,jet}}}, \tag{6.15}$$

where $N(p_{\mathrm{T,ch\,jet}})$ is the measured yield in each $p_{\mathrm{T,ch\,jet}}$ interval corrected for the acceptance × reconstruction efficiency, and the b-hadron feed-down contribution, and is unfolded for the detector effects; $\Delta p_{\mathrm{T,ch\,jet}}$ is the bin width and $\Delta\eta_{\mathrm{jet}}$ is the

Table 6.1: Systematic uncertainties as a function of $p_{\mathrm{T,ch\,jet}}$ for $R = 0.4$ at $\sqrt{s} = 5.02$ TeV.

Source (%) / $p_{\mathrm{T,ch\,jet}}$ (GeV/c)	Raw Yield Extraction	Topological Selection	B Feed-Down	Unfolding	Tracking Eff. ($\mathrm{D^0}$ Meson)	Tracking Eff. (Jet Energy Scale)	Normalization	Total
5 – 6	3.8	3.4	+ 3.9 – 6.5	2.8		1.6		+ 9 – 10.4
6 – 8	4.0	4.3	+ 3.9 – 6.6	1.0		2.0		+ 9.2 – 10.6
8 – 10	3.8	5.6	+ 5.3 – 8.9	0.6		2.4		+ 10.5 – 12.7
10 – 14	4.8	7.5	+ 6.6 – 11.1	4.6	5	3.1	Luminosity 2.1 BR 0.8	+ 13.6 – 16.2
14 – 20	6.9	10.7	+ 9.3 – 16.1	4.3		4.3		+ 17.8 – 22.1
20 – 30	10.2	15.8	+ 10.6 – 19.1	1.4		6.1		+ 23.1 – 28.1
30 – 50	18.6	25.3	+ 14 – 23.8	12.3		9.6		+ 38.2 – 42.7

jet-reconstruction acceptance: $\Delta\eta_{\mathrm{jet}} = 1.8 - 2R$, where R is the jet radius; $\mathcal{L}_{\mathrm{int}}$ is the experimentally measured integrated luminosity and BR is the branching ratio of the studied hadronic decay channel.

The $p_{\mathrm{T,ch\,jet}}$-differential cross sections of $\mathrm{D^0}$ jets in pp collisions are shown in Fig. 6.15 for $\sqrt{s} = 5.02$ TeV and compared to PYTHIA 8 and POWHEG + PYTHIA 8 predictions. The top panels show the cross sections for different R values of (a) 0.2, (b) 0.3, (c) 0.4, and (d) 0.6. The bottom panels show the Monte-Carlo-over-data ratios for each jet radius separately. Jets are only considered if they contain a $\mathrm{D^0}$ meson with $p_{\mathrm{T,D^0}} > 2$ GeV/c to avoid fluctuations in the $p_{\mathrm{T,ch\,jet}}$ spectra due to the rapidly falling $\mathrm{D^0}$-meson reconstruction efficiency at lower $p_{\mathrm{T,D^0}}$. It was studied in the $\sqrt{s} = 7$ TeV [57] analysis that a lower cut on the $\mathrm{D^0}$-meson p_{T} of $p_{\mathrm{T,D^0}} > 3$ GeV/c had a negligible effect on the reported $\mathrm{D^0}$-jet $p_{\mathrm{T,ch\,jet}}$-differential cross sections above 5 GeV/c. Therefore, a lower selection of $p_{\mathrm{T,D^0}} > 2$ GeV/c should have basically no impact on the same reported range of $p_{\mathrm{T,ch\,jet}}$ spectra. The data allow us to reach the maximum $p_{\mathrm{T,D^0}}$ at 36 GeV/c, while the $p_{\mathrm{T,ch\,jet}}$ reached is 50 GeV/c.

The results are compared to the predictions of PYTHIA 8.210 [98] Monash-2013 tune [86] Monte Carlo event generator. It is based on leading order pQCD calculations of matrix elements of parton-level hard scattering and it uses the Lund string hadronization model [99, 100]. It over-predicts the data for all three jet radii R with the the discrepancy being larger for $\sqrt{s} = 13$ TeV. Including inelastic non-diffractive processes and the Colour Reconnection model [21], which implements beyond leading-colour string configurations, in the PYTHIA 8 tune (referred to as PYTHIA 8 Soft Mode 2) improves the agreement with the data.

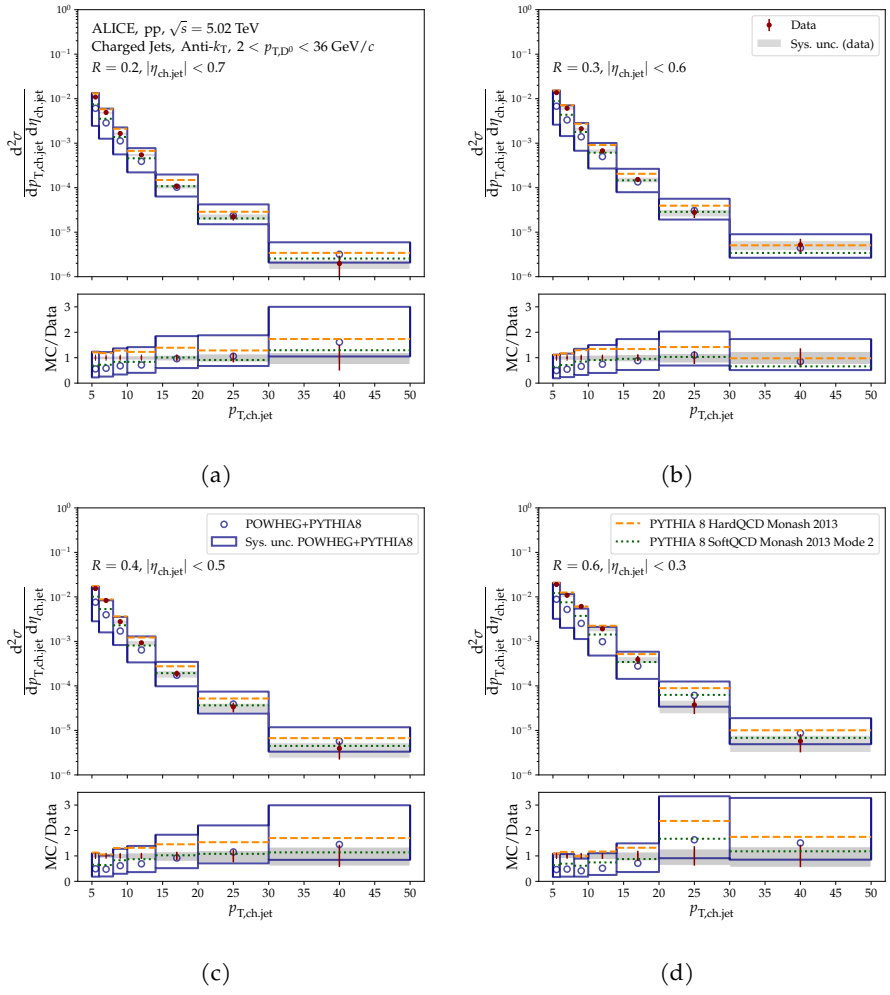

Figure 6.15: Top panels: The $p_{T,ch\,jet}$-differential cross sections of charm jets tagged with D^0 mesons for different R values of (a) 0.2, (b) 0.3, (c) 0.4, and (d) 0.6 in pp collisions at $\sqrt{s} = 5.02$ TeV compared to PYTHIA 8 HardQCD Monash 2013 (dashed lines), PYTHIA 8 SoftQCD Monash 2013 Mode 2 (dotted lines) and POWHEG hvq + PYTHIA 8 (open circles) predictions. The shaded bands indicate the systematic uncertainty on the cross section. Bottom panels: ratios of Monte-Carlo predictions to the data.

However in this case, the model under-predicts the measurements at low $p_{T,ch\,jet} \lesssim 10$ GeV/c.

The presented POWHEG + PYTHIA 8 predictions interface NLO pQCD POWHEG calculations with the PYTHIA 8 Monte Carlo parton shower within the POWHEG Box framework [98, 101]. The heavy-flavour processes are chosen [102]. The outgoing partons from POWHEG are passed to PYTHIA 8 event-by-event

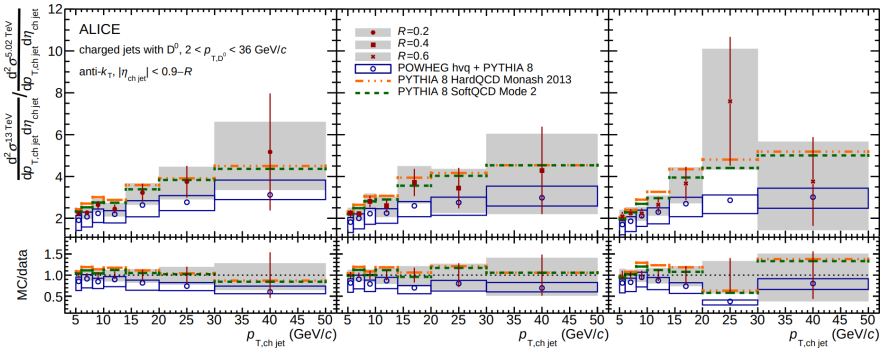

Figure 6.16: Top: Ratios of $p_{\mathrm{T,ch\,jet}}$-differential cross section of charm jets tagged with D^0 mesons in pp collisions of $\sqrt{s} = 13$ TeV to $\sqrt{s} = 5.02$ TeV for $R = 0.2$ (left, circles), $R = 0.4$ (centre, squares) and $R = 0.6$ (right, crosses) compared to PYTHIA 8 HardQCD Monash 2013 (dashed-dotted lines), PYTHIA 8 SoftQCD Monash 2013 Mode 2 (dashed lines) and POWHEG hvq + PYTHIA 8 (open circles) predictions. The shaded bands indicate the systematic uncertainty on the cross section ratios. Bottom: Ratios of Monte-Carlo predictions to the data.

where the subsequent parton shower, hadronization and generation of the underlying event are performed. To configure the simulations, the CT10nlo set of the parton-distribution function was used, while the renormalization and factorization scales were set to $\mu_{\mathrm{R}} = \mu_{\mathrm{F}} = \mu_0 = \sqrt{m_{\mathrm{c}}^2 + p_{\mathrm{T}}^2}$, and the default charm-quark mass to 1.5 GeV/c^2. The shown theoretical uncertainties were estimated by varying the simulation parameters. The biggest uncertainties in the POWHEG framework come from variations of the scales: $0.5\,\mu_0 < \mu_{\mathrm{R,F}} < 2.0\,\mu_0$ with $0.5 < \mu_{\mathrm{R}}/\mu_{\mathrm{F}} < 2$, additionally, the charm-quark mass was varied from 1.5 GeV/c^2 to 1.3 and 1.7 GeV/c^2. The POWHEG + PYTHIA 8 calculations describe the measured cross sections within the experimental and theoretical uncertainties. At $p_{\mathrm{T,ch\,jet}} > 14$ GeV/c (20 GeV/c) the central values of the predictions agree with the data for $\sqrt{s} = 5.02$ TeV ($\sqrt{s} = 13$ TeV). For the lower-$p_{\mathrm{T,ch\,jet}}$ range the experimental results are close to the upper bands of the POWHEG + PYTHIA 8 calculations and as in the case of PYTHIA 8 predictions, the agreement is better for $\sqrt{s} = 5.02$ TeV than for $\sqrt{s} = 13$ TeV. The low-$p_{\mathrm{T,ch\,jet}}$ region is particularly challenging to describe theoretically due to the dominance of various non-perturbative effects, such as multiparton interactions, fragmentation of partons into jets, and other soft processes.

6.5.2 *Collision-energy cross-section ratios*

The energy dependence of the $p_{\mathrm{T,ch\,jet}}$-differential cross section of D^0 jets was probed via the ratio of cross sections at $\sqrt{s} = 13$ TeV and $\sqrt{s} = 5.02$ TeV, shown for different jet radii R in Fig. 6.16. A hardening of the $p_{\mathrm{T,ch\,jet}}$ spectra with the

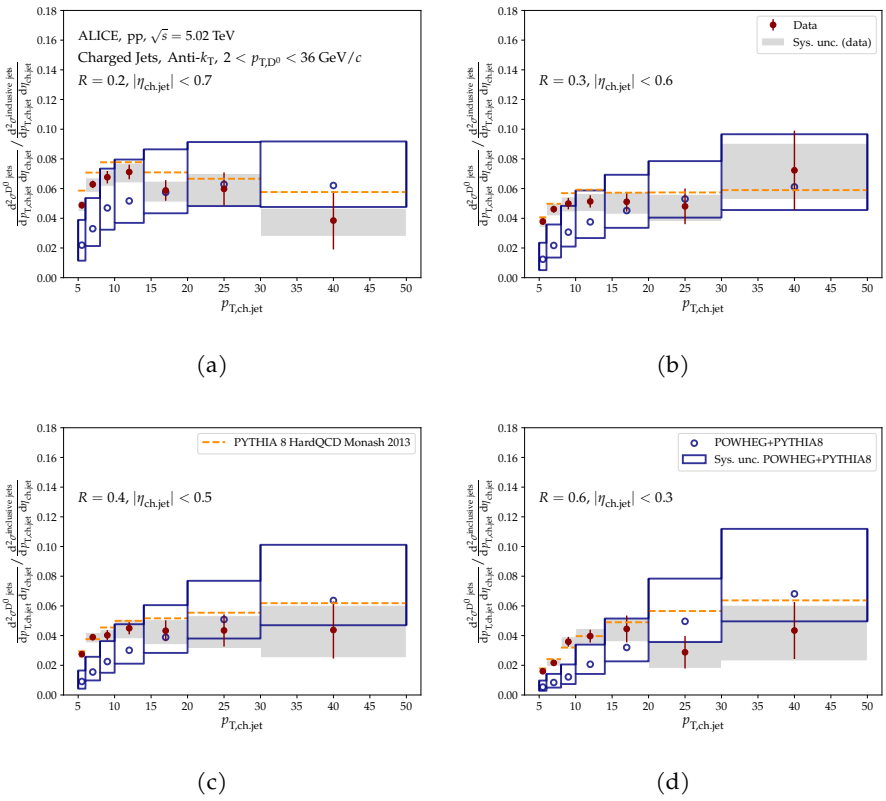

Figure 6.17: The fraction of D^0 jets over inclusive charged jets in pp collisions at $\sqrt{s} = 5.02$ TeV for (a) $R = 0.2$, (b) $R = 0.3$, (c) $R = 0.4$, and (d) $R = 0.6$ compared to PYTHIA 8 HardQCD Monash 2013 (dashed lines) and POWHEG hvq + PYTHIA 8 (open circles) predictions. The data cross-section ratios are shown by closed red circles, while the shaded bands indicate the systematic uncertainty on the data cross-section ratios, and the open boxes represent the theoretical uncertainties on the POWHEG predictions.

centre-of-mass energy can be observed. Both PYTHIA 8 settings describe data well within the current uncertainties for all the jet radii. PYTHIA 8 with Colour Reconnection describes the data slightly better. POWHEG + PYTHIA 8 under-predicts the measured cross-section ratios, with the data being on the upper edge of the theory-uncertainty band.

6.5.3 *D^0-jet fraction of inclusive charged jets*

Inclusive charged jets refer to all charged jets irrespective of whether they contain D^0 mesons or not. The fraction of charged jets containing D^0 mesons was also measured by taking the ratios of D^0-jet cross sections measured in this analysis to

the inclusive charged-jet cross sections measured previously by ALICE in another analysis (See Ref. [103]). This was done for all the four jet radii, the results of which are shown in Fig. 6.17. The data used in the inclusive charged-jet analysis were taken in a different time period than the data used in D^0-jet analysis. Therefore, all the uncertainties were considered to be uncorrelated.

In the kinematic range $5 < p_{T,ch\,jet} < 10$ GeV/c, the fraction of D^0 jets tends to increase as $p_{T,ch\,jet}$ increases for all the jet radii. However, the D^0-jet fraction decreases as the jet radius (R) increases, from approximately 0.05–0.07 at $R = 0.2$ to around 0.015–0.04 at $R = 0.6$. As $p_{T,ch\,jet}$ exceeds ≈ 10 GeV/c, the dependence on $p_{T,ch\,jet}$ tends to level off due to the hardening of the jets[2]. The trend of D^0-jet fractions matches well with the results from PYTHIA 8 using the Monash tune. The POWHEG + PYTHIA 8 calculations underestimate the data slightly for lower $p_{T,ch\,jet}$, but are within the margin of uncertainties for higher $p_{T,ch\,jet}$.

6.5.4 *Cross-section ratios for different R*

The comparison of charged-particle jet production with different jet radii allows us to study the behaviour of the parton shower, which is a complex process that involves both perturbative and non-perturbative effects. Perturbative effects arise from the hard-scattering process, while non-perturbative effects come from the hadronization process and soft interactions between partons in the shower. By varying the jet radii, we can control the relative importance of these effects and study their interplay. This helps us to better understand the underlying physics and to improve our theoretical models of jet production. Shown in Fig. 6.18 are ratios of $p_{T,ch\,jet}$-differential cross section of D^0 jets reconstructed with jet radius $R = 0.2$ with respect to $R = 0.4$ and 0.6 for collision energy of $\sqrt{s} = 5.02$ TeV. The statistical uncertainties are treated as fully uncorrelated, meaning that they are assumed to arise independently from different sources and are not influenced by any correlations. However, in reality, some events can affect multiple measurements, which can create correlations between them. For example, in this case, the jets from smaller-cone sizes are typically included in the larger-cone sizes, and thus they are not statistically independent. This means that summing the statistical uncertainties in quadrature might lead to overestimation of the total uncertainty since it assumes that the uncertainties are fully uncorrelated. Therefore, the correlations between different measurements were carefully considered and their impact on the overall uncertainty was quantified accordingly. To determine theoretical uncertainties for cross-section ratios between two jet-radii in the POWHEG framework, the renormalization and factorization scales and the charm-quark mass were varied simultaneously. The maximum upward and downward variations were used as the uncertainty bound.

2 A jet is said to harden when it becomes more focused and less spread out as its energy increases. This is characterized by an energy distribution within the jet that becomes increasingly peaked towards the highest-energy particles. Jets harden because the emission of higher-energy particles is more likely to align with the direction of the initial high-energy particle, resulting in a more collimated jet.

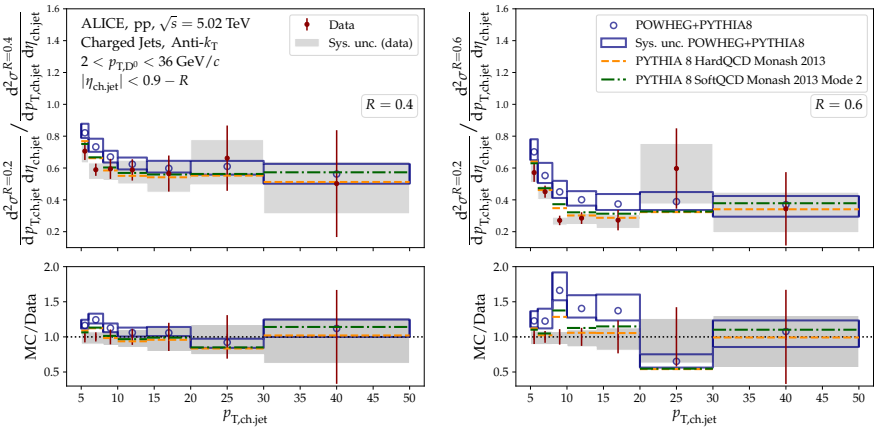

Figure 6.18: Top: Ratios of $p_{T,ch\,jet}$-differential cross section of charm jets tagged with D^0-mesons for different R: $\sigma(R = 0.2)/\sigma(R = 0.4)$ (left) and $\sigma(R = 0.2)/\sigma(R = 0.6)$ (right) in pp collisions at $\sqrt{s} = 5.02$ TeV compared to PYTHIA 8 HardQCD Monash 2013 (dashed-dotted lines), PYTHIA 8 SoftQCD Monash 2013 Mode 2 (dashed lines) and POWHEG + PYTHIA 8 (open circles) predictions. The shaded bands indicate the systematic uncertainty on the cross section ratios. Bottom: ratios of Monte-Carlo predictions to the data for $\sigma(R = 0.2)/\sigma(R = 0.4)$ and $\sigma(R = 0.2)/\sigma(R = 0.6)$, respectively.

The observed departure from unity of the cross-section ratios is due to the emission of QCD radiation. For both collision energies, the ratios of $\sigma(R = 0.2)$ to $\sigma(R = 0.4)$ and $\sigma(R = 0.2)$ to $\sigma(R = 0.6)$ decrease as $p_{T,ch\,jet}$ increases. For $p_{T,ch\,jet}$ greater than 10 GeV/c, the ratios remain roughly constant within the given uncertainties. The shape can be qualitatively described by the presented PYTHIA 8 and POWHEG + PYTHIA 8 predictions. However, at lower $p_{T,ch\,jet}$ of $5 - 10$ GeV/c POWHEG + PYTHIA 8 calculations overestimate the data with the discrepancy being larger for the $\sigma(R = 0.2)/\sigma(R = 0.6)$ ratio, which is expected to be more sensitive to the underlying-event contribution. The default PYTHIA 8 and PYTHIA 8 with Soft Mode 2 agree well with our measurements within the uncertainties, with the largest deviations from the data also at low $p_{T,ch\,jet}$ for $\sqrt{s} = 13$ TeV and $R = 0.6$. The differences seen between the predictions of the two PYTHIA 8 modes in the $p_{T,ch\,jet}$-differential cross sections largely cancel in the R ratios.

6.6 SUMMARY

In this chapter, studies of the production of charm jets tagged with fully reconstructed D^0 mesons, using data obtained from proton–proton collisions at $\sqrt{s} = 5.02$ TeV with the ALICE detector at the CERN-LHC, were presented. The measurements were carried out for charged-particle jets reconstructed with

different jet radii, i. e. $R = 0.2$, 0.3, 0.4, and 0.6. A similar analysis was also done for $\sqrt{s} = 13$ TeV with $R = 0.2$, 0.4, and 0.6 by the ALICE collaboration [94, 95]. Results obtained were differential in $p_{\mathrm{T,ch\,jet}}$ and were compared to predictions of the LO PYTHIA 8 Monte Carlo event generator with two Colour Reconnection modes, and to POWHEG NLO pQCD calculations coupled to PYTHIA 8.

The PYTHIA 8 predictions with the Colour Reconnection Soft Mode 2 setting provide the best description of the $p_{\mathrm{T,ch\,jet}}$-differential cross sections for both energies and all jet radii. Within the experimental and theoretical uncertainties, the measurements are also in agreement with the POWHEG + PYTHIA 8 calculations. Cross section ratios between $\sqrt{s} = 13$ and 5.02 TeV increase with $p_{\mathrm{T,ch\,jet}}$ indicating hardening as the collision energy rises. The cross-section ratios between different jet-radii $\sigma(R = 0.2)/\sigma(R = 0.4, 0.6)$ fall sharply and then flatten out for $p_{\mathrm{T,ch\,jet}} > 10$ GeV/c indicating QCD radiation at low $p_{\mathrm{T,ch\,jet}}$ and an increasing collimation of jets at higher $p_{\mathrm{T,ch\,jet}}$. Measurements for different R values down to low $p_{\mathrm{T,ch\,jet}}$ can constrain pQCD, hadronization and underlying event (UE) effects in models. Studies for smaller R values are more sensitive to non-perturbative hadronization effects while contributions from the UE are more important for large R. The ratios are well described by the PYTHIA 8 predictions but are systematically over-predicted by the POWHEG + PYTHIA 8 calculations, especially for $p_{\mathrm{T,ch\,jet}} < 20$ GeV/c and $\sqrt{s} = 13$ TeV.

The overall good agreement of the data with Monte-Carlo generators and pQCD calculations in most of the measured kinematic ranges implies that the charm-quark production is sufficiently modelled in the presented predictions in most of the investigated kinematic ranges. Studies done for charm jet fragmentation in pp collisions will be presented and compared to fragmentation predictions in Ch. 8. Furthermore, pp results at $\sqrt{s} = 5.02$ TeV are at the same centre-of-mass energy as ALICE Pb–Pb collision data and can be used as a reference for studies of charm jet production in the QGP medium and the cold-nuclear matter effects in p–Pb collisions.

7 COLD NUCLEAR-MATTER EFFECTS ON CHARM-JET PRODUCTION

7.1 PHYSICS GOALS

This chapter deals with studies on charm-jet production in proton–lead collisions with the aim to investigate cold nuclear-matter (CNM) effects on heavy-flavour (charm) production. Such studies are fundamental in order to decouple the CNM effects from hot nuclear-matter effects present in heavy-ion collisions. The measurements done in the previous chapter will serve as the *vacuum* reference for p–Pb measurements. The data collected in p–Pb collisions are taken at $\sqrt{s_{\mathrm{NN}}} = 5.02$ TeV. The studies include the investigation of D^0 jets with jet radius $R = 0.3$ in the $\eta - \phi$ cylindrical plane. We aim to quantify the modification of jet production in p–Pb collisions by comparing it with the production in pp collisions using the so-called nuclear modification factor R_{pPb}.

7.2 NUCLEAR MODIFICATION FACTOR R_{pPb}

The nuclear modification factor for proton–nucleus (pA) collisions compared to proton–proton (pp) collisions as a function of the jet transverse-momentum is defined using production cross-sections $\frac{d\sigma}{dp_{\mathrm{T}}}$ in the respective collision systems as

$$R_{\mathrm{pA}} = \frac{\left(\frac{d\sigma}{dp_{\mathrm{T}}}\right)_{\mathrm{pA}}}{\mathrm{A} \times \left(\frac{d\sigma}{dp_{\mathrm{T}}}\right)_{\mathrm{pp}}} \tag{7.1}$$

where A is the nucleus mass number. This notion of nuclear scaling is due to the presence of A nucleons colliding with free protons. If there are no cold nuclear-matter effects present, the production results from pA collisions should simply be an aggregate of the production results from A number of pp collisions. In our measurements, the nucleus is a lead ion, thus $\mathrm{A} = 208$, and R_{pA} is otherwise referred to as R_{pPb}. Thus, the basic aim is to find the $p_{\mathrm{T,ch\,jet}}$-differential production cross-section of D^0 jets of $R = 0.3$ in p–Pb collisions[1]. The procedure is mostly similar to that in the previous chapter for pp collisions except for an additional subtraction of the contribution from the underlying event.

1 The radius 0.3 is strategically selected to prevent significant contributions from the underlying event and therefore neither be too narrow like $R = 0.2$ nor be too broad like $R = 0.4$ and 0.6.

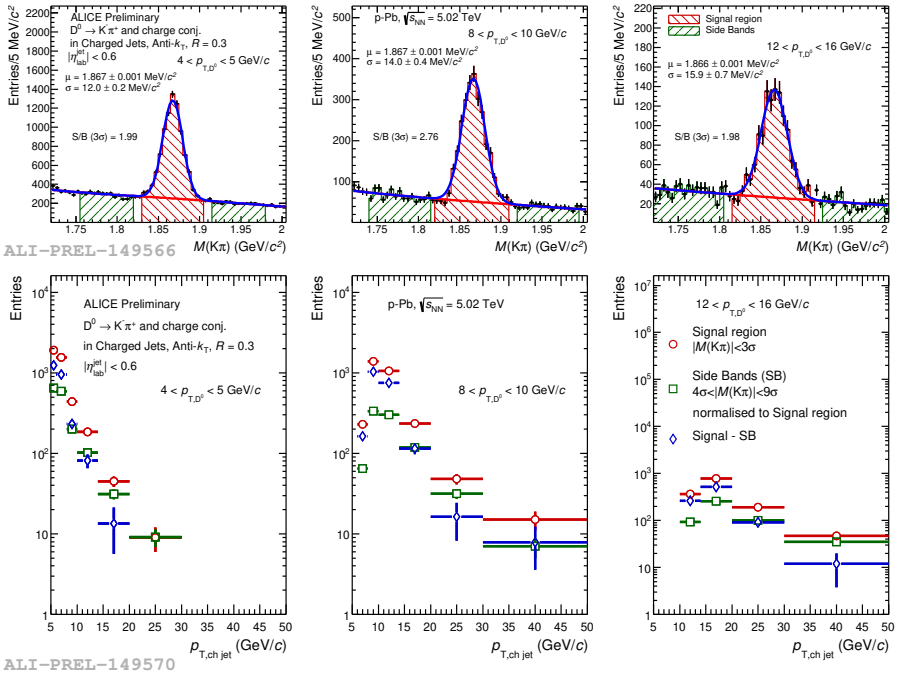

Figure 7.1: Top panel: invariant-mass distribution of D^0-jet candidates with $5 < p_{T,ch\,jet} < 50$ GeV/c for $R = 0.3$ in p–Pb collisions at $\sqrt{s} = 5.02$ TeV and the required D^0-meson transverse-momenta in intervals $4 < p_{T,D^0} < 5$ GeV/c (left), $8 < p_{T,D^0} < 10$ GeV/c (centre), $12 < p_{T,D^0} < 16$ GeV/c (right). The total fit function is represented by the blue solid line while the red solid line represents the total background fit function. The red and green shaded areas correspond to the peak and side-band regions respectively. Bottom panel: Distributions of the D^0-jet candidates in the peak region are shown in red circles, while in the sideband region are shown in green squares. The blue diamonds represent the subtracted distributions corresponding to the raw signals.

7.3 UNDERLYING-EVENT SUBTRACTED $p_{T,ch\,jet}$-DIFFERENTIAL RAW YIELDS

Using knowledge described in Ch. 5 and 6, D^0-jet candidates were analysed in p_{T,D^0} intervals within $3 < p_{T,D^0} < 36$ GeV/c (see Fig. 7.1). It is important to note here that the transverse momenta are obtained after the underlying event has been subtracted using the Eq. 5.14 ($p_{T,j}^{corr} = p_{T,j} - \rho A_j$). The lower bound of p_{T,D^0} was set at 3 GeV/c, instead of 2 GeV/c as in the previous chapter, to avoid major contamination from the underlying event. Because of this and in order to maintain consistency, the reference measurement of pp collisions will also use a lower-bound of 3 GeV/c instead of 2 GeV/c. Following Eq. 6.2, a Gaussian function for modelling the signal along with an exponential for the combinatorial background and a double Gaussian for the reflections was used to describe the invariant-mass distribution of D^0 candidates

in individual bins of p_{T,D^0}. The signal region was defined as $|M_{K\pi} - \mu_{fit}| < 3\sigma_{fit}$ while the sideband background regions were $4\sigma_{fit} < |M_{K\pi} - \mu_{fit}| < 9\sigma_{fit}$. The mean and standard deviation of the Gaussian fits are represented as usual by μ_{fit} and σ_{fit} respectively.

The signal (red shaded) and sideband (green shaded) regions from the top panel are represented in the bottom panel of the figure by red circles and green squares respectively. The sideband distributions (green squares) in the bottom panel were especially scaled to match the amount of background yield calculated from the fit in the signal region. Then the $p_{T,ch\,jet}$-background distributions were subtracted from the $p_{T,ch\,jet}$-signal distributions to give the $p_{T,ch\,jet}$-differential raw-yield distributions (blue diamonds).

7.4 CORRECTIONS

As done in the previous chapter, the resulting $p_{T,ch\,jet}$-differential raw yields here should be corrected in essentially three steps: for D^0-jet reconstruction efficiency, for the jet contribution from B-meson decays, and lastly, for the momentum smearing due to detector effects.

7.4.1 *Underlying event and background fluctuations*

After subtracting the underlying event (as described in Sec. 5.2.3), it is important to estimate the background fluctuations introduced. This is done using the statistical approach of *random cones* (as explained in Sec. 5.2.4). In the third correctional step of unfolding for momentum-smearing effects, we incorporate the estimated background fluctuations into the detector-response matrix. When selecting events for the random-cones procedure, we ensure that they include D^0-jet candidates and that the event's leading jet has a $p_T > 5$ GeV/c. The leading jet of an event is the jet with the highest p_T. To avoid any possible signal contamination, the leading jet is excluded from the random-cones procedure.

The left panel in Fig. 7.2 displays the δp_T distribution of the fluctuations, which is obtained event by event from data using Eq. 5.16. This distribution measures the difference in track p_T that is either present or absent in the conical section, which is randomly chosen, relative to the expected background. Jets that overlap with the cone can also contribute to non-zero δp_T. As shown in the figure, δp_T peaks around zero as expected and decreases with a tail as the $p_{T,ch\,jet}$ increases. Additionally, δp_T falls sharply on the negative side. The tail on the positive side is a result of the occasional overlap of the jet fragments present in p–Pb events with the signal jets in the region probed by the random cone.

To include the background fluctuations in the detector-response matrix, a separate background-fluctuation matrix (See the right panel of Fig. 7.2) is created using the δp_T distribution. Assuming that the δp_T distribution of the background fluctuations is independent of the specific jet-p_T in the $p_{T,ch\,jet}$ spectrum, the background-fluctuation matrix is prepared by shifting the δp_T distribution along

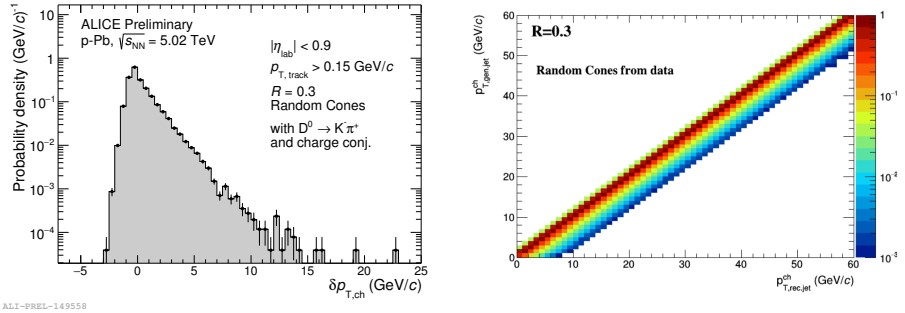

Figure 7.2: D^0 jets in p–Pb events with $R = 0.3$. Left panel: δp_T distribution of background fluctuations obtained from data using the method of *random cones*. Right panel: the background-fluctuation matrix based on the δp_T distribution.

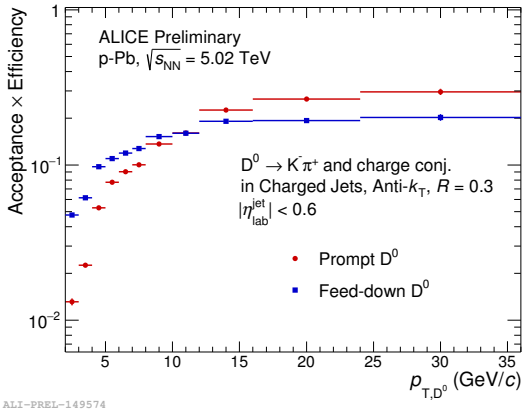

Figure 7.3: Product of detector acceptance and efficiency for reconstruction of prompt (red) and non-prompt feed-down (blue) D^0 jets as a function of transverse momentum of D^0 meson, p_{T,D^0}, with $R = 0.3$.

the $p^{det}_{T,ch\,jet}$ axis by the same amount as the corresponding row of the $p^{part}_{T,ch\,jet}$ interval.

7.4.2 *Reconstruction efficiency*

The reconstruction efficiency of jets tagged with prompt-D^0 mesons, taking into account both acceptance and efficiency (Acceptance × Efficiency), was computed using Monte Carlo PYTHIA 6 + GEANT 3 simulations anchored to the data and is displayed in red in Fig. 7.3 for $R = 0.3$ with $|\eta_{jet}| < 0.9 - R$. The same distribution for non-prompt D^0 jets is represented by blue data points.

The p_{T,D^0}-dependent reconstruction efficiency was then applied to raw-$p_{T,ch\,jet}$ yields obtained from individual p_{T,D^0} intervals shown in the bottom panel of

Fig. 7.1 using the invariant-mass analysis. After the efficiency correction, the $p_{\mathrm{T,ch\,jet}}$ distributions were summed up from the individual $p_{\mathrm{T,D^0}}$ intervals to obtain the final efficiency-corrected $p_{\mathrm{T,ch\,jet}}$ distribution, as summarized in Eq. 6.3.

7.4.3 *B-meson decay contribution*

To remove non-prompt $\mathrm{D^0}$ jets, which constitute the primary source of contamination in measuring $\mathrm{D^0}$ jets from charm-quark decays, we use simulations based on theoretical calculations. This method closely follows the procedure described in Sec. 6.3.2, with the additional consideration of background fluctuations arising from the analysis of p–Pb collision systems, which feature a significant underlying event (UE) and background fluctuations post-subtraction of UE, that are not present in pp collisions.

The $p_{\mathrm{T,ch\,jet}}$ distributions of non-prompt $\mathrm{D^0}$ jets are calculated at the particle level in different intervals of $\mathrm{D^0}$-meson transverse momentum using POWHEG + PYTHIA 6 simulations. These distributions are then corrected by the $p_{\mathrm{T,D^0}}$-dependent reconstruction-efficiency ratio $\frac{\epsilon^{b\to \mathrm{D^0}}}{\epsilon^{c\to \mathrm{D^0}}}$ before being summed over all $p_{\mathrm{T,D^0}}$ intervals to give one $p_{\mathrm{T,ch\,jet}}$ distribution. A detector-response matrix $RM^{b\to \mathrm{D^0}}(p^{\mathrm{part}}_{\mathrm{T,ch\,jet}}, p^{\mathrm{det}}_{\mathrm{T,ch\,jet}})$ is calculated separately using PYTHIA 6 + GEANT 3 simulations. The background-fluctuation matrix prepared from the method of *random cones* is embedded into the detector-response matrix by multiplying each bin content of the fluctuation matrix with the corresponding bin content of the response matrix.

The detector-level $p_{\mathrm{T,ch\,jet}}$ distribution representing the B-meson decay contribution is now prepared by smearing the efficiency-ratio scaled particle-level distribution with the updated response matrix $RM^{b\to \mathrm{D^0}}_{bkg}(p^{\mathrm{part}}_{\mathrm{T,ch\,jet}}, p^{\mathrm{det}}_{\mathrm{T,ch\,jet}})$. This step of subtracting the B-meson decay (*B feed-down*) contribution (sans the embedding of background fluctuations) was explained earlier in Eq. 6.10. With the updated response matrix, the equation for B-feed-down subtraction becomes

$$\begin{aligned} N^{c\to \mathrm{D^0}}(p^{\mathrm{det}}_{\mathrm{T,ch\,jet}}) = {} & N(p^{\mathrm{det}}_{\mathrm{T,ch\,jet}}) \\ & - RM^{b\to \mathrm{D^0}}_{bkg}(p^{\mathrm{part}}_{\mathrm{T,ch\,jet}}, p^{\mathrm{det}}_{\mathrm{T,ch\,jet}}) \cdot \\ & \sum_{p_{\mathrm{T,D^0}}} \left(\frac{\epsilon^{b\to \mathrm{D^0}}}{\epsilon^{c\to \mathrm{D^0}}}(p_{\mathrm{T,D^0}}) \cdot N^{POWHEG}(p_{\mathrm{T,D^0}}, p^{\mathrm{part}}_{\mathrm{T,ch\,jet}}) \right). \end{aligned} \tag{7.2}$$

The detector-response matrices calculated using PYTHIA 6 + GEANT 3 simulations for prompt and non-prompt $\mathrm{D^0}$ jets are shown in Fig 7.4. After being combined with the background-fluctuation matrix (Fig. 7.2 right panel), the updated response matrices are shown in Fig. 7.5.

The results of the B-feed-down subtraction procedure can be seen in Fig. 7.6. On the left panel, we have the reconstruction-efficiency-corrected $\vec{p}_{\mathrm{ch\,jet}}$ yield shown in green, from which we subtract the B-feed-down contribution shown in solid blue lines. The dashed bands represent the systematic uncertainties for B-feed-down

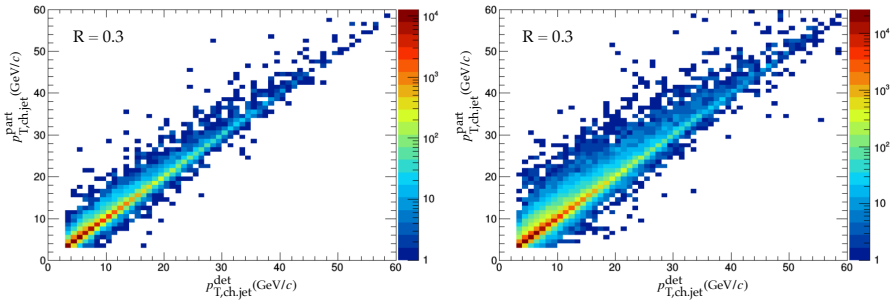

Figure 7.4: Detector-response matrices calculated with the PYTHIA part of the simulation of p–Pb events at $\sqrt{s_{NN}} = 5.02$ TeV, for prompt (left) and non-prompt (right) D^0 jets with $R = 0.3$.

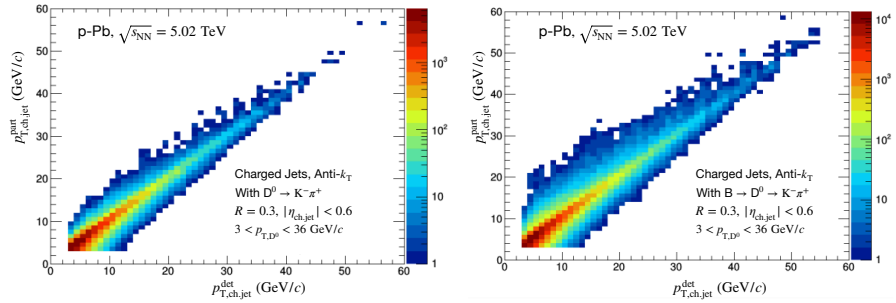

Figure 7.5: Combined detector-response matrices for D^0 jets in p–Pb events with $R = 0.3$ by uniting the responses from PYTHIA with the background fluctuations derived from data-driven δp_T distribution (see Fig. 7.2). Left panel is for prompt-D^0 jets while the right panel shows non-prompt D^0 jets.

subtraction and will be explained in Sec. 7.5.5. The remaining yield, after subtracting the B-feed-down yield from the efficiency-corrected yield, is shown in red. The fraction of B feed-down in the reconstruction-efficiency-corrected $p_{T,ch\,jet}$ spectrum is shown on the right panel. It can be seen that the B-feed-down fraction is slightly higher at higher p_T.

7.4.4 *Unfolding*

Similar to measurements in proton–proton collisions, the unfolding procedure is essential in addressing the momentum smearing introduced in the measured jet-p_T spectrum due to the finite-momentum resolution and tracking inefficiency of our detectors. In p–Pb collisions, the fluctuations in background-momentum density are also responsible for smearing a jet's underlying-event-subtracted momentum. Such smearing effects are undone by using a response matrix (Fig. 7.5 left panel) that is a combination of the PYTHIA-based detector-response matrix for prompt-D^0

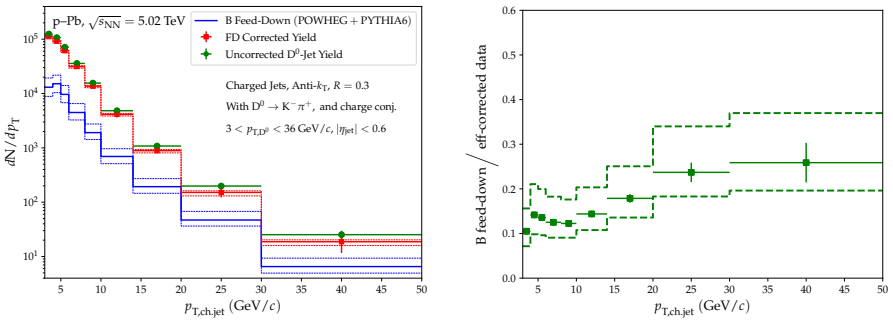

Figure 7.6: Subtraction of B-feed-down contribution from the admixture of prompt and non-prompt D^0-jets in p–Pb events with $R = 0.3$. Left panel: Green points represent the reconstruction-efficiency-corrected yield, blue points are the B feed-down contribution, the red points are the B feed-down subtracted yield. Right panel: the fraction of B feed-down (blue points from left panel) in the reconstruction-efficiency-corrected spectrum (green points from left panel).

jets (Fig. 7.4 left panel) and the background-fluctuation matrix (Fig. 7.2). Using the updated detector-response matrix, the efficiency-corrected and B-feed-down-subtracted yield is unfolded using the Bayesian approach as described in details in Sec. 5.2.6 and applied in Sec. 6.3.3. The unfolding procedure serves the opposite purpose of momentum smearing done in Sec. 7.4.3, which is why the momentum smearing performed earlier on non-prompt D^0 jets in Sec. 7.4.3 is usually referred to as *folding*.

By unfolding the measured spectra for these detector-specific distortions, a direct comparison with theoretical models and other independent experimental results becomes possible.

The efficiency-corrected and B-feed-down-subtracted *measured* spectrum is shown in blue on the left panel of Fig. 7.7, which is then unfolded with the Bayesian approach with a regularization parameter of 3 and is shown in red. A quick validation of the stability of this procedure can be seen with the green spectrum which is found by folding the unfolded spectrum back using the detector-response matrix. Ratios of the refolded and unfolded spectra to the measured spectrum are shown on the right-bottom panel. Although there is a slight deviation in some p_T bins, overall, it is a good match to the measured spectrum. The $p_{T,ch\,jet}$-dependent relative-statistical uncertainties displayed on the right-top panel are less than 30%. The regularization parameter was selected based on the Pearson coefficients shown in Fig. 7.8 and the method described in Sec. 5.2.8. The parameter value of 3 exhibited the smallest anti-correlation and the least extreme structures in the Pearson correlation coefficients.

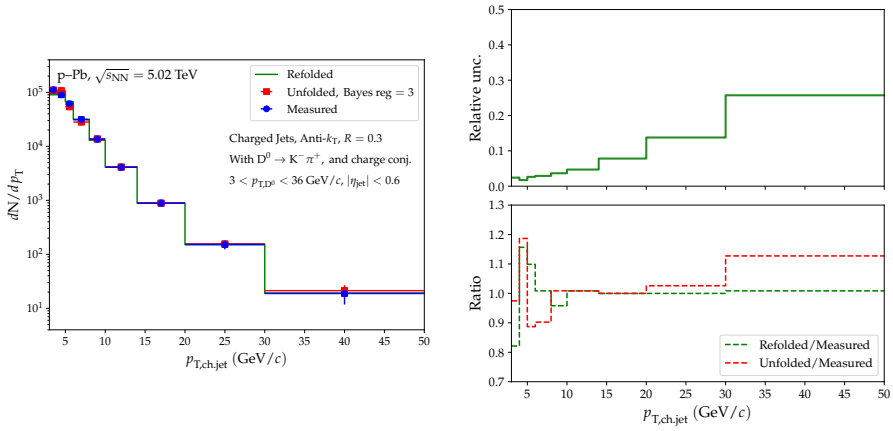

Figure 7.7: Left: Bayesian unfolding of efficiency and B-feed-down subtracted D^0-jet $p_{T,ch\,jet}$ spectrum (blue *measured* points) in p–Pb events with $R = 0.3$. The red points are the unfolded spectrum with regularization parameter of 3. This was again folded back using the same response matrix to check for consistency if the original *measured* spectrum could be reached. Right (top): the relative uncertainties of the unfolded spectrum as a function of $p_{T,ch\,jet}$. Right (bottom): the ratios of refolded and unfolded spectra to measured spectrum as a function of $p_{T,ch\,jet}$.

7.5 SYSTEMATIC UNCERTAINTIES

The sources considered for systematic uncertainties in this analysis for p–Pb collisions are similar to the ones in pp collisions explored in the previous chapter (see Sec. 6.4) in addition to the sources for uncertainties in background fluctuations. They are categorized in the following groups:

1. Topological selection,
2. Raw-yield extraction,
3. B-feed-down subtraction,
4. Unfolding and background fluctuation matrix,
5. Track-reconstruction efficiency, and
6. Normalization.

7.5.1 *Topological selection*

To account for discrepancies in the D^0-meson topological-selection variables between data and Monte Carlo distributions, a systematic uncertainty was assigned. Seven sets of variable selections were tested, with four being less stringent (loose-1, 2, 3, 4) and three being more stringent (tight-1, 2, 3) than the

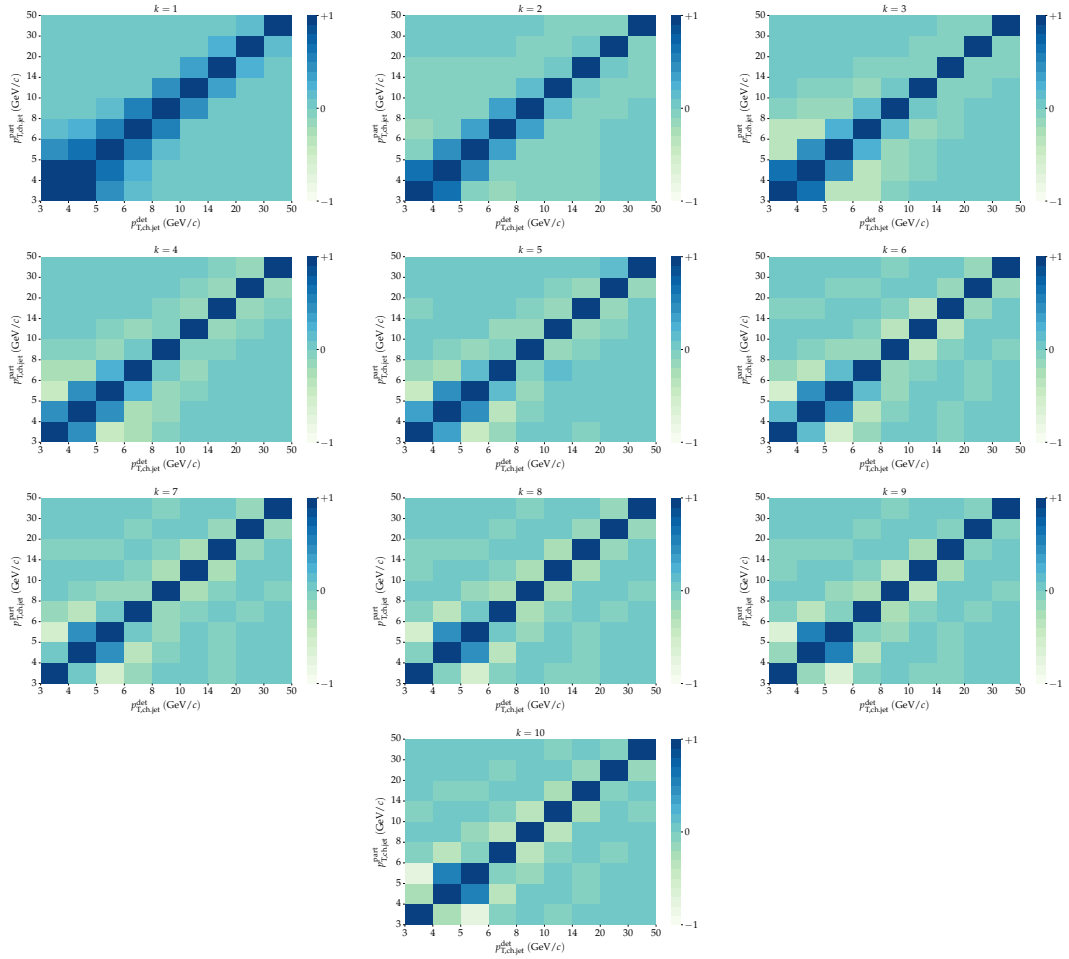

Figure 7.8: Pearson coefficients obtained for 10 different regularization parameters or iterations after unfolding the measured spectrum of D^0 jets with $R = 0.3$ in p–Pb collisions at $\sqrt{s_{NN}} = 5.02$ TeV. These are used to determine the default regularization for Bayesian unfolding by looking for the smallest amount of both anti-correlation and extreme structures between the $p_{T,ch\,jet}^{part}$ and $p_{T,ch\,jet}^{det}$ axes.

default set. These variations were chosen to probe any possible imperfection in the Monte Carlo simulation, even though the selection criteria were already relatively loose at high p_{T,D^0}. The results of the different selection cut sets are shown in the top panel of Fig. 7.9 as ratios of reconstruction efficiencies to the default cut set. The bottom-left panel of the same figure shows the ratios of the efficiency-corrected, B-feed-down-subtracted, and unfolded $p_{T,ch\,jet}$-differential D^0-jet distributions resulting from the different selection-cut sets compared to the default set. The root-mean-square values of these ratios, which serve as the

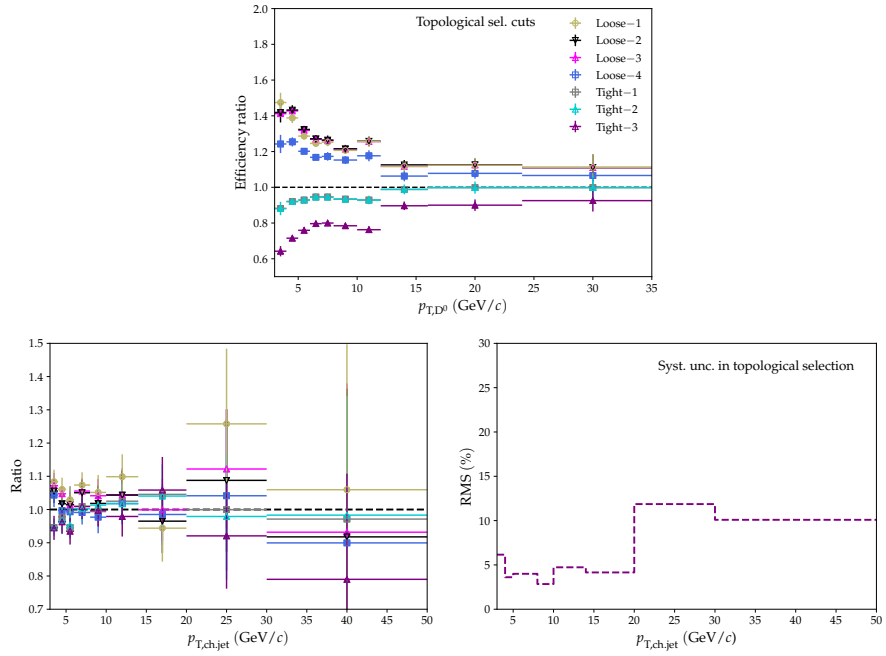

Figure 7.9: Top: p_{T,D^0}-dependent ratios of reconstruction efficiencies with different topological selection cuts compared to the default set of selection cuts for D^0 jets with $R = 0.3$ in p–Pb events at $\sqrt{s_{NN}} = 5.02$ TeV. Bottom left: ratios of $p_{T,ch\,jet}$ spectra from different topological-selection cuts compared to that from the default selection cuts. Bottom right: root-mean-square values of the ratios from the left panel to be taken as the systematic uncertainties for this source of topological selection cuts.

systematic uncertainties, are shown on the bottom-right panel and are at most 12%.

7.5.2 *Raw-yield extraction: multi-trial*

The stability of the invariant mass fit performed to the D^0-jet candidates in order to determine the signal and background D^0 meson distributions was checked by considering several possible variations to the invariant mass fitting conditions. The varied conditions were as in pp collisions:

- width (σ_{fit}) of the Gaussian signal kept free, fixed to the MC values, or fixed to 15% above or lower than MC values (4 variations),
- assumed shape of the background function (3 variations: exponential, linear, second-order polynomial),
- free mean (μ_{fit}) of the Gaussian signal and also fixed to the MC values from Particle Data Group (2 variations),

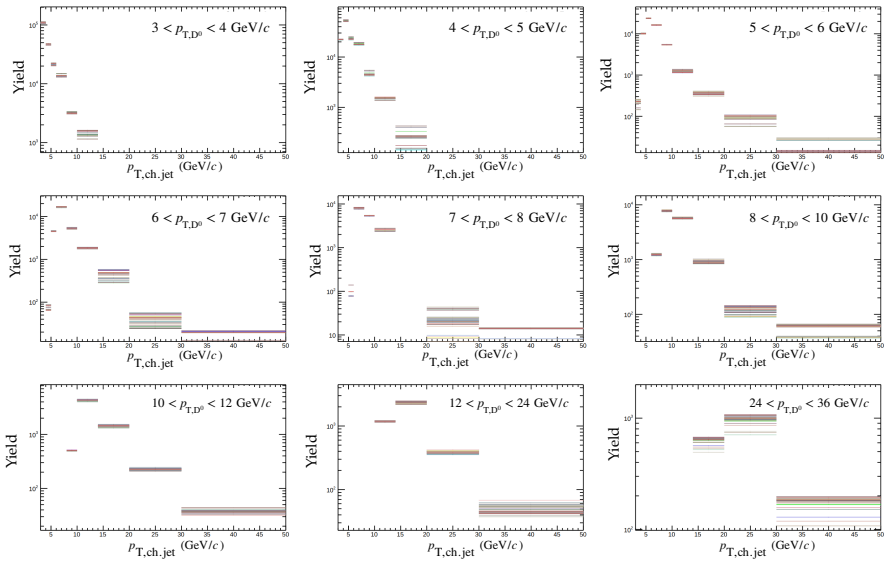

Figure 7.10: Multi-trials for D^0 jets with $R = 0.3$ in p–Pb events at $\sqrt{s_{NN}} = 5.02$ TeV. Each plot refers to reconstruction-efficiency-corrected $p_{T,ch\,jet}$ spectra from multiple trials within a specific p_{T,D^0} interval. These are then summed up and root-mean-square values of their ratios to the default trial are taken as systematic uncertainties as shown in Fig. 7.11.

- lower limit of the fit range was 1.72 (default), 1.74 GeV/c^2 (2 variations),
- upper limit of the fit range was 2.00, 2.03 (default) GeV/c^2 (2 variations), and
- mass bin width was 5 and 10 MeV/c^2 (2 variations).

A maximum of $4 \times 3 \times 2 \times 2 \times 2 \times 2 = 192$ combinations (*multi-trials*) of the above variations were considered for nine different p_{T,D^0} bins in $3 < p_{T,D^0} < 36$ GeV/c. In Fig. 7.10, efficiency-corrected yields from all the trials are seen in each p_{T,D^0} interval. These yields were then summed up to get $p_{T,ch\,jet}$-differential yields for each trial and then ratios were taken to the default variation. Their root-mean-square values are shown in Fig. 7.11 and serve as the systematic uncertainties from multi-trial approach to raw-yield extraction. A maximum of 5% uncertainty is obtained in the highest p_T bin.

7.5.3 *Raw-yield extraction: signal and sideband ranges*

The defined signal and sideband ranges were varied in units of the Gaussian signal width (σ_{fit}) to determine the systematic uncertainties due to this source. With $a\sigma_{fit}$ for signal and $b\sigma_{fit} < |M_{K\pi} - \mu_{fit}| < c\sigma_{fit}$ for the sidebands, the default configuration was defined to be 3, 4, and 9. Some new variations for determining

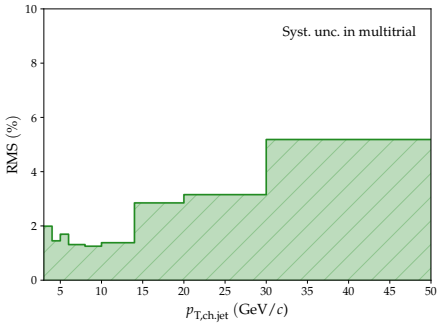

Figure 7.11: Root-mean-square values of ratios of multitrials from Fig. 7.10 to the default trial are taken as systematic uncertainties for D^0 jets with $R = 0.3$ in p–Pb events at $\sqrt{s_{NN}} = 5.02$ TeV.

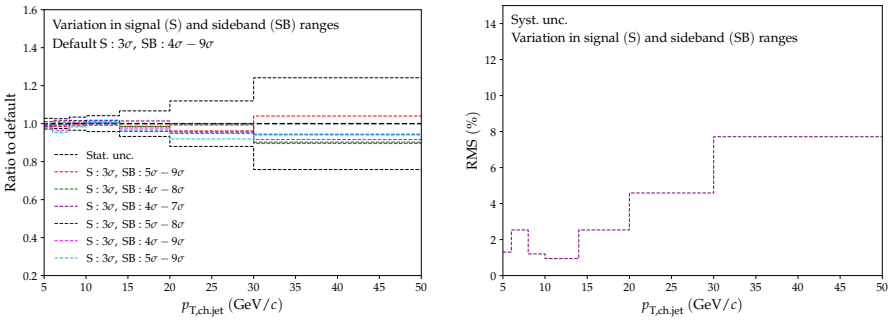

Figure 7.12: Left: Ratios for different variations were done to the default configuration in the signal and side-band ranges during the invariant mass fit for the raw-yield extraction of D^0 jets in p–Pb collisions at $\sqrt{s_{NN}} = 5.02$ TeV. Right: The root-mean-square values from the ratios on the left are taken here as the final systematic uncertainties in the source mentioned.

systematic uncertainties were considered with the triplet values for a, b, c being $(3, 5, 9)$, $(3, 4, 8)$, $(3, 4, 7)$, $(3, 5, 8)$, $(2, 4, 9)$, and $(2, 5, 9)$. Ratios of the yields from those variations were taken with respect to the default variation. Their root-mean-square values are shown on the right panel of Fig. 7.12, which were taken as systematic uncertainties from this source. It shows a maximum of 8% deviation in the highest p_T bin. The maximum extent of statistical uncertainties from all the variations can also be seen on the left panel in black dashes.

7.5.4 *Raw-yield extraction: reflections*

D^0 reflections were introduced in Sec. 5.1.6 and 6.2. Specific to this analysis, they have been explained in the current chapter in Sec. 7.3. The sources of systematic

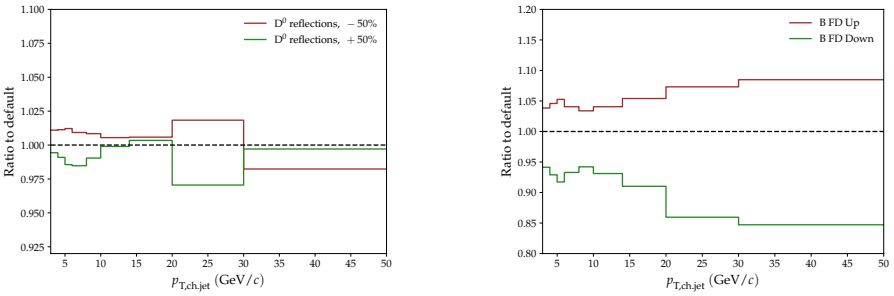

Figure 7.13: Left panel: Ratios of D^0 jet spectra due to modified estimation of D^0 reflections. The maximum from the upper and downward variations are taken as symmetric systematic uncertainties. Right panel: Ratios of spectra with B-feed-down subtraction done with multiple variations in the input for non-prompt D^0-jet simulations. The upward and downward variations serve as asymmetric systematic uncertainties.

uncertainties from this source are as described in Sec. 6.4.3. The contribution of D^0 reflections assumed using Monte Carlo simulations was increased to a maximum of another 50% and reduced by 50%. The changed yields were compared to the default configuration, and their maximum deviation per $p_{T,ch\,jet}$ bin was taken as the uncertainty. This is shown on the left panel in Fig. 7.13.

7.5.5 *B-feed-down subtraction*

The B-feed-down contribution estimated in Sec. 7.4.3 refers to the following configuration: beauty-quark mass = 4.75 GeV/c^2, $\mu_R$and μ_F= transverse mass of beauty quark i. e. $\mu_0 = \sqrt{m_b^2 + p_T^2}$. Just as in Sec. 6.4.4, we obtained other possible variations from the following settings: beauty-quark mass = 4.5 and 5 GeV/c^2, and $(\mu_R/\mu_0,\ \mu_F/\mu_0) = (2,2), (2,1), (1,2), (0.5,1), (1,0.5)$ and $(0.5,0.5)$. The dashed bands seen in Fig. 7.6 are a result of the maximum upward and downward deviations from all these possible variations. The deviations are shown as a ratio on the right panel in the Fig. 7.13. It was estimated to be 7–15% for the $p_{T,ch\,jet}$-differential spectrum of $R = 0.3$ wide D^0 jets in p–Pb collisions.

7.5.6 *Unfolding: Stability in Bayesian approach*

USE OF PRIOR FUNCTIONS The baseline prior provided in Bayesian unfolding is the Monte Carlo distribution obtained at the particle level from PYTHIA. However, other functions were also provided as a prior to the unfolding procedure from a modified power-law function:

$$f(p_{T,ch.jet}) = p_{T,ch.jet}^{-a} e^{-\frac{ab}{p_{T,ch.jet}}}, \tag{7.3}$$

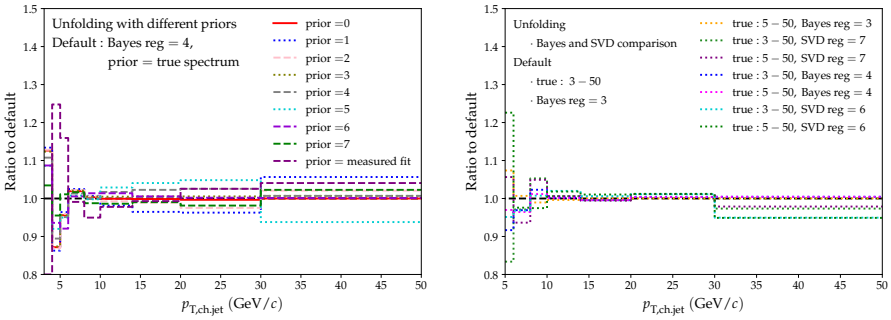

Figure 7.14: Left panel: different prior functions were used for checking the stability in Bayesian unfolding. They are shown here as a ratio to the standard prior of Monte Carlo distribution. Their root-mean-square values are the systematic uncertainties from this source. Right panel: the ratios of different variations in the true particle level kinematic range coupled with Bayesian unfolding with different regularization and SVD unfolding with its three regularization parameters are shown. Their root-mean-square values are systematic uncertainties from this source for D^0 jets in p–Pb collisions with $R = 0.3$ at $\sqrt{s_{NN}} = 5.02$ TeV.

where a is the power-law index, and b is the position of the local maximum of the distribution. The prior functions used are the following: (i) $a = 3$, $b = 4$ GeV/c, (ii) $a = 4$, $b = 4$ GeV/c, (iii) $a = 5$, $b = 4$ GeV/c, (iv) $a = 6$, $b = 4$ GeV/c, (v) $a = 7$, $b = 4$ GeV/c, (vi) $a = 4.5$, $b = 3$ GeV/c, (vii) $a = 4.5$, $b = 5$ GeV/c, and (viii) a fit to the measured spectrum. The unfolded spectra from each of these prior functions are compared to the default unfolded distribution and the root-mean-square values of the resulting deviations serve as systematic uncertainties from this source. This can be seen on the left panel in Fig. 7.14 which shows how the different prior functions behave in unfolding the measured spectrum.

7.5.7 *Unfolding: Stability against change in ranges and SVD unfolding*

The default kinematic range used in the Bayesian unfolding procedure is $3 < p_{T,ch jet} < 50$ GeV/c both at the detector (measured) level and particle (true) level while also considering the underflow and overflow bins. As a systematic check, the particle level range was varied by changing its minimum kinematic reach to 5 GeV/c. This setting was combined with another Bayesian iteration parameter of 4 apart from default 3. Additionally, unfolding was done with the SVD algorithm (see Sec. 5.2.7) using the two values of 6 and 7 as regularization parameters. The regularization parameters were chosen based on the Pearson coefficients for SVD unfolding, just as it was done earlier in this chapter for Bayesian unfolding. So in total, seven extra variations were checked against the default configuration, all with measured $3 - 50$ GeV/c. They were

- true: $5 - 50$ GeV/c, Bayesian regularization = 3

- true: $3-50$ GeV/c, SVD regularization = 7
- true: $5-50$ GeV/c, SVD regularization = 7
- true: $3-50$ GeV/c, Bayesian regularization = 4
- true: $5-50$ GeV/c, Bayesian regularization = 4
- true: $3-50$ GeV/c, SVD regularization = 6
- true: $5-50$ GeV/c, SVD regularization = 6

The uncertainties are found from the root-mean-square values of these deviations. They are a maximum of 12% for the lowest $p_{\mathrm{T,ch\,jet}}$-bin.

7.5.8 *Background-fluctuation matrix*

The background-fluctuation matrix embedded in the detector-response matrix for the unfolding procedure is determined using the data-driven method of *random cones* (see Sec. 7.4.1). Twelve different kinds of events were considered to build the δp_{T} distributions and consequently the background fluctuation matrices. The following three groups of events were considered:

1. all events containing D^0-jet candidates,
2. all events having a D^0-jet candidate as their leading jet, and
3. all events irrespective of having a D^0-jet candidate or not (inclusive jets).

For each group, four separate conditions were imposed to have events:

- with $p_{T,lead} > 5$ GeV/c, and excluding the leading jet from the *random cone*,
- with $p_{T,lead} > 5$ GeV/c, where the *random cone* is placed perpendicular to the leading jet,
- with $p_{T,lead} > 10$ GeV/c, and excluding the leading jet from the *random cone*, and
- with $p_{T,lead} > 10$ GeV/c, where the *random cone* is placed perpendicular to the leading jet,

The default method for obtaining the background-fluctuation matrix uses the first configuration, in which all events containing D^0-jet candidates were used, with the leading jet having a $p_{T,lead} > 5$ GeV/c and excluded from the random cone. The twelve δp_{T} distributions are shown in Fig. 7.15. Each background-fluctuation matrix was combined with the PYTHIA-based detector-response matrix, and the measured D^0-jet distribution was unfolded. Ratios of the unfolded spectra to the default configuration and their root-mean-square values are shown in Fig. 7.16.

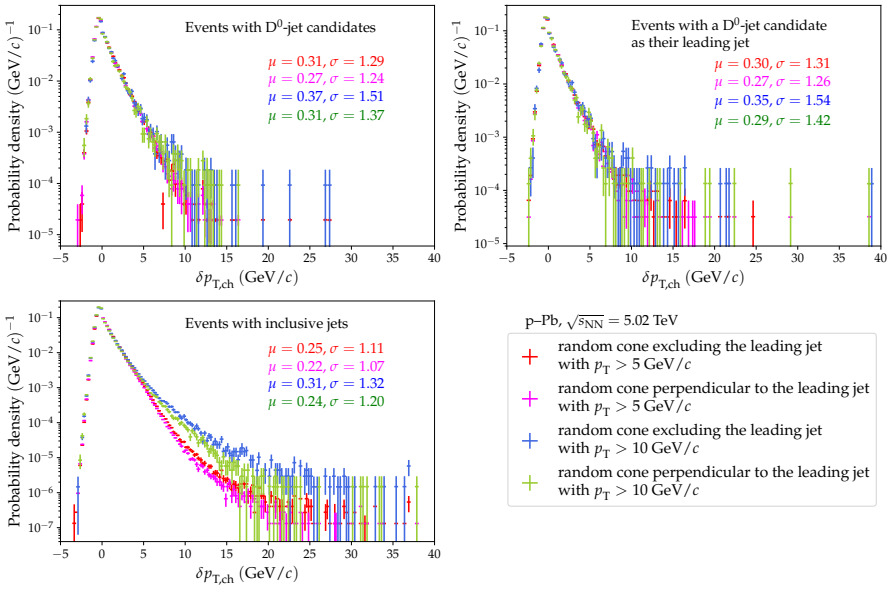

Figure 7.15: The δp_{T} distributions for different background fluctuations due to events containing (a) top left panel: at least a D^0-jet candidate, (b) top right panel: a D^0-jet candidate with a leading D^0-jet in the event, and (c) bottom panel: all kinds of jets.

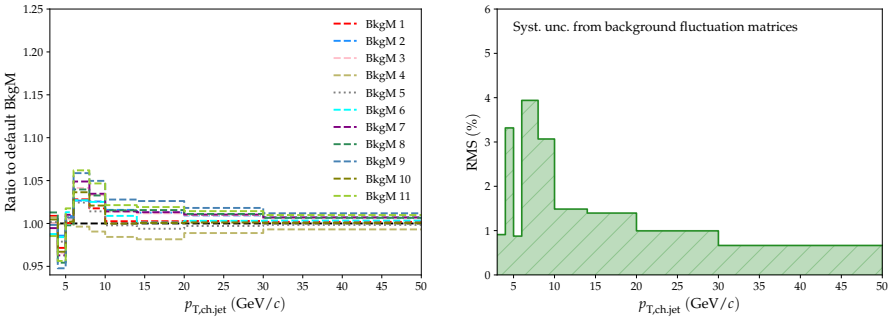

Figure 7.16: Left panel: ratios of $p_{\mathrm{T,ch\,jet}}$ spectra of D^0-jets due to different background fluctuation matrices as a ratio to the default fluctuation matrix. Right panel: root-mean-square values of the ratios from left panel to be considered as the systematic uncertainties from said source.

7.5.9 *Tracking efficiency*

Uncertainties on the tracking efficiency affect the measurement in two particular ways.

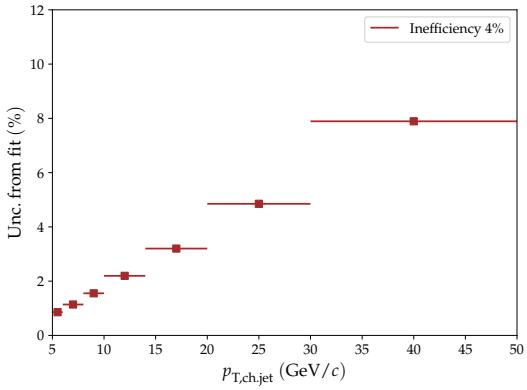

Figure 7.17: Systematic uncertainty due to jet energy scale for D^0 jets with $R = 0.3$ in p–Pb events at $\sqrt{s_{NN}} = 5.02$ TeV.

- Firstly, an uncertainty on the D^0-meson reconstruction efficiency is introduced. This was evaluated for the D^0 mesons to be about 3% and mostly p_T-independent. Since the reconstruction efficiency was evaluated to be mostly $p_{T,ch\,jet}$-independent, it could be assumed that the measurement of D^0 jets is affected by a similar amount of 3%.
- The second uncertainty is that of the jet-energy scale, where the effect of the limited momentum resolution and tracking efficiency of the jet tracks is probed as it has an effect on the detector response. This effect was estimated by building a new detector-response matrix where 4% of the reconstructed tracks in the simulation used to build the original response were randomly rejected while building the new response. Unfolding was done using the modified response, and the resulting distribution was compared against the originally unfolded distribution. The deviations are shown in Fig. 7.17 which are taken as the systematic-uncertainty values from the source of jet-energy scale.

The relative systematic uncertainties on the $p_{T,ch\,jet}$-differential cross sections for D^0 jets with $R = 0.3$ are summarized in Tab. 7.1. There is also an uncertainty on the normalization of the $p_{T,ch\,jet}$-differential cross section due to the D^0-meson branching-ratio uncertainty of 0.8% and also due to an uncertainty of 3.7% on the luminosity for $\sqrt{s_{NN}} = 5.02$ TeV.

7.5.10 *Correlated systematic uncertainties for R_{pPb}*

7.5.10.1 *B-feed-down subtraction*

When the systematic uncertainties were determined for B-feed-down subtraction, multiple variations were considered in producing the non-prompt D^0-jet

Table 7.1: Uncertainties as a function of $p_{\mathrm{T,ch\,jet}}$ for D^0 jets with $R = 0.3$ at $\sqrt{s_{\mathrm{NN}}} = 5.02$ TeV.

Source	Uncertainty (%)						
$p_{\mathrm{T,ch\,jet}}$ (GeV/c)	5 – 6	6 – 8	8 – 10	10 – 14	14 – 20	20 – 30	30 – 50
Topological selection	4	4	4	4	4	10	10
Multi-trial	2	2	2	2	3	3	5
Signal and sideband ranges	1	2	1	1	3	5	8
Reflections	2	2	1	1	1	3	1
B feed-down	+5,−8	+4,−7	+4,−6	+4,−7	+5,−9	+7,−14	+8,−15
Unfolding: priors	9	2	2	2	2	3	3
Unfolding: ranges, SVD	12	3	3	1	1	1	3
Bkg. fluctuations	1	4	3	2	2	1	1
Tracking Eff. (D^0 Meson)	5	5	5	5	5	5	5
Tracking Eff. (Jet Energy Scale)	1	1	2	2	3	5	8
Total Systematic Uncertainty	18	11	11	10	13	20	23
Normalization Uncertainty	3.8						
Statistical	3	3	4	5	8	14	26

Table 7.2: Normalization systematic uncertainties.

Source	Uncertainty (%)
Branching Ratio	0.8
Luminosity	3.7
Total	3.8

simulations (see Sec. 7.5.5). So this correlation was addressed while calculating the nuclear modification factor R_{pPb} by taking the ratio of the cross sections in p–Pb collisions to the ones in pp collisions for each configuration separately. Table 7.3 shows the varied configurations for the beauty-quark mass (m_{b}) and the renormalization (μ_{R}) and factorization (μ_{F}) scales. The variations 1 to 7 are compared to the default configuration, which has $\left(\frac{m_{\mathrm{b}}}{\mathrm{GeV}/c^2}, \frac{\mu_{\mathrm{R}}}{\sqrt{m_{\mathrm{b}}^2+p_{\mathrm{T}}^2}}, \frac{\mu_{\mathrm{F}}}{\sqrt{m_{\mathrm{b}}^2+p_{\mathrm{T}}^2}}\right) = (4.75, 1, 1)$. The corresponding results can be seen in Fig. 7.18. The left panel shows the nuclear modification factors (R_{pPb}) from the eight configurations, while the right panel shows the ratios of all the nuclear modification factors from the seven variations to the nuclear modification factor from the default configuration. The maximum upward and downward deviations from unity on the right panel are taken as the final systematic uncertainty in R_{pPb} due to B-feed-down subtraction.

Table 7.3: The different configurations used in producing non-prompt D^0-jet simulations.

Configuration	$\frac{m_b}{GeV/c^2}$	$\frac{\mu_R}{\sqrt{m_b^2+p_T^2}}$	$\frac{\mu_F}{\sqrt{m_b^2+p_T^2}}$
Default	4.75	1	1
Variation 1	4.75	0.5	1
Variation 2	4.75	1	2
Variation 3	4.75	2	2
Variation 4	4.75	1	0.5
Variation 5	4.75	0.5	0.5
Variation 6	5	1	1
Variation 7	4.5	1	1

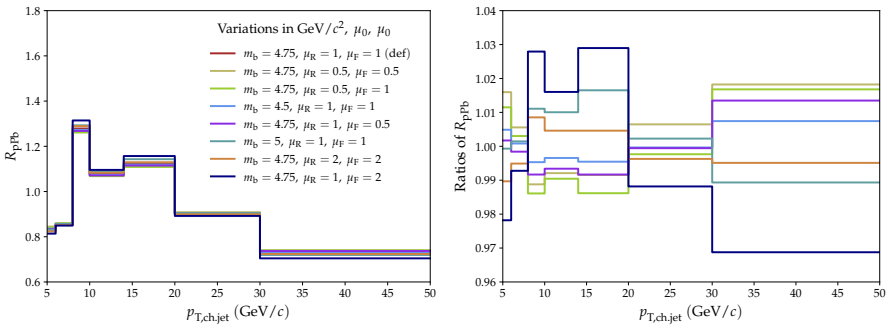

Figure 7.18: Left panel: nuclear modification factor R_{pPb} due to different configurations provided as input in getting non-prompt D^0 jets. Right panel: ratios of the different factors to the central modification factor from the left, with the maximum upward and maximum downward deviations serving as correlated systematic uncertainties in R_{pPb} due to B-feed-down subtraction.

7.5.10.2 *Branching fraction*

The uncertainty from the branching fraction of the D^0-meson decay was also considered to be correlated. They are supposed to be identical for both p–Pb and pp collisions, so that the correlated uncertainty from this source was completely zero.

The other uncertainties were considered to be uncorrelated for R_{pPb} and they were all added in quadrature.

Table 7.4: Systematic uncertainties in R_{pPb} due to B-feed-down subtraction as a function of $p_{\mathrm{T,ch\,jet}}$ for D^0 jets with $R = 0.3$ at $\sqrt{s_{\mathrm{NN}}} = 5.02$ TeV.

Source	Uncertainty (%)						
$p_{\mathrm{T,ch\,jet}}$ (GeV/c)	5 – 6	6 – 8	8 – 10	10 – 14	14 – 20	20 – 30	30 – 50
B feed-down	+2,−2	+1,−1	+3,−1	+2,−1	+3,−1	+1,−1	+2,−3

Table 7.5: Parameters of the POWHEG + PYTHIA 6 simulations of $\mathrm{c\bar{c}}$ events used to compare with our measurement.

Parameter	Central value	Variations
m_{c}	1.5 GeV/c^2	1.3, 1.7 GeV/c^2
PDF	CT10nlo (11000)	-
nPDF	EPS09nlo	-
$\left(\frac{\mu_{\mathrm{R}}}{\sqrt{m_{\mathrm{c}}^2+p_T^2}}, \frac{\mu_{\mathrm{F}}}{\sqrt{m_{\mathrm{c}}^2+p_T^2}}\right)$	$(1,1)$	$(0.5,0.5)$, $(0.5,1)$, $(1,0.5)$, $(2,2)$, $(2,1)$, $(1,2)$

7.6 PHYSICS RESULTS

In this section, we present the $p_{\mathrm{T,ch\,jet}}$-differential cross section of D^0 jets with $R = 0.3$ in minimum bias p–Pb collisions at $\sqrt{s_{\mathrm{NN}}} = 5.02$ TeV. The presented cross section has been corrected for reconstruction efficiency within the detector acceptance, B-feed-down subtraction, and unfolded for the momentum resolution of the detector and the background fluctuations of the underlying-event subtraction. The cross section is determined using the relation already established in the previous chapter in Eq. 6.15:

$$\frac{\mathrm{d}^2\sigma}{\mathrm{d}p_{\mathrm{T,ch\,jet}}\mathrm{d}\eta_{\mathrm{jet}}}(p_{\mathrm{T,ch\,jet}}) = \frac{1}{\mathcal{L}_{\mathrm{int}}}\frac{1}{\mathrm{BR}}\frac{N(p_{\mathrm{T,ch\,jet}})}{\Delta\eta_{\mathrm{jet}}\Delta p_{\mathrm{T,ch\,jet}}}.$$

In Fig. 7.19, the left panel shows the cross section as red filled circles with grey filled boxes indicating their systematic uncertainties. The ratio of data to theory is shown in the bottom panel. The theory points which are represented by blue open circles and are calculated using POWHEG + PYTHIA 6 with CT10nlo parton-density function and EPS09nlo nuclear parton-density function scaled by the atomic mass number of lead ions (208). The corresponding blue boxes show the systematic uncertainties from the theory. The maximum upward and downward deviations of cross sections calculated from different variations in the charm-quark mass, the renormalization scale, and the factorization scale (see Tab. 7.5) resulted in the systematic uncertainties from theory and are shown by blue boxes. The ratio shows that the measured spectrum agrees with the NLO pQCD theoretical predictions

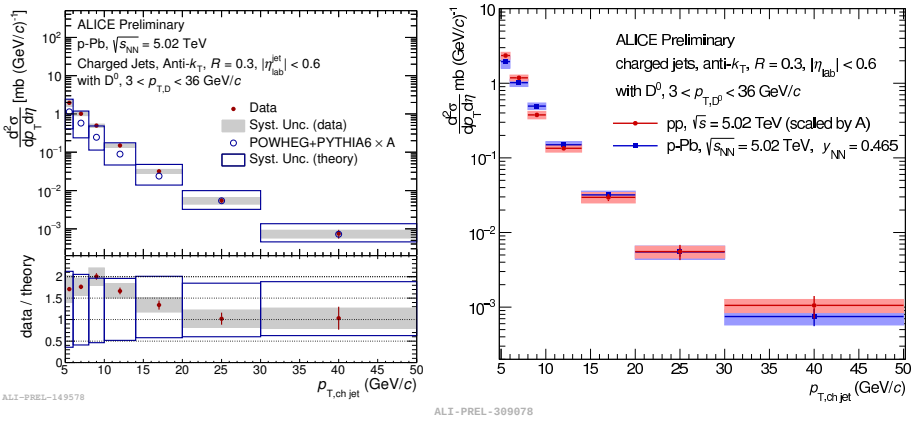

Figure 7.19: Left panel: cross section of D^0 jets in p–Pb collisions at $\sqrt{s_{NN}} = 5.02$ TeV shown as solid red circles with systematic uncertainties shown as grey filled boxes. The measurements are compared to theoretical predictions shown as blue circles with their systematic uncertainties shown as blue boxes. Right panel: The measurements for D^0-jet cross section are shown in blue for p–Pb collisions and in red for pp collisions scaled by lead-nucleus mass number.

within uncertainties. The right panel shows the $p_{T,ch\,jet}$-differential cross section for D^0 jets with $R = 0.3$ in p–Pb collisions (blue) at $\sqrt{s_{NN}} = 5.02$ TeV alongside the $p_{T,ch\,jet}$-differential D^0-jet cross section in pp collisions (red) at $\sqrt{s} = 5.02$ TeV scaled by the atomic mass number of lead, equivalent to the number of binary nucleon–nucleon collisions. The systematic uncertainties for the measurements are shown in boxes in their respective colours. It is important to note here that both the measurements for D^0 jets in p–Pb as well as pp collisions are done in the kinematic range $5 < p_{T,ch\,jet} < 50$ GeV/c with $p_{T,D^0} > 3$ GeV/c.

The ratio of the cross section in p–Pb collisions to the scaled one in pp collisions gives us the nuclear modification factor for D^0 jets in p–Pb collisions (R_{pPb}). It was defined earlier in this chapter for minimum-bias proton–nucleus collisions (see Eq. 7.1). R_{pPb} can be seen in green in Fig. 7.20. The green solid squares represent the measured R_{pPb} with statistical uncertainties as vertical error bars, and systematic uncertainties as green squares. Also shown is the nuclear modification factor R_{AA} for Pb–Pb collisions in black. This was measured earlier in a separate analysis in the ALICE collaboration. The cross section calculated for D^0 jets in Pb–Pb collisions was in the 0–20% centrality class using the data collected by ALICE in 2015. The cross section of D^0 jets in p–Pb collisions measured using the data collected by ALICE in 2016 and discussed in this chapter was used as a data reference for R_{AA}.

Both the cross sections in Pb–Pb and p–Pb collisions were measured before the cross section in pp collisions was determined. The cross section in p–Pb collisions could be used as a data reference for Pb–Pb collisions under the assumption that no cold nuclear matter effects were present for D^0 jets in p–Pb collisions at $\sqrt{s_{NN}} = 5.02$ TeV within the specified kinematic range for Pb–Pb collisions i. e.

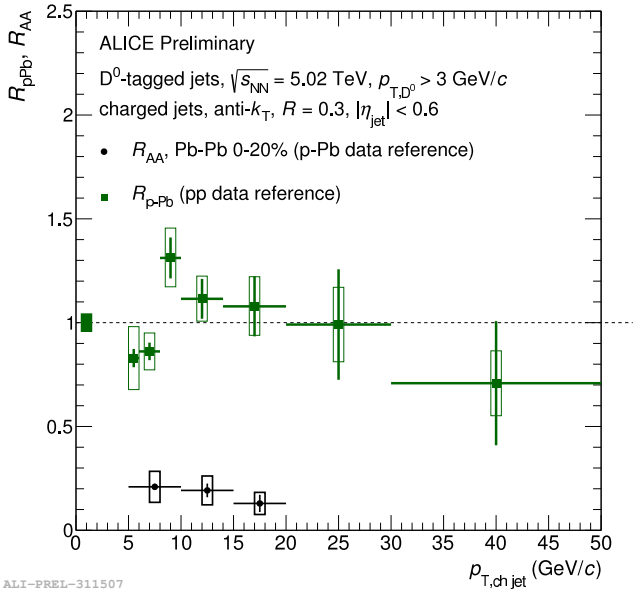

Figure 7.20: Nuclear modification factor R_{pPb} for D^0 jets with $R = 0.3$ in p–Pb events at $\sqrt{s_{\mathrm{NN}}} = 5.02$ TeV, and $p_{\mathrm{T,D}^0} > 3$ GeV/c. Also shown is the nuclear modification factor R_{AA} for D^0 jets in the same radius for Pb–Pb collisions at $\sqrt{s_{\mathrm{NN}}} = 5.02$ TeV at centrality class of 0–20% with the p–Pb data reference.

$5 < p_{\mathrm{T,ch\,jet}} < 20$ GeV/c. The assumption was later confirmed by measuring R_{pPb} by comparing cross sections for D^0 jets in p–Pb collisions with the same in pp collisions (data for which was collected in 2017). As one can see, R_{pPb} conforms to unity within statistical and systematic uncertainties in the reported kinematic range. One should also keep in mind that, to be used as a baseline reference for D^0-jet measurements in Pb–Pb collisions, the cross-section measurements from the current analysis were redone in the required coarser kinematic bins 5–10–15–20 GeV/c. Finally, it can be concluded that no large modification of the initial parton distributions is present and the production of jets tagged with D^0 mesons is devoid of any final state effects.

7.7 SUMMARY

In this chapter, the $p_{\mathrm{T,ch\,jet}}$-differential production-cross-section of D^0-tagged charged-particle jets in p–Pb collisions at $\sqrt{s_{\mathrm{NN}}} = 5.02$ TeV was investigated in the kinematic range $5 < p_{\mathrm{T,ch\,jet}} < 50$ GeV/c, with $p_{\mathrm{T,D}^0} > 3$ GeV/c. It was observed that the measurements agreed with POWHEG + PYTHIA 6 Monte Carlo simulations within their uncertainties. The cross-section measurement served two purposes,

- it provided a reference measurement for Pb–Pb collision system, and
- the nuclear modification factor R_{pPb} could be measured using a reference from the pp collision system.

Now that the pp measurement is available, it can be used as a reference for measuring R_{AA}.

It is also interesting to note that the absence of any cold nuclear matter effects within the relatively large experimental uncertainties in the measured kinematic range is a validation to the use of the p–Pb measurement as a reference for the Pb–Pb measurement. Also, in the predictions presented for cold nuclear matter effects in p–Pb collisions at $\sqrt{s_{\mathrm{NN}}} = 8.16$ TeV (see Ref. [104]) using EPS09 nPDF, no major nuclear modification was expected with the exception of p_{T} values lower than 5 GeV/c. What can also be probed for the D^0 jets in p–Pb collisions is the possible modification in the fragmentation function defined by the parallel momentum fraction carried by the constituent D^0 meson in a jet. In this thesis, the fragmentation function of D^0 jets has not been studied for the p–Pb collision system, but it has been studied for the pp collision system and will be presented in the next chapter.

8 FRAGMENTATION OF CHARM JETS IN VACUUM

8.1 PHYSICS TARGET

After probing the production of charm jets in vacuum and in proton–lead collisions, their fragmentation in vacuum is investigated in order to establish a reference measurement for similar studies in Pb–Pb and p–Pb collision systems and to test QCD calculations. In order to study charm-jet fragmentation, a variable is constructed representing the momentum carried by the charm hadron of choice, a D^0 meson, as the fraction of the full momentum of its charged-particle jet along the jet momentum axis

$$z_{\parallel}^{\mathrm{ch}} = \frac{\vec{p}_{\mathrm{ch\,jet}} \cdot \vec{p}_{\mathrm{D^0}}}{\vec{p}_{\mathrm{ch\,jet}} \cdot \vec{p}_{\mathrm{ch\,jet}}}, \tag{8.1}$$

where $\vec{p}_{\mathrm{D^0}}$ is the D^0 momentum and $\vec{p}_{\mathrm{ch\,jet}}$ is the total track-based jet momentum. Presented in this chapter are results on $z_{\parallel}^{\mathrm{ch}}$ distributions of D^0 jets in pp collisions at $\sqrt{s} = 5.02$ TeV in the following jet transverse momentum intervals: 5–7, 7–10, 10–15 and 15–50 GeV/c for four jet radii: $R = 0.2$, 0.3, 0.4 and 0.6.

8.2 RAW YIELDS DIFFERENTIAL IN $z_{\parallel}^{\mathrm{ch}}$

Using the strategy established in Chapter 5, and similar to the procedures followed in the previous two analyses, D^0-jet candidates are analysed in various intervals of $p_{\mathrm{T,D^0}}$ as allowed by the $p_{\mathrm{T,ch\,jet}}$ interval they were being probed in. The details are summarized in Tab. 8.1.

Table 8.1: Ranges of $p_{\mathrm{T,D^0}}$ (in GeV/c) for the investigation of the invariant-mass distribution in different $p_{\mathrm{T,ch\,jet}}$ intervals for different jet radii in pp collisions at $\sqrt{s} = 5.02$ TeV.

	$p_{\mathrm{T,ch\,jet}}$ (GeV/c) intervals				
R	2–5	5–7	7–10	10–15	15–50
	$p_{\mathrm{T,D^0}}$ (GeV/c) ranges				
0.2	2–5	2–7	4–10	5–15	10–36
0.3	2–5	2–7	3–10	5–15	5–36
0.4	2–5	2–7	3–10	5–15	5–36
0.6	2–5	2–7	3–10	5–15	5–36

For all the jet radii, it can be seen that the upper limit of $p_{\mathrm{T,D^0}}$ is exactly the same as each of the $p_{\mathrm{T,ch\,jet}}$ intervals except for the highest $p_{\mathrm{T,ch\,jet}}$ interval since the signal containing $\mathrm{D^0}$ mesons with $p_{\mathrm{T,D^0}} > 36$ GeV/c is practically zero. It can be seen that the lower limit of $p_{\mathrm{T,D^0}}$ can be smaller than the lower bound of the corresponding $p_{\mathrm{T,ch\,jet}}$ interval, because even charged jets will in general have more constituents[1].

The 2–5 GeV/c $p_{\mathrm{T,ch\,jet}}$ range is not included in the final results, but it is used in the complete analysis to account for any potential migration between neighbouring $p_{\mathrm{T,ch\,jet}}$ bins (see Sec. 6.3.3). The reason for this is that some jets may have been measured within this range, but their true $p_{\mathrm{T,ch\,jet}}$ value could be greater than 5 GeV/c. Similarly, some jets measured with a $p_{\mathrm{T,ch\,jet}}$ value greater than 5 GeV/c could actually have a true $p_{\mathrm{T,ch\,jet}}$ value less than 5 GeV/c. By including the 2–5 GeV/c range in the analysis, the potential bin migration between these neighbouring $p_{\mathrm{T,ch\,jet}}$ bins is taken into account. This allows for the unfolding procedure described in Sec. 8.3.3 to accurately correct for any possible feed-in/feed-out effects between the neighbouring bins, which is crucial for obtaining accurate results in the desired range of 5–50 GeV/c for $p_{\mathrm{T,ch\,jet}}$.

Now, using Eq. 6.2, the invariant-mass distributions were obtained in the intervals of $p_{\mathrm{T,D^0}}$ as tabulated in Tab. 8.1 for each jet R. The top panel in Fig. 8.1 shows examples of $M(\mathrm{K}\pi)$ distributions in a few $p_{\mathrm{T,D^0}}$ intervals while the bottom panel shows the raw yields of $\mathrm{D^0}$ jets as a function of the momentum fraction $z_{\parallel}^{\mathrm{ch}}$ extracted for the signal and sideband $M(\mathrm{K}\pi)$ regions in those $p_{\mathrm{T,D^0}}$ intervals. The sideband distributions were normalized to the background yield in the peak region and subtracted from the signal-region distributions in order to obtain the raw $\mathrm{D^0}$-jet $z_{\parallel}^{\mathrm{ch}}$ distributions.

8.3 CORRECTIONS

There are three steps of correction applied to the raw $z_{\parallel}^{\mathrm{ch}}$ distributions obtained in the previous section, (a) reconstruction efficiency and acceptance of $\mathrm{D^0}$ mesons, (b) subtraction of contribution from beauty jets, and (c) unfolding.

8.3.1 *Reconstruction efficiency*

The Monte Carlo PYTHIA 6 event generator and GEANT 3 simulations were used to calculate the possible number of $\mathrm{D^0}$ jets produced at the detector level as well as the generator level along with their kinematic properties. The ratio of the generator-level $\mathrm{D^0}$ jets for which a detector-level $\mathrm{D^0}$ jet could be found to all the generated $\mathrm{D^0}$ jets within $|\eta_{\mathrm{jet}}| < 0.9 - R$ was calculated to give the required reconstruction efficiency within the detector acceptance. The detector-level $\mathrm{D^0}$ jets were required to pass all the data-analysis selection requirements as well. Since the efficiency is dependent on the $\mathrm{D^0}$-meson topological selections, a strong dependence is observed

1 It can be noted that the $\mathrm{D^0}$, in spite of being an electrically neutral particle, is still an effective constituent of a charged jet via its charged decay products, a kaon and a pion.

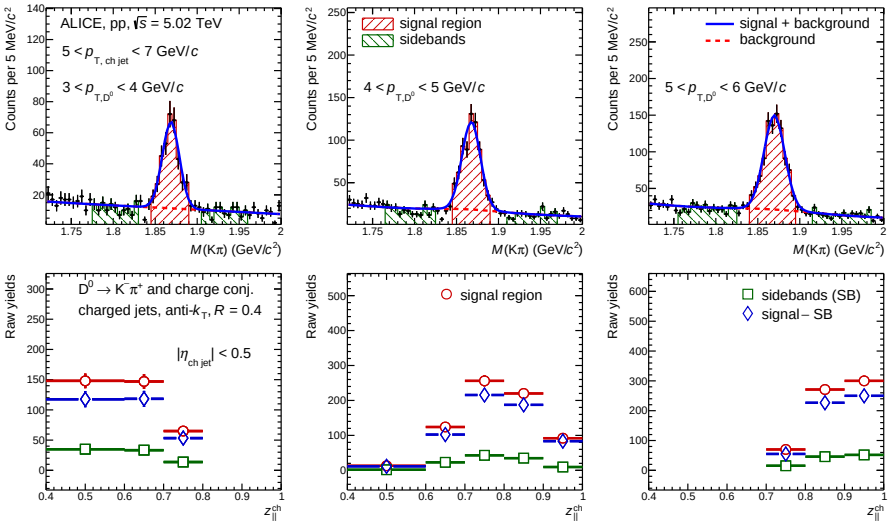

Figure 8.1: Top panel: invariant-mass distributions of D^0-jet candidates with $2 < p_{T,ch\,jet} < 50$ GeV/c. Bottom panel: distributions of the D^0-jet candidates in the peak region are shown in red.

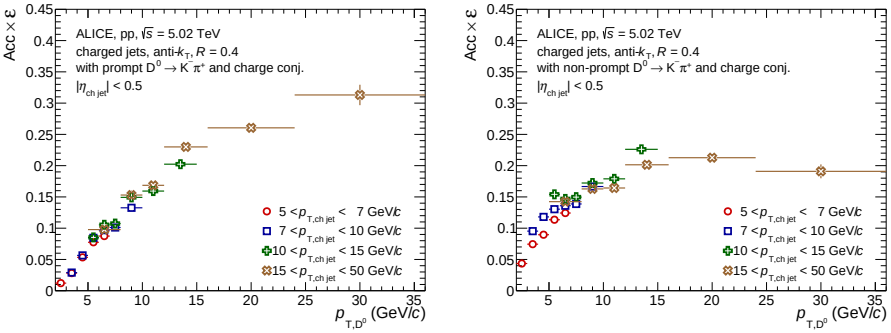

Figure 8.2: Product of acceptance and efficiency for charged jets tagged with prompt D^0 mesons as a function of p_{T,D^0} is shown in different $p_{T,ch\,jet}$ intervals on the left panel. The same for charged jets tagged with non-prompt D^0 mesons is shown on the right panel.

on p_{T,D^0}. Negligible dependence is seen on $p_{T,ch\,jet}$. This is evident in Fig. 8.2 for both prompt D^0 jets (left) as well as non-prompt D^0 jets (right). The product of acceptance and efficiency seems to follow the same pattern across all four $p_{T,ch\,jet}$ intervals. It was used to correct the raw yields obtained in different p_{T,D^0} intervals as described earlier in the chapter. The scaled $z_{\parallel}^{ch}$ distributions from each p_{T,D^0}

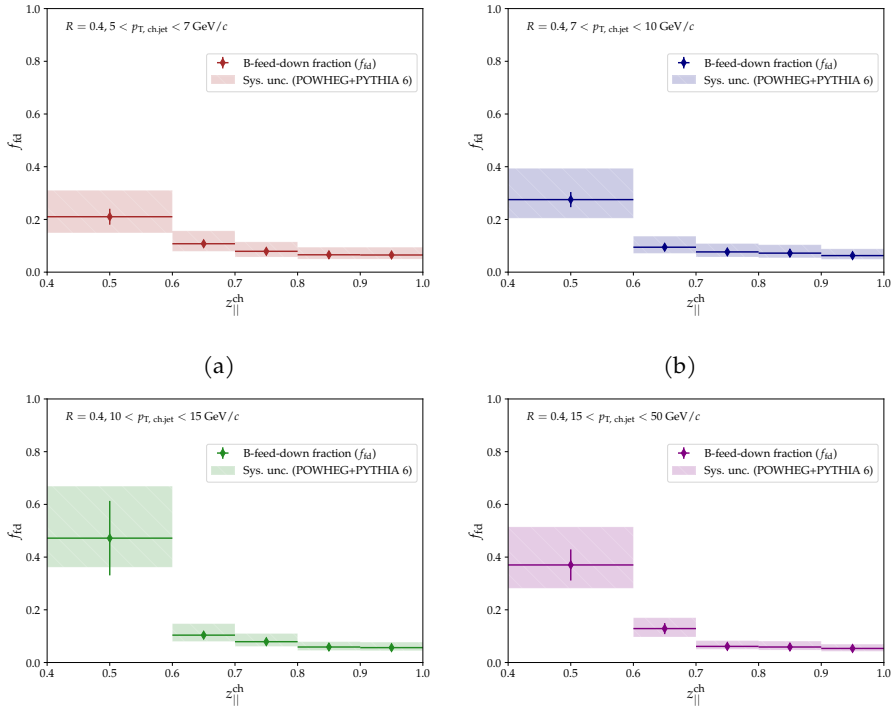

Figure 8.3: The fraction f_{fd} of D^0 mesons in jets coming from B feed-down as a function of the momentum fraction $z_{\parallel}^{\mathrm{ch}}$ in various $p_{\mathrm{T,ch\,jet}}$ intervals: (a) 5–7 GeV/c, (b) 7–10 GeV/c, (c) 10–15 GeV/c, and (d) 15–50 GeV/c.

intervals were summed up to give efficiency corrected $z_{\parallel}^{\mathrm{ch}}$ yields in each $p_{\mathrm{T,ch\,jet}}$ interval according to the following relation adapted from Eq. 6.3.

$$N(z_{\parallel}^{\mathrm{ch,det}}, p_{\mathrm{T,ch\,jet}}^{\mathrm{det}}) = \sum_{p_{\mathrm{T,D^0}}} \frac{N^{raw}(p_{\mathrm{T,D^0}}, z_{\parallel}^{\mathrm{ch,det}}, p_{\mathrm{T,ch\,jet}}^{\mathrm{det}})}{\epsilon^{c\to \mathrm{D^0}}(p_{\mathrm{T,D^0}})} \tag{8.2}$$

8.3.2 *B-meson decay contribution*

The contribution of non-prompt D^0 mesons was subtracted from the efficiency-corrected $z_{\parallel}^{\mathrm{ch}}$ yields to get the required prompt D^0 jets using the following relation adapted from Eq. 6.10 as described in Sec. 6.3.2.

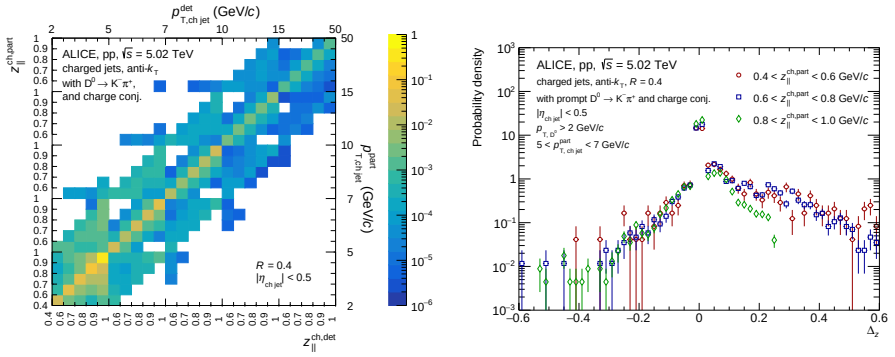

Figure 8.4: Left: detector-response matrix used for unfolding the two-dimensional $z_{\parallel}^{\mathrm{ch}}$–$p_{\mathrm{T,ch\,jet}}$ distribution with $R = 0.4$ in pp collisions at $\sqrt{s} = 5.02$ TeV with both detector and particle levels in $0.4 < z_{\parallel}^{\mathrm{ch}} < 1$ and $2 < p_{\mathrm{T,ch\,jet}} < 50$ GeV/c. Right: probability density distribution of the residuals (Δ_z) of the momentum fraction $z_{\parallel}^{\mathrm{ch}}$ in $5 < p_{\mathrm{T,ch\,jet}}^{\mathrm{part}} < 10$ GeV/c, $10 < p_{\mathrm{T,ch\,jet}}^{\mathrm{part}} < 20$ GeV/c and $20 < p_{\mathrm{T,ch\,jet}}^{\mathrm{part}} < 30$ GeV/c.

$$N^{\mathrm{c}\to\mathrm{D}^0}(z_{\parallel}^{\mathrm{ch,det}}, p_{\mathrm{T,ch\,jet}}^{\mathrm{det}}) = N(z_{\parallel}^{\mathrm{ch,det}}, p_{\mathrm{T,ch\,jet}}^{\mathrm{det}}) - N^{\mathrm{b}\to\mathrm{D}^0}(z_{\parallel}^{\mathrm{ch,det}}, p_{\mathrm{T,ch\,jet}}^{\mathrm{det}}) \tag{8.3}$$

$$\begin{aligned} \text{with } N^{\mathrm{b}\to\mathrm{D}^0}(z_{\parallel}^{\mathrm{ch,det}}, p_{\mathrm{T,ch\,jet}}^{\mathrm{det}}) = RM^{\mathrm{b}\to\mathrm{D}^0}(z_{\parallel}^{\mathrm{ch,part}}, z_{\parallel}^{\mathrm{ch,det}}, p_{\mathrm{T,ch\,jet}}^{\mathrm{part}}, p_{\mathrm{T,ch\,jet}}^{\mathrm{det}}) \cdot \\ \sum_{p_{\mathrm{T,D}^0}} \left(\frac{\epsilon^{\mathrm{b}\to\mathrm{D}^0}}{\epsilon^{\mathrm{c}\to\mathrm{D}^0}}(p_{\mathrm{T,D}^0}) \cdot \right. \\ \left. N^{\mathrm{POWHEG}}(p_{\mathrm{T,D}^0}, z_{\parallel}^{\mathrm{ch,part}}, p_{\mathrm{T,ch\,jet}}^{\mathrm{part}}) \right) \end{aligned} \tag{8.4}$$

The b-hadron feed-down fraction (beauty-jet contribution out of all D^0 jets) is given by

$$f_{\mathrm{fd}} = \frac{N^{\mathrm{b}\to\mathrm{D}^0}(z_{\parallel}^{\mathrm{ch,det}}, p_{\mathrm{T,ch\,jet}}^{\mathrm{det}})}{N(z_{\parallel}^{\mathrm{ch,det}}, p_{\mathrm{T,ch\,jet}}^{\mathrm{det}})}. \tag{8.5}$$

It is shown in Fig. 8.3 for each $p_{\mathrm{T,ch\,jet}}$ interval as a function of $z_{\parallel}^{\mathrm{ch}}$ for D^0 jets with $R = 0.4$.

8.3.3 *Unfolding the two dimensional spectra*

The momentum smearing of constituent tracks of the D^0 jets caused mainly by the finite resolution of detectors is corrected by taking the Bayesian approach to unfold the b-hadron feed-down subtracted spectra using the procedure established in Sec. 6.3.3.

The $z_{\parallel}^{\mathrm{ch}}$ distributions obtained for different $p_{\mathrm{T,ch\,jet}}$ intervals form a two-dimensional distribution in $z_{\parallel}^{\mathrm{ch}}$ (0.4–1.0) and $p_{\mathrm{T,ch\,jet}}$ (2–50 GeV/c). Earlier, the analysis was done in a single dimension in $z_{\parallel}^{\mathrm{ch}}$ for separate $p_{\mathrm{T,ch\,jet}}$ intervals, which is equivalent to the two-dimensional approach of analysing distributions combined together in $z_{\parallel}^{\mathrm{ch}}$ and $p_{\mathrm{T,ch\,jet}}$. To correct the distribution across $z_{\parallel}^{\mathrm{ch}}$ and $p_{\mathrm{T,ch\,jet}}$, a $z_{\parallel}^{\mathrm{ch}}$-and-$p_{\mathrm{T,ch\,jet}}$ distribution was prepared for each jet radius by combining all five b-hadron feed-down subtracted $z_{\parallel}^{\mathrm{ch}}$ distributions for the five $p_{\mathrm{T,ch\,jet}}$ intervals. A response matrix containing $z_{\parallel}^{\mathrm{ch}}$ and $p_{\mathrm{T,ch\,jet}}$ information at the detector and particle level was prepared for unfolding this two-dimensional distribution, which was four-dimensional in $z_{\parallel}^{\mathrm{ch,det}}$, $z_{\parallel}^{\mathrm{ch,part}}$, $p_{\mathrm{T,ch\,jet}}^{\mathrm{det}}$ and $p_{\mathrm{T,ch\,jet}}^{\mathrm{part}}$. The required response matrix is shown in Fig. 8.4 (left). Similar to Eq. 6.14, the resolutions of the $z_{\parallel}^{\mathrm{ch}}$ measurements were studied by examining the probability density distributions of the residuals

$$\Delta_z(p_{\mathrm{T,ch\,jet}}^{\mathrm{part}}) = \frac{z_{\parallel}^{\mathrm{ch,det}}(p_{\mathrm{T,ch\,jet}}^{\mathrm{part}}) - z_{\parallel}^{\mathrm{ch,part}}(p_{\mathrm{T,ch\,jet}}^{\mathrm{part}})}{z_{\parallel}^{\mathrm{ch,part}}(p_{\mathrm{T,ch\,jet}}^{\mathrm{part}})} \tag{8.6}$$

in different $p_{\mathrm{T,ch\,jet}}$ intervals. The resolution on $z_{\parallel}^{\mathrm{ch}}$ can be obtained as the width of the distribution of residuals Δ_z. The probability density distributions of the residuals of $z_{\parallel}^{\mathrm{ch}}$ in the interval $5 < p_{\mathrm{T,ch\,jet}}^{\mathrm{part}} < 7$ GeV/c are shown on the right panel of Fig. 8.4.

8.3.4 *Response matrix and reconstruction-efficiency correction*

The response matrix shown in Fig. 8.4 (left) has $z_{\parallel}^{\mathrm{ch,det}}$ and $z_{\parallel}^{\mathrm{ch,part}}$ ranging from 0.4 to 1 with the smallest divisions being $0.4-0.6$, $0.6-0.7$, $0.7-0.8$, $0.9-1.0$. Its other axes $p_{\mathrm{T,ch\,jet}}^{\mathrm{det}}$ and $p_{\mathrm{T,ch\,jet}}^{\mathrm{part}}$ range from 2 to 50 GeV/c with their smallest divisions being $2-5$, $5-7$, $7-10$, $10-15$ and $15-50$ GeV/c. Every two-dimensional interval in $(p_{\mathrm{T,ch\,jet}}^{\mathrm{part}}, p_{\mathrm{T,ch\,jet}}^{\mathrm{det}})$ contains a two-dimensional $(z_{\parallel}^{\mathrm{ch,part}}, z_{\parallel}^{\mathrm{ch,det}})$ distribution.

While a four-dimensional histogram was filled in using the first four variables, it was also scaled using its $p_{\mathrm{T,D^0}}$ information by the inverse of $p_{\mathrm{T,D^0}}$-dependent prompt reconstruction efficiency in Fig. 8.2 (left). It is worth noting that the reconstruction efficiency prepared in Sec. 8.3.1 was a distribution in particle-level transverse momentum of $\mathrm{D^0}$, $p_{\mathrm{T,D^0}}^{\mathrm{part}}$. The scaling of the response matrix ensures a similar treatment as used for the measured data. This scaling was done to the prompt response matrix for unfolding measured spectra from data:

$$\begin{aligned}\overline{RM}^{\mathrm{c\to D^0}}&(z_{\parallel}^{\mathrm{ch,part}}, z_{\parallel}^{\mathrm{ch,det}}, p_{\mathrm{T,ch\,jet}}^{\mathrm{part}}, p_{\mathrm{T,ch\,jet}}^{\mathrm{det}}) \\ &= \sum_{p_{\mathrm{T,D^0}}} \frac{RM^{\mathrm{c\to D^0}}(p_{\mathrm{T,D^0}}, z_{\parallel}^{\mathrm{ch,part}}, z_{\parallel}^{\mathrm{ch,det}}, p_{\mathrm{T,ch\,jet}}^{\mathrm{part}}, p_{\mathrm{T,ch\,jet}}^{\mathrm{det}})}{\epsilon^{c\to \mathrm{D^0}}(p_{\mathrm{T,D^0}})},\end{aligned} \tag{8.7}$$

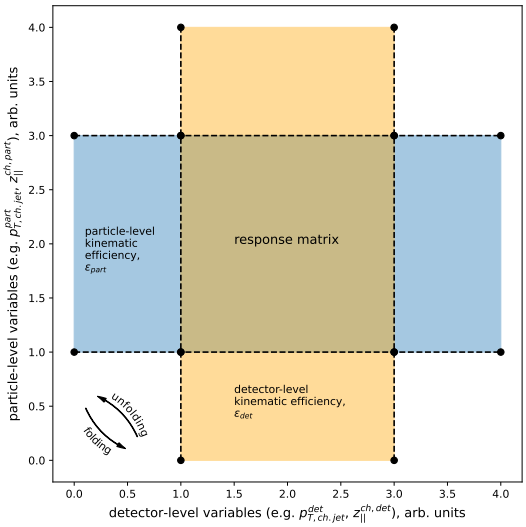

Figure 8.5: Corrections due to kinematic efficiency when filling up a response matrix. See text for details.

as well as the non-prompt response matrix for folding non-prompt simulations:

$$\overline{RM}^{\mathrm{b}\to\mathrm{D}^0}(z_{\parallel}^{\mathrm{ch,part}}, z_{\parallel}^{\mathrm{ch,det}}, p_{\mathrm{T,ch\,jet}}^{\mathrm{part}}, p_{\mathrm{T,ch\,jet}}^{\mathrm{det}}) = \sum_{p_{\mathrm{T,D}^0}} \frac{RM^{\mathrm{b}\to\mathrm{D}^0}(p_{\mathrm{T,D}^0}, z_{\parallel}^{\mathrm{ch,part}}, z_{\parallel}^{\mathrm{ch,det}}, p_{\mathrm{T,ch\,jet}}^{\mathrm{part}}, p_{\mathrm{T,ch\,jet}}^{\mathrm{det}})}{\epsilon^{\mathrm{c}\to\mathrm{D}^0}(p_{\mathrm{T,D}^0})}. \tag{8.8}$$

8.3.5 *Correction of spectra by kinematic efficiency*

Another correction is determined while building the response matrix; it is called the kinematic efficiency. Let us refer to Fig. 8.5 where this concept is sketched. The vertical axis represents particle-level *kinematic* variables like $p_{\mathrm{T,ch\,jet}}^{\mathrm{part}}$ and $z_{\parallel}^{\mathrm{ch,part}}$ whereas the horizontal axis represents such detector-level variables like $p_{\mathrm{T,ch\,jet}}^{\mathrm{det}}$ and $z_{\parallel}^{\mathrm{ch,det}}$, all in arbitrary units.

Let us define $N_{\mathrm{in}}^{\mathrm{det}}$to be the number of D^0 jets in a selected range with respect to particle-level kinematics, and $N_{\mathrm{out}}^{\mathrm{det}}$those outside the range, where both numbers are taken inside the selected range with respect to detector-level kinematics. Analogously, $N_{\mathrm{in}}^{\mathrm{part}}$and $N_{\mathrm{out}}^{\mathrm{part}}$would be the equivalent numbers inside or outside with respect to detector-level kinematics, both taken inside the selected range with respect to particle-level kinematics. The detector-level kinematic efficiency is then

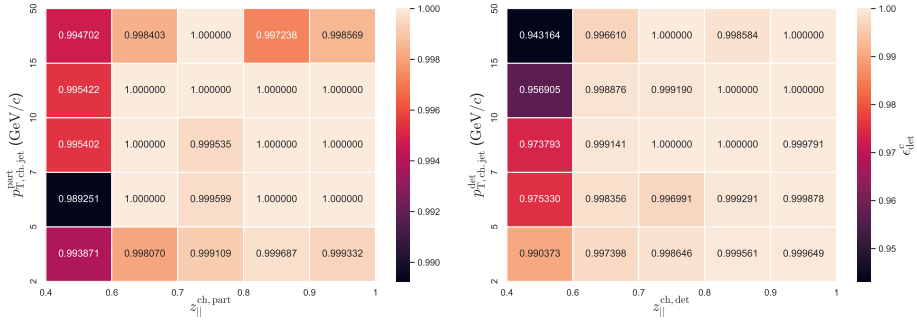

(a) (b)

Figure 8.6: Distributions of kinematic efficiency for prompt D^0 jets at (a) particle and (b) detector levels.

the fraction of jets in the detector-level kinematic range that are also found in the particle-level kinematic range and is given by:

$$\epsilon_{\mathrm{det}} = \frac{N_{\mathrm{in}}^{\mathrm{det}}}{N_{\mathrm{in}}^{\mathrm{det}} + N_{\mathrm{out}}^{\mathrm{det}}}. \tag{8.9}$$

Similarly, the particle-level kinematic efficiency is then the fraction of jets in the particle-level kinematic range that are also found in the detector-level kinematic range and is given by:

$$\epsilon_{\mathrm{part}} = \frac{N_{\mathrm{in}}^{\mathrm{part}}}{N_{\mathrm{in}}^{\mathrm{part}} + N_{\mathrm{out}}^{\mathrm{part}}}. \tag{8.10}$$

Thus, a value of $\epsilon_{\mathrm{part}} = 0.99$ means 1% of such D^0 jets were omitted. The values of kinematic efficiency must always be 1 or less for any given $z_{\parallel}^{\mathrm{ch}}$–$p_{\mathrm{T,ch\,jet}}$ interval.

These kinematic efficiencies describe the effects of bin migration. For the beauty-jet simulations, the non-prompt kinematic efficiency $\epsilon_{\mathrm{part}}^{b}$ is first used to take care of the related losses. Then, the folding with the non-prompt response matrix is done followed by a division by the non-prompt detector-level kinematic efficiency $\epsilon_{\mathrm{det}}^{b}$ for the corresponding gain.

The measured distribution is corrected in a similar way, where losses are initially addressed by multiplying with the prompt detector-level kinematic efficiency $\epsilon_{\mathrm{det}}^{c}$. This is followed by the unfolding with the prompt response matrix. Finally, the gains due to the division by the prompt particle-level kinematic efficiency $\epsilon_{\mathrm{part}}^{c}$ are addressed.

Kinematic efficiency distributions at particle and detector levels for prompt D^0 jets are shown in Fig. 8.6 (a) and (b) respectively. The correction due to $\epsilon_{\mathrm{part}}^{\mathrm{c}}$ (i. e. the deviation from unity in Eq. 8.10) has mostly been less than 0.1% except at the low-$z_{\parallel}^{\mathrm{ch}}$ values, where it is about 1%. Similar is the correction due to $\epsilon_{\mathrm{det}}^{\mathrm{c}}$ with values at low $z_{\parallel}^{\mathrm{ch}}$ and high $p_{\mathrm{T,ch\,jet}}$ reaching about 6%. Likewise, corrections due to

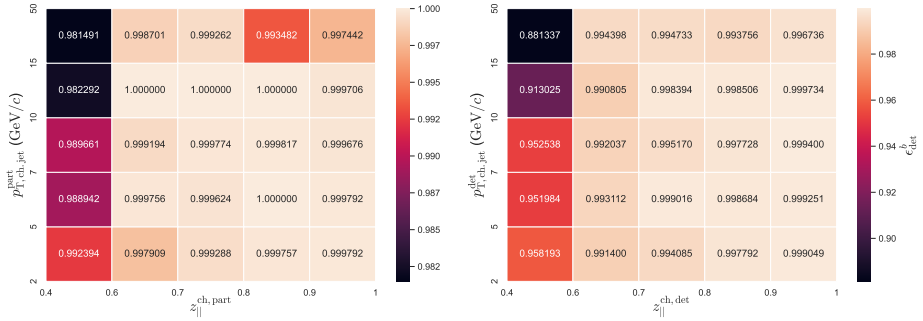

(a) (b)

Figure 8.7: Distributions of kinematic efficiency for non-prompt D^0 jets at (a) particle and (b) detector levels.

kinematic efficiency on non-prompt D^0 jets could reach around 2% in the low-$z_{\parallel}^{ch}$–high-$p_{T,ch\,jet}$ regions at particle level, and 12% at the detector level. The particle-level and detector-level kinematic efficiencies for non-prompt D^0 jets are shown in Fig. 8.7 (a) and (b) respectively. This correction of spectra by kinematic efficiencies was significant in this chapter, unlike one-dimensional $p_{T,ch\,jet}$ distributions in earlier chapters because they had a buffer zone (2–5 GeV/c) throughout their analyses that was not reported in the final results. However, the two-dimensional $z_{\parallel}^{ch}$–$p_{T,ch\,jet}$ distributions in this chapter have a strict boundary at $z_{\parallel}^{ch} = 0.4$. Kinematic-efficiency correction is here to alleviate the boundary effects due to the absence of such buffer.

To conclude this section, the detector-level distribution for non-prompt D^0 jets given in Eq. 8.3 and 8.4 as

$$N^{b\to D^0}(z_{\parallel}^{ch,det}, p_{T,ch\,jet}^{det}) = \overline{RM}^{b\to D^0}(z_{\parallel}^{ch,part}, z_{\parallel}^{ch,det}, p_{T,ch\,jet}^{part}, p_{T,ch\,jet}^{det}) \cdot \sum_{p_{T,D^0}} \left(\frac{\epsilon^{b\to D^0}}{\epsilon^{c\to D^0}}(p_{T,D^0}) \cdot N^{POWHEG}(p_{T,D^0}, z_{\parallel}^{ch,part}, p_{T,ch\,jet}^{part}) \right) \tag{8.11}$$

rather becomes

$$N^{\mathrm{b}\to\mathrm{D}^0}(z_{\parallel}^{\mathrm{ch,det}}, p_{\mathrm{T,ch\,jet}}^{\mathrm{det}}) = \frac{1}{\epsilon_{\mathrm{det}}^{\mathrm{b}}(z_{\parallel}^{\mathrm{ch,det}}, p_{\mathrm{T,ch\,jet}}^{\mathrm{det}})} \cdot \Big[\overline{RM}^{\mathrm{b}\to\mathrm{D}^0}(z_{\parallel}^{\mathrm{ch,part}}, z_{\parallel}^{\mathrm{ch,det}}, p_{\mathrm{T,ch\,jet}}^{\mathrm{part}}, p_{\mathrm{T,ch\,jet}}^{\mathrm{det}}) \cdot \Big\{\epsilon_{\mathrm{part}}^{\mathrm{b}}(z_{\parallel}^{\mathrm{ch,part}}, p_{\mathrm{T,ch\,jet}}^{\mathrm{part}}) \cdot \sum_{p_{\mathrm{T,D}^0}} \left(\frac{\epsilon^{\mathrm{b}\to\mathrm{D}^0}}{\epsilon^{\mathrm{c}\to\mathrm{D}^0}}(p_{\mathrm{T,D}^0}) \cdot N^{\mathrm{POWHEG}}(p_{\mathrm{T,D}^0}, z_{\parallel}^{\mathrm{ch,part}}, p_{\mathrm{T,ch\,jet}}^{\mathrm{part}})\right) \Big\}\Big]. \tag{8.12}$$

The unfolding procedure conducted along with kinematic-efficiency correction to get the particle-level prompt D^0 jets is depicted as

$$N^{\mathrm{c}\to\mathrm{D}^0}(z_{\parallel}^{\mathrm{ch,part}}, p_{\mathrm{T,ch\,jet}}^{\mathrm{part}}) = \frac{1}{\epsilon_{\mathrm{part}}^{\mathrm{c}}(z_{\parallel}^{\mathrm{ch,part}}, p_{\mathrm{T,ch\,jet}}^{\mathrm{part}})} \cdot \Big[\overline{RM}^{\mathrm{c}\to\mathrm{D}^0}(z_{\parallel}^{\mathrm{ch,part}}, z_{\parallel}^{\mathrm{ch,det}}, p_{\mathrm{T,ch\,jet}}^{\mathrm{part}}, p_{\mathrm{T,ch\,jet}}^{\mathrm{det}}) \odot \Big\{\epsilon_{\mathrm{det}}^{\mathrm{c}}(z_{\parallel}^{\mathrm{ch,det}}, p_{\mathrm{T,ch\,jet}}^{\mathrm{det}}) \cdot N^{\mathrm{c}\to\mathrm{D}^0}(z_{\parallel}^{\mathrm{ch,det}}, p_{\mathrm{T,ch\,jet}}^{\mathrm{det}}) \Big\}\Big]. \tag{8.13}$$

The dots in the equation represent the multiplication for every bin in $z_{\parallel}^{\mathrm{ch}}$ and $p_{\mathrm{T,ch\,jet}}$, and all quantities are vector or matrix-valued. The equation is given for one component of the vector, but it applies to all components. The circled dot represents the unfolding procedure.

8.4 SYSTEMATIC UNCERTAINTIES

Several sources were considered for studying the systematic uncertainties for the $z_{\parallel}^{\mathrm{ch}}$–$p_{\mathrm{T,ch\,jet}}$ distributions in a manner similar to the previous two chapters.

8.4.1 *Topological selection*

Four sets of topological selections were taken where the product of impact parameters of the daughters of a D^0 meson, K and π, was varied by $\pm5\%$ and $\pm10\%$ from its default values and so were the cosine of the pointing angle, and the normalized decay length. Yields from the new sets of topological selections were compared to the default set as ratios, and the root-mean-square values of those ratios served as systematic uncertainties. This was done separately for $z_{\parallel}^{\mathrm{ch}}$ distributions in all $p_{\mathrm{T,ch\,jet}}$ intervals. Results for D^0 jets with $R = 0.4$ are shown in Fig. 8.8. The uncertainty values tend to be higher in low-$z_{\parallel}^{\mathrm{ch}}$ regions $0.4 < z_{\parallel}^{\mathrm{ch}} < 0.6$, going as high as 18% in the interval $7 < p_{\mathrm{T,ch\,jet}} < 10$ GeV/c.

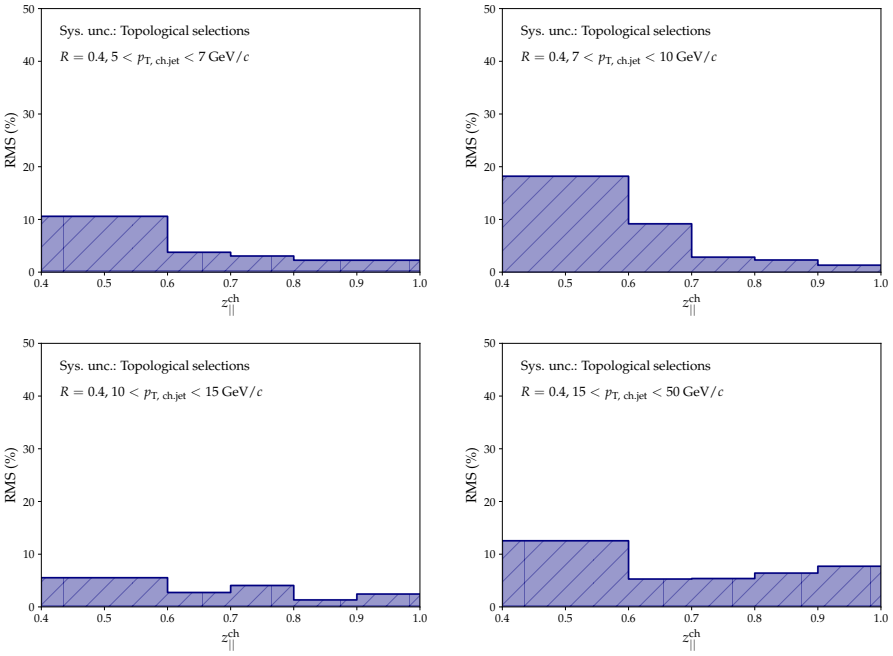

Figure 8.8: Systematic uncertainties due to variation in topological selections for D^0 jets with $R = 0.4$ in pp collisions at $\sqrt{s} = 5.02$ TeV.

8.4.2 *Raw-yield extraction: multi-trial*

Multiple trials were done to create a unique variation every time a function was fit to the invariant mass distributions of D^0 jets while extracting the raw yields of $z_{||}^{ch}$ (see Sec. 8.2). A maximum of 96 combinations were taken by altering one condition at a time from the list below.

- The width (σ) of the Gaussian signal was either kept free or fixed to 1.1 or 1 or 0.9 times MC values.
- The shape of the background function was either of exponential or of linear form.
- The mean (μ) of the signal was either kept free or fixed to the PDG value.
- The lower limit of fit ranges of invariant mass distributions was either 1.72 or 1.74 GeV/c^2.
- The upper limit of those fit ranges was either 2.00 or 2.03 GeV/c^2.
- The bin width of the invariant mass was either 5 or 10 MeV/c^2.

A final yield from each variation was taken as a ratio to the default configuration, and the root-mean-square values of all the yield-ratios were considered as systematic

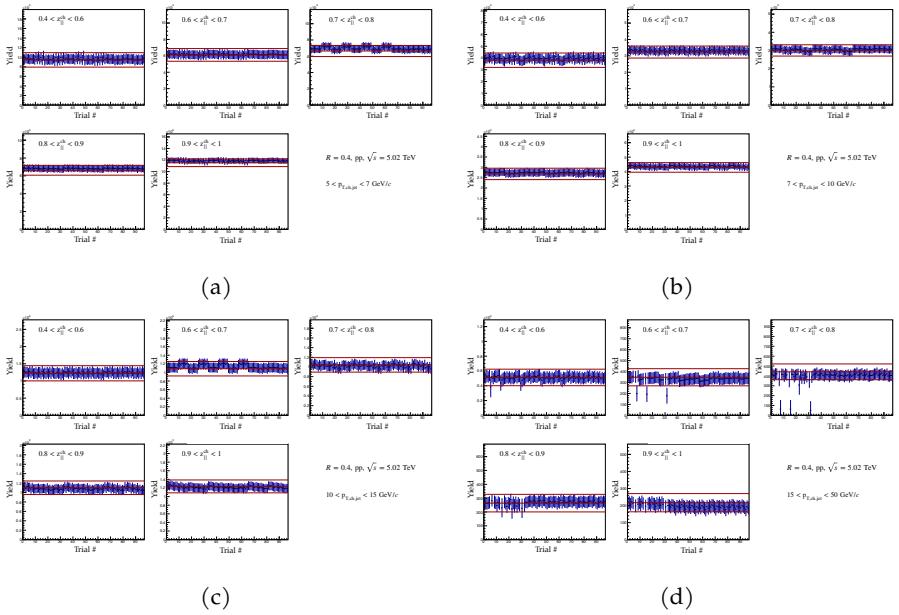

Figure 8.9: Multi-trial raw-yield extraction of D^0-jet yields with jets of $R = 0.4$ in pp collisions at $\sqrt{s} = 5.02$ TeV. Yields are shown in every $z_{\parallel}^{\mathrm{ch}}$ bin in the ranges 0.4–0.6, 0.6–0.7, 0.7–0.8, 0.8–0.9, 0.9–1 for each $p_{\mathrm{T,ch\,jet}}$ interval: (a) 5–7 GeV/c, (b) 7–10 GeV/c, (c) 10–15 GeV/c, and (d) 15–50 GeV/c.

uncertainties from this source. The results of these yield variations for all trials can be seen in Fig. 8.9. The corresponding systematic uncertainties are shown in Fig. 8.10 with a maximum of $\approx 10.5\%$ in the interval $15 < p_{\mathrm{T,ch\,jet}} < 50$ GeV/c.

8.4.3 *Raw-yield extraction: signal and sideband ranges*

Gaussian distributions fit to the invariant mass ($M_{\mathrm{K}\pi}$) had a specific width (σ_{fit}). The signal was extracted in the ranges of $|M_{\mathrm{K}\pi} - \mu_{\mathrm{fit}}| < n_1\sigma_{\mathrm{fit}}$ and the background distributions were determined from sidebands in the ranges of $n_2\sigma_{\mathrm{fit}} < |M_{\mathrm{K}\pi} - \mu_{\mathrm{fit}}| < n_3\sigma_{\mathrm{fit}}$ with the default configuration being $n_1 = 2$, $n_2 = 4$, and $n_3 = 9$. Four new spectra were extracted by having four variations of the sideband ranges: n_2 and n_3 were assigned either (3, 8), or (4, 10), or (4, 12), or (4, 15). To make a comparison, the ratios of these spectra to the default spectrum were obtained for each jet radius in the four $p_{\mathrm{T,ch\,jet}}$ intervals. The uncertainties were determined from the root-mean-square values of the ratios, and are shown in Fig. 8.11. Systematic uncertainties from this source were found to lie within 3%.

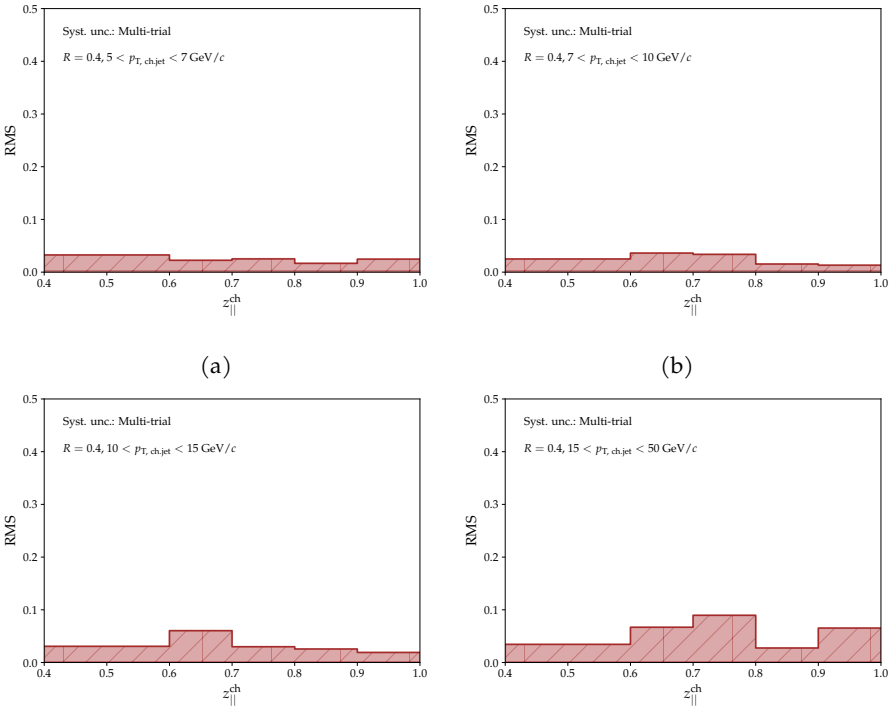

Figure 8.10: Systematic uncertainties due to multi-trial extraction of $z_{\parallel}^{ch}$ yields for jets with $R = 0.4$ in pp collisions at $\sqrt{s} = 5.02$ TeV: the root-mean-square values of deviations from unity of the yield-ratios are taken as systematic uncertainty values. (See text for details.)

8.4.4 *Raw-yield extraction: D^0 reflections*

D^0 reflections are D^0 candidates where the mass hypotheses for the two decay daughters have been swapped (see Sec. 5.1.6 and 6.2). Possible systematic uncertainties were determined by overestimating and underestimating the amount of D^0 reflections from MC simulations by 50%. The resulting yields were taken as a ratio to yields from the default configuration. Maximum deviations in each $z_{\parallel}^{ch}$–$p_{T,ch\,jet}$ interval served as the values of systematic uncertainties, which were found to be smaller than 4% as shown in Fig. 8.12 for $R = 0.4$.

8.4.5 *B-feed-down subtraction*

Contribution of D^0 jets from beauty quarks was determined by using POWHEG + PYTHIA 6 simulations (see Sec. 8.3.2) with a configuration where the mass of the beauty quark (m_b) was 4.75 GeV/c^2 while the renormalization scale

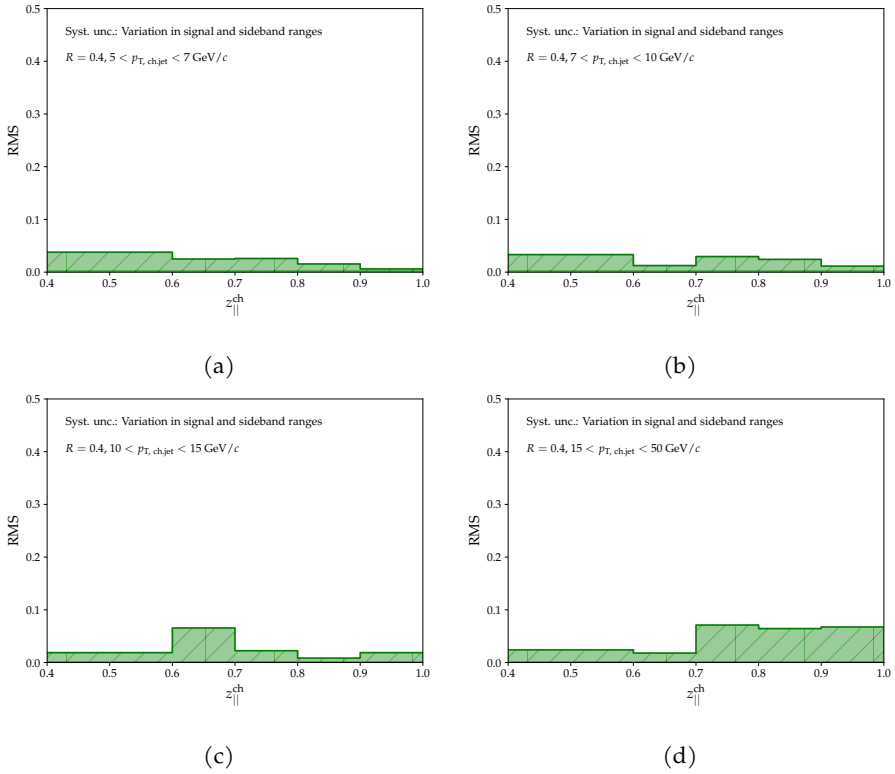

Figure 8.11: Systematic uncertainties due to the variation in ranges of signal and sideband regions during the extraction of $z_{\parallel}^{ch}$ yields of D^0 jets with $R = 0.4$ in pp collisions at $\sqrt{s} = 5.02$ TeV: root-mean-square values of deviations from unity of the ratios of different variations to the default spectrum are taken as systematic-uncertainty values.

(μ_R) and the factorization scale (μ_F) were both equal to the transverse mass of the beauty quark $(\mu_0 = \sqrt{m_b^2 + p_T^2})$. The quark mass was changed twice to 4.5 and 5 GeV/c^2 to give two variations, and the other scales were changed in pairs to give 6 more variations: $(\mu_R/\mu_0,\ \mu_F/\mu_0) = (2,2), (2,1), (1,2), (0.5,1), (1,0.5), (0.5,0.5)$. The maximum upper and lower bounds of the relative yields of these eight variations when compared to the default configuration were taken as systematic uncertainties as shown in Fig. 8.13 for $R = 0.4$. The lowest $z_{\parallel}^{ch}$ region 0.4–0.6 has the highest uncertainties as compared to other $z_{\parallel}^{ch}$ regions, reaching a maximum of about 20%. Said $z_{\parallel}^{ch}$ region also has the highest fraction of non-prompt D^0 jets as seen earlier in Fig. 8.3 where the bands represent the fraction due to the eight variations in POWHEG + PYTHIA 6 simulations mentioned above.

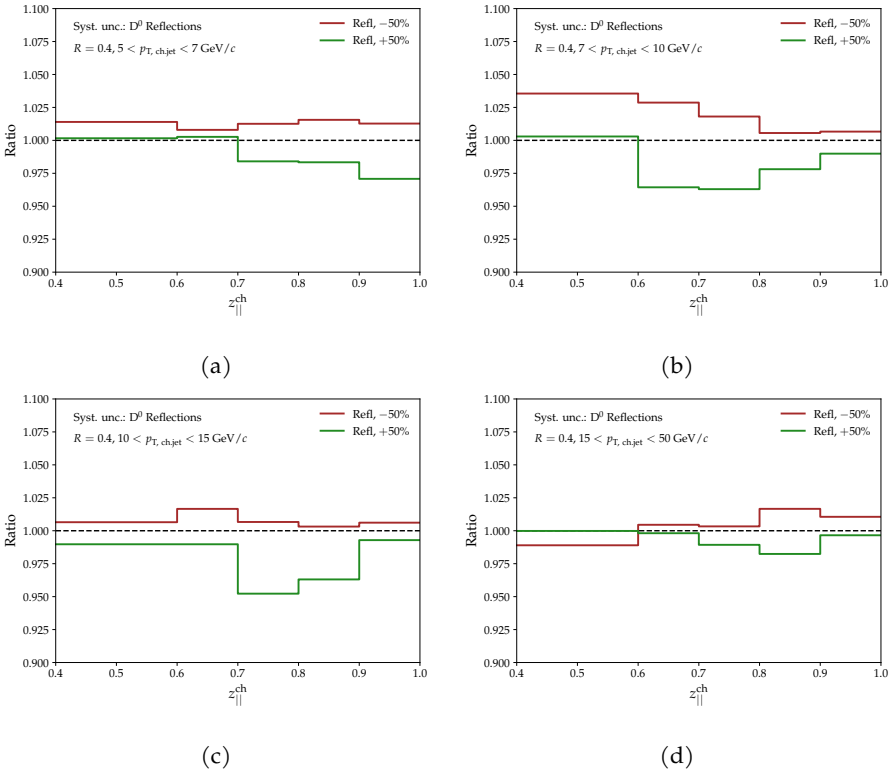

Figure 8.12: Ratios of raw $z_{\parallel}^{\mathrm{ch}}$-yields with 50% higher and lower D^0 reflections are compared to the default $z_{\parallel}^{\mathrm{ch}}$ raw-yield for D^0 jets with $R = 0.4$. The deviations from unity were taken as systematic uncertainties from this source.

8.4.6 *Bayesian unfolding and a closure test*

Bayesian unfolding of $z_{\parallel}^{\mathrm{ch}}$–$p_{\mathrm{T,ch\,jet}}$ distributions was found to be stable by doing several checks similar to those described in Sec. 6.4.5, specifically by providing different *prior* distributions and also by altering the *regularization* used in the unfolding procedure. Systematic uncertainties were finally taken from a MC closure test (see Sec. 6.4.7 where the ability of the unfolding procedure to unfold and close the detector-level D^0-jet distributions on to the true particle-level distributions was tested by conducting multiple (10) *experiments*. An experiment meant dividing the MC sample of prompt D^0 jets randomly into a response matrix and a test sample such that 4/5 of the statistics were used to obtain the response matrix and the remaining 1/5 for the test sample, and then allowing the test sample to go through the steps of reconstruction-efficiency correction and Bayesian unfolding. A comparison was made by taking the ratios of these test yields to the particle-level yields. Systematic uncertainties were determined by

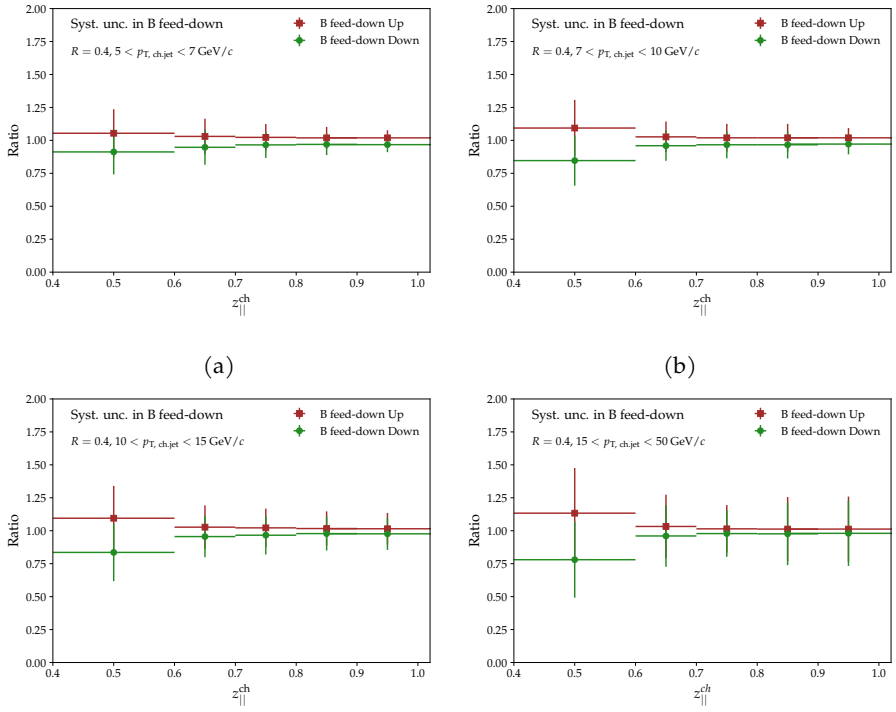

Figure 8.13: Beauty feed-down subtracted $z_{||}^{ch}$ spectra for D^0 jets with $R = 0.4$: the upward and downward variations are shown in red and green (see text for more details). The deviations from unity are taken as systematic uncertainties from this source.

taking the mean values of the deviations of these ratios from unity and are shown in Fig. 8.14 where a maximum of about 11% was reached.

8.4.7 *Tracking efficiency*

Uncertainties in the tracking efficiency of TPC and ITS leads to uncertainties in the jet energy scale (JES) and the D^0-meson reconstruction efficiency. With the exact procedure described in Sec. 6.4.8, systematic uncertainties in JES were found to follow a linear trend in $z_{||}^{ch}$ where the highest value for D^0 jets with $R = 0.4$ was 12% in the $0.4 < z_{||}^{ch} < 0.6$ region for the $10 < p_{T,ch\,jet} < 15$ GeV/c interval.

For the second source of systematic uncertainties involving the reconstruction efficiency of D^0 mesons, uncertainties were treated as correlated and therefore negligible owing to the fact that the $z_{||}^{ch}$ distributions are normalized at the end. The relative systematic uncertainties from all the sources listed above are summarized in the Tab. 8.4. Likewise, the systematic uncertainties due to

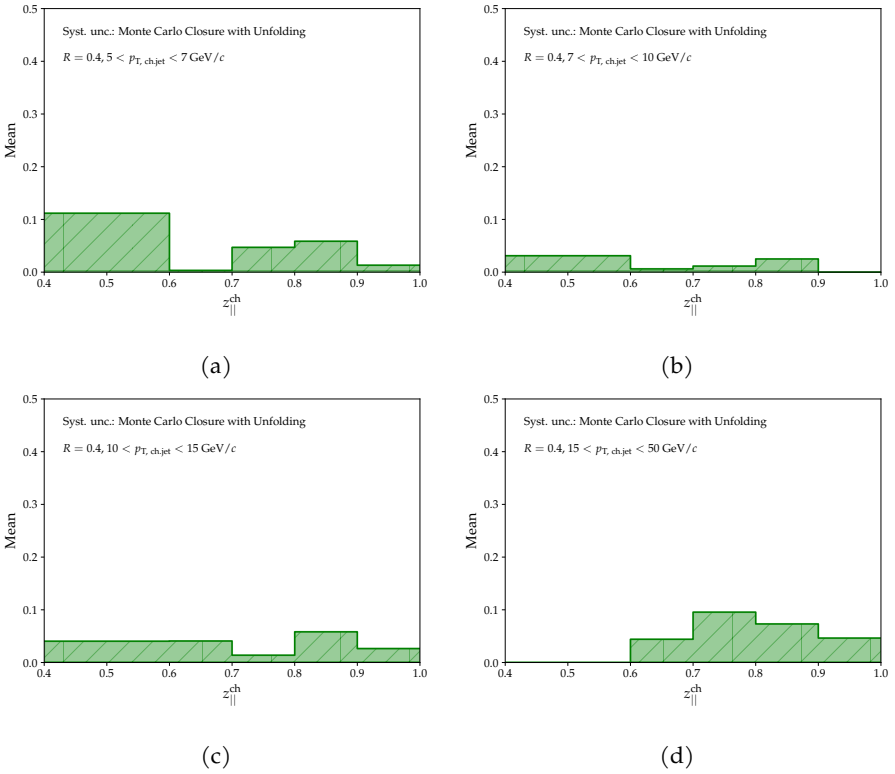

Figure 8.14: Monte Carlo closure test for the Bayesian unfolding of D^0-jet $z_{||}^{ch}$–$p_{T,ch\,jet}$ yields with $R = 0.4$ in pp collisions at $\sqrt{s} = 5.02$ TeV: mean values of deviations of the ratios of yields from various *experiments* to the particle-level yield are shown here as systematic uncertainties from this source.

uncertainties on the branching ratio of D^0 mesons and on the luminosity determination were individually considered as correlated and therefore neglected.

All the relative uncertainties were then added in quadrature to give the final systematic uncertainties for the $z_{||}^{ch}$ distributions per $p_{T,ch\,jet}$ interval.

8.5 PHYSICS RESULTS

The final $z_{||}^{ch}$ distributions were obtained in two small steps. Firstly, for each jet R and in each $p_{T,ch\,jet}$ interval, the $z_{||}^{ch}$-differential yield ($d^2N/dz_{||}^{ch}d\eta_{jet}$) was calculated in a similar manner as was the $p_{T,ch\,jet}$-differential cross section in the previous two chapters. Secondly, the yield was normalized by its total integral in

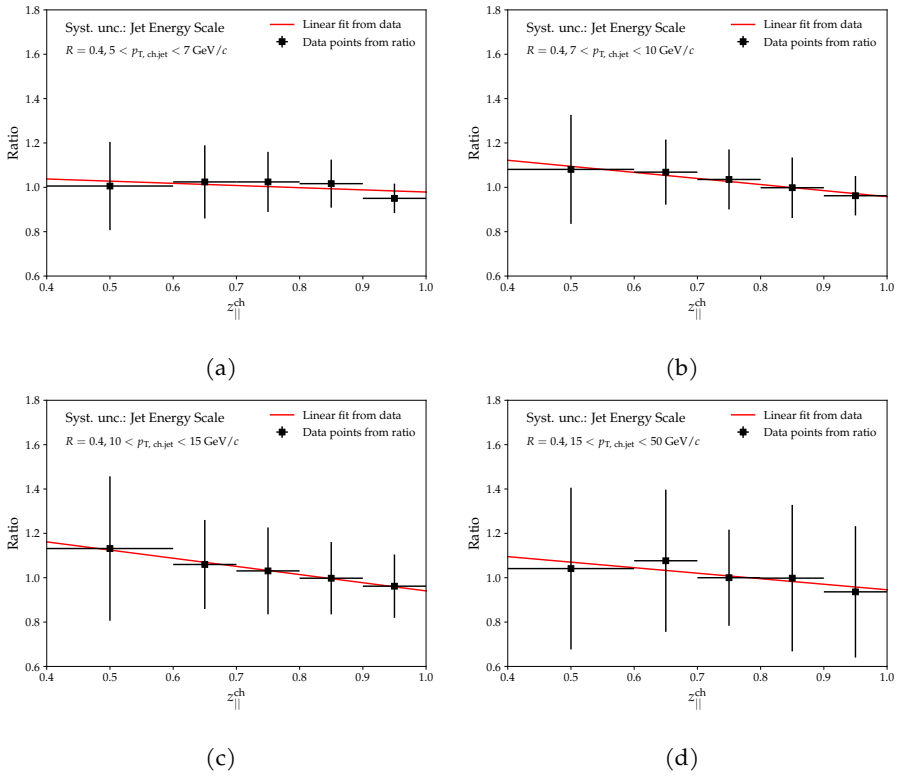

Figure 8.15: Systematic uncertainty from jet-energy-scale effects on unfolding of D^0-jet $z_{\parallel}^{ch}$–$p_{T,ch\,jet}$ yields in four $p_{T,ch\,jet}$ intervals in pp collisions with $R = 0.4$ at $\sqrt{s} = 5.02$ TeV: unfolded results from a modified response having a random selection of 96% of simulated tracks are compared to the results from using default response having all 100% tracks.

the corresponding $p_{T,ch\,jet}$ interval to finally give $z_{\parallel}^{ch}$ probability density distributions expressed as

$$\frac{1}{N}\frac{d^2N}{dz_{\parallel}^{ch}d\eta_{jet}}(z_{\parallel}^{ch}, p_{T,ch\,jet}) = \frac{1}{N(p_{T,ch\,jet})}\frac{N(z_{\parallel}^{ch}, p_{T,ch\,jet})}{\Delta\eta_{jet}\Delta z_{\parallel}^{ch}}. \tag{8.14}$$

Such normalization helps to better compare the shape of $z_{\parallel}^{ch}$ probability density distributions across different $p_{T,ch\,jet}$ intervals as well as different jet radii. Refer to Fig. 8.16, 8.17, 8.18 and 8.19 for D^0 jets with $R = 0.2$, 0.3, 0.4 and 0.6 respectively. Each figure starts with the lowest $p_{T,ch\,jet}$ interval on the top left and ends up with the highest $p_{T,ch\,jet}$ interval on the bottom right. It can be observed in Fig. 8.16 for $R = 0.2$ that the majority of D^0 jets tend to be on the higher side of $z_{\parallel}^{ch}$ in the interval $5 < p_{T,ch\,jet} < 7$ GeV/c. This implies that almost all the momentum of a jet is carried by its constituent D^0 meson in this $p_{T,ch\,jet}$ interval. As one moves towards higher

$p_{\mathrm{T,ch\,jet}}$, it becomes increasingly clear that more and more momentum of the jet gets shared with its constituent particles other than the D^0 meson in it. This trend of fragmentation softening with increase in $p_{\mathrm{T,ch\,jet}}$ is observed for all the jet radii. It is also interesting to notice that as the jet radius is increased to have more particles included, from Fig. 8.16 to Fig. 8.19 for increasing R, the share of the jet momentum carried by the constituent D^0 meson starts further decreasing.

The measurements from data as well as the theoretical predictions the data are compared with are shown in these figures, and both data and theory have the same kinematic restrictions as stated earlier in this chapter in Tab. 8.1.

LO pQCD PYTHIA 8 predictions are shown with both Monash and Mode 2 tunes as well as the NLO pQCD POWHEG calculations coupled with PYTHIA 8 parton shower. All the three theoretical predictions seem to agree with data for the regions $7 < p_{\mathrm{T,ch\,jet}} < 50$ GeV/c within uncertainties. However, data suggest a softer fragmentation as compared to the predictions in the lowest $p_{\mathrm{T,ch\,jet}}$ region, $5 < p_{\mathrm{T,ch\,jet}} < 7$. The differences in the $z_{\parallel}^{\mathrm{ch}}$-distribution shapes predicted by HardQCD Monash and SoftQCD Mode 2 tunes are quite small, although, Monash predicts a slightly harder fragmentation in the low $p_{\mathrm{T,ch\,jet}}$ regions and with smaller R. In comparison, POWHEG calculations for $z_{\parallel}^{\mathrm{ch}}$ shapes show a larger disagreement with data and predict a harder fragmentation in the lowest $p_{\mathrm{T,ch\,jet}}$ region as compared to Monash and Mode 2 tunes. The disagreement also tends to become more significant in the $7 < p_{\mathrm{T,ch\,jet}} < 10$ GeV/c region with increasing R.

8.6 SUMMARY

Fragmentation of charm jets in vacuum was studied in this chapter by looking into the D^0 jets produced in proton–proton collisions at $\sqrt{s} = 5.02$ TeV and studying the fraction of a jet's momentum carried by its constituent D^0 meson along the same direction as the jet-momentum axis. The D^0 jets were reconstructed with different values of jet-resolution parameter, or jet radius, $R = 0.2, 0.3, 0.4$ and 0.6. Results obtained were differential in $z_{\parallel}^{\mathrm{ch}}$ and $p_{\mathrm{T,ch\,jet}}$ and were compared to the Leading Order calculations from the PYTHIA 8 Monte Carlo event generator using two colour reconnection modes, HardQCD Monash and SoftQCD Mode 2. A comparison was also done with the NLO pQCD calculations using the POWHEG method coupled with parton showers from PYTHIA 8. Data suggest a softer fragmentation in the lowest $p_{\mathrm{T,ch\,jet}}$ interval as compared to all three theoretical predictions. This disagreement between data and theory, however, is prominent for NLO POWHEG calculations. The agreement between data and model calculations is generally good for D^0 jets with $p_{\mathrm{T,ch\,jet}} > 7$ GeV/c for all R except for $R = 0.6$ which sees agreement from $p_{\mathrm{T,ch\,jet}} > 10$ GeV/c. These discrepancies at low $p_{\mathrm{T,ch\,jet}}$ aside, a sufficiently good description between data and theory is seen in most of the kinematic range measured. This indicates that the models have the description of charm-quark production, fragmentation and hadronization under control, and therefore, they can be used in establishing a good theoretical baseline for studies in p–Pb and Pb–Pb collisions. The $z_{\parallel}^{\mathrm{ch}}$ distributions reported here can also serve as an

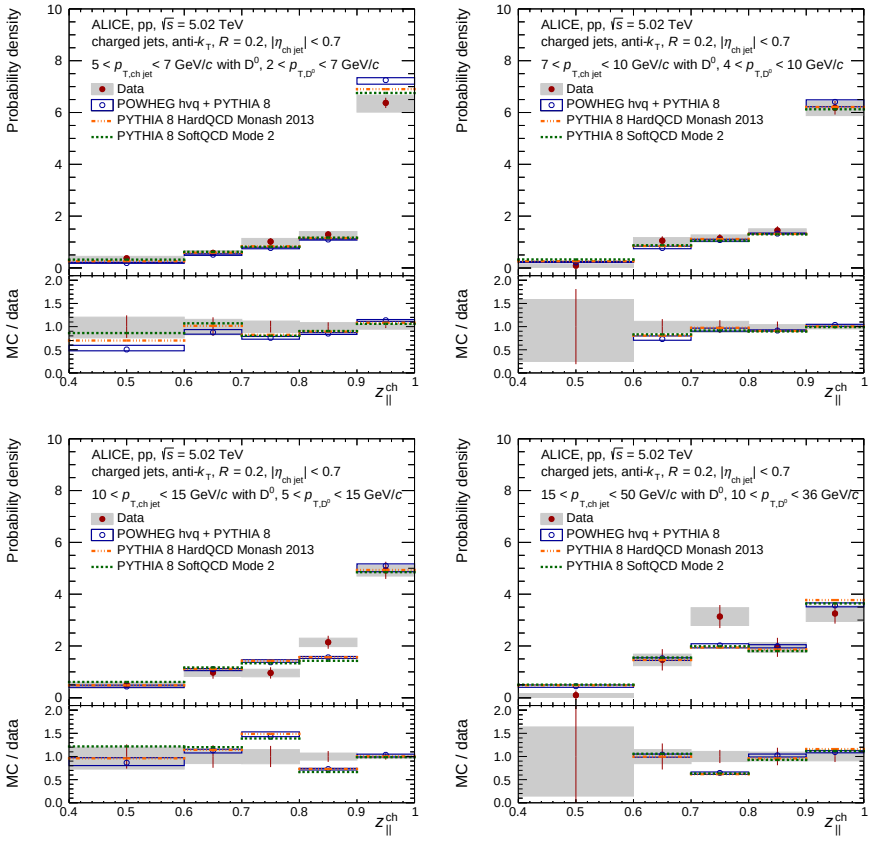

Figure 8.16: The $z_{\parallel}^{\mathrm{ch}}$-differential probability density distributions of D^0 jets with $R = 0.2$ in four $p_{\mathrm{T,ch\,jet}}$ intervals in pp collisions at $\sqrt{s} = 5.02$ TeV. The data are compared to the POWHEG + PYTHIA 8, PYTHIA 8 HardQCD Monash 2013, and PYTHIA 8 SoftQCD Mode 2 theoretical predictions.

important input for the global fit analyses aimed at constraining the gluon fragmentation functions. It should also be noted that the results from pp collisions at $\sqrt{s} = 5.02$ TeV are at the same centre-of-mass energy as p–Pb and Pb–Pb collision data ALICE has collected and thus, can be used as a reference for studies of cold and hot nuclear matter effects on charm-jet fragmentation in p–Pb and Pb–Pb collision systems respectively.

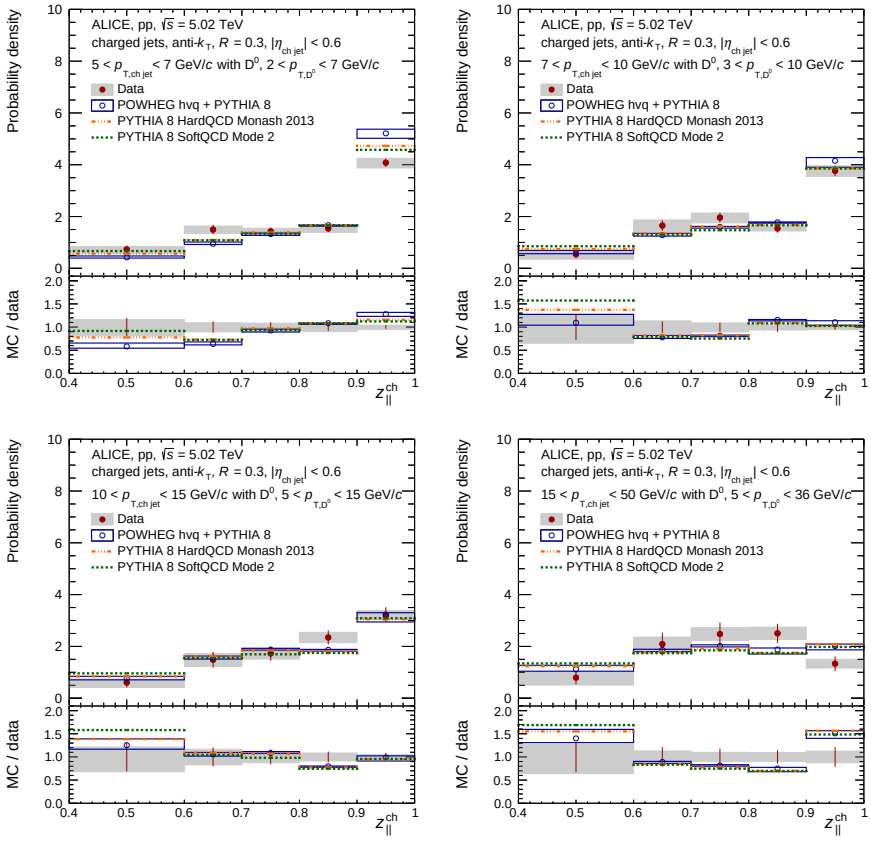

Figure 8.17: The $z_{\parallel}^{ch}$-differential probability density distributions of D^0 jets with $R = 0.3$ in four $p_{T,ch\,jet}$ intervals in pp collisions at $\sqrt{s} = 5.02$ TeV. The data are compared to the POWHEG + PYTHIA 8, PYTHIA 8 HardQCD Monash 2013, and PYTHIA 8 SoftQCD Mode 2 theoretical predictions.

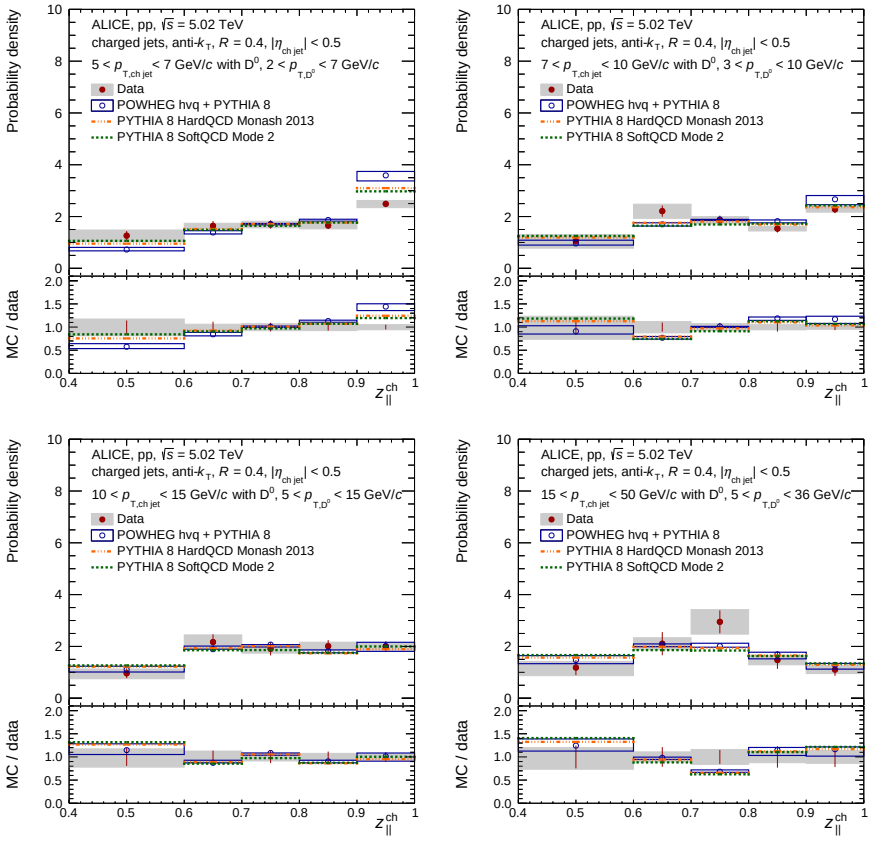

Figure 8.18: The $z_{\parallel}^{\text{ch}}$-differential probability density distributions of D^0 jets with $R = 0.4$ in four $p_{T,\text{ch jet}}$ intervals in pp collisions at $\sqrt{s} = 5.02$ TeV. The data are compared to the POWHEG + PYTHIA 8, PYTHIA 8 HardQCD Monash 2013, and PYTHIA 8 SoftQCD Mode 2 theoretical predictions.

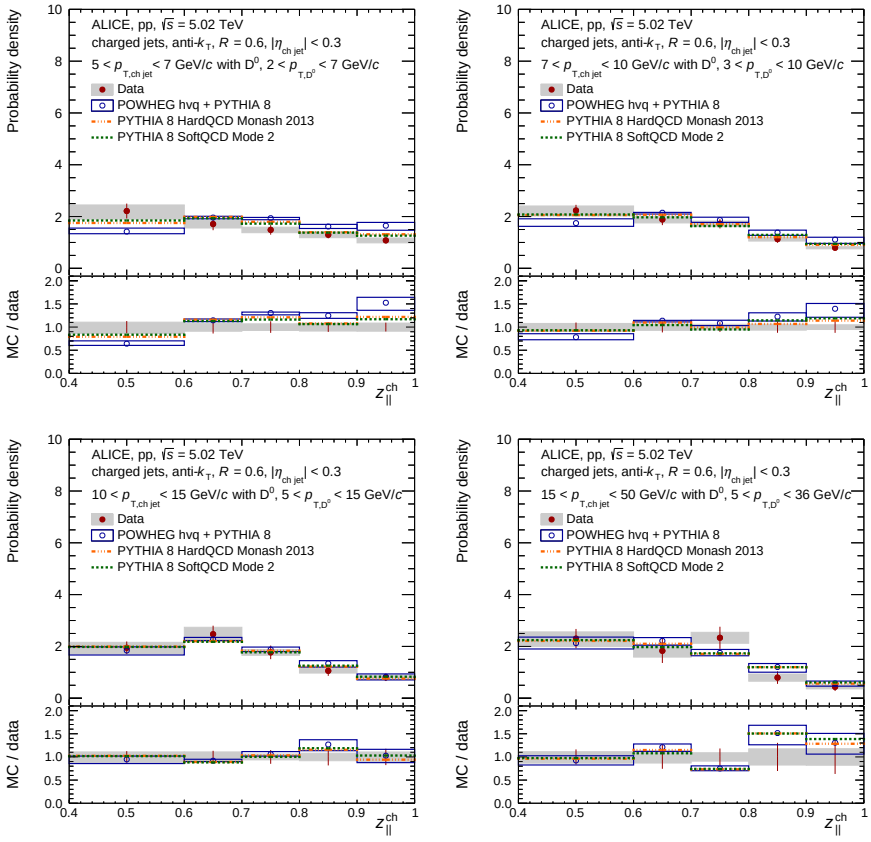

Figure 8.19: The $z_{\parallel}^{ch}$-differential probability density distributions of D^0 jets with $R = 0.6$ in four $p_{T,ch\,jet}$ intervals in pp collisions at $\sqrt{s} = 5.02$ TeV. The data are compared to the POWHEG + PYTHIA 8, PYTHIA 8 HardQCD Monash 2013, and PYTHIA 8 SoftQCD Mode 2 theoretical predictions.

$p_{\mathrm{T,ch\,jet}}$ (GeV/c)	$z_{\parallel}^{\mathrm{ch}}$	Topological selection	Raw-yield extraction	Beauty feed-down	Unfolding	Tracking eff. (JES)	Total
5 – 7	0.4 – 0.6	12	7.9	+9.3, −16.3	11	2	+20.5, −24.4
	0.6 – 0.7	8.8	5.6	+6 , −10.1	9.9	2	+15.7, −17.7
	0.7 – 0.8	5.3	6.5	+3.5, − 5.9	7.7	2	+12.1, −13
	0.8 – 0.9	3.9	3.5	+2.5, − 4.4	6.1	2	+ 8.7, − 9.4
	0.9 – 1.0	1.2	3.2	+2.2, − 3.7	1.3	2	+ 4.7, − 5.6
7 – 10	0.4 – 0.6	41.3	19.4	+33.7, −58	12.3	7	+58.5, −75.2
	0.6 – 0.7	7.7	4.2	+ 4.5, − 8	2.9	5	+11.4, −13.2
	0.7 – 0.8	3.2	6.1	+ 3.2, − 5.8	7.7	3.6	+11.4, −12.4
	0.8 – 0.9	0.6	2.5	+ 2.4, − 4.4	1	2.3	+ 4.3, − 5.7
	0.9 – 1.0	2.1	2.3	+ 2.1, − 3.5	0.9	0.8	+ 4, − 4.9
10 – 15	0.4 – 0.6	10.5	5.2	+12.9, −22.4	6	8.1	+20.1, −27.2
	0.6 – 0.7	5.8	5.2	+ 5.2, − 8.2	9.1	4.8	+13.9, −15.3
	0.7 – 0.8	7.1	7.3	+ 3.5, − 6.2	9.9	2.6	+14.8, −15.7
	0.8 – 0.9	1.4	3.6	+ 1.8, − 3	6.1	0.4	+ 7.4, − 7.8
	0.9 – 1.0	1.1	1.8	+ 1.9, − 2.9	1.7	2.1	+ 3.9, − 4.5
15 – 50	0.4 – 0.6	34.9	25.8	+44.5, −72.2	3.7	14	+63.8, −85.5
	0.6 – 0.7	6.4	7.8	+ 3.8, − 5.7	2.2	10	+14.9, −15.5
	0.7 – 0.8	3.5	6.2	+ 1.3, − 2.1	3.7	7.3	+10.9, −11
	0.8 – 0.9	5.6	6	+ 1.5, − 2.5	1.3	4.6	+ 9.6, − 9.8
	0.9 – 1.0	4.8	7	+ 1.6, − 2.6	2.5	1.6	+ 9.1, − 9.4

Table 8.2: Relative systematic uncertainties in $z_{\parallel}^{\mathrm{ch}}$–$p_{\mathrm{T,ch\,jet}}$ distributions for D^0 jets with R = 0.2.

$p_{T,ch\,jet}$ (GeV/c)	$z_{\parallel}^{ch}$	Topological selection	Raw-yield extraction	Beauty feed-down	Unfolding	Tracking eff. (JES)	Total
5 – 7	0.4 – 0.6	6.8	5.5	+7.4, −12.3	8.3	8	+16.2, −19
	0.6 – 0.7	4	3.6	+3.4, − 5.7	4.5	5.1	+ 9.3, −10.4
	0.7 – 0.8	2.7	4.9	+2.7, − 4.6	4.9	3.2	+ 8.5, − 9.3
	0.8 – 0.9	3.2	3	+2.2, − 3.9	7.7	1.4	+ 9.2, − 9.8
	0.9 – 1.0	1.1	3.4	+2, − 3.4	0.7	0.7	+ 4.2, − 5
7 – 10	0.4 – 0.6	18.6	9.7	+15.3, −26.2	5.1	8.3	+27.7, −35
	0.6 – 0.7	9.8	6.3	+ 3.2, − 5.6	2.3	5.1	+13.3, −14.1
	0.7 – 0.8	1.8	7.9	+ 2.2, − 5.7	1.4	2.9	+ 9 , −10.4
	0.8 – 0.9	1.9	4	+ 2.4, − 4.2	1.2	0.7	+ 5.2, − 6.3
	0.9 – 1.0	1.9	4	+ 2, − 3.2	0.3	1.7	+ 5.2, − 5.7
10 – 15	0.4 – 0.6	4.3	7.2	+16.9, −29.1	2.1	10.1	+21.5, −32
	0.6 – 0.7	4.6	13.5	+ 4.6, − 7.6	1.4	6.3	+16.4, −17.4
	0.7 – 0.8	5.9	9.4	+ 2.7, − 4.5	0.6	3.7	+12 , −12.5
	0.8 – 0.9	1.6	7.7	+ 1.7, − 2.6	2.5	1.1	+ 8.5, − 8.7
	0.9 – 1.0	1.9	3.5	+ 1.8, − 2.8	1.8	1.7	+ 5 , − 5.5
15 – 50	0.4 – 0.6	16.5	5.8	+16.4, −28.9	5.2	12	+27.3, −36.2
	0.6 – 0.7	4.2	10	+ 2.9, − 4.4	1.7	6.2	+12.9, −13.3
	0.7 – 0.8	4.4	3	+ 1.6, − 2.6	8	2.3	+10 , −10.2
	0.8 – 0.9	2.3	3.9	+ 1.1, − 1.9	8.1	1.5	+ 9.5, − 9.6
	0.9 – 1.0	6.9	5.2	+ 1.8, − 2.9	6.8	5.8	+12.6, −12.8

Table 8.3: Relative systematic uncertainties in $z_{\parallel}^{ch}$–$p_{T,ch\,jet}$ distributions for D^0 jets with $R = 0.3$.

$p_{\mathrm{T,ch\,jet}}$ (GeV/c)	$z_{\parallel}^{\mathrm{ch}}$	Topological selection	Raw-yield extraction	Beauty feed-down	Unfolding	Tracking eff. (JES)	Total
5 – 7	0.4 – 0.6	10.6	5.2	+5.4, – 8.9	11.2	2.8	+17.4, −18.8
	0.6 – 0.7	3.8	3.5	+3, – 5.1	0.4	1.3	+ 6.1, – 7.4
	0.7 – 0.8	3.1	4	+2.2, – 3.7	4.7	0.3	+ 7.3, – 7.8
	0.8 – 0.9	2.3	2.8	+1.8, – 3.2	5.9	0.6	+ 7.2, – 7.7
	0.9 – 1.0	2.3	3.9	+1.9, – 3.2	1.3	1.7	+ 5.3, – 5.9
7 – 10	0.4 – 0.6	18.2	5.5	+ 9.3, −15.4	3.2	9.4	+23.4, −26.4
	0.6 – 0.7	9.2	5.3	+ 2.5, – 4.2	0.7	5.3	+12.1, −12.6
	0.7 – 0.8	2.9	5.8	+ 2 , – 3.3	1.2	2.6	+ 7.4, – 7.8
	0.8 – 0.9	2.4	3.6	+ 1.9, – 3.3	2.5	0.1	+ 5.3, – 6
	0.9 – 1.0	1.4	2	+ 1.7, – 2.8	0	3.1	+ 4.3, – 4.8
10 – 15	0.4 – 0.6	5.6	3.8	+9.4, −16.5	4	12.3	+17.4, −22
	0.6 – 0.7	2.8	9.1	+2.7, – 4.6	4.1	6.9	+12.7, −13.2
	0.7 – 0.8	4.1	6.1	+2.1, – 3.3	1.4	3.3	+ 8.4, – 8.8
	0.8 – 0.9	1.4	4.6	+1.5, – 2.3	5.8	0.4	+ 7.7, – 7.9
	0.9 – 1.0	2.5	2.8	+1.5, – 2.3	2.7	4.4	+ 6.5, – 6.8
15 – 50	0.4 – 0.6	12.6	4.3	+13.3, −21.9	0	7	+20.1, −26.6
	0.6 – 0.7	5.4	7	+ 3.2, – 4	4.4	3.3	+10.9, −11.1
	0.7 – 0.8	5.5	11.4	+ 1.3, – 2.1	9.6	0.8	+16 , −16.1
	0.8 – 0.9	6.5	7.2	+ 1.3, – 2.3	7.3	1.6	+12.3, −12.5
	0.9 – 1.0	7.8	9.4	+ 1.3, – 1.9	4.6	4.3	+13.8, −13.9

Table 8.4: Relative systematic uncertainties in $z_{\parallel}^{\mathrm{ch}}$–$p_{\mathrm{T,ch\,jet}}$ distributions for D^0 jets with R = 0.4.

$p_{T,ch\,jet}$ (GeV/c)	$z_{\parallel}^{ch}$	Topological selection	Raw-yield extraction	Beauty feed-down	Unfolding	Tracking eff. (JES)	Total
5 – 7	0.4 – 0.6	5	5.3	+3.5, – 5.6	8.1	7.1	+10.6, –14.1
	0.6 – 0.7	5.8	3.3	+2.5, – 4.3	3.3	2.7	+ 8.3, – 9
	0.7 – 0.8	2.8	2.9	+2 , – 3.3	5.3	0.2	+ 7 , – 7.4
	0.8 – 0.9	4	2.8	+1.6, – 2.8	5.8	3	+ 8.3, – 8.6
	0.9 – 1.0	2.3	4.6	+1.6, – 2.8	2.6	6.2	+ 8.6, – 8.9
7 – 10	0.4 – 0.6	3.8	3	+4.1, –6.7	2.8	3.6	+7.8, –9.4
	0.6 – 0.7	1.1	4.8	+2.2, –3.7	3.2	1.6	+6.5, –7.1
	0.7 – 0.8	3.7	3.7	+1.6, –2.6	2.5	0.3	+6 , –6.4
	0.8 – 0.9	4.1	4.4	+1.6, –2.6	0.3	1	+6.3, –6.6
	0.9 – 1.0	1.4	3.8	+1.4, –2.4	0.4	2.4	+4.9, –5.3
10 – 15	0.4 – 0.6	2.8	4.4	+4.4, –7.7	4.7	6.9	+10.8, –12.5
	0.6 – 0.7	4.6	8.5	+2 , –3.2	4.1	1.7	+10.8, –11.1
	0.7 – 0.8	3.9	3.9	+1.6, –2.3	1.5	1.7	+ 6.2, – 6.4
	0.8 – 0.9	3.2	4.2	+1.5, –2.1	3.1	5.1	+ 8.1, – 8.2
	0.9 – 1.0	3.2	3.1	+1.2, –1.6	3.6	8.9	+10.7, –10.7
15 – 50	0.4 – 0.6	3.1	3.8	+6.6, –9.7	3.6	6.9	+11.3, –13.4
	0.6 – 0.7	9.6	7.7	+2.8, –3.8	1.6	2	+12.9, –13.2
	0.7 – 0.8	5.9	6.6	+1.3, –1.9	0	1.3	+ 9 , – 9.1
	0.8 – 0.9	12.9	10.7	+1.2, –1.9	0.9	4.6	+17.4, –17.5
	0.9 – 1.0	9.8	11.9	+0.9, –1.7	3.6	8.2	+17.8, –17.9

Table 8.5: Relative systematic uncertainties in $z_{\parallel}^{ch}$–$p_{T,ch\,jet}$ distributions for D^0 jets with $R = 0.6$.

9 SUMMARY

We are curious, therefore we know. We are curious about the Universe. We look at the sky and ask questions like "What are these shiny objects at night?" or "Why is it so bright during the day?" We start searching for answers to those questions and end up with new questions like "How did the Universe begin?" and "How was it when it formed?" With the Big Bang theory, we now believe that the Universe was not the same stars and planets as we see today, but it was just a very hot liquid called the quark–gluon plasma (QGP) then. Now, what is this liquid, how does it behave, and what are its properties? When we get to know something, we end up doing something useful with that piece of knowledge. This has always happened throughout the history of human civilization. The ability of controlling fire enabled us to cook food and reduce diseases by killing pathogens in the food. Einstein's theories on gravity enabled us to use satellites to accurately navigate on earth in real-time. When Tim-Berners Lee invented the Web at CERN to manage and share information over the internet, nobody could have imagined the profound impact such an invention would have on the world today. I believe that our collective research on QGP would definitely help us understand strong interactions at the subatomic level. I am curious and am very much looking forward to what technological advancements would unfold from research in particle physics that we are yet to fathom.

The research presented in this thesis is an attempt at furthering our knowledge of strong interactions between quarks and gluons, the fundamental particles that are confined in proton-and-neutron-like hadrons but freely flow in a hot medium, i. e. the QGP.

We began this thesis with Ch. 1 where the motivation and curiosity driving the research presented in this thesis was introduced. Chapter 2 expanded on the motivation by introducing strong interactions and how research in particle physics is done. With Ch. 3 the reader was introduced to the motivation behind studying heavy-flavour jets. Chapter 4 introduced the experimental set-up used to conduct the research in this thesis. The strategy behind the analyses was described in Ch. 5. Charm jets were reconstructed by clustering charged particles using the anti-k_{T} algorithm, and ensuring that the jets contained a D^0 meson among their constituent particles. The anti-k_{T} algorithm ensured that two closest particles with the highest energies were clustered before combining the next particle into the cluster in forming a jet. Before a jet could be reconstructed from the charged particles in an event, the constituent D^0 meson was reconstructed from its daughter particles who were then replaced by the four-momentum of their mother D^0 in the collection of charged particles in the event. Chapters 6, 7, and 8 described the three analyses done for charm jets, all at the centre-of-mass energy $\sqrt{s_{\mathrm{NN}}} = 5.02$ TeV.

Firstly, the production cross section of charm jets in pp collisions was reported in Ch. 6. In the next chapter, the production cross section of charm jets in p–Pb

collisions was reported along with the nuclear modification factor. A measurement of the fragmentation function of charm jets in pp collisions was reported in the following chapter by looking into the jet momentum carried by its constituent charm meson (D^0). Charm jets in pp collisions were clustered with four radii, $R = 0.2, 0.3, 0.4$ and 0.6, while those in p–Pb collisions were clustered with $R = 0.3$.

The results presented in this thesis are compared to various Leading-Order (LO) and Next-to-Leading-Order (NLO) PYTHIA models. The PYTHIA program is used to generate high-energy collision events. Theory and models for various physics aspects are present in PYTHIA, including hard and soft interactions, parton distributions, initial and final-state parton showers, multiparton interactions, fragmentation and decay [86].

The pp results in Ch. 6 and 8 are compared to two LO models and an NLO model. One LO model is the original hadronization model in PYTHIA simulating the following hard processes: $gg \to c\bar{c}$ and $q\bar{q} \to c\bar{c}$. The second LO model uses Colour Reconnection (CR) in hadronization and includes all soft processes. The NLO model uses the POWHEG BOX in order to generate partonic events, i. e. parton splittings and gluon radiation, at NLO.

The LO model with CR and soft processes provides the best description of cross section and fragmentation distribution of charm jets in pp collisions as compared to the LO model with hard processes only. Data measurements show agreements to POWHEG + PYTHIA 8 predictions within experimental and theoretical uncertainties. Charm production is modelled sufficiently well in the current mechanisms, and these results are publicly available in Ref. [95].

The parton distribution function for the proton was obtained from the LHAPDF 6 interpolator with the PDF set CT10nlo [105]. For simulating p–Pb collisions, the nuclear parton distribution function inside a lead ion was taken from the EPS09nlo [106]. Like the cross section of charm jets in pp collisions, the cross section in p–Pb collisions for charm jets with $R = 0.3$ presented in Ch. 7 also agrees to POWHEG + PYTHIA 6 NLO theoretical predictions within the data and theoretical uncertainties. Also, the nuclear modification factor R_{pPb} was found to conform to unity within statistical and systematic uncertainties. There seems to be an absence of large modifications in the initial parton distributions along with an absence of final-state effects on the production of charm jets with $p_{\mathrm{T}} > 5$ GeV/c.

10 OUTLOOK

Excitingly, there are numerous directions that a potential future research can take from here. One potential avenue in p–Pb collisions is to investigate possible nuclear modifications in the fragmentation function of charm jets. ALICE is already measuring the production and fragmentation of charm jets tagged with D^0 mesons in Pb–Pb collisions. A first measurement of the R_{AA} in Pb–Pb collisions was done by analysing the 2015 data for Pb–Pb collisions, and using the p–Pb measurement presented in this thesis (done with the 2016 p–Pb data) as a reference (see Fig. 7.20). Now the 2018 Pb–Pb collision data with higher statistics are being analysed. The pp results in Ch. 6 and 8 done using the 2017 pp data should provide the necessary reference measurements. Such analyses of the production and fragmentation of charm jets could be crucial and could shed light on the effects of cold- and hot-nuclear matter on heavy-flavour jets. In particular, we can better understand ways in which particles move and energy transfers through the medium (transport properties). The measurement of the momentum and angular distributions of the heavy-flavour jets can provide information about the medium transport properties, such as its viscosity and thermal conductivity. The amount of energy loss depends on the medium properties, such as its density and temperature. We can improve our modelling of the medium-induced parton-energy loss by measuring the energy loss of the heavy-flavour jets.

Charm jets here are identified by tagging them with fully reconstructed D^0 mesons, which was driven by several factors like their large branching ratio for hadronic decays. This allows for a high statistical significance of the reconstructed charm jets, and their relatively clean signal compared to other charm hadrons. But future collision runs at a higher centre-of-mass energy can pave the way for reconstructing charged jets with other charm hadrons like $D^{\pm}$, $D_s^{\pm}$, $D^{*\pm}$ and $\Lambda_c^{\pm}$. This could certainly provide additional information on the production and fragmentation of charm quarks.

Studying jet substructure and groomed jets can help learn about the properties of charm jets better. Jet substructure techniques can help identify the sub-jets within a larger jet and can be used to distinguish between quark-initiated and gluon-initiated jets. Groomed jets, such as trimmed or pruned jets, can help reduce the effects of pile-up and underlying event, leading to better jet energy resolution and more precise measurements of jet properties. In the context of heavy-flavour jets, studying substructure and grooming techniques can help distinguish between different heavy-flavour hadrons within the jet, and can provide additional information on the fragmentation patterns of these hadrons. It can also help in identifying and measuring properties of heavy-flavour jets produced in more complex environments such as heavy-ion collisions.

What can also help is studying full jets instead of just charged jets to get a more complete picture of the properties of the charm quark and its fragmentation.

Charged jets contain only charged particles, while full jets include all particles, including neutral particles such as photons and neutral hadrons. The inclusion of neutral particles in the jet reconstruction can provide new information on the energy and momentum distribution within the jet, which could help better understand the properties of the charm quark.

I am sure there are many other exciting directions one can take from the results presented in this thesis. With new upgrades to the detectors at CERN, and pushing the boundaries of collision energies, the future looks very promising and is certainly poised to get even more exciting.

BIBLIOGRAPHY

[1] Edward V. Shuryak. "Quantum Chromodynamics and the Theory of Superdense Matter." In: *Phys. Rept.* 61 (1980), pp. 71–158. DOI: 10.1016/0370-1573(80)90105-2.

[2] Johann Rafelski. "Connecting QGP-Heavy Ion Physics to the Early Universe." In: *Nucl. Phys. B Proc. Suppl.* 243-244 (2013). Ed. by Roberto Battiston and Sergio Bertolucci, pp. 155–162. DOI: 10.1016/j.nuclphysbps.2013.09.017. arXiv: 1306.2471 [astro-ph.CO].

[3] Eemeli Annala, Tyler Gorda, Aleksi Kurkela, Joonas Nättilä, and Aleksi Vuorinen. "Evidence for quark-matter cores in massive neutron stars." In: *Nature Phys.* 16.9 (2020), pp. 907–910. DOI: 10.1038/s41567-020-0914-9. arXiv: 1903.09121 [astro-ph.HE].

[4] Ulrich W. Heinz and Maurice Jacob. "Evidence for a new state of matter: An Assessment of the results from the CERN lead beam program." In: (Jan. 2000). arXiv: nucl-th/0002042.

[5] Miklos Gyulassy and Larry McLerran. "New forms of QCD matter discovered at RHIC." In: *Nucl. Phys. A* 750 (2005). Ed. by D. Rischke and G. Levin, pp. 30–63. DOI: 10.1016/j.nuclphysa.2004.10.034. arXiv: nucl-th/0405013.

[6] Anton Andronic, Peter Braun-Munzinger, Krzysztof Redlich, and Johanna Stachel. "Decoding the phase structure of QCD via particle production at high energy." In: *Nature* 561.7723 (2018), pp. 321–330. DOI: 10.1038/s41586-018-0491-6. arXiv: 1710.09425 [nucl-th].

[7] K. Adcox et al. "Suppression of hadrons with large transverse momentum in central Au+Au collisions at $\sqrt{s_{NN}} = 130$-GeV." In: *Phys. Rev. Lett.* 88 (2002), p. 022301. DOI: 10.1103/PhysRevLett.88.022301. arXiv: nucl-ex/0109003.

[8] C. Adler et al. "Disappearance of back-to-back high p_T hadron correlations in central Au+Au collisions at $\sqrt{s_{NN}} = 200$-GeV." In: *Phys. Rev. Lett.* 90 (2003), p. 082302. DOI: 10.1103/PhysRevLett.90.082302. arXiv: nucl-ex/0210033.

[9] P. A. Zyla et al. "Review of Particle Physics." In: *PTEP* 2020.8 (2020), p. 083C01. DOI: 10.1093/ptep/ptaa104.

[10] David Griffiths. *Introduction to elementary particles*. 2008. ISBN: 978-3-527-40601-2.

[11] Valerie Buxbaum. "Cross Section and Luminosity Physics Cheat Sheet." In: (2022). URL: https://cds.cern.ch/record/2800578.

[12] Richard Keith Ellis, William James Stirling, and Bryan R Webber. *QCD and collider physics*. Cambridge monographs on particle physics, nuclear physics, and cosmology. Photography by S. Vascotto. Cambridge: Cambridge University Press, 2003, p. 24. DOI: 10.1017/CBO9780511628788. URL: https://cds.cern.ch/record/318585.

[13] Michael E. Peskin and Daniel V. Schroeder. *An Introduction to quantum field theory*. Reading, USA: Addison-Wesley, 1995. ISBN: 978-0-201-50397-5.

[14] Michiel Botje. *PP-II QCD Lectures 2013*. Lectures at Utrecht University, Utrecht. 2013. URL: https://www.nikhef.nl/~h24/qcdcourse/.

[15] R. L. Workman. "Review of Particle Physics." In: *PTEP* 2022 (2022), p. 083C01. DOI: 10.1093/ptep/ptac097.

[16] Markus Cristinziani and Martijn Mulders. "Top-quark physics at the Large Hadron Collider." In: *J. Phys. G* 44.6 (2017), p. 063001. DOI: 10.1088/1361-6471/44/6/063001. arXiv: 1606.00327 [hep-ex].

[17] Ahmed Ali, E. Pietarinen, G. Kramer, and J. Willrodt. "A QCD Analysis of the High-Energy e+ e- Data from PETRA." In: *Phys. Lett. B* 93 (1980), pp. 155–160. DOI: 10.1016/0370-2693(80)90116-1.

[18] Christian Bierlich et al. "A comprehensive guide to the physics and usage of PYTHIA 8.3." In: (Mar. 2022). arXiv: 2203.11601 [hep-ph].

[19] Johannes Bellm et al. "Herwig 7.0/Herwig++ 3.0 release note." In: *Eur. Phys. J. C* 76.4 (2016), p. 196. DOI: 10.1140/epjc/s10052-016-4018-8. arXiv: 1512.01178 [hep-ph].

[20] Andy Buckley et al. "General-purpose event generators for LHC physics." In: *Phys. Rept.* 504 (2011), pp. 145–233. DOI: 10.1016/j.physrep.2011.03.005. arXiv: 1101.2599 [hep-ph].

[21] Jesper R. Christiansen and Peter Z. Skands. "String Formation Beyond Leading Colour." In: *JHEP* 08 (2015), p. 003. DOI: 10.1007/JHEP08(2015)003. arXiv: 1505.01681 [hep-ph].

[22] T. Sjostrand and Peter Z. Skands. "Multiple interactions and the structure of beam remnants." In: *JHEP* 03 (2004), p. 053. DOI: 10.1088/1126-6708/2004/03/053. arXiv: hep-ph/0402078.

[23] Torbjorn Sjostrand and Maria van Zijl. "A Multiple Interaction Model for the Event Structure in Hadron Collisions." In: *Phys. Rev. D* 36 (1987), p. 2019. DOI: 10.1103/PhysRevD.36.2019.

[24] Simone Alioli, Paolo Nason, Carlo Oleari, and Emanuele Re. "A general framework for implementing NLO calculations in shower Monte Carlo programs: the POWHEG BOX." In: *JHEP* 06 (2010), p. 043. DOI: 10.1007/JHEP06(2010)043. arXiv: 1002.2581 [hep-ph].

[25] Liliana Apolinário, Yen-Jie Lee, and Michael Winn. "Heavy quarks and jets as probes of the QGP." In: (Mar. 2022). arXiv: 2203.16352 [hep-ph].

[26] Johann Rafelski and R. Hagedorn. "From Hadron Gas to Quark Matter. 2." In: *International Symposium on Statistical Mechanics of Quarks and Hadrons*. Oct. 1980.

[27] E. Andersen et al. "Strangeness enhancement at mid-rapidity in Pb Pb collisions at 158-A-GeV/c." In: *Phys. Lett. B* 449 (1999), pp. 401–406. DOI: 10.1016/S0370-2693(99)00140-9.

[28] F. Antinori et al. "Enhancement of hyperon production at central rapidity in 158-A-GeV/c Pb-Pb collisions." In: *J. Phys. G* 32 (2006), pp. 427–442. DOI: 10.1088/0954-3899/32/4/003. arXiv: nucl-ex/0601021.

[29] Anthony R. Timmins. "Overview of Strangeness Production at the STAR Experiment." In: *J. Phys. G* 36 (2009). Ed. by Feng Liu, Zhigang Xiao, and Pengfei Zhuang, p. 064006. DOI: 10.1088/0954-3899/36/6/064006. arXiv: 0812.4080 [nucl-ex].

[30] S. Acharya et al. "Direct observation of the dead-cone effect in quantum chromodynamics." In: *Nature* 605.7910 (2022). [Erratum: Nature 607, E22 (2022)], pp. 440–446. DOI: 10.1038/s41586-022-04572-w. arXiv: 2106.05713 [nucl-ex].

[31] Daniel Dominguez. "Illustration of the dead-cone effect." In: (2022). General Photo. URL: https://cds.cern.ch/record/2809214.

[32] Michelangelo L. Mangano. "Two lectures on heavy quark production in hadronic collisions." In: *Proc. Int. Sch. Phys. Fermi* 137 (1998). Ed. by I. I. Y. Bigi and L. Moroni, pp. 95–137. DOI: 10.3254/978-1-61499-222-6-95. arXiv: hep-ph/9711337.

[33] A. Adare et al. "Nuclear-Modification Factor for Open-Heavy-Flavor Production at Forward Rapidity in Cu+Cu Collisions at $\sqrt{s_{NN}} = 200$ GeV." In: *Phys. Rev. C* 86 (2012), p. 024909. DOI: 10.1103/PhysRevC.86.024909. arXiv: 1204.0754 [nucl-ex].

[34] Sa Wang, Wei Dai, Enke Wang, Xin-Nian Wang, and Ben-Wei Zhang. "Heavy-Flavour Jets in High-Energy Nuclear Collisions." In: *Symmetry* 15 (2023), p. 727. DOI: 10.3390/sym15030727. arXiv: 2303.14660 [nucl-th].

[35] Sarah Charley. "What is luminosity?" General Photo. 2021. URL: https://www.symmetrymagazine.org/article/what-is-luminosity.

[36] Nestor Armesto. "Nuclear shadowing." In: *J. Phys. G* 32 (2006), R367–R394. DOI: 10.1088/0954-3899/32/11/R01. arXiv: hep-ph/0604108.

[37] Michele Arneodo. "Nuclear effects in structure functions." In: *Phys. Rept.* 240 (1994), pp. 301–393. DOI: 10.1016/0370-1573(94)90048-5.

[38] A. Andronic et al. "Heavy-flavour and quarkonium production in the LHC era: from proton–proton to heavy-ion collisions." In: *Eur. Phys. J. C* 76.3 (2016), p. 107. DOI: 10.1140/epjc/s10052-015-3819-5. arXiv: 1506.03981 [nucl-ex].

[39] Alberto Accardi. "Cronin effect in proton nucleus collisions: A Survey of theoretical models." In: (Dec. 2002). arXiv: hep-ph/0212148.

[40] Ivan Vitev. "Non-Abelian energy loss in cold nuclear matter." In: *Phys. Rev. C* 75 (2007), p. 064906. DOI: 10.1103/PhysRevC.75.064906. arXiv: hep-ph/0703002.

[41] L. Adamczyk et al. "Measurements of D^0 and D^* Production in $p + p$ Collisions at $\sqrt{s} = 200$ GeV." In: *Phys. Rev. D* 86 (2012), p. 072013. DOI: 10.1103/PhysRevD.86.072013. arXiv: 1204.4244 [nucl-ex].

[42] D. Acosta et al. "Measurement of prompt charm meson production cross sections in $p\bar{p}$ collisions at $\sqrt{s} = 1.96$ TeV." In: *Phys. Rev. Lett.* 91 (2003), p. 241804. DOI: 10.1103/PhysRevLett.91.241804. arXiv: hep-ex/0307080.

[43] B. Abelev et al. "Measurement of charm production at central rapidity in proton-proton collisions at $\sqrt{s} = 7$ TeV." In: *JHEP* 01 (2012), p. 128. DOI: 10.1007/JHEP01(2012)128. arXiv: 1111.1553 [hep-ex].

[44] Betty Abelev et al. "D_s^+ meson production at central rapidity in proton–proton collisions at $\sqrt{s} = 7$ TeV." In: *Phys. Lett. B* 718 (2012), pp. 279–294. DOI: 10.1016/j.physletb.2012.10.049. arXiv: 1208.1948 [hep-ex].

[45] R Aaij et al. "Prompt charm production in pp collisions at sqrt(s)=7 TeV." In: *Nucl. Phys. B* 871 (2013), pp. 1–20. DOI: 10.1016/j.nuclphysb.2013.02.010. arXiv: 1302.2864 [hep-ex].

[46] Georges Aad et al. "Measurement of $D^{*\pm}$, $D^{\pm}$ and $D_s^{\pm}$ meson production cross sections in pp collisions at $\sqrt{s} = 7$ TeV with the ATLAS detector." In: *Nucl. Phys. B* 907 (2016), pp. 717–763. DOI: 10.1016/j.nuclphysb.2016.04.032. arXiv: 1512.02913 [hep-ex].

[47] Jaroslav Adam et al. "Transverse momentum dependence of D-meson production in Pb-Pb collisions at $\sqrt{s_{NN}} = 2.76$ TeV." In: *JHEP* 03 (2016), p. 081. DOI: 10.1007/JHEP03(2016)081. arXiv: 1509.06888 [nucl-ex].

[48] Roel Aaij et al. "Measurements of prompt charm production cross-sections in pp collisions at $\sqrt{s} = 13$ TeV." In: *JHEP* 03 (2016). [Erratum: JHEP 09, 013 (2016), Erratum: JHEP 05, 074 (2017)], p. 159. DOI: 10.1007/JHEP03(2016)159. arXiv: 1510.01707 [hep-ex].

[49] Jaroslav Adam et al. "D-meson production in p-Pb collisions at $\sqrt{s_{NN}}$ =5.02 TeV and in pp collisions at $\sqrt{s}$ =7 TeV." In: *Phys. Rev. C* 94.5 (2016), p. 054908. DOI: 10.1103/PhysRevC.94.054908. arXiv: 1605.07569 [nucl-ex].

[50] J. Adam et al. "Measurement of D-meson production versus multiplicity in p-Pb collisions at $\sqrt{s_{NN}} = 5.02$ TeV." In: *JHEP* 08 (2016), p. 078. DOI: 10.1007/JHEP08(2016)078. arXiv: 1602.07240 [nucl-ex].

[51] Roel Aaij et al. "Measurements of prompt charm production cross-sections in pp collisions at $\sqrt{s} = 5$ TeV." In: *JHEP* 06 (2017), p. 147. DOI: 10.1007/JHEP06(2017)147. arXiv: 1610.02230 [hep-ex].

[52] Shreyasi Acharya et al. "Measurement of D-meson production at mid-rapidity in pp collisions at $\sqrt{s} = 7$ TeV." In: *Eur. Phys. J. C* 77.8 (2017), p. 550. DOI: 10.1140/epjc/s10052-017-5090-4. arXiv: 1702.00766 [hep-ex].

[53] David d'Enterria, Kari J. Eskola, Ilkka Helenius, and Hannu Paukkunen. "Confronting current NLO parton fragmentation functions with inclusive charged-particle spectra at hadron colliders." In: *Nucl. Phys. B* 883 (2014), pp. 615–628. DOI: 10.1016/j.nuclphysb.2014.04.006. arXiv: 1311.1415 [hep-ph].

[54] B. I. Abelev et al. "Measurement of D* Mesons in Jets from p+p Collisions at s**(1/2) = 200-GeV." In: *Phys. Rev. D* 79 (2009), p. 112006. DOI: 10.1103/PhysRevD.79.112006. arXiv: 0901.0740 [hep-ex].

[55] Vardan Khachatryan et al. "Measurement of $B\bar{B}$ Angular Correlations based on Secondary Vertex Reconstruction at $\sqrt{s} = 7$ TeV." In: *JHEP* 03 (2011), p. 136. DOI: 10.1007/JHEP03(2011)136. arXiv: 1102.3194 [hep-ex].

[56] Daniele P. Anderle, Tom Kaufmann, Marco Stratmann, Felix Ringer, and Ivan Vitev. "Using hadron-in-jet data in a global analysis of D^* fragmentation functions." In: *Phys. Rev. D* 96.3 (2017), p. 034028. DOI: 10.1103/PhysRevD.96.034028. arXiv: 1706.09857 [hep-ph].

[57] Shreyasi Acharya et al. "Measurement of the production of charm jets tagged with D^0 mesons in pp collisions at $\sqrt{s} = 7$ TeV." In: *JHEP* 08 (2019), p. 133. DOI: 10.1007/JHEP08(2019)133. arXiv: 1905.02510 [nucl-ex].

[58] Albert M Sirunyan et al. "Measurements of the charm jet cross section and nuclear modification factor in pPb collisions at $\sqrt{s_{NN}} = 5.02$ TeV." In: *Phys. Lett. B* 772 (2017), pp. 306–329. DOI: 10.1016/j.physletb.2017.06.053. arXiv: 1612.08972 [nucl-ex].

[59] *The Large Hadron Collider in the Geneva area*. © CERN, GeoEye, by courtesy of e-GEOS, processed by UNOSAT. URL: https://visit.cern/content/lhc_puzzle.

[60] "LHC Machine." In: *JINST* 3 (2008). Ed. by Lyndon Evans and Philip Bryant, S08001. DOI: 10.1088/1748-0221/3/08/S08001.

[61] G. Aad et al. "The ATLAS Experiment at the CERN Large Hadron Collider." In: *JINST* 3 (2008), S08003. DOI: 10.1088/1748-0221/3/08/S08003.

[62] S. Chatrchyan et al. "The CMS Experiment at the CERN LHC." In: *JINST* 3 (2008), S08004. DOI: 10.1088/1748-0221/3/08/S08004.

[63] K. Aamodt et al. "The ALICE experiment at the CERN LHC." In: *JINST* 3 (2008), S08002. DOI: 10.1088/1748-0221/3/08/S08002.

[64] A. Augusto Alves Jr. et al. "The LHCb Detector at the LHC." In: *JINST* 3 (2008), S08005. DOI: 10.1088/1748-0221/3/08/S08005.

[65] Arturo Tauro. "ALICE Schematics." General Photo. 2017. URL: https://cds.cern.ch/record/2263642.

[66] dukwon (https://physics.stackexchange.com/users/73214/dukwon). *What is charged particle multiplicity density?* Physics Stack Exchange. URL:https://physics.stackexchange.com/q/277822 (version: 2016-09-02). eprint: https://physics.stackexchange.com/q/277822. URL: https://physics.stackexchange.com/q/277822.

[67] J. Alme et al. "The ALICE TPC, a large 3-dimensional tracking device with fast readout for ultra-high multiplicity events." In: *Nucl. Instrum. Meth. A* 622 (2010), pp. 316–367. DOI: 10.1016/j.nima.2010.04.042. arXiv: 1001.1950 [physics.ins-det].

[68] K Aamodt et al. "Alignment of the ALICE Inner Tracking System with cosmic-ray tracks." In: *JINST* 5 (2010), P03003. DOI: 10.1088/1748-0221/5/03/P03003. arXiv: 1001.0502 [physics.ins-det].

[69] A. Akindinov et al. "Performance of the ALICE Time-Of-Flight detector at the LHC." In: *Eur. Phys. J. Plus* 128 (2013), p. 44. DOI: 10.1140/epjp/i2013-13044-x.

[70] Antonin Maire and David Dobrigkeit Chinellato. "ALICE sub-detectors highlighted (LHC runs 1+2 // runs 3+4)." General Photo. 2017. URL: https://cds.cern.ch/record/2302924.

[71] K. Aamodt et al. "Production of pions, kaons and protons in *pp* collisions at $\sqrt{s} = 900$ GeV with ALICE at the LHC." In: *Eur. Phys. J. C* 71 (2011), p. 1655. DOI: 10.1140/epjc/s10052-011-1655-9. arXiv: 1101.4110 [hep-ex].

[72] E. Abbas et al. "Performance of the ALICE VZERO system." In: *JINST* 8 (2013), P10016. DOI: 10.1088/1748-0221/8/10/P10016. arXiv: 1306.3130 [nucl-ex].

[73] ALICE. *More details on the ALICE Data Analysis*. URL: https://alice.cern/node/5527.

[74] ALICE. *AliRoot (ALICE Software)*. URL: https://github.com/alisw/AliRoot.

[75] I. Antcheva et al. "ROOT: A C++ framework for petabyte data storage, statistical analysis and visualization." In: *Comput. Phys. Commun.* 180 (2009), pp. 2499–2512. DOI: 10.1016/j.cpc.2009.08.005. arXiv: 1508.07749 [physics.data-an].

[76] P. A. Zyla et al. "Review of Particle Physics." In: *PTEP* 2020.8 (2020), p. 083C01. DOI: 10.1093/ptep/ptaa104.

[77] ALICE. *AliRoot (ALICE Software), Cosine of decay angle (theta*) in the rest frame of the mother particle for 2-prong decays.* URL: https://github.com/alisw/AliRoot/blob/6827e56/STEER/AOD/AliAODRecoDecay.cxx#L262.

[78] Cristian George Ivan. "Open charm analysis with the ALICE detector in pp collisions at LHC." PhD thesis. Utrecht U., 2009. arXiv: 1005.4954 [hep-ex].

[79] Matteo Cacciari, Gavin P. Salam, and Gregory Soyez. "FastJet User Manual." In: *Eur. Phys. J. C* 72 (2012), p. 1896. DOI: 10.1140/epjc/s10052-012-1896-2. arXiv: 1111.6097 [hep-ph].

[80] T. Adye. *RooUnfold, a framework for unfolding within the ROOT environment*. Jan. 2021. URL: https://gitlab.cern.ch/RooUnfold/RooUnfold.

[81] Gavin P. Salam. "Towards Jetography." In: *Eur. Phys. J. C* 67 (2010), pp. 637–686. DOI: 10.1140/epjc/s10052-010-1314-6. arXiv: 0906.1833 [hep-ph].

[82] Matteo Cacciari and Gavin P. Salam. "Pileup subtraction using jet areas." In: *Phys. Lett. B* 659 (2008), pp. 119–126. DOI: 10.1016/j.physletb.2007.09.077. arXiv: 0707.1378 [hep-ph].

[83] Matteo Cacciari, Juan Rojo, Gavin P. Salam, and Gregory Soyez. "Jet Reconstruction in Heavy Ion Collisions." In: *Eur. Phys. J. C* 71 (2011), p. 1539. DOI: 10.1140/epjc/s10052-011-1539-z. arXiv: 1010.1759 [hep-ph].

[84] Betty Abelev et al. "Measurement of Event Background Fluctuations for Charged Particle Jet Reconstruction in Pb-Pb collisions at $\sqrt{s_{NN}} = 2.76$ TeV." In: *JHEP* 03 (2012), p. 053. DOI: 10.1007/JHEP03(2012)053. arXiv: 1201.2423 [hep-ex].

[85] Glen Cowan. "A Survey of Unfolding Methods for Particle Physics." In: *Proc. Advanced Statistical Techniques in Particle Physics* (2002). URL: http://www.ippp.dur.ac.uk/Workshops/02/statistics/proceedings/cowan.pdf.

[86] Torbjörn Sjöstrand, Stefan Ask, Jesper R. Christiansen, Richard Corke, Nishita Desai, Philip Ilten, Stephen Mrenna, Stefan Prestel, Christine O. Rasmussen, and Peter Z. Skands. "An introduction to PYTHIA 8.2." In: *Comput. Phys. Commun.* 191 (2015), pp. 159–177. DOI: 10.1016/j.cpc.2015.01.024. arXiv: 1410.3012 [hep-ph].

[87] R Brun, R Hagelberg, M Hansroul, and J C Lassalle. *Simulation program for particle physics experiments, GEANT: user guide and reference manual*. Geneva: CERN, 1978. URL: https://cds.cern.ch/record/118715.

[88] Alexander G. Ramm. "Linear ill-posed problems and dynamical systems." In: *arXiv e-prints*, math-ph/0008011 (Aug. 2000), math–ph/0008011. arXiv: math-ph/0008011 [math-ph].

[89] Suresh B. Srinivasamurthy. "Methods of Solving Ill-Posed Problems." In: *arXiv e-prints*, arXiv:1205.5323 (May 2012), arXiv:1205.5323. arXiv: 1205.5323 [math.NA].

[90] G. D'Agostini. "A multidimensional unfolding method based on Bayes' theorem." In: *Nuclear Instruments and Methods in Physics Research Section A: Accelerators, Spectrometers, Detectors and Associated Equipment* 362.2 (1995), pp. 487–498. ISSN: 0168-9002. DOI: https://doi.org/10.1016/0168-9002(95)00274-X. URL: https://www.sciencedirect.com/science/article/pii/016890029500274X.

[91] G. D'Agostini. *Improved iterative Bayesian unfolding*. 2010. arXiv: 1010.0632 [physics.data-an].

[92] Tim Adye. "Unfolding algorithms and tests using RooUnfold." In: *PHYSTAT 2011*. Geneva: CERN, May 2011. DOI: 10.5170/CERN-2011-006.313. arXiv: 1105.1160 [physics.data-an].

[93] Andreas Hocker and Vakhtang Kartvelishvili. "SVD approach to data unfolding." In: *Nucl. Instrum. Meth. A* 372 (1996), pp. 469–481. DOI: 10.1016/0168-9002(95)01478-0. arXiv: hep-ph/9509307.

[94] Jakub Kvapil. "Production of charm jets tagged with D^0 mesons in pp collisions at $\sqrt{s} = 13$ TeV with ALICE." Presented 21 Apr 2022. 2022. URL: https://cds.cern.ch/record/2811560.

[95] "Measurement of the production of charm jets tagged with D^0 mesons in pp collisions at $\sqrt{s} = 5.02$ and 13 TeV." In: (Apr. 2022). arXiv: 2204.10167 [nucl-ex].

[96] Shreyasi Acharya et al. "Measurements of inclusive jet spectra in pp and central Pb-Pb collisions at $\sqrt{s_{\mathrm{NN}}} = 5.02$ TeV." In: *Phys. Rev. C* 101.3 (2020), p. 034911. DOI: 10.1103/PhysRevC.101.034911. arXiv: 1909.09718 [nucl-ex].

[97] Shreyasi Acharya et al. "Measurement of D^0, D^+, D^{*+} and D_s^+ production in pp collisions at $\sqrt{s} = 5.02$ TeV with ALICE." In: *Eur. Phys. J. C* 79.5 (2019), p. 388. DOI: 10.1140/epjc/s10052-019-6873-6. arXiv: 1901.07979 [nucl-ex].

[98] Torbjorn Sjostrand, Stephen Mrenna, and Peter Z. Skands. "A Brief Introduction to PYTHIA 8.1." In: *Comput. Phys. Commun.* 178 (2008), pp. 852–867. DOI: 10.1016/j.cpc.2008.01.036. arXiv: 0710.3820 [hep-ph].

[99] Bo Andersson, G. Gustafson, G. Ingelman, and T. Sjostrand. "Parton Fragmentation and String Dynamics." In: *Phys. Rept.* 97 (1983), pp. 31–145. DOI: 10.1016/0370-1573(83)90080-7.

[100] Torbjorn Sjostrand. "Jet Fragmentation of Nearby Partons." In: *Nucl. Phys. B* 248 (1984), pp. 469–502. DOI: 10.1016/0550-3213(84)90607-2.

[101] Stefano Frixione, Paolo Nason, and Carlo Oleari. "Matching NLO QCD computations with Parton Shower simulations: the POWHEG method." In: *JHEP* 11 (2007), p. 070. DOI: 10.1088/1126-6708/2007/11/070. arXiv: 0709.2092 [hep-ph].

[102] Stefano Frixione, Paolo Nason, and Giovanni Ridolfi. "A Positive-weight next-to-leading-order Monte Carlo for heavy flavour hadroproduction." In: *JHEP* 09 (2007), p. 126. DOI: 10.1088/1126-6708/2007/09/126. arXiv: 0707.3088 [hep-ph].

[103] Shreyasi Acharya et al. "Measurement of charged jet cross section in *pp* collisions at $\sqrt{s} = 5.02$ TeV." In: *Phys. Rev. D* 100.9 (2019), p. 092004. DOI: 10.1103/PhysRevD.100.092004. arXiv: 1905.02536 [nucl-ex].

[104] Javier L. Albacete et al. "Predictions for Cold Nuclear Matter Effects in p+Pb Collisions at $\sqrt{s_{_{NN}}} = 8.16$ TeV." In: *Nucl. Phys. A* 972 (2018), pp. 18–85. DOI: 10.1016/j.nuclphysa.2017.11.015. arXiv: 1707.09973 [hep-ph].

[105] Andy Buckley, James Ferrando, Stephen Lloyd, Karl Nordström, Ben Page, Martin Rüfenacht, Marek Schönherr, and Graeme Watt. "LHAPDF6: parton density access in the LHC precision era." In: *Eur. Phys. J. C* 75 (2015), p. 132. DOI: 10.1140/epjc/s10052-015-3318-8. arXiv: 1412.7420 [hep-ph].

[106] K. J. Eskola, H. Paukkunen, and C. A. Salgado. "EPS09 - Global NLO analysis of nuclear PDFs and their uncertainties." In: *PoS* High-pT physics09 (2009). Ed. by Kari J. Eskola, Peter Lévai, Andreas Morsch, Vojtech Petracek, and Jan Rak, p. 019. DOI: 10.22323/1.080.0019. arXiv: 0903.1956 [hep-ph].

[107] 1642-1727 Newton Isaac, ed. *Isaac Newton letter to Robert Hooke, 1675*. URL: https://discover.hsp.org/Record/dc-9792/Description#tabnav, https://digitallibrary.hsp.org/index.php/Detail/objects/9792.

SAMENVATTING

We zijn nieuwsgierig, daarom weten we. We zijn nieuwsgierig naar het Universum. We kijken naar de lucht en stellen vragen als "Wat zijn die glimmende objecten 's nachts?" of "Waarom is het zo helder overdag?" We gaan op zoek naar antwoorden op die vragen en eindigen met nieuwe vragen zoals "Hoe is het universum ontstaan?" en "Hoe was het toen het ontstond?" Met de Big Bang-theorie geloven we nu dat het Universum niet dezelfde sterren en planeten was als we nu zien, maar dat het destijds gewoon een zeer hete vloeistof genaamd quark-gluon plasma (QGP) was. Nu, wat is deze vloeistof, hoe gedraagt hij zich en wat zijn zijn eigenschappen? Als we iets leren, eindigen we met iets nuttigs doen met dat stukje kennis. Dit is altijd gebeurd in de geschiedenis van de menselijke beschaving. Het vermogen om vuur te beheersen stelde ons in staat voedsel te koken en ziekten te verminderen door pathogenen in het voedsel te doden. Einstein's theorieën over zwaartekracht stelden ons in staat satellieten te gebruiken om op aarde in realtime nauwkeurig te navigeren. Toen Tim-Berners Lee bij CERN het Web uitvond om informatie te beheren en te delen via internet, kon niemand begrijpen hoe dat vandaag de dag de wereld zou vormgeven. Ik geloof dat ons gezamenlijk onderzoek naar QGP ons zeker zou helpen sterke interacties op subatomair niveau te begrijpen. Ik ben nieuwsgierig en kijk erg uit naar de technologische vooruitgang die zou voortvloeien uit onderzoek in de deeltjesfysica dat we nog moeten doorgronden.

Dit proefschrift is een poging om een deuk te maken en onze kennis van sterke interacties tussen quarks en gluonen, de fundamentele deeltjes die gevangen zitten in proton- en neutronachtige hadronen maar vrij stromen in een hete medium, d.w.z. het QGP, te vergroten.

We begonnen dit proefschrift met Hoofdstuk 1, waarin de motivatie en nieuwsgierigheid die het onderzoek in dit proefschrift aansturen, werden geïntroduceerd. Hoofdstuk 2 breidde de motivatie uit door sterke interacties te introduceren en de manier waarop onderzoek in de deeltjesfysica wordt gedaan. Met Hoofdstuk 3 werd de lezer geïntroduceerd in de motivatie achter het bestuderen van jets met een zware smaak. Hoofdstuk 4 introduceerde de experimentele opstelling die werd gebruikt om het onderzoek in dit proefschrift uit te voeren. De strategie achter de analyses werd beschreven in Hoofdstuk 5. Charm jets werden gereconstrueerd door geladen deeltjes te clusteren met behulp van het anti-k_T algoritme, en ervoor te zorgen dat de jets een D^0 meson bevatten onder hun samenstellende deeltjes. Het anti-k_T-algoritme zorgde ervoor dat de twee dichtstbijzijnde deeltjes met de hoogste energie werden geclusterd voordat het volgende deeltje in de cluster werd gecombineerd om een jet te vormen. Voordat een jet kon worden gereconstrueerd uit de geladen deeltjes in een event, werd het samenstellende D^0 meson gereconstrueerd uit zijn dochterdeeltjes die vervolgens werden vervangen door het viermomentum van hun moeder D^0 in de verzameling geladen deeltjes in het event. Hoofdstukken 6, 7, en 8 beschrijven de

drie analyses die zijn uitgevoerd voor charmejets, alle bij de massacentrumenergie $\sqrt{s_{\mathrm{NN}}} = 5,02$ TeV.

Ten eerste werd in Hoofdstuk 6 de productiekruisdoorsnede van charm jets in pp-botsingen gerapporteerd. In het volgende hoofdstuk werd de productiekruisdoorsnede van charm jets in p–Pb-botsingen gerapporteerd, samen met de nucleaire modificatiefactor. In het daaropvolgende hoofdstuk werd een meting van de fragmentatiefunctie van charm-jets in pp-botsingen gerapporteerd door te kijken naar het jet-momentum gedragen door zijn constituerende charm meson (D^0). Charm jets in pp-botsingen werden geclusterd met vier stralen, $R = 0,2$, $0,3$, $0,4$ en $0,6$, terwijl die in p-Pb-botsingen werden geclusterd met $R = 0,3$.

De resultaten die in deze thesis worden gepresenteerd, worden vergeleken met verschillende Leading-Order (LO) en Next-to-Leading-Order (NLO) PYTHIA-modellen. Het PYTHIA-programma wordt gebruikt om botsingen met hoge energie te genereren. Theorie en modellen voor verschillende fysische aspecten zijn aanwezig in PYTHIA, waaronder harde en zachte interacties, partondistributies, initiële en eindtoestand-parton-showers, meervoudige-parton-interacties, fragmentatie en verval [86].

De pp-resultaten in Hoofdstuk 6 en 8 worden vergeleken met twee LO-modellen en een NLO-model. Een LO-model is het oorspronkelijke hadronisatiemodel in PYTHIA dat de volgende harde processen simuleert: $\mathrm{gg} \to \mathrm{c\bar{c}}$ en $\mathrm{q\bar{q}} \to \mathrm{c\bar{c}}$. Het tweede LO-model gebruikt Kleur Herbinding (CR voor *Colour Reconnection* in het Engels) in hadronisatie en omvat alle zachte processen. Het NLO-model gebruikt de POWHEG BOX om partonische gebeurtenissen te genereren, d.w.z. parton splijtingen en gluonstraling, op NLO-niveau.

Het LO-model met CR en zachte processen geeft de beste beschrijving van de doorsnede en fragmentatieverdeling van charm jets in pp-botsingen in vergelijking met het LO-model met alleen harde processen. Data-metingen tonen overeenkomsten met POWHEG + PYTHIA 8-voorspellingen binnen experimentele en theoretische onzekerheden. De productie van charm wordt voldoende goed gemodelleerd in de huidige mechanismen, en deze resultaten zijn openbaar beschikbaar (Zie [95]).

De partondichtheidsfunctie voor het proton werd verkregen uit de LHAPDF-6-interpolator met de PDF-set CT10nlo [105]. Voor het simuleren van p–Pb-botsingen werd de nucleaire partondichtheidsfunctie in een loodion genomen van de EPS09nlo [106]. Net als de doorsnede van charm-jets in pp-botsingen, stemt de doorsnede in p–Pb-botsingen voor charm-jets met $R = 0,3$ die wordt gepresenteerd in Hoofdstuk 7 ook overeen met POWHEG + PYTHIA 6 NLO-theoretische voorspellingen binnen de gegevens- en theoretische onzekerheden. Ook werd gevonden dat de nucleaire modificatiefactor R_{pPb} overeenkomt met één binnen statistische en systematische onzekerheden. Er lijkt een afwezigheid te zijn van grote modificaties in de initiële partondistributies samen met een afwezigheid van eindtoestandseffecten op de productie van charm-jets met $p_{\mathrm{T}} > 5$ GeV/c.

ସାରାଂଶ

ଆମେ ଜିଜ୍ଞାସୁ, ତେଣୁ ଆମେ ଜାଣୁ । ଆମେ ବ୍ରହ୍ମାଣ୍ଡକୁ ନେଇ ଜିଜ୍ଞାସୁ ଅଟୁ । ଆମେ ଯେବେ ଆକାଶକୁ ଦେଖୁ, ''ରାତ୍ରି ଆକାଶରେ ସେହି ଜାଜ୍ୱଲ୍ୟମାନ ବସ୍ତୁଗୁଡ଼ିକ କଣ ହୋଇପାରେ?'' କିମ୍ବା ''ଦିବାଲୋକରେ କାହିଁକି ଏତେ ଉଜ୍ଜ୍ୱଳ?'' ଭଳି ମନରେ ଅନେକ ପ୍ରଶ୍ନବାଚୀ । ଆମେ ସେହି ପ୍ରଶ୍ନର ଉତ୍ତର ଖୋଜିବା ଆରମ୍ଭ କରୁ ଏବଂ ''ବ୍ରହ୍ମାଣ୍ଡ କିପରି ଆରମ୍ଭ ହେଲା?'' ଓ ''ଏହା କିପରି ସୃଷ୍ଟି ହେଲା?'' ପରି ନୂତନ ପ୍ରଶ୍ନଗୁଡ଼ିକ ସହିତ ଶେଷରେ ଉପନୀତ ହୋଇଥାଉ । ବୃହତ ବିସ୍ଫୋଟ ସିଦ୍ଧାନ୍ତ (the Big Bang theory) ସହିତ, ଆମେ ବର୍ତ୍ତମାନ ବିଶ୍ୱାସ କରୁ ଯେ ସୃଷ୍ଟି ହେବା ସମୟରେ ବ୍ରହ୍ମାଣ୍ଡ ଆଜିର ଗ୍ରହ ନକ୍ଷତ୍ର ଭଳି ନଥାଇ କ୍ୱାର୍କ୍-ଗ୍ଲୁଓନ୍ ପ୍ଲାଜ୍ମା (କ୍ୱା.ଗ୍ଲୁ.ପ୍ଲା / କ୍ୟୁଜିପି / QGP) ନାମକ ଏକ ଅତ୍ୟଧିକ ଗରମ ତରଳ ଥିଲା । ବର୍ତ୍ତମାନ, ଏହି ତରଳ କ'ଣ, ଏହା କିପରି ବ୍ୟବହାର କରେ ଏବଂ ଏହାର ଗୁଣଗୁଡ଼ିକ କ'ଣ? ଯେତେବେଳେ ଆମେ କିଛି ଜାଣୁ, ସେହି ଜ୍ଞାନ ସହିତ ଆମେ କିଛି ଉପଯୋଗୀ କାର୍ଯ୍ୟ କରିଥାଉ । ଏହା ମାନବ ସଭ୍ୟତାର ଇତିହାସରେ ସର୍ବଦା ଘଟି ଆସିଛି । ଅଗ୍ନି ନିୟନ୍ତ୍ରଣ କରିବାର କ୍ଷମତା ଆମକୁ ଖାଦ୍ୟ ରାନ୍ଧିବା ଏବଂ ଖାଦ୍ୟରେ ଜୀବାଣୁକୁ ମାରି ରୋଗ ହ୍ରାସ କରିବାରେ ସକ୍ଷମ କଲା । ମାଧ୍ୟାକର୍ଷଣ ଉପରେ ଆଇନଷ୍ଟାଇନଙ୍କ ସିଦ୍ଧାନ୍ତ ଆମକୁ ମନୁଷ୍ୟ ନିର୍ମିତ ଉପଗ୍ରହଗୁଡ଼ିକ ବ୍ୟବହାର କରିବାରେ ସକ୍ଷମ କଲା ଯଦ୍ୱାରା ଆମେ ସଠିକ୍ ଭାବେ ପୃଥିବୀରେ ଦିଗ ଚାଳନ କରି ପାରିଥାଉ । ଯେତେବେଳେ ଟିମ୍-ବର୍ଣ୍ଣର୍ସ୍ ଲି ସର୍ନ୍ (CERN) ଠାରେ ଇଣ୍ଟରନେଟ୍ (internet) ମାଧ୍ୟମରେ ସୂଚନା ପରିଚାଳନା ଏବଂ ବାଣ୍ଟିବା ପାଇଁ ୱେବ୍ (Web) ଉଦ୍ଭାବନ କରିଥିଲେ, କେହି କେବେ ଭାବି ପାରି ନଥିବେ ତାହା ଆଜି ବିଶ୍ୱରେ ଏଭଳି ପ୍ରଭାବ ପକେଇବ । ମୋର ବିଶ୍ୱାସ ଯେ କ୍ୱାର୍କ୍-ଗ୍ଲୁଓନ୍ ପ୍ଲାଜ୍ମା ଉପରେ ଆମର ସାମୂହିକ ଗବେଷଣା ଆମକୁ ଉପ-ପରମାଣୁ ସ୍ତର (subatomic level) ରେ ଶକ୍ତିଶାଳୀ ପାରସ୍ପରିକତା (strong interactions) କୁ ବୁଝିବାରେ ନିଶ୍ଚିତ ଭାବେ ସାହାଯ୍ୟ କରିବ । କଣିକା ପଦାର୍ଥ ବିଜ୍ଞାନର ଗବେଷଣାରୁ କ'ଣ ବୈଷୟିକ ପ୍ରଗତି ହେବ ଯାହାକୁ ଆମେ ଏପର୍ଯ୍ୟନ୍ତ ଜାଣିନାହୁଁ, ତାହାକୁ ନେଇ ମୁଁ ଜିଜ୍ଞାସୁ ଏବଂ ଅତ୍ୟନ୍ତ ଉତ୍ସୁକ ।

ଏହି ପ୍ରବନ୍ଧରେ ପ୍ରଦର୍ଶିତ ଗବେଷଣା କ୍ୱାର୍କ୍ ଏବଂ ଗ୍ଲୁଓନ୍ ମଧ୍ୟରେ ହେଉଥିବା ଶକ୍ତିଶାଳୀ ପାରସ୍ପରିକତା ବିଷୟରେ ଆମର ଜ୍ଞାନକୁ ଆଉ ପାଦେ ଆଗକୁ ବଢ଼ାଇବା ରେ ଏକ ଛୋଟ ପ୍ରୟାସ, କ୍ୱାର୍କ୍ ଏବଂ ଗ୍ଲୁଓନ୍ - ସେହି ମୌଳିକ କଣିକାଗୁଡ଼ିକ ଯାହା ପ୍ରୋଟନ୍ ଏବଂ ନ୍ୟୁଟ୍ରନ୍ ଭଳି ହାଡ୍ରନ୍ ରେ ସୀମିତ ଥାନ୍ତି କିନ୍ତୁ ମୁକ୍ତ ଭାବରେ ଏକ ଉତପ୍ତମାଧ୍ୟମ (ଯଥା କ୍ୱାର୍କ୍-ଗ୍ଲୁଓନ୍ ପ୍ଲାଜ୍ମା) ରେ ପ୍ରବାହିତ ହୋଇଥାନ୍ତି ।

ଆମେ ଏହି ପ୍ରବନ୍ଧ ଅଧ୍ୟାୟ ୧ ସହିତ ଆରମ୍ଭ କଲୁ ଯେଉଁଠାରେ ଏହି ପ୍ରବନ୍ଧରେ ପ୍ରଦର୍ଶିତ ଗବେଷଣାକୁ ଚଳାଉଥିବା ପ୍ରେରଣା ଏବଂ ଜିଜ୍ଞାସା ପ୍ରବର୍ତ୍ତିତ ହୋଇଥିଲା । ଏହି ଗବେଷଣା ପାଇଁ ପ୍ରେରଣା ଉପରେ ଅଧ୍ୟାୟ ୨ ରେ ଶକ୍ତିଶାଳୀ ପାରସ୍ପରିକତା ଏବଂ କଣିକା ପଦାର୍ଥ ବିଜ୍ଞାନରେ ଗବେଷଣାକରିବାର ପଦ୍ଧତି ର ପରିଚୟ ଦେଇ ବିସ୍ତାର କରାଗଲା । ପାଠକ ଅଧ୍ୟାୟ ୩ ସାହାଯ୍ୟରେ ଭାରୀ-ସ୍ୱାଦ (heavy flavour) ଜେଟ୍ ମାନଙ୍କର ଅଧ୍ୟୟନ ପଛରେ ପ୍ରେରଣା ସହିତ ପରିଚିତ ହେଲେ । ଏହି ପ୍ରବନ୍ଧ ରେ ଗବେଷଣା କରିବା ପାଇଁ ବ୍ୟବହୃତ ପରୀକ୍ଷାମୂଳକ ବ୍ୟବସ୍ଥା ଆମେ ଅଧ୍ୟାୟ ୪ ରେ ଉପସ୍ଥାପନ କରିଥିଲୁ । ବିଶ୍ଳେଷଣ ପଛରେ ରଣନୀତି ଅଧ୍ୟାୟ ୫ ରେ ବର୍ଣ୍ଣନା କରାଯାଇଥିଲା । ଆଣ୍ଟି-କେଟି ଗଣାଣତତ୍ତ୍ୱ (anti-k_{T} algorithm) ବ୍ୟବହାର କରି ଆବେଶିତ (charged) କଣିକାଙ୍କୁ ଗୁଚ୍ଛ (cluster) ବ୍ୟବସ୍ଥାରେ ଏକାଠି କରି ଜେଟ୍ ବନାଯାଇଥିଲା ଏବଂ ପ୍ରତ୍ୟେକ ଆବେଶିତ ଜେଟ୍ ଏକ ଚାର୍ମ୍ ଜେଟ୍ ହେବା ପାଇଁ ତାହାର ଉପାଦାନ କଣିକା ମଧ୍ୟରେ ଏକ ଡି୦ ମେସନ୍ ର ଉପସ୍ଥିତି ସୁନିଶ୍ଚିତ କରାଯାଇଥିଲା । ଆଣ୍ଟି-କେଟି ଗଣାଣତତ୍ତ୍ୱ ଏହା ସୁନିଶ୍ଚିତ କଲା ଯେ ଏକ ଜେଟ୍ ଗଠନ କରିବାରେ ସର୍ବୋଚ୍ଚ ଶକ୍ତି ସହିତ ସବୁଠୁ ନିକଟତମ ଦୁଇଟି କଣିକା ସର୍ବ ପ୍ରଥମେ ଗୁଚ୍ଛିତ ହୋଇଥାନ୍ତୁ । ଏକ ଘଟଣାର ଆବେଶିତ କଣିକାଗୁଡ଼ିକରୁ ଏକ ଜେଟ୍ ପୁନଃନିର୍ମାଣ ହେବା ପୂର୍ବରୁ, ସର୍ବ ପ୍ରଥମେ ଏହାର ଉପାଦାନ ଡି୦ ମେସନ୍ କୁ ନିଜ ଶିଶୁ କଣିକାଙ୍କଠୁ ପୁନଃନିର୍ମାଣ କରାଯାଇଥିଲା ଯାହା ପରେ ସେମାନଙ୍କୁ ତାଙ୍କ ମାତା ଡି୦ ମେସନ୍ ର ୪-ଗତି ଦ୍ୱାରା ସେହି ଘଟଣାର ଆବେଶିତ କଣିକା ସଂଗ୍ରହରେ ବଦଳା ଯାଇଥିଲା । ଚାର୍ମ୍ ଜେଟ୍ ପାଇଁ କେନ୍ଦ୍ର-ସଂଭାବିତ ଉର୍ଜା $\sqrt{\text{ଏସ}_{\text{ନ୍ୟୁନ୍ୟୁ}}}$ = ୫.୦୨ ଟିଇଭି ରେ କରାଯାଇଥିବା ତିନୋଟି ବିଶ୍ଳେଷଣକୁ ଅଧ୍ୟାୟ ୬, ୭, ଏବଂ ୮ ରେ ବର୍ଣ୍ଣନା କରାଯାଇଛି ।

ପ୍ରଥମତଃ, ପ୍ରୋଟନ୍-ପ୍ରୋଟନ୍ ସଂଘର୍ଷରେ ଚାର୍ମ୍ ଜେଟ୍ ର ଉତ୍ପାଦନ କ୍ରସ୍ ବିଭାଗ ଅଧ୍ୟାୟ ୬ ରେ ବୃତ୍ତାନ୍ତ କରାଯାଇଥିଲା । ପରବର୍ତ୍ତୀ ଅଧ୍ୟାୟରେ, ପ୍ରୋଟନ୍-ସୀସା ସଂଘର୍ଷରେ ଚାର୍ମ୍ ଜେଟ୍ ର ଉତ୍ପାଦନ କ୍ରସ୍ ବିଭାଗ ସହିତ ପରମାଣୁ ପରିବର୍ତ୍ତନ କାରକ ବୃତ୍ତାନ୍ତ କରାଯାଇଥିଲା । ଚାର୍ମ୍ ଜେଟ୍ ର ଗତି କେତେ ମାତ୍ରା ରେ ନିଜ ଉପାଦାନ ଚାର୍ମ୍ ମେସନ୍ (ଡି୦) ଦ୍ୱାରା ବହନ କରାଯାଇଛି ତାହା ଦେଖି ପ୍ରୋଟନ୍-ପ୍ରୋଟନ୍ ସଂଘର୍ଷରେ ଚାର୍ମ୍ ଜେଟ୍ ର ଖଣ୍ଡବିଖଣ୍ଡନ କାର୍ଯ୍ୟର ଏକ ମାପ ପରବର୍ତ୍ତୀ ଅଧ୍ୟାୟରେ ବର୍ଣନା କରାଯାଇଥିଲା । ପ୍ରୋଟନ୍-ପ୍ରୋଟନ୍ ସଂଘର୍ଷରେ ଚାର୍ମ୍ ଜେଟ୍ ଗୁଡିକ ଚାରୋଟି ବ୍ୟାସାର୍ଦ୍ଧ, ବ୍ୟାସାର୍ଦ୍ଧ = ୦.୨, ୦.୩, ୦.୪, ଏବଂ ୦.୬, ସହିତ ଗୁଚ୍ଛିତ ହୋଇଥିବାବେଳେ ପ୍ରୋଟନ୍-ସୀସା ସଂଘର୍ଷରେ ଥିବା ଚାର୍ମ୍ ଜେଟ୍ ଗୁଡିକ ବ୍ୟାସାର୍ଦ୍ଧ = ୦.୩ ସହିତ ଗୁଚ୍ଛିତ ହୋଇଥିଲେ ।

ଏହି ପ୍ରବନ୍ଧରେ ଉପସ୍ଥାପିତ ଫଳାଫଳକୁ ବିଭିନ୍ନ ଅଗ୍ରଣୀ-କ୍ରମ (ଅ.କ୍ର / LO) ଏବଂ ଅଗ୍ରଣୀର-ପରବର୍ତ୍ତୀ-କ୍ରମ (ଅ.ପ.କ୍ର / NLO) ପିଥିଆ ମଡେଲ୍ ସହିତ ତୁଳନା କରାଯାଇଛି । ଉଚ୍ଚ-ଶକ୍ତି ପଦାର୍ଥ ସଂଘର୍ଷ ଘଟଣା ସୃଷ୍ଟି କରିବାକୁ ପିଥିଆ କାର୍ଯ୍ୟକ୍ରମ ବ୍ୟବହୃତ ହୋଇଛି । କଠିନ ଏବଂ ନରମ ପାରସ୍ପରିକତା, ପାର୍ଟନ୍ ବଣ୍ଟନ, ପ୍ରାରମ୍ଭିକ ଏବଂ ଅନ୍ତିମ ସ୍ଥିତି ପାର୍ଟନ୍ ସାୱାର, ମଲ୍ଟିପାର୍ଟନ୍ ପାରସ୍ପରିକତା ଖଣ୍ଡବିଖଣ୍ଡନ ଏବଂ କ୍ଷୟ ସମିତ ଭୌତିକ ପରିପ୍ରେକ୍ଷ୍ୟରେ ବିଭିନ୍ନ ସିଦ୍ଧାନ୍ତ ଏବଂ ମଡେଲ୍ ପିଥିଆ ରେ ଉପସ୍ଥିତ [୯୪] ।

ଅଧ୍ୟାୟ ୬ ଏବଂ ୮ ରେ ପ୍ରୋଟନ୍-ପ୍ରୋଟନ୍ ଫଳାଫଳଗୁଡିକ ଦୁଇଟି ଅ.କ୍ର ମଡେଲ୍ ଏବଂ ଏକ ଅ.ପ.କ୍ର ମଡେଲ୍ ସହିତ ତୁଳନା କରାଯାଇଛି । ଗୋଟିଏ ଅ.କ୍ର ମଡେଲ୍ ହେଉଛି ପିଥିଆ ରେ ମୂଳ ହାଡ୍ରୋନାଇଜେସନ୍ ମଡେଲ୍, ଯାହା ନିମ୍ନଲିଖିତ କଠିନ ପ୍ରକ୍ରିୟାଗୁଡ଼ିକୁ ଅନୁକରଣ କରେ: $gg \to c\bar{c}$ ଏବଂ $qq \to c\bar{c}$ । ଦ୍ୱିତୀୟ ଅ.କ୍ର ମଡେଲ୍ ହାଡ୍ରୋନାଇଜେସନ୍ ରେ ରଙ୍ଗ ପୁନଃ-ସଂଯୋଗ (Colour Reconnection / ର.ପୁ / CR) ବ୍ୟବହାର କରେ ଏବଂ ସମସ୍ତ ନରମ ପ୍ରକ୍ରିୟା ଅନ୍ତର୍ଭୁକ୍ତ କରେ । ପାର୍ଟନିକ ଘଟଣା, ଯଥା ଅ.ପ.କ୍ର ରେ ହେଉଥିବା ପାର୍ଟନ୍ ବିଭାଜନ ଏବଂ ଗ୍ଲୁଓନ୍ ବିକିରଣ, ସୃଷ୍ଟି କରିବାକୁ ଅ.ପ.କ୍ର ମଡେଲ୍ ପୌହେଗ ବାକ୍ସ (POWHEG BOX) ବ୍ୟବହାର କରେ ।

ପ୍ରୋଟନ୍-ପ୍ରୋଟନ୍ ସଂଘର୍ଷରେ ଚାର୍ମ୍ ଜେଟ୍ ଙ୍କର କ୍ରସ୍ ବିଭାଗ ଏବଂ ତାଙ୍କ ଖଣ୍ଡବିଖଣ୍ଡନ ବଣ୍ଟନ ର କେବଳ କଠିନ ପ୍ରକ୍ରିୟା ଥିବା ଅ.କ୍ର ମଡେଲ୍ ତୁଳନାରେ ରଙ୍ଗ ପୁନଃ-ସଂଯୋଗ ଏବଂ ନରମ ପ୍ରକ୍ରିୟା ଥିବା ଅ.କ୍ର ମଡେଲ୍ ସର୍ବୋତ୍ତମ ବର୍ଣ୍ଣନା ପ୍ରଦାନ କରେ । ଡାଟା ମାପଗୁଡିକ ପୌହେଗ + ପିଥିଆ ୮ ପୂର୍ବାନୁମାନ ସହ ପରୀକ୍ଷାମୂଳକ ଏବଂ ତତ୍ତ୍ୱଗତ ଅନିଶ୍ଚିତତା ମଧ୍ୟରେ ସହମତି ଦେଖାଇଛନ୍ତି । ଚାର୍ମ୍ ଉତ୍ପାଦନ ସାମ୍ପ୍ରତିକ ଯନ୍ତ୍ରକୌଶଳରେ ଯଥେଷ୍ଟ ଭଲ ଭାବରେ ମଡେଲ୍ ହୋଇଛି, ଏବଂ ଏହି ଫଳାଫଳଗୁଡ଼ିକ ସର୍ବସାଧାରଣରେ ପତ୍ରିକା [୮୪] ରେ ଉପଲବ୍ଧ । ସିଟି୧୦ଅ.ପ.କ୍ର (CT10nlo) ପାର୍ଟନ୍ ବଣ୍ଟନ କାର୍ଯ୍ୟ (ପା.ବ.କା. / ପିଡିଏଫ / PDF) ସମୁଚ କୁ ନିୟୋଜିତ କରି (ଲେ.ଉ.ଆ.ପା.ବ.କା ୬ / LHAPDF6) ଇଣ୍ଟରପୋଲେଟରର ସାହାଯ୍ୟରେ ପ୍ରୋଟନ୍ ମଧ୍ୟରେ ପାର୍ଟନ୍ ର ବଣ୍ଟନ ନିର୍ଣ୍ଣୟ କରାଯାଇଥିଲା [୫୪] । ପ୍ରୋଟନ୍-ସୀସା ସଂଘର୍ଷକୁ ଅନୁକରଣ କରିବା ପାଇଁ, ଏକ ସୀସା ଆୟନ ଭିତର ର ଆଣବିକ ପାର୍ଟନ୍ ବଣ୍ଟନ କାର୍ଯ୍ୟ (ଆ.ପା.ବ.କା / nPDF) ଇପିଏସ୦୯ଅ.ପ.କ୍ର (EPS09nlo) ସମୁଚ ରୁ ନିଆଯାଇଥିଲା [୬୯] । ପ୍ରୋଟନ୍-ପ୍ରୋଟନ୍ ସଂଘର୍ଷରେ ଚାର୍ମ୍ ଜେଟ୍ ର କ୍ରସ୍ ବିଭାଗ ପରି, ଅଧ୍ୟାୟ ୬ ରେ ଉପସ୍ଥାପିତ ବ୍ୟାସାର୍ଦ୍ଧ = ୦.୩ ର ଚାର୍ମ୍ ଜେଟ୍ ପାଇଁ ପ୍ରୋଟନ୍-ସୀସା ସଂଘର୍ଷରେ କ୍ରସ୍ ବିଭାଗ ମଧ୍ୟ ପୌହେଗ + ପିଥିଆ ୬ ଅ.ପ.କ୍ର ପୂର୍ବାନୁମାନ ସହ ପରୀକ୍ଷାମୂଳକ ଏବଂ ତତ୍ତ୍ୱଗତ ଅନିଶ୍ଚିତତା ମଧ୍ୟରେ ସହମତି ଦେଖାଇଛି । ଆହୁରି ମଧ୍ୟ, ଆଣବିକ ରୂପାନ୍ତରଣ କାରକ ଆର ପ୍ରୋ-ସି ପରିସଂଖ୍ୟାନ ଏବଂ ବ୍ୟବସ୍ଥିତ ଅନିଶ୍ଚିତତା ମଧ୍ୟରେ ଏକତା ସହିତ ମେଳ ଖାଉଥିବାର ଦେଖିବାକୁ ମିଳିଥିଲା । $\hat{p}_T$ > ୫ ଗି.ଇ.ଭି / ସି ର ଅନୁପ୍ରସ୍ଥ ଗତି ଥିବା ଚାର୍ମ୍ ଜେଟ୍ ର ଉତ୍ପାଦନ ଉପରେ ଚୂଡ଼ାନ୍ତ-ସ୍ଥିତି ପ୍ରଭାବର ଅନୁପସ୍ଥିତି ସହିତ ପ୍ରାରମ୍ଭିକ ପାର୍ଟନ୍ ବିତରଣରେ ବୃହତ ପରିବର୍ତ୍ତନଗୁଡ଼ିକର ଅନୁପସ୍ଥିତି ଦେଖାଯାଉଛି ।

ACKNOWLEDGEMENTS

"*If I have seen further, it is by standing on the shoulders of giants*," wrote Issac Newton once in a letter to Robert Hook in February 1675 [107]. And so have I, seen further.

André, thank you. You are no longer among us to read this thesis, but thank you so much for giving me this opportunity. I miss talking to you, your passion during the group meetings, your encouraging words post presentations, your jokes on Alessandro, and your "*so on and so forth*"s. I know how much you wanted to award the degree yourself. I will always treasure my memories of you.

Alessandro, thank you for pushing me to complete the thesis. This manuscript wouldn't have seen the day had it not been for your fast and efficient action and comments. Your guidance proved to be so helpful. You have been the only constant in this journey, being there when André interviewed me, to the end. Thank you for everything :)

Thomas, thank you so much for giving such a detailed look into this manuscript. Your active involvement during group meetings, irrespective of who is presenting or what topic is being presented, always helped me (and I am sure everyone else) gather a more generic physics perspective and that has been so inspiring.

Barbara, Cristina, you were my work parents. I could always go to the both of you and you listened to me. Outside office, you were my best friends. We went ice skating, bowling, bike riding, to bars, Keukenhof. You helped me put my feet on the ground in the Netherlands. I can never thank you enough. Love you both.

Every now and then, Barbara gave me tips on what she knew. I used to fail to grasp what she meant then. But in the end, I did realise and understand. Now I appreciate and thank her in my mind every time I hear her talking and advising me in my head :D. I was happy to have someone into all of Linux, Vim, Git, and LaTeXaround in the group/collaboration. Some things may be quite common, but some were not, and I am very happy I was on this side of the team. (Looking at you Mac/Emacs people.)

Marco, thank you so much for having an answer to so many of my questions, be it physics or otherwise. Our numerous walks around the Singel, visits to ALICE underground, and your offices at CERN and UU, the Texel walk, and so many more moments have always taught me so much. Your approach to understanding anything and everything has always resonated with me and inspired me. Thanks again.

Fabio, your leadership and active involvement in the HFCJ PAG really brought the physics out and gave meaning to the technical details in the analyses.

Jakub, it was really great collaborating with you. Thanks for the various meaningful discussions in the physics analyses.

Hadi Hassan, thanks for taking over from Barbara in running the trains for me and being so helpful and kind throughout, debugging the settings for wagons. Without you, completing various analyses wouldn't have been possible.

Thank you **Raimond** for leading the group at UU and ALICE, for various administrative help, and for bringing Subatomic Physics and Gravitational Waves together into GRASP. **Marta**, thank you for bringing so much energy to the group, and hosting the get-togethers at your home during the dull COVID time. Thanks **Rihan** and **Reshma** for giving me the little home since I landed in the Netherlands.

Thanks **Zhanna** for so many fun and learning moments while we were being Teaching Assistants. There were so many moments of confusion and doubts, as well as light-bulb moments. I learnt so much in our preparatory sessions, evaluating sessions, and every other discussion. Thank you for all your support and always having my back :)

Henrique, you always kept your doors open and answered my questions. You never shied away from giving all the crucial help I needed. You also helped me outside physics. Thank you :) Thanks **Luuk** and **Lennart** for being my PhD buddies. Thanks Lennart for cooking such delicious food for Luuk and me in Munich, and making us cook as well :D. We shared so many moments and I learnt a lot from you guys. **Mike**, thanks for being a part of the Haldane moment and so many other moments at UU and outside. **Jacopo**, life at Utrecht would have been very dull had it not been for you. Thank you a lot. Thanks **Davide** (Caffari), **Davide** (Lodato), **Annelis**, **Peter**, **Rene**, **Jae**, and **Monique**, for being a part of this journey. You were great colleagues and my life at UU was enriching because of you guys.

Ton, thanks so much for showing me around in Geneva, the all-you-can-eat restaurant there, and also showing me around the mechanical lab at UU, and sharing so many of your life experiences with me. Every moment was priceless.

I truly thank various institutions for organizing events that allowed me to meet various legends of the Physics community: Utrecht University for Gerard 't Hooft and Duncan Haldane in Utrecht, Nikhef for Francis Halzen in Amsterdam, Starmus for Robert Wilson and Barry Barish in Zurich, and Leiden University for Andrei Linde in Leiden, It was so much inspiring to meet them in real life, about whom I had only known from books and news.

Jajati sir and **Tapan** sir, you believed in me, and introduced me to high-energy physics. The numerous instances over the years when I met and conversed with you, both together and independently, it was always so much inspiring! Thank you Jajati sir for the numerous physics discussions, for introducing me to LaTeX, showing me around various labs at VECC, and giving me essential life lessons. I will forever be grateful. Tapan sir, thank you so much believing in me and inspiring me, for showing me where I can improve and grow, be it in my presentation skills, or in the field of physics, or in socializing. Thank you for the impromptu tests :D, for the underground visit to ALICE, and most importantly for introducing me to Sonia. You have had such a big role in shaping my life. **Mamata** ma'am, thank you for teaching me so much about life, and for the delicious meals. I very much appreciate.

Sonia, thank you dear. I am so lucky to have met you. Thank you for giving up all your career plans and joining me in life. You helped me so much in bringing this PhD to a conclusion, this belongs to you too. Love you forever. **Arpit**, when you first called me to tell me that you were coming to Utrecht, I was elated. And when you actually arrived at the Utrecht Centraal, and spoke in Odia with me, I suddenly

started feeling like at home, I had found a mini-Odisha! You gave me Cooking 101, and taught me how to eat with chopsticks. Our cycle rides including the ones with Brompton in and around Utrecht, and to other cities brought me so much joy, including in our times of crises. Our trips together in Switzerland were so crazy and fun, the ice-skating, the dangerous terrain we hiked, the skydiving, paragliding, and so many more countless memories. Our talks, discussions, sharing of ideas and visions, common thoughts and differences in opinions, thanks for everything. **Rahul**, thanks for the safe car ride, you know, in Switzerland. **Swarnenda**, thanks for all the weekend parties, intellectual discussions, and making the journey so much enjoyable. It's not easy to find someone one can hold a healthy argument and discussion with. You have been that someone. Thank you. I hope the Brompton purchase was just the beginning of a series of rides together. **Bharati**, from QM to CERN-Fermi Lab to this day, we have had so many experiences together. I learnt a lot from your learnings from before, during and after your PhD, and your critical and honest suggestions. Thanks for being there always. My **Vees**: **Somu**, **Chikna**, **Rana**, **Parida**, **Jena**, **Bimal**, and **Pranit**, thank you for your support since I have known you. Thank you both **Abinash** and **Swayam** for inspiring and encouraging me at so many stages in my physics journey. Thanks **Scott**, **Iris**, **Frisia**, and **Anton** for being so welcoming and helpful in this journey. Scott, your patience while engaging in Dutch with me, and while introducing me to your world is much appreciated. Thank you for being such a good friend.

Mama, **Papa**, thank you for all the evergreen love and support. I learnt and have been learning so much from you. Your care, and constant nudges and worries about my PhD pushed me towards completing this chapter in life. Words here won't be enough. You are the best. Thanks **Bibhu** for being the best bro. Your support in this journey has been priceless. Thank you **Ajaa** for constantly querying about my PhD and pushing me towards completion. You aren't here anymore, but I miss you. I wish I could tell you, I got it. **Aayi**, **Jeje-Maa**, **Mamu-Maayeen**, **Mausa-Mausi**, **Bada Mamu-Maayeen** thank you so much for your love and care. Thank you so very much for being my family.

COURSE OF LIFE

CAREER AND EDUCATION

2023-present
Cloud Engineer
TRKKN/OMG-NL
The Netherlands

2021-2022
Cloud Engineer
Annalect/OMG-NL
The Netherlands

2017-2021
PhD Researcher, Particle Physics
GRASP, Utrecht University and ALICE, CERN
The Netherlands and Switzerland

PhD Thesis

CHARM JETS:
PRODUCTION AND FRAGMENTATION OF
D^0-TAGGED CHARGED-PARTICLE JETS
IN SMALL COLLISION SYSTEMS

2011-2016
5-Year Integrated MSc in Physics
Physics and Astronomy, NIT Rourkela
India

Master's Thesis

THE STANDARD MODEL:
CALCULATING FERMION MASSES
USING THE HIGGS MECHANISM

2008-2010
Higher Secondary Education
Physics, Chemistry, Mathematics, Biology
BJB Junior College, Bhubaneswar
India

1996-2008
Kindergarten-Secondary Education
DAV Public School, CSPur, Bhubaneswar
India

PUBLICATIONS

arXiv:2204.10167
Measurement of the production of charm jets tagged with D^0 mesons in pp collisions at $\sqrt{s} = 5.02$ and 13 TeV
Journal of High Energy Physics

arXiv:2001.11339
Heavy-flavour jet production and charm fragmentation with ALICE at LHC
Springer Proceedings in Physics

arXiv:1510.07057
Population I Cepheids and understanding star formation history of the Small Magellanic Cloud
Research in Astronomy and Astrophysics